Fracture network characterization in enhanced geothermal systems by induced seismicity analysis

Version courte

Table des matières

Chapitre 1

Introduction

Les démarches énergétiques actuelles de nombreux pays du monde visent à accroître la part des énergies renouvelables afin de réduire les émissions de CO2. Le principal avantage de l'énergie géothermique par rapport à la plupart des autres sources d'énergie renouvelables est sa capacité à fournir une puissance de base sans grandes fluctuations comme l'énergie éolienne ou solaire (IEA, 2017). Pourtant, les systèmes hydrothermaux les plus viables économiquement et comparativement faciles à exploiter ne se trouvent pas en abondance sur Terre. Dans les pays ne disposant pas de ressources hydrothermales importantes, les systèmes géothermiques améliorés (EGS) devront jouer un rôle important pour parvenir à une augmentation significative de l'utilisation de l'énergie géothermique.

Les EGS visent à accéder à de la saumure chaude dans des réservoirs dont la perméabilité naturelle est trop faible pour permettre une extraction directe à des débits économiquement suffisants. Ils sont principalement situés dans des réservoirs fracturés et nécessitent une augmentation artificielle de la perméabilité du réseau de fractures par stimulation du réservoir (Breede et al., 2013). L'approche de stimulation la plus couramment utilisée est la stimulation hydraulique, au cours de laquelle un fluide à haute pression est injecté dans le sous-sol pour induire un mouvement de cisaillement sur les fractures qui conduit à une augmentation de leur ouverture (McClure et Horne, 2014). Dans les régions où les températures des réservoirs sont très élevées, la stimulation thermique est une technique largement utilisée. Les différences de température élevées entre le fluide injecté et la roche réservoir provoquent l'élargissement des fractures préexistantes ainsi que la création de nouvelles fractures par fissuration thermique (Axelsson et al., 2006).

Si des minéraux colmatent les fractures, ils peuvent être dissous en injectant des produits chimiques spéciaux dans le cadre d'une opération de stimulation chimique (PORTIER et al., 2009).

La stimulation du réservoir est un processus techniquement complexe qui implique des processus hydro-mécano-chimiques couplés entre le puits de forage, la roche réservoir et la saumure. La recherche dans ce domaine est en cours et les expériences des dernières décennies ont déjà permis de grandes avancées. Cependant, la stimulation des réservoirs sur les sites EGS s'accompagne régulièrement d'une sismicité induite, en particulier lors des opérations de stimulation hydraulique (EVANS et al., 2012). La majorité des événements sismiques induits lors du développement et de l'exploitation des réservoirs géothermiques sont d'une magnitude inférieure à celle qui causerait des dommages ou serait ressentie par la population (EVANS et al., 2012). Néanmoins, la sismicité induite peut atteindre des magnitudes inattendues et conduire à l'abandon d'un projet (HÄRING et al., 2008).

Si la sismicité induite est un risque potentiel dans le développement et l'exploitation des EGS, elle peut également être un outil précieux pour la caractérisation des réservoirs (CUENOT et al., 2008 ; DEICHMANN et al., 2014 ; LENGLINÉ et al., 2017). L'objectif de cette thèse est de démontrer comment la sismicité induite dans les systèmes géothermiques améliorés peut être utilisée pour caractériser le réseau de failles souterraines. Les points principaux sont d'identifier la géométrie du réseau de failles et de comprendre sa réaction mécanique pendant les opérations de stimulation du réservoir qui conduisent à la sismicité induite.

Pour comprendre théoriquement pourquoi la sismicité est induite pendant la stimulation des systèmes géothermiques améliorés, le chapitre 2 présente le contexte géomécanique de la génération des séismes. Le chapitre 3 donne un aperçu des techniques de détection et de localisation des tremblements de terre. Le chapitre 4 présente les deux sites EGS de Rittershoffen et de Soultz-sous-Forêts. Dans la partie principale de la thèse, deux cas différents de caractérisation de réseaux de failles à partir de la sismicité induite sont présentés. La première étude (chapitre 5) est une interprétation détaillée de la sismicité induite lors de la stimulation du puits GRT1 du réservoir géothermique profond de Rittershoffen. La deuxième étude (chapitre 6) présente une nouvelle méthode pour mettre en évidence la géométrie du réseau de failles dans les nuages sismiques qui ne présentent pas de caractéristiques planaires évidentes.

Chapitre 2

Géomécanique des séismes

Les contraintes dans la masse rocheuse souterraine sont le résultat de différentes forces qui agissent sur elle, comme la surcharge des roches au-dessus ou les forces tectoniques. La roche peut alors répondre à ces contraintes par une déformation élastique, une déformation ductile ou une déformation fragile. Lors d'une déformation fragile, la roche se brise et une fracture est créée. La contrainte de cisaillement libérée sur de telles fractures par le glissement des masses rocheuses est à l'origine des tremblements de terre (REID, 1910).

Les contraintes en chaque point de la masse rocheuse peuvent être décrites par le tenseur de contraintes (SHEARER, 2019), un tenseur symétrique d'ordre 2 à six composantes indépendantes. Pour tout champ de contrainte, on peut trouver un ensemble de trois plans orthogonaux de sorte qu'il n'y a que des contraintes normales et aucune contrainte de cisaillement agissant sur ces plans et le tenseur de contrainte prend donc une forme diagonale :

$$\sigma = \begin{pmatrix} \sigma_1 & 0 & 0 \\ 0 & \sigma_2 & 0 \\ 0 & 0 & \sigma_3 \end{pmatrix}, \tag{2.1}$$

avec $\sigma_1 \geq \sigma_2 \geq \sigma_3$ étant les contraintes principales.

Dans un réservoir souterrain, on suppose normalement que la contrainte verticale σ_v causée par le poids des terrains est l'une des contraintes principales (système de contrainte de Anderson (ANDERSON, 1951)). Les deux autres contraintes principales sont alors la contrainte horizontale maximum

σ_H et la contrainte horizontale minimum σ_h.

L'apparition du glissement sur une faille préexistante ou la création d'une nouvelle fracture dépend des contraintes normales et cisaillantes qui agissent sur celle-ci, lesquelles dépendent de l'orientation de la fracture par rapport au champ de contraintes local défini par les contraintes principales. Le cercle de Mohr visualise les relations possibles entre les contraintes normales et de cisaillement agissant sur un plan d'orientation quelconque (Fig. 2.1, à gauche) (MOHR, 1914). Si le système de coordonnées est choisi de manière à ce que les axes soient parallèles aux directions des contraintes principales du champ de contraintes local, le centre (a,b) et le rayon r du cercle de Mohr sont donnés par :

$$(a, b) = \left(\frac{1}{2}(\sigma_1 + \sigma_3),\ 0 \right) \tag{2.2}$$

$$r = \frac{1}{2}(\sigma_1 - \sigma_3). \tag{2.3}$$

Pour décider si un plan avec une certaine orientation est stable ou non, on peut appliquer un critère de glissement qui divise les conditions stables des conditions instables. Un critère couramment appliqué est le critère de Coulomb (COULOMB, 1773). Le glissement est atteint lorsque :

$$\tau = \mu\sigma + c \tag{2.4}$$

La contrainte de cisaillement τ s'oppose à la friction causée par la contrainte normale σ agissant sur le plan et le coefficient de friction μ de l'interface ainsi que la cohésion c que possède le matériau. Le critère de rupture de Coulomb peut être tracé avec le cercle de Mohr dans le diagramme σ-τ (Fig. 2.1, à gauche). Si le cercle de Mohr touche ou croise le critère de rupture, les failles ayant une orientation dans la zone où le cercle de Mohr se trouve au-dessus du critère de rupture glissent. L'angle θ entre un plan de faille ayant une orientation optimale pour la rupture et la direction de σ_1 dépend de l'angle de frottement $\phi = \arctan \mu$ de l'interface.

Dans la croûte terrestre, les fractures et les failles sont dans un état stable jusqu'à ce qu'un événement ou un processus modifie les conditions de telle
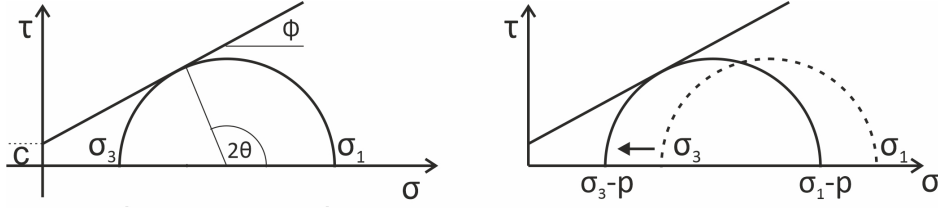
FIGURE 2.1 – Cercle de Mohr et critère de rupture de Coulomb (ligne droite). A gauche : le plan de faille orienté de façon optimale pour la rupture a l'angle θ à la direction σ_1. c est la cohésion, ϕ est l'angle de frottement de la roche. A droite : la pression de pore p réduit les contraintes totales et peut faire passer le cercle de Mohr de conditions stables à instables.

sorte que le critère de rupture soit atteint. Lors des opérations de stimulation dans les réservoirs géothermiques, on suppose que la cause la plus fréquente de cette perturbation des roches et donc de la sismicité induite est la pression du fluide appliquée. La raison pour laquelle les fractures glissent sous une pression de fluide accrue est que la pression du fluide interstitiel agit contre la masse rocheuse (TERZAGHI, 1936). Ainsi, la pression de pore p réduit la contrainte dans la masse rocheuse $\sigma_t ot$ à la contrainte dite effective $\sigma_e ff$:

$$\sigma_{i,eff} = \sigma_{i,tot} - p \,, \tag{2.5}$$

Lorsque l'on étudie la rupture d'une roche à l'aide de l'analyse de Mohr-Coulomb, il faut considérer la contrainte effective et non la contrainte totale (Fig. 2.1, à droite). L'injection de fluide entraîne une augmentation de la pression interstitielle, les contraintes effectives agissant sur la roche sont diminuées et la rupture s'ensuit, ce qui entraîne la création d'une perméabilité plus élevée.

Chapitre 3

Détection et localisation des tremblements de terre

3.1 Techniques de détection

Les algorithmes de détection largement utilisés sont basés sur la détection dite STA/LTA, également appelée détecteurs d'énergie. L'énergie moyenne sur une courte fenêtre temporelle de la forme d'onde (STA) est comparée à l'énergie moyenne sur une fenêtre temporelle plus longue (LTA). Si le rapport entre les deux est supérieur à un certain seuil, une détection est déclarée (ALLEN, 1982 ; WITHERS et al., 1998). Les détecteurs STA/LTA sont capables d'identifier les tremblements de terre avec des arrivées d'ondes P et S importantes, mais ont une capacité de détection limitée lorsqu'il s'agit d'événements de faible magnitude ou d'environnements bruyants.

Au cours des dernières années, un deuxième type de détecteur a été plus largement appliqué, basé sur la technique dite de corrélation de forme d'onde (LENGLINÉ et al., 2016 ; SHELLY et al., 2007 ; SKOUMAL et al., 2015). Contrairement à la détection STA/LTA, la détection par cette nouvelle technique exploite les similitudes dans la forme des ondes sismiques. La détection par corrélation de formes d'ondes nécessite une base de données initiale des séismes connus, les événements dits "templates", fournissant une référence pour les formes d'onde possibles des événements. L'algorithme de détection calcule le coefficient de corrélation, CC, entre le template et les données de forme d'onde continue. Si le coefficient de corrélation dépasse un seuil spécifié,

une nouvelle détection est déclarée (SLINKARD et al., 2014).

L'avantage de cette méthode est sa capacité de détecter des événements de faible magnitude dans des environnements bruyants (GIBBONS et RINGDAL, 2006 ; SCHAFF et WALDHAUSER, 2010). Naturellement, le catalogue sismique final généré par la détection par cette approche dépend fortement de la base de données initiale car seuls les nouveaux événements dont les formes d'onde sont suffisamment similaires aux temmlates sont détectés. Dans le chapitre 5 de cette thèse, la détection par corrélation de forme d'onde est utilisée pour obtenir un catalogue complet de la sismicité induite pendant la stimulation du réservoir de Rittershoffen.

3.2   Techniques de localisation

La localisation d'un tremblement de terre se réfère généralement à son hypocentre, donc à la position spatiale de la libération d'énergie dans le sous-sol. Pour localiser un tremblement de terre, il faut connaître les temps d'arrivée des ondes sismiques aux stations sismiques, les coordonnées des stations sismiques et un modèle de vitesse qui spécifie les vitesses des ondes dans la section du sous-sol parcourue par les ondes de la source au récepteur (KARASÖZEN et KARASÖZEN, 2020 ; LOMAX et al., 2011). La localisation des séismes est un problème inverse non linéaire. L'origine est déterminée en minimisant les résidus entre les temps d'arrivée observés et prévus des ondes sismiques (ondes P et/ou S) aux stations sismiques.

La localisation des tremblements de terre est toujours sujette à des erreurs, qui sont une combinaison d'erreurs de mesure et de modélisation entraînant des incertitudes et des inexactitudes de localisation (KINNAERT et al., 2016). La cause la plus importante des imprécisions de localisation est l'utilisation d'un modèle de vitesse non représentatif des conditions réelles du sous-sol (BARDAINNE et GAUCHER, 2010 ; KINNAERT et al., 2016).

Les méthodes de localisation relative des séismes tentent de corriger les inexactitudes de localisation entre les séismes en tirant parti de l'observation que le biais introduit dû à un modèle de vitesse inexact tend à être presque constant pour les séismes spatialement proches (LIN et SHEARER, 2005). Plusieurs algorithmes de relocalisation relative ont été développés. Dans l'étude de la sismicité induite sur le site de Rittershoffen présentée au chapitre 5, le logiciel HypoDD est utilisé, qui est basé sur une approche

linéaire à double différence (DD) (WALDHAUSER et ELLSWORTH, 2000). L'algorithme DD a été choisi parce qu'il permet l'utilisation directe de différences de temps de parcours de haute précision obtenues par corrélation croisée des formes d'onde des ondes P et/ou S.

Chapitre 4

Les sites géothermiques de Soultz-sous-Forêts et Rittershoffen

Soultz-sous-Forêts et Rittershoffen sont deux sites géothermiques voisins dans la partie française du Fossé du Rhin supérieur (URG). Le socle granitique faillé est recouvert de couches sédimentaires d'épaisseures variables qui ont été bien explorées car elles abritent le champ pétrolifère de Pechelbronn-Merkwiller (BRUN et WENZEL, 1991). Ces investigations ont mis en évidence des anomalies thermiques avec des gradients de température élevés à Soultz et Rittershoffen (HAAS et HOFFMANN, 1929 ; PRIBNOW et SCHELLSCHMIDT, 2000) liées à des zones de failles qui mettent en contact l'URG à des structures de type horst et graben (BÄCHLER et al., 2003 ; BAILLIEUX et al., 2013).

Soultz-sous-Forêts est le tout premier site géothermique qui a été développé dans l'URG. Son histoire et les caractéristiques du site sont bien documentées (par exemple BARIA et al., 1999 ; GENTER et al., 2010 ; SCHILL et al., 2017). À Soultz, le socle cristallin qui abrite le réservoir géothermique est constitué de granites fortement fracturés et les principales voies de transmission sont des zones de failles à grande échelle de fractures fortement groupées. Le développement du site de Soultz a commencé en 1987. Au total, quatre puits de production/injection ont été forés, dont trois, GPK2/GPK3/GPK4, atteignant environ 5 km de profondeur et une température de réservoir d'environ 200°C. Le site géothermique de Rittershoffen est situé à proximité de

Soultz-sous-Forêts, à environ 6 km à l'est. On accède au réservoir par le doublet de puits GRT1/GRT2, qui cible une zone de faille à 2,5 km de profondeur juste en dessous de la transition entre la couverture sédimentaire et le socle granitique et qui extrait une saumure chaude d'environ 170° (Baujard et al., 2017 ; Aichholzer et al., 2016).

Chapitre 5

Activation de failles par injection répétée de fluide : étude de cas du système géothermique de Rittershoffen, France

5.1 Introduction

Ce chapitre présente une étude qui utilise la sismicité induite pour suivre le développement du système de failles du réservoir géothermique profond de Rittershoffen, causé par l'injection répétée de fluides. D'avril à juin 2013, le puits GRT1 a subi une séquence de stimulation thermique, chimique et hydraulique (BAUJARD et al., 2017). Comme ces injections individuelles ont été effectuées dans le même intervalle de profondeur, elles permettent de suivre la réaction du système de failles à chaque étape.

La détection par corrélation de template, la localisation relative et le regroupement des formes d'onde sont utilisés pour obtenir une nouvelle base de données complète rendant compte de la séquence de l'ensemble de la stimulation du GRT1. Les principaux points analysés dans cette étude sont l'état mécanique du réseau de failles et les variations associées au cours de la séquence d'injection, la caractérisation des mécanismes à l'origine de la sismicité induite et la distribution spatiale et temporelle des événements.

5.2   Données et Méthodes

5.2.1   Réseau de surveillance sismique et base de données

Le site géothermique de Rittershoffen a été surveillé pendant toutes les étapes du développement et de la production du réservoir par un réseau permanent composé de 12 stations. Lors de la stimulation thermique du GRT1, le réseau permanent était le seul opérationnel. En juin 2013, 5 stations temporaires supplémentaires ont été déployées et étaient opérationnelles pendant les stimulations chimiques et hydrauliques du GRT1 (MAURER et al., 2020).

Le catalogue publié et décrit en détail dans MAURER et al. (2020) constitue la base de données initiale pour cette étude. Ce catalogue a été généré par détection automatique basée sur une méthode STA/LTA et vérifié manuellement. Pour la stimulation thermique de GRT1, le catalogue initiale contient 146 événements et pour la stimulation hydraulique 990 événements. Pour la stimulation chimique, aucun événement sismique n'est détécté dans le catalogue.

5.2.2   Détection des tremblements de terre par corrélation de forme d'ondes

L'algorithme de détection par corréaltion utilisé dans cette étude est similaire à celui de LENGLINÉ et al. (2017), mais tous les événements du catalogue précédemment mentionné sont utilisés comme templates au lieu afin de minimiser les risques de manquer des détections. Avant la corrélation, les formes d'onde sont prétraitées, ré-échantillonnées à 100 Hz et filtrées avec un filtre passe-bande de 10 à 45 Hz pour améliorer le rapport signal/bruit. La corrélation est calculée sur six canaux avec les qui sont ceux les plus disponibles dans la base de données des modèles. La procédure de corrélation renvoie le coefficient de corrélation de Pearson moyen sur ces 6 canaux, qui doit dépasser un seuil donné pour qu'une nouvelle détection soit prise en compte.

Une approche adaptative au cas par cas similaire à celle de SLINKARD et al. (2014) et SLINKARD et al. (2016) est utilisée pour faire une sélection objective du seuil de corrélation afin d'atteindre un taux de fausses alarmes donné. Le seuil est fixé de telle sorte que la probabilité pour chaque modèle

d'effectuer une fausse détection est de 1/10 000 par jour. Pour éviter les doublons dans le catalogue final, les détections d'un même événement sont fusionnées et attribuées au template qui a détecté l'événement présentant la corrélation la plus élevée. Les formes d'onde des événements détectés sont ensuite extraites pour calculer les différences de temps de parcours entre les événements qui sont nécessaires pour les localisations relatives.

5.2.3   Relocalisation relative des événements détectés

La relocalisation est effectuée avec le logiciel HypoDD (WALDHAUSER et ELLSWORTH, 2000) dans le modèle de vitesse 1D utilisé par KINNAERT et al. (2016). Les différences de temps de parcours entre les événements détectés sont calculées par corrélation des formes d'onde extraites de tous les canaux, puis filtrées selon les critères suivants : elles doivent avoir été calculées avec un coefficient de corrélation supérieur ou égal à 0,5 et pour la même paire d'événements, ce coefficient de corrélation doit avoir été atteint sur au moins 6 canaux. Cela garantit que la relation d'une paire d'événements est stable et évite de donner trop de poids aux valeurs aberrantes. Les localisations initiales de tous les événements sont fixés sur le puits de GRT1 à 2300 m de profondeur, où l'injection hydraulique a eu lieu.

5.2.4   Analyse de par cluster

Pour trouver des familles de formes d'onde similaires parmi les événements, un algorithme modifié de k-means clsutering a été appliqué (ARTHUR et VASSILVITSKII, 2007 ; LLOYD, 1982). L'algorithme original de k-means vise à partitionner n observations en k groupes en minimisant la somme des carrés des distances euclidiennes entre chaque membre du groupe et la moyenne du groupe. Cependant, d'autres mesures de distance que la variance peuvent être appliquées. Le nombre k de familles doit être spécifié au préalable et les centres des familles sont adaptés à chaque itération pour trouver la meilleure représentation de chacune des familles. Dans le cas présent, le k-means clustering est effectué sur les valeurs de corrélation de chaque événement avec tous les autres événements. Ainsi, la matrice de corrélation croisée entre tous les événements est utilisée, en traitant chaque ligne de la matrice comme une observation appartenant à un seul événement. La distance de corrélation de Pearson (coefficient de corrélation de 1-Pearson) est utilisée comme mesure de la distance pour le regroupement des moyennes k.

5.3   Résultats

5.3.1   Aperçu et statistiques de détection

La stimulation thermique a été réalisée en avril 2013 avec des débits allant jusqu'à 25 L/s (BAUJARD et al., 2017 ; MAURER et al., 2020). Le catalogue final contient 328 événements pour la stimulation thermique, nouvelles détections et les événements initiaux. 285 des événements détectés ont été relocalisés, les événements restants ne répondaient pas aux critères appliqués pour la relocalisation relative. Après une stimulation chimique sismique calme, la stimulation hydraulique a été réalisée en juin 2013. Le débit d'injection a été augmenté progressivement jusqu'à 80 L/s, puis diminué progressivement jusqu'à l'arrêt. Directement après la stimulation, un test d'injection a été effectué à des débits allant jusqu'à 60 L/s (BAUJARD et al., 2017 ; MAURER et al., 2020). Le catalogue final de la stimulation hydraulique contient 2980 événements, templates et nouvelles détections ensemble. Parmi ces événements, 2824 ont été relocalisés.

Au cours de la stimulation thermique, le début de la sismicité s'est produit près de 24 heures après le début de l'injection à un débit de 20 L/s et une pression de 2,7 MPa. Aucune corrélation claire dans le développement du débit, de la pression et du taux de sismicité ne peut être observée. La sismicité détectée pendant l'intervalle d'injection de la stimulation hydraulique commence à un débit de 26,5 L/s et une PSH de 1,1 MPa (DHP = 1,5 MPa). Contrairement à la stimulation thermique, après le début de la sismicité, le taux de sismicité suit de près le développement du débit et de la pression pendant les étapes d'injection jusqu'à un taux de sismicité de 415 événements/heure au débit et à la pression maximum. Lors du test d'injection suivant, seuls quatre événements sont détectés. Après une période de calme de quatre jours suivant l'arrêt, la sismicité augmente à nouveau avec une explosion soudaine de 399 événements en deux heures.

5.3.2   Répartition spatiale des événements sismiques

La carte des épicentres après relocalisations relatives (Fig. 5.1, en haut) montre que les événements sismiques induits pendant la stimulation thermique et l'intervalle d'injection de la stimulation hydraulique sont disposés dans un nuage allongé SW-NE. Ils occupent en partie la même partie du

réservoir, mais le nuage de stimulation hydraulique est plus grand et s'étend plus loin vers le sud-est. Un sous-ensemble de 56 événements de l'intervalle de stimulation hydraulique lié à l'injection est séparé du nuage principal et se trouve au même endroit que les événements de l'intervalle de sismicité retardée, qui forment un second segment de faille. Il s'étend au nord du GRT1 vers le GRT2 avec des orientations variables du SW-NE au N-S. La coupe transversale en profondeur (Fig. 5.1, en bas) montre que les trois nuages sismiques sont alignés horizontalement et situés approximativement dans la même plage de profondeur entre 2150 et 2400 m.

Pour la stimulation thermique et l'intervalle d'injection de la stimulation hydraulique, les orientations les mieux adaptées sont similaires avec N24°+/-7°E ayant une inclinaison de 88°+/-6°W et N15°+/-9°E ayant une inclinaison de 86°+/-8°W respectivement. Pour l'intervalle retardé de la stimulation hydraulique, l'orientation moyenne la mieux adaptée est à N5°+/-4°E avec une inclinaison de 80°+/-8°W. À l'intérieur du volume occupé par les événements de la stimulation thermique et hydraulique, aucune distinction spatiale ne peut être faite entre les deux ensembles. Cela montre que ce sont probablement les mêmes structures sur le plan de la faille qui ont été activées pendant les deux séquences de stimulation, de sorte que les deux stimulations ont eu un effet similaire sur la faille dans cette partie du réservoir. Pour la stimulation thermique, aucune migration des événements dans le temps ne peut être observée. Pour l'intervalle de la stimulation hydraulique lié à l'injection, les premiers événements se concentrent principalement dans le volume précédemment activé par la stimulation thermique. Les événements ultérieurs migrent vers le sud-est et vers le haut, dans une région où le réservoir était auparavant inactif.

5.3.3 Regroupement spatial et temporel des formes d'onde

L'analyse par clustering montre que, avec des valeurs croissantes de k, les nuages d'événements de stimulation thermique et de l'intervalle d'injection de la stimulation hydraulique sont de plus en plus divisés en familles séparées dans l'espace avec un chevauchement relativement mineur. k = 8 est le nombre maximum approprié de familles pour représenter les nuages sismiques (Fig. 5.2). Le fait que le nuage d'événements puisse être divisé en parcelles spatiales de plus en plus petites avec un nombre croissant de familles montre que la proximité spatiale des événements semble avoir une influence majeure

sur la similarité des formes d'onde.

Malgré l'intervalle de temps de deux mois et la stimulation chimique entre les deux, les mêmes familles de formes d'onde actives pendant la stimulation thermique sont réactivées pendant la stimulation hydraulique. Cela montre que la mécanique des zones de faille pendant le glissement sismique reste largement la même et semble être indépendante du temps et du fonctionnement de la stimulation appliquée. Les événements sismiques retardés ont des formes d'onde clairement distinctes de la sismicité liée à l'injection, ce qui indique des mécanismes d'activation de failles différents.

5.4   Discussion

Pendant la stimulation thermique et hydraulique, une faille avec un pendage presque vertical et une direction NNE-SSW a été activée. En partant de l'hypothèse courante que la pression de fluide est responsable du glissement sismique, une analyse Mohr-Coulomb a été réalisée pour analyser le développement mécanique de la faille. En raison de la chute de la WHP de 2,7 à 1,1 MPa lors de l'apparition de la sismicité de la stimulation thermique à la stimulation hydraulique, il devient évident que le critère de rupture de la faille doit avoir changé entre les deux stimulations. L'apparition de la sismicité pendant la stimulation hydraulique pourrait être expliquée sans cohésion sur la faille déjà activée en utilisant un coefficient de friction $\mu = 0,95$, ce qui serait en accord avec les valeurs obtenues pour le réservoir de Soultz (CORNET et al., 2007). En supposant un coefficient de frottement constant, la cohésion c aurait été de 1,1 MPa au moment de l'apparition de la sismicité pendant la stimulation thermique sur une faille orientée de manière optimale dans le champ de contrainte (CORNET et al., 2007). Pour $\mu = 0,95$, l'orientation optimale d'un plan de faille pour la rupture serait N13°+/-10°E avec une inclinaison verticale. Ainsi, la criticité du plan de faille dans le champ de contrainte local peut être confirmée. La mécanique des failles montre que malgré la libération des contraintes pendant la stimulation thermique, les fractures étaient plus critiques avant la stimulation hydraulique qu'avant la stimulation thermique. Cela s'explique notamment par l'impact de la stimulation chimique qui a eu lieu immédiatement avant la stimulation hydraulique. Des réactions minérales auraient pu modifier l'état mécanique le long de certaines parties de la faille, entraînant une réactivation à une pression plus faible.
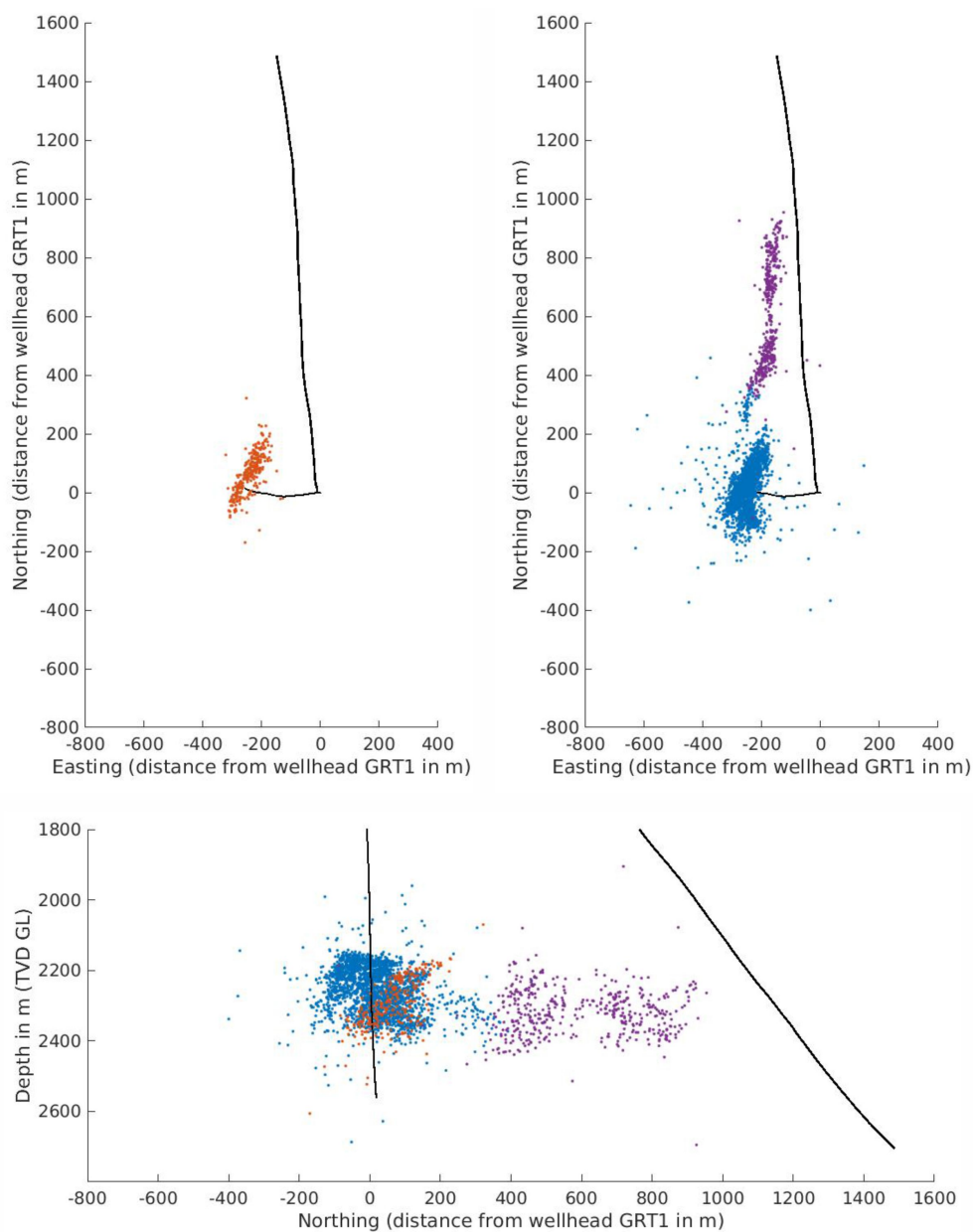
FIGURE 5.1 – En haut : vue en carte des événements relocalisés induits pendant la stimulation thermique (côté gauche, points orange) et la stimulation hydraulique (côté droit, l'intervalle sismique lié à l'injection de la stimulation hydraulique est en bleu, l'intervalle sismique retardé en violet) ; Trajectoires des puits GRT1 et GRT2 en lignes noires. En bas : Coupe transversale en profondeur des événements relocalisés.
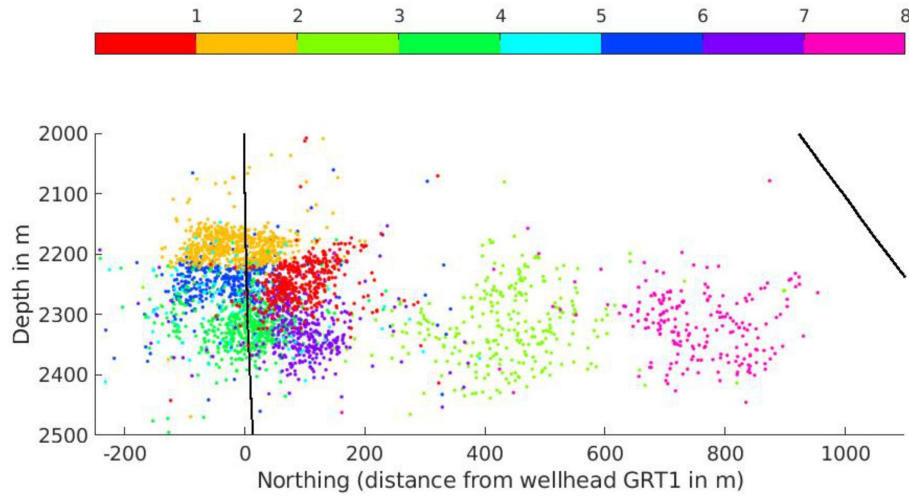
FIGURE 5.2 – Distribution spatiale des familles pour k = 8 familles en coupe. Les différents groupes sont représentés dans des couleurs différentes selon la barre de couleur.

Après la première phase de la stimulation hydraulique, le nuage sismique commence à migrer le long de la faille, après l'augmentation du débit à 40 L/s à un DHP de 2,4 MPa. L'analyse de Mohr-Coulomb du début de cette migration le long de la partie de la faille jusqu'alors calme sur le plan sismique montre qu'elle est caractérisée par une cohésion de 0,9 MPa, ce qui correspond à la cohésion déterminée de la faille au début de la sismicité pendant la stimulation thermique. L'analyse des familles confirme l'idée qu'il y a un changement dans le comportement sismique de la faille à un débit d'injection supérieur à 40 L/s : il y a une division spatiale importante entre les familles dans les deux parties de la faille, la zone activée pendant les deux stimulations étant plus proche du puits et la zone devenant active seulement pendant la stimulation hydraulique après le début de la migration.

Un sous-ensemble de 65 événements induits à la fin de l'injection pendant la stimulation hydraulique est spatialement séparé du reste du nuage, situé sur une seconde faille qui est redevenue active quatre jours plus tard pendant l'intervalle sismique retardé. L'analyse par clustering montre que 72 % des événements du sous-ensemble appartiennent à un autre groupe uniquement actif pendant l'intervalle retardé, tandis que les autres appartiennent à des groupes ayant des formes d'onde caractéristiques pour l'intervalle lié à l'injection. Le regroupement d'événements appartenant à des familles si différentes laisse supposer une transition des mécanismes d'activation de la faille qui a lieu sur la deuxième faille.

5.5   Conclusion

Un catalogue sismique complet de la sismicité induite par la stimulation du puits GRT1, Rittershoffen, a été établi par la détection par corrélation de forme d'ondes. Dans l'ensemble, le nombre d'événements a triplé par rapport au catalogue des initial. Les événements ont été relocalisés par une procédure de relocalisation relative et triés en groupes de formes d'onde. Ce traitement a permis une évaluation détaillée de la distribution temporelle et spatiale des événements sismiques induits pendant la séquence de stimulation du GRT1.

Deux segments de failles sismogéniques ont pu être détectés sans qu'il y ait de connexion spatiale continue de la sismicité d'une structure à l'autre. Le premier segment, coupé par le puits GRT1, a une direction NNE-SSW et est très critique dans le champ de contrainte local. Il a été activé sismiquement lors de la stimulation thermique et hydraulique. La faille non perturbée a une cohésion d'environ 1 MPa pour un coefficient de frottement supposé de 0,95. La stimulation chimique a apparemment causé une réduction de la cohésion, permettant la réactivation sismique de la même partie de la faille à une pression de fluide plus faible pendant la stimulation hydraulique.

La deuxième faille a une orientation variant de NNE-SSW à N-S et est située au nord de la première. Elle a été principalement active pendant l'intervalle de sismicité retardée de quatre jours après l'arrêt de la stimulation hydraulique, mais un sous-ensemble d'événements induits pendant la phase d'injection tardive est également situé sur cette faille. L'analyse par clustering suggère que la sismicité retardée a été causée par un mécanisme différent de la sismicité liée à l'injection et qu'à la fin de l'injection, une transition du mécanisme d'activation de la faille a eu lieu.

Chapitre 6

Identification pseudo-probabiliste de réseaux de fractures dans des nuages sismiques, en fonction des paramètres de source

6.1 Introduction

La caractérisation de réseaux de fractures à partir de la sismicité induite repose sur la localisation précise des événements pour révéler les structures qui sont à l'origine de cette sismicité. Cependant, dans certains cas, le réseau de failles peut rester flou, car la sismicité forme un nuage spatial assez dense, ce qui rend les caractéristiques individuelles difficiles à détecter. Les méthodes les plus courantes proposées pour mettre en évidence des réseaux de fractures à partir de nuages de sismicité sont par exemple la méthode dite des trois points de FEHLER et al. (2001) visant à identifier les directions principales de plans, la méthode dite de « collapsing » de JONES et STEWART (1997) et la détection de structures dans un nuage de point utilisant une transformée de Hough en 3D (SARTI et TUBARO, 2002 ; WANG et ALREGIB, 2014). Toutes ces méthodes supposent que la sismicité appartient à des structures planes et s'appuient uniquement sur les hypocentres des séismes pour détecter ces dernières.

Dans ce travail, une approche probabiliste est développée et appliquée. En

23

plus de l'hypocentre du séisme, la magnitude et le mécanisme au foyer sont pris en compte dans celle-ci. Ainsi, une distribution spatiale de plans de fractures potentiels sera associée à chaque séisme conduisant à un réseau pseudo-probabiliste de fractures lorsque toutes sont considérées conjointement. Dans ce qui suit, cette méthode, appelée identification pseudo-probabiliste de réseau de fractures (PPFN pour « Pseudo Probabilistic Fracture Network » en anglais), est décrite en détail et sa capacité à détecter et à localiser les structures dominantes dans les nuages sismiques est démontrée à partir de cas synthétiques. Enfin, la méthode PPFN est appliquée au catalogue de sismicité induite générée lors de la stimulation hydraulique du puits GPK2 du site géothermique de Soultz-sous-Forêts (France).

6.2 Identification pseudo-probabiliste de réseaux de fractures (PPFN)

La méthode PPFN vise à détecter la distribution spatiale de fractures dans un nuage sismique en estimant la connectivité entre toute position spatiale et chaque séisme. L'hypothèse intrinsèque est qu'il est plus probable que deux séismes appartiennent à la même structure lorsqu'ils sont spatialement proches que lorsqu'ils sont éloignés. On suppose également que la magnitude d'un séisme est liée à la taille de son plan de rupture et que deux séismes dont les plans de rupture se recoupent spatialement appartiennent à la même structure. La première étape de la méthodologie consiste à mailler le volume du nuage sismique avec des cellules cubiques. Ensuite, le vecteur de connexion entre chaque séisme et le centre de chaque cellule est calculé. Ensuite, chaque cellule se voit attribuer un poids selon différents schémas de pondération possibles dépendants de la longueur et de la direction du vecteur de connexion et des propriétés à la source du séisme. Dans le cas de la pondération par la distance, chaque cellule se voit attribuer un poids dépendant de la longueur du vecteur de connexion d, calculé selon une distribution gaussienne :

$$W_d = \exp\left(-\frac{d^2}{2 \cdot \sigma_d^2}\right), \tag{6.1}$$

où l'écart-type σ_d est un paramètre libre qui affecte la forme de la distribution du poids. Plus σ_d est choisi grand, plus la fonction de pondération diminue lentement avec la distance, de sorte que des séismes plus éloignés se

verraient plus fortement liés. Dans ce qui suit, la PPFN basée sur ce schéma de pondération est appelée PPFN-Distance.

Pour un séisme donné de source supposée circulaire, son rayon, r, peut être estimé à partir de sa magnitude M (MADARIAGA, 1976 ; BRUNE, 1970 ; SATO et HIRASAWA, 1973). On peut alors considérer que toute cellule située dans ce rayon de source est entièrement connectée au séisme et se voit attribuer un poids de 1. Au-delà de cette distance, une pondération de type gaussienne est appliquée, similaire à la pondération de la distance, mais en tenant compte de la magnitude du séisme :

$$W_M = \exp\left(-\frac{d^2 - r^2(M)}{2 \cdot \sigma_M^2(M)}\right),\qquad(6.2)$$

avec

$$\sigma_M(M) = F \cdot r(M)\,,\qquad(6.3)$$

où F est un paramètre libre, qui influence la forme de la courbe. Dans ce qui suit, ce type de pondération sera appelée PPFN-Magnitude.

En appliquant les fonctions de pondération pour chaque cellule, on obtient autant de valeurs différentes que de séismes dans le nuage. Toutes ces valeurs sont ensuite additionnées par cellule, ce qui donne une distribution 3D des pondérations W couvrant le volume étudié et prenant en compte l'ensemble des informations apportées par les séismes. Au final, il sera plus probable d'avoir des structures passant par les cellules aux poids élevés. Les PPFN-Distance et -Magnitude relient les cellules dans toutes les directions à partir de l'hypocentre d'un séisme. Il est pourtant possible d'inclure également une information directionnelle, pour attribuer des valeurs plus élevées aux cellules qui se trouvent probablement dans la direction réelle du plan de faille. Ceci peut être réalisé en considérant les mécanismes au foyer des séismes, s'ils sont disponibles. Là encore, une fonction de pondération de type gaussienne est formulée, cette fois en fonction de l'angle spatial α entre l'orientation du plan de faille donnée par le mécanisme focal et l'orientation du vecteur liant le séisme à chaque cellule :

$$W_f = \exp\left(-\frac{\alpha^2}{2 \cdot \sigma_f^2}\right),\qquad(6.4)$$

où σ_f, l'écart-type, est un paramètre libre qui affecte la forme de la distribution de probabilité. En appliquant la pondération directionnelle, les cellules situées le long du plan de rupture d'un séisme se voient attribuer un poids plus élevé que les autres.

La pondération par la distance ou la magnitude et la pondération par le mécanisme au foyer peuvent maintenant être combinées pour limiter les zones de poids élevé autour des événements, tant en taille qu'en orientation. Ceci est fait en multipliant la PPFN-Distance ou la PPFN-Magnitude par la PPFN-Mécanisme au foyer. En dernier lieu, la PPFN est normalisée à partir d'une distribution obtenue pour un nuage de points aléatoire de telle sorte que les valeurs finales W > 0 indiquent les cellules où se trouvent probablement des fractures.

6.3 Évaluation de la méthode PPFN sur des cas synthétiques

La méthode PPFN a été testée sur différents ensembles de données synthétiques afin de confirmer le fonctionnement attendu et de tester l'influence des paramètres σ_d pour la PPFN-Distance, F pour la PPFN-Magnitude et σ_f pour la PPFN-Mécanisme au foyer. Les PPFN-Distance et -Magnitude permettent d'identifier les plans réels présents dans les cas synthétiques. Les précisions avec lesquelles le centre, les dimensions et l'orientation des plans peuvent être déterminées dépendent du paramétrage. La combinaison avec la pondération apportée par les mécanismes au foyer permet de déterminer plus précisément l'orientation des plans, mais peut conduire à une surestimation de leurs dimensions.

Le choix des paramètres σ_d et F devrait dépendre de la taille du plan et de la densité des séismes sur le plan. Dans tous les cas, σ_d et $\sigma_M(\overline{M})$ doivent être inférieurs à la taille du plan pour éviter une surestimation de sa taille. Pour des densités élevées de séismes, des valeurs faibles de σ_d et $\sigma_M(\overline{M})$, de l'ordre de 1/6 la dimension du plan, conduisent à des résultats relativement précis alors que pour des densités de séismes faibles, des valeurs plus élevées, de l'ordre de la moitié de la dimension du plan, doivent être choisies pour relier un nombre suffisant de séismes afin de détecter le plan.

Pour la PPFN-Mécanisme au foyer, σ_f doit être choisi en fonction des

incertitudes du mécanisme au foyer. Si les incertitudes sur les orientations des plans focaux excèdent 10°, il semble que cette information n'apporte pas de contrainte supplémentaire à la PPFN-Distance ou PPFN-Magnitude.

6.4 Application de la PPFN à la sismicité induite lors de la stimulation de GPK2, Soultz-sous-Forêts

Pour cette étude, on utilise la sismicité induite lors de la stimulation hydraulique du puits GPK2 en juin-juillet 2000, décrite en détail dans Cuenot et al. (2008). L'ensemble des données consiste en 7215 séismes localisés avec une magnitude maximale du moment MW de 2,5. Ce jeu de données est appelé ci-après le « grand » jeu de données. En outre, des mécanismes au foyer ont été calculés par Schoenball et al. (2012) pour un sous-ensemble du grand jeu de données contenant 715 séismes de MW > 1, ci-après appelé le « petit » jeu de données.

Les résultats de l'application de la méthode PPFN sont globalement cohérents entre le « grand » et le « petit » jeu de données en ce qui concerne la PPFN-Distance et la PPFN-Magnitude. Comme déjà observé pour les cas synthétiques, les paramètres σ_d et F ont une influence majeure sur les résultats : la zone des poids élevés est plus petite avec de petites valeurs des paramètres qu'avec des grandes valeurs. Dans tous les cas, la PPFN met en évidence un ellipsoïde asymétrique de poids élevés dans la partie nord plus profonde du nuage avec une orientation plongeant fortement vers l'OSO. La partie sud du nuage, moins profonde, est plus ou moins mise en évidence par des poids élevés en fonction de ces mêmes paramètres.

La figure 6.1 montre les résultats pour le grand jeu de données pour la PPFN-Magnitude avec F = 1/2, 1 et 2. Pour F = 1/2, les détails de la structure de la faille deviennent visibles : la faille principale profonde est reliée à la partie sud supérieure du nuage par une branche plus étroite de poids élevés, tandis que la partie sud inférieure du nuage ne contient que de petites zones isolées de poids élevés dépassant le seuil W = 0.

Comme il existe des mécanismes focaux pour le petit jeu de données, la distance et la magnitude PPFN sont maintenant combinées avec le mécanisme focal PPFN. Le PPFN commun donne des résultats différents de
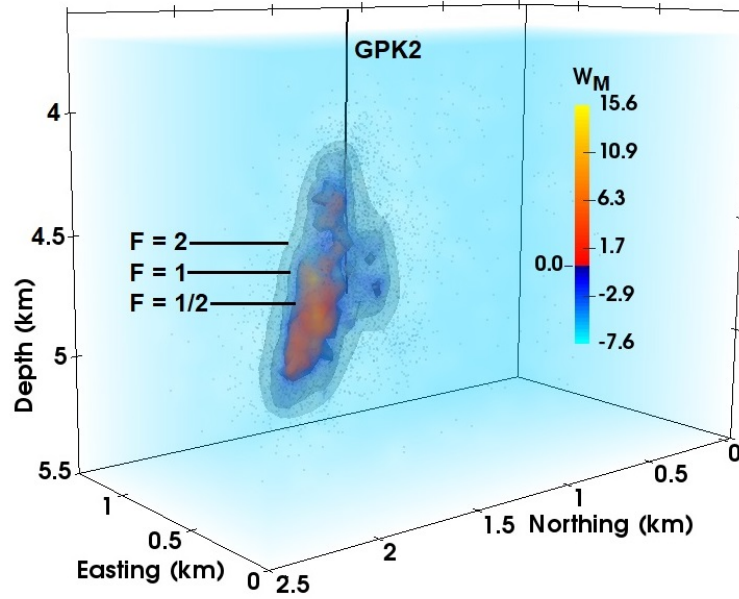
FIGURE 6.1 – PPFN-Magnitude appliquée au grand jeu de données de GPK2 pour différentes valeurs de F : F = 1/2 en carte couleur et contour pour WM = 0, F = 1 avec contour pour WM = 0 et F = 2 comme contour pour WM = 0.

ceux obtenus pour la distance et la magnitude PPFN seules. L'orientation de l'ellipsoïde des poids élevés dans la partie nord plus profonde du nuage est légèrement modifiée et la partie sud du nuage n'est plus mise en évidence. Cela peut indiquer que le nuage sismique qui s'y trouve présente une grande variabilité des orientations du plan de rupture tel que défini par les mécanismes focaux et ne peut pas mettre en valeur une direction préférée.

6.5   Discussion

Dans ce chapitre, les résultats de la méthode PPFN sont comparés à ceux obtenus par des analyses postérieures sur le réseau de failles présent dans le réservoir géothermique de Soultz-sous-Forêts. SAUSSE et al. (2010) ont recueilli des informations à partir de diagraphies, de carottes et d'analyses de sismicité pour proposer un modèle 3D de failles du réservoir de Soultz. Dans ce qui suit, seule la partie de leur modèle pertinente pour la présente étude est prise en compte.

La faille principale GPK3-FZ4770 traverse les puits GKP1, GKP2 et
GPK3 à différentes profondeurs. SAUSSE et al. (2010) ont supposé que le
nuage sismique associé à GPK2 était également induit sur cette faille et donc
que GPK3-FZ4770 et la zone de fracture MS-GPK2-2000a qu'ils ont dérivée
d'une analyse de cluster sismique correspondaient à une seule et même struc-
ture. En outre, le modèle contient trois zones de failles profondes traversant
GPK2 à 4760 m, 4890 m et 5060 m de profondeur mesurée. Ces trois plans,
MS-GPK2-2000a et GPK3-FZ4770, sont représentés sur la figure 6.2 sous
forme de plans verts et gris avec nos résultats de la PPFN.

On peut voir que GPK3-FZ4770 traverse le nuage sismique de GPK2 plu-
tôt en périphérie, tandis que MS-GPK2-2000a s'aligne bien avec la structure
principale détectée par la PPFN. Les trois plus petites zones de failles qui
traversent GPK2 à 4760 m, 4890 m et 5060 m de profondeurs mesurées se
situent dans la plage de profondeur où le nuage sismique GPK2 est le plus
proche du puits. Ces trois structures s'adaptent assez bien à la partie sud du
nuage sismique en termes d'orientation et de position. Il est possible qu'une,
deux ou toutes ces zones de failles s'étendent plus au nord et en profondeur
dans la zone principale du nuage sismique et deviennent plus actives sur
le plan sismique. Elles s'adapteraient alors à la structure principale à forte
inclinaison vers l'ouest que nous avons détectée avec la PPFN.

6.6   Conclusion

La PPFN est une nouvelle méthode permettant de visualiser en trois di-
mensions des réseaux de failles ou de fractures tirés d'un nuage de sismicité
induite sous forme de pseudo-probabilités. Ainsi, non seulement la position,
mais également la distance, la magnitude et le mécanisme au foyer pour
chaque séisme et entre les séismes peuvent être inclus pour caractériser le ré-
servoir. Les paramètres associés garantissent un lien avec les caractéristiques
physiques des ruptures qui sous-tendent les séismes. Les tests sur données
synthétiques ont montré le potentiel de la méthode PPFN : elle fonctionne
bien pour identifier la taille, l'orientation et l'emplacement des plans dans
un nuage de séismes s'il y a une densité de fractures suffisante et si les pa-
ramètres d'échelle sont cohérents avec l'échelle d'investigation. L'application
de la PPFN aux deux jeux de données de GPK2 a fourni un aperçu des prin-
cipales caractéristiques du nuage sismique, qui consistent en une structure
dominante dans la partie nord plus profonde du nuage et une structure secon-
daire située dans la partie sud supérieure, qui peut être reliée à la structure
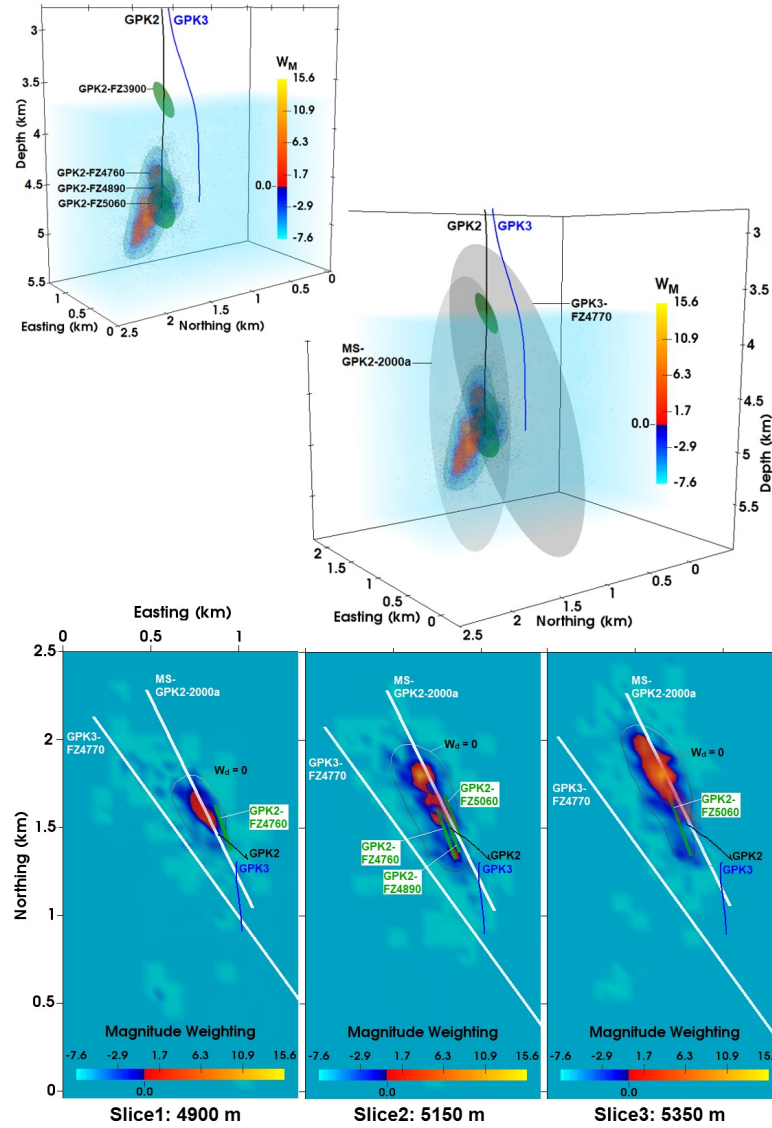
FIGURE 6.2 – PPFN appliquée au grand jeu de données du nuage sismique de GPK2 et zones de failles proches de GPK2. En haut à gauche : PPFN-Magnitude avec F = 1/2 en carte couleur, PPFN-Distance avec d = 50 m en contour au seuil de Wd = 0 et les quatre zones de failles identifiées au puits en plans verts. Au milieu à droite : le plan MS-GPK2-2000a obtenu par analyse du cluster sismique de GPK2 et la zone de faille GPK3-FZ4770, tous deux déterminés par Sausse et al. (2010), sont ajoutés et représentés par des plans gris. En bas : trois sections à différentes profondeurs, des plans de failles représentés sous forme de segments verts et blancs. Pour l'ensemble des graphes, les points noirs représentent les séismes, la courbe noire représente la trajectoire de GPK2 et la courbe bleue, celle du puits GPK3. La position, l'orientation et la taille des plans de failles sont tirés de SAUSSE et al. (2010).

principale nord. La structure principale de la faille dans la partie inférieure nord du nuage coïncide également avec une structure détectée par SAUSSE et al. (2010) à partir du nuage sismique de GPK2 par une analyse de cluster.

Chapitre 7

Conclusion et perspectives

Les opérations de stimulation des réservoirs dans les systèmes géothermiques améliorés sont généralement accompagnées d'une sismicité induite (BREEDE et al., 2013). Ces réservoirs sont principalement situés dans des roches fracturées où les principales voies d'écoulement des fluides sont des zones de failles, qui contiennent de nombreuses fractures à petite échelle (VIDAL et GENTER, 2018). La sismicité induite lors des opérations de stimulation est une expression de la réaction des zones de failles à l'injection de fluides et peut être utilisée comme un outil d'imagerie pour mettre en évidence les failles sismogènes dans le réservoir et en déduire leur état mécanique (e.g. LENGLINÉ et al., 2017). Ceci est d'une importance capitale car la sismicité induite reste une préoccupation majeure dans le développement des systèmes de géothermie profonde en tant que contributeurs au bouquet énergétique vert.

Dans cette thèse, deux concepts de caractérisation des réseaux de failles à partir de l'analyse de la sismicité induite et leur application à deux sites EGS différents dans le bassin rhénan supérieur ont été présentés. Le premier concept s'est basé sur l'application d'une procédure de traitement optimale pour obtenir un catalogue sismique complet et précis, et permettre ainsi une interprétation approfondie du réservoir (chapitre 5). La procédure a été appliquée à la séquence de stimulations thermique, chimique et hydraulique du puits GRT1 du réservoir géothermique de Rittershoffen et s'est avérée efficace pour mettre en évidence le réseau de failles et donner un aperçu des processus géo-mécaniques dans le réservoir. L'interprétation du catalogue obtenu a permis de mieux comprendre les effets des différentes étapes de stimulation sur le réseau de failles. La détermination des incertitudes de

localisation et le calcul des mécanismes au foyer pourraient constituer des étapes supplémentaires pour améliorer encore l'interprétation de la sismicité induite dans le réservoir de Rittershoffen.

Le deuxième concept est basé sur une nouvelle méthode pseudo-probabiliste, la PPFN, développée pour découvrir des structures à l'intérieur de nuages sismiques et qui a fait ses preuves sur des jeux de données synthétiques ainsi que sur le nuage sismique de GPK2, Soultz-sous-Forêts (chapitre 6). Cette méthode s'applique typiquement si la géométrie du réseau de fractures reste floue malgré la localisation précise des événements, ou lorsque cette dernière n'est pas possible, et que le nuage sismique présente une forme plutôt compacte et dense. Contrairement à d'autres méthodes géométriques, la PPFN utilise non seulement les hypocentres des séismes mais aussi les magnitudes et les mécanismes au foyer pour dériver une carte en trois dimensions de pseudo-probabilité de fractures dans la zone couverte par le nuage sismique. Cela permet d'inclure des contraintes géophysiques. Une caractéristique unique de la méthode PPFN est son caractère pseudo-probabiliste. Cela permet d'obtenir une vue plus complète du nuage sismique et de mieux comprendre la fiabilité du réseau de fractures proposé. Pour affiner encore la PPFN, il faudrait concevoir un jeu de données synthétiques plus complexe et peut-être plus représentatif des nuages sismiques réels. Le PPFN devrait également être testé sur d'autres sites où de la sismicité a été induite afin de vérifier son applicabilité.

Les deux études présentées sur les réservoirs de Soultz-sous-Forêts et de Rittershoffen ont montré qu'il est possible d'améliorer l'état des connaissances sur le réseau de fractures souterraines par l'analyse de la sismicité induite avec la méthodologie appropriée. Il faut cependant garder à l'esprit que cette capacité d'imagerie est limitée aux structures sismogènes à grande échelle, de sorte que seule une partie du réseau de fractures est identifié. Cependant, la sismicité induite met en évidence les failles qui sont fortement affectées par les opérations de stimulation du réservoir et qui sont probablement responsables de l'augmentation de l'injectivité/productivité. Ces failles sont également les structures qui présentent le plus grand risque de générer des séismes et donc celles que les opérateurs du site géothermique doivent connaître pour limiter, si ce n'est éviter, les séismes majeurs.

References

Aichholzer, C., P. Duringer, S. Orciani et A. Genter (2016). « New stratigraphic interpretation of the Soultz-sous-Forêts 30-year-old geothermal wells calibrated on the recent one from Rittershoffen (Upper Rhine Graben, France) ». In : *Geothermal Energy* 4.13. doi : `10.1186/s40517-016-0055-7`.

Allen, R. (1982). « Automatic phase pickers : Their present use and future prospects ». In : *Bulletin of the Seismological Society of America* 72.6, p. 225-242.

Anderson, E. M. (1951). *The Dynamics of Faulting and Dyke Formation with Applications to Britain*. Oliver et Boyd. 224 p.

Arthur, D. et S. Vassilvitskii (2007). « k-means++ : the advantages of careful seeding ». **presentedat** : *Proceedings of the eighteenth annual ACM-SIAM symposium on Discrete algorithms*. USA, p. 1027-1035.

Axelsson, G., S. Thórhallsson et G. Björnsson (2006). « Stimulation of geothermal wells in basaltic rock in Iceland ». **presentedat** : ENGINE Workshop 3, Stimulation of reservoir and microseismicity. Zürich, Switzerland.

Bächler, D., T. Kohl et L. Rybach (2003). « Impact of graben-parallel faults on hydrothermal convection—Rhine Graben case study ». In : *Physics and Chemistry of the Earth, Parts A/B/C* 28.9, p. 431-441. doi : `10.1016/S1474-7065(03)00063-9`.

Baillieux, P., E. Schill, J.-B. Edel et G. Mauri (2013). « Localization of temperature anomalies in the Upper Rhine Graben : insights from geophysics and neotectonic activity ». In : *International Geology Review* 55.14, p. 1744-1762. doi : `10.1080/00206814.2013.794914`.

BARDAINNE, T. et E. GAUCHER (2010). « Constrained tomography of realistic velocity models in microseismic monitoring using calibration shots ». In : *Geophysical Prospecting* 58.5, p. 739-753. DOI : `10.1111/j.1365-2478.2010.00912.x`.

BARIA, R., J. BAUMGÄRTNER, A. GÉRARD, R. JUNG et J. GARNISH (1999). « European HDR research programme at Soultz-sous-Forêts (France) 1987–1996 ». In : *Geothermics* 28.4, p. 655-669. DOI : `10.1016/S0375-6505(99)00036-X`.

BAUJARD, C., A. GENTER, E. DALMAIS, V. MAURER, R. HEHN, R. ROSILLETTE, J. VIDAL et J. SCHMITTBUHL (2017). « Hydrothermal characterization of wells GRT-1 and GRT-2 in Rittershoffen, France : Implications on the understanding of natural flow systems in the rhine graben ». In : *Geothermics* 65, p. 255-268. DOI : `10.1016/j.geothermics.2016.11.001`.

BREEDE, K., K. DZEBISASHVILI, X. LIU et G. FALCONE (2013). « A systematic review of enhanced (or engineered) geothermal systems : past, present and future ». In : *Geothermal Energy* 1.4. DOI : `10.1186/2195-9706-1-4`.

BRUN, J. P. et F. WENZEL (1991). « Crustal-scale structure of the southern Rhinegraben from ECORS-DEKORP seismic reflection data ». In : *Geology* 19.7, p. 758-762. DOI : `10.1130/0091-7613(1991)019<0758:CSSOTS>2.3.CO;2`.

BRUNE, J. N. (1970). « Tectonic stress and the spectra of seismic shear waves from earthquakes ». In : *Journal of Geophysical Research (1896-1977)* 75.26, p. 4997-5009. DOI : `10.1029/JB075i026p04997`.

CORNET, F. H., T. BÉRARD et S. BOUROUIS (2007). « How close to failure is a granite rock mass at a 5km depth ? » In : *International Journal of Rock Mechanics and Mining Sciences* 44.1, p. 47-66. DOI : `10.1016/j.ijrmms.2006.04.008`.

COULOMB, C. (1773). « Application des règles de maxima et minima à quelques problèmes de statique relatifs à l'Architecture ». In : *Mémoires de Mathématiques et de Physiques présentés à l'Académie Royale des Sciences* 7, p. 343-382.

CUENOT, N., C. DORBATH et L. DORBATH (2008). « Analysis of the Microseismicity Induced by Fluid Injections at the EGS Site of Soultz-sous-Forêts (Alsace, France) : Implications for the Characterization of the Geo-

thermal Reservoir Properties ». In : *Pure and Applied Geophysics* 165.5, p. 797-828. DOI : 10.1007/s00024-008-0335-7.

DEICHMANN, N., T. KRAFT et K. F. EVANS (2014). « Identification of faults activated during the stimulation of the Basel geothermal project from cluster analysis and focal mechanisms of the larger magnitude events ». In : *Geothermics* 52, p. 84-97. DOI : 10.1016/j.geothermics.2014.04.001.

EVANS, K. F., A. ZAPPONE, T. KRAFT, N. DEICHMANN et F. MOIA (2012). « A survey of the induced seismic responses to fluid injection in geothermal and CO2 reservoirs in Europe ». In : *Geothermics* 41, p. 30-54. DOI : 10.1016/j.geothermics.2011.08.002.

FEHLER, M., A. JUPE et H. ASANUMA (2001). « More Than Cloud : New techniques for characterizing reservoir structure using induced seismicity ». In : *The Leading Edge* 20.3, p. 324-328. DOI : 10.1190/1.1438942.

GENTER, A., K. EVANS, N. CUENOT, D. FRITSCH et B. SANJUAN (2010). « Contribution of the exploration of deep crystalline fractured reservoir of Soultz to the knowledge of enhanced geothermal systems (EGS) ». In : *Comptes Rendus Geoscience* 342.7, p. 502-516. DOI : 10.1016/j.crte.2010.01.006.

GIBBONS, S. J. et F. RINGDAL (2006). « The detection of low magnitude seismic events using array-based waveform correlation ». In : *Geophysical Journal International* 165.1, p. 149-166. DOI : 10.1111/j.1365-246X.2006.02865.x.

HAAS, I. O. et C. R. HOFFMANN (1929). « Temperature Gradient in Pechelbronn Oil-Bearing Region, Lower Alsace : Its Determination and Relation to Oil Reserves ». In : *AAPG Bulletin* 13.10, p. 1257-1273. DOI : 10.1306/3D932884-16B1-11D7-8645000102C1865D.

HÄRING, M. O., U. SCHANZ, F. LADNER et B. C. DYER (2008). « Characterisation of the Basel 1 enhanced geothermal system ». In : *Geothermics* 37.5, p. 469-495. DOI : 10.1016/j.geothermics.2008.06.002.

IEA (2017). *Geothermal Power Report 2017*. International Energy Agency. URL : https://iea-gia.org/publications-2/working-group-publications/#Annex-X (visité le 26/10/2020).

JONES, R. H. et R. C. STEWART (1997). « A method for determining significant structures in a cloud of earthquakes ». In : *Journal of Geophysical Research : Solid Earth* 102 (B4), p. 8245-8254. DOI : 10.1029/96JB03739.

KARASÖZEN, E. et B. KARASÖZEN (2020). « Earthquake location methods ». In : *GEM - International Journal on Geomathematics* 11.13. DOI : 10.1007/s13137-020-00149-9.

KINNAERT, X., E. GAUCHER, U. ACHAUER et T. KOHL (2016). « Modelling earthquake location errors at a reservoir scale : a case study in the Upper Rhine Graben ». In : *Geophysical Journal International* 206.2, p. 861-879. DOI : 10.1093/gji/ggw184.

LENGLINÉ, O., M. BOUBACAR et J. SCHMITTBUHL (2017). « Seismicity related to the hydraulic stimulation of GRT1, Rittershoffen, France ». In : *Geophysical Journal International* 208.3, p. 1704-1715. DOI : 10.1093/gji/ggw490.

LENGLINÉ, O., Z. DUPUTEL et V. FERRAZZINI (2016). « Uncovering the hidden signature of a magmatic recharge at Piton de la Fournaise volcano using small earthquakes ». In : *Geophysical Research Letters* 43.9, p. 4255-4262. DOI : 10.1002/2016GL068383.

LIN, G. et P. SHEARER (2005). « Tests of relative earthquake location techniques using synthetic data ». In : *Journal of Geophysical Research : Solid Earth* 110 (B4). DOI : 10.1029/2004JB003380.

LLOYD, S. (1982). « Least squares quantization in PCM ». In : *IEEE Transactions on Information Theory* 28.2, p. 129-137. DOI : 10.1109/TIT.1982.1056489.

LOMAX, A., A. MICHELINI et A. CURTIS (2011). « Earthquake Location, Direct, Global-Search Methods ». In : *Extreme Environmental Events : Complexity in Forecasting and Early Warning*. Sous la dir. de MEYERS, R. A. New York, NY : Springer, p. 230-254. DOI : 10.1007/978-1-4419-7695-6_16.

MADARIAGA, R. (1976). « Dynamics of an expanding circular fault ». In : *Bulletin of the Seismological Society of America* 66.3, p. 639-666.

MAURER, V., E. GAUCHER, M. GRUNBERG, R. KOEPKE, R. PESTOURIE et N. CUENOT (2020). « Seismicity induced during the development of

the Rittershoffen geothermal field, France ». In : *Geothermal Energy* 8.1, p. 5. DOI : `10.1186/s40517-020-0155-2`.

MCCLURE, M. W. et R. N. HORNE (2014). « An investigation of stimulation mechanisms in Enhanced Geothermal Systems ». In : *International Journal of Rock Mechanics and Mining Sciences* 72, p. 242-260. DOI : `10.1016/j.ijrmms.2014.07.011`.

MOHR, O. (1914). *Abhandlungen aus dem gebiete der technischen mechanik.* Berlin : Ernst & Sohn.

PORTIER, S., F.-D. VUATAZ, P. NAMI, B. SANJUAN et A. GÉRARD (2009). « Chemical stimulation techniques for geothermal wells : experiments on the three-well EGS system at Soultz-sous-Forêts, France ». In : *Geothermics* 38.4, p. 349-359. DOI : `10.1016/j.geothermics.2009.07.001`.

PRIBNOW, D. et R. SCHELLSCHMIDT (2000). « Thermal tracking of upper crustal fluid flow in the Rhine graben ». In : *Geophysical Research Letters* 27.13, p. 1957-1960. DOI : `10.1029/2000GL008494`.

REID, H. F. (1910). *The California Earthquake of April 18, 1906, Volume II : The Mechanics of the Earthquake.* Report of the State Earthquake Investigation Commission. Carnegie Institution of Washington.

SARTI, A. et S. TUBARO (2002). « Detection and characterisation of planar fractures using a 3D Hough transform ». In : *Signal Processing* 82.9, p. 1269-1282. DOI : `10.1016/S0165-1684(02)00249-9`.

SATO, T. et T. HIRASAWA (1973). « Body Wave Spectra from Propagating Shear Cracks ». In : *Journal of Physics of the Earth* 21.4, p. 415-431. DOI : `10.4294/jpe1952.21.415`.

SAUSSE, J., C. DEZAYES, L. DORBATH, A. GENTER et J. PLACE (2010). « 3D model of fracture zones at Soultz-sous-Forêts based on geological data, image logs, induced microseismicity and vertical seismic profiles ». In : *Comptes Rendus Geoscience* 342.7, p. 531-545. DOI : `10.1016/j.crte.2010.01.011`.

SCHAFF, D. P. et F. WALDHAUSER (2010). « One Magnitude Unit Reduction in Detection Threshold by Cross Correlation Applied to Parkfield (California) and China Seismicity ». In : *Bulletin of the Seismological Society of America* 100.6, p. 3224-3238. DOI : `10.1785/0120100042`.

SCHILL, E., A. GENTER, N. CUENOT et T. KOHL (2017). « Hydraulic performance history at the Soultz EGS reservoirs from stimulation and long-term circulation tests ». In : *Geothermics* 70, p. 110-124. DOI : 10.1016/j.geothermics.2017.06.003.

SCHOENBALL, M., C. BAUJARD, T. KOHL et L. DORBATH (2012). « The role of triggering by static stress transfer during geothermal reservoir stimulation ». In : *Journal of Geophysical Research : Solid Earth* 117 (B9). DOI : 10.1029/2012JB009304.

SHEARER, P. M. (2019). *Introduction to Seismology.* 2nd edition. Cambridge, UK : Cambridge University Press. 443 p.

SHELLY, D. R., G. C. BEROZA et S. IDE (2007). « Non-volcanic tremor and low-frequency earthquake swarms ». In : *Nature* 446.7133, p. 305-307. DOI : 10.1038/nature05666.

SKOUMAL, R. J., M. R. BRUDZINSKI et B. S. CURRIE (2015). « Distinguishing induced seismicity from natural seismicity in Ohio : Demonstrating the utility of waveform template matching ». In : *Journal of Geophysical Research : Solid Earth* 120.9, p. 6284-6296. DOI : 10.1002/2015JB012265.

SLINKARD, M., D. SCHAFF, N. MIKHAILOVA, S. HECK, C. YOUNG et P. G. RICHARDS (2014). « Multistation Validation of Waveform Correlation Techniques as Applied to Broad Regional Monitoring ». In : *Bulletin of the Seismological Society of America* 104.6, p. 2768-2781. DOI : 10.1785/0120140140.

SLINKARD, M., S. HECK, D. SCHAFF, N. BONAL, D. DAILY, C. YOUNG et P. RICHARDS (2016). « Detection of the Wenchuan Aftershock Sequence Using Waveform Correlation with a Composite Regional Network ». In : *Bulletin of the Seismological Society of America* 106.4, p. 1371-1379. DOI : 10.1785/0120150333.

TERZAGHI, K. (1936). « The shearing resistance of saturated soils and the angle between planes of shear ». In : *Proceedings of the First International Conference on Soil Mechanics and Foundation Engineering.* Cambridge, Massachusetts : Harvard University Press, p. 54-56.

VIDAL, J. et A. GENTER (2018). « Overview of naturally permeable fractured reservoirs in the central and southern Upper Rhine Graben : Insights from geothermal wells ». In : *Geothermics* 74, p. 57-73. DOI : 10.1016/j.geothermics.2018.02.003.

Waldhauser, F. et W. L. Ellsworth (2000). « A Double-Difference Earthquake Location Algorithm : Method and Application to the Northern Hayward Fault, California ». In : *Bulletin of the Seismological Society of America* 90.6, p. 1353-1368. doi : 10.1785/0120000006.

Wang, Z. et G. AlRegib (2014). « Automatic fault surface detection by using 3D Hough transform ». In : *SEG Technical Program Expanded Abstracts 2014, Denver, Colorado*, p. 1439-1444. doi : 10.1190/segam2014-1590.1.

Withers, M., R. Aster, C. Young, J. Beiriger, M. Harris, S. Moore et J. Trujillo (1998). « A comparison of select trigger algorithms for automated global seismic phase and event detection ». In : *Bulletin of the Seismological Society of America* 88.1, p. 95-106.

Fracture network characterization in enhanced geothermal systems by induced seismicity analysis

DISSERTATION

of

M. Sc. Rike Köpke

submitted to

the Department of
Civil Engineering, Geo and Environmental Sciences
of the Karlsruhe Institute of Technology (KIT)

and the École Doctorale
Sciences de la Terre et de l'Environnement
of the University of Strasbourg

Day of the oral defence: December 16, 2020

Supervisors: Prof. Dr. Thomas Kohl
Dr. Jean Schmittbuhl, Directeur de Recherches

ii

Fracture network characterization in enhanced geothermal systems by induced seismicity analysis

Zur Erlangung des akademischen Grades einer

DOKTORIN DER NATURWISSENSCHAFTEN

an die Fakultät für
Bauingenieur-, Geo- und Umweltwissenschaften
des Karlsruher Instituts für Technologie (KIT)

eingereichte

DISSERTATION

von

M. Sc. Rike Köpke

aus Frankfurt (Oder).

Tag der mündliche Prüfung: 16. Dezember 2020

Referent: Prof. Dr. Thomas Kohl
Korreferent: Dr. Jean Schmittbuhl, Directeur de Recherches

Karlsruhe 2020

Fracture network characterization in enhanced geothermal systems by induced seismicity analysis

THÈSE dirigée par :
Mr. SCHMITTBUHL, Jean   Directeur de Recherches, Dr., Université de Strasbourg
Mr. KOHL, Thomas   Prof. Dr., Karlsruhe Institute of Technology

RAPPORTEURS :
Mr. RIETBROCK, Andreas   Prof. Dr., Karlsruhe Institute of Technology
Mr. FISCHER, Tomáš   Prof. Dr., Charles University Prague

AUTRES MEMBRES DU JURY :
Mr. RIVERA, Luis   Prof. Dr., Université de Strasbourg
Mr. HILGERS, Christoph   Prof. Dr., Karlsruhe Institute of Technology

Abstract

Fracture networks in underground reservoirs are important pathways for fluid flow and therefore a deciding factor in the development of geothermal reservoirs. Yet, they are difficult to characterize since they usually cannot be directly accessed. Subject of the doctoral project is to study induced seismicity in enhanced geothermal systems to characterize the underground fracture network. The main objectives are to get a better understanding of the structures controlling the fluid flow and the processes responsible for induced seismicity.

The first part of this work focuses on the case study of the Rittershoffen deep geothermal reservoir. It is demonstrated how the integration of advanced processing techniques like template matching detection, relative relocation and waveform clustering can lead to a deeper insight into the structure of the fault system and its reaction to repeated fluid injection. The well GRT1 at Rittershoffen offers unique conditions for such a study. It underwent a sequence of thermal, chemical and hydraulic stimulation, giving the opportunity to perform a detailed monitoring of the seismic response of the fault systems to fluid injections with different operational set-ups. By the applied processing, a much higher level of detail in the tempo-spatial resolution was derived than in previous studies on the induced seismicity at Rittershoffen. The results demonstrate the development of the successively activated fault network over the injection steps by tracing the influence of the different stimulations and allow for an analysis of the mechanisms behind the induced seismicity. Two spatially separated fault segments became seismically active over the course of the stimulation sequence, one during the injections itself, the other at the very end of the hydraulic stimulation and then again four days after shut-in. Seismicity on this two fault segments shows distinct characteristics in terms of event migration and waveform clusters, hinting at different fault activation mechanism. Seismicity on the first fault shows similar characteristics for the thermal and hydraulic stimulation

in the area active during both injections. The well-known geological setting and unique operational set-up in combination with the detailed analysis allowed to derive a deeper understanding of the hydro-mechanical interactions in the reservoir and demonstrated a change in the mechanical state of the fault between seismicity onset during thermal and hydraulic stimulation. In the case of the seismicity induced at Rittershoffen, the relative re-location of the events made two planar fault segments apparent, whose orientations and extends are well confined. Yet, it may be that despite the precise re-location of induced seismic events, the associated structures in other underground reservoirs remain unclear because the seismicity forms a rather dense spatial cloud, which makes individual features difficult to detect. Therefore, in the second part of this work, a new method is proposed to highlight the fracture network in seismic clouds that do not form apparent planar structures. With this method, the likelihood of having a fracture at a given location is computed from the distribution of seismic events and their source parameters. The result takes the form of a so-called Pseudo Probabilistic Fracture Network (PPFN). Contrary to other methods that try to highlight fracture networks in seismic clouds, the PPFN takes into account not only the event hypocenters but also their magnitudes and focal mechanisms, to keep a closer link with the geophysical properties of the earthquakes. The basic principle of the PPFN is to estimate the connectivity between any spatial position in the seismic cloud and the events based on the distance to each event, the minimum size of the rupture plane derived from the event magnitude, and the orientation provided by the focal mechanism. The PPFN is tested on a set of synthetic datasets, where it is demonstrated that the method is able to reproduce fault planes placed in a cloud of randomly distributed events. The PPFN is then applied to the seismic cloud induced during the stimulation of the GPK2 well, at Soultz-sous-Forêts deep geothermal site. It reveals a large prominent fault in the deep-northern part of the seismic cloud, supporting conclusions from previous work, and a minor structure in the southern upper part, which may be a branch of the main fault.

Zusammenfassung

Kluftnetzwerke in unterirdischen Reservoiren sind wichtige Fließwege für Fluide und daher ein entscheidender Faktor bei der Entwicklung geothermischer Systeme. Sie sind jedoch schwer zu charakterisieren, da sie in der Regel nicht direkt zugänglich sind. Gegenstand dieser Dissertation ist die Untersuchung der induzierten Seismizität in sogenannten Enhanced geothermal systems zur Charakterisierung des unterirdischen Kluftnetzwerks. Ziel ist das Erlangen eines besseren Verständnisses der Strukturen, die den Fluidfluss steuern, und der Prozesse, die für die induzierte Seismizität verantwortlich sind.

Der erste Teil dieser Arbeit konzentriert sich auf die Fallstudie des tiefen geothermischen Reservoirs Rittershoffen. Es wird gezeigt, wie die Integration moderner Analysemethoden wie Template Matching Detection, relative Erdbebenlokation und Waveform-Clustering zu einem tieferen Einblick in die Struktur des Störungssystems und seiner Reaktion auf wiederholte Fluidinjektion führen kann. Die Bohrung GRT1 in Rittershoffen bietet einzigartige Bedingungen für eine solche Untersuchung. Es wurde einer Sequenz bestehend aus thermischer, chemischer und hydraulischer Stimulation unterzogen, wodurch sich die Möglichkeit ergibt, die seismische Reaktion des Störungssystems auf Fluidinjektionen mit verschiedenen operativen Parametern zu überwachen. Durch die angewandte Methodik in der Datenprozessierung konnte ein deutlich höherer Detailgrad in der zeitlichen und räumlichen Auflösung der induzierten Seismizität erreicht werden als in vorhergehenden Studien. Das Ergebnis zeigt die Entwicklung des sukzessiv aktivierten Störungssystems über die verschiedenen Injektionsschritte hinweg. Dies ermöglicht den Einfluss der verschiedenen Stimulationen auf das Reservoir nachzuvollziehen sowie eine Analyse der Mechanismen, die zu der induzierten Seismizität führten. Zwei räumlich getrennte Störungssegmente wurden im Verlauf der Stimulationssequenz seismisch aktiv, eines während der Injektionen selbst, das andere ganz am Ende der hydraulischen Stimulation und ein weiteres Mal vier

Tage nach Einstellen der Fluidinjektion. Die seismischen Ereignisse assoziiert mit diesen beiden Störungssegmenten zeigen deutliche Unterschiede in Bezug auf räumlich-zeitliche Migration und Wellenformen, was auf unterschiedliche Aktivierungsmechanismen beider Störungen hindeutet. Die Seismizität auf der ersten Störung zeigt ähnliche Charakteristika für thermische und hydraulische Stimulation in dem Bereich des Reservoirs, der während beider Injektionsvorgänge seismisch aktiv war. Das gut charakterisierte geologische Umfeld und die einzigartige Stimulationsabfolge ermöglichen in Kombination mit der detaillierten Analyse ein tieferes Verständnis der hydromechanischen Wechselwirkungen im Reservoir und zeigen eine Änderung des mechanischen Zustands der ersten Störung zwischen dem Einsetzen der Seismizität während der thermischen und der hydraulischen Stimulation.

Im Fall der in Rittershoffen induzierten Seismizität machte die relative Relokalisierung der Ereignisse zwei planare Störungssegmente sichtbar, deren Orientierungen und Ausdehnungen gut eingegrenzt werden konnten. In anderen Fällen kann es jedoch sein, dass trotz genauer Verortung der induzierten seismischen Ereignisse das zugrundeliegende Störungssystem im Reservoir unklar bleibt, weil die Seismizität eine räumlich dichte Wolke bildet, wodurch einzelne Strukturen schwer zu identifizieren sind. Deshalb wird im zweiten Teil dieser Arbeit eine neue Methode vorgeschlagen, um das Störungsnetzwerk in seismischen Wolken, die keine klar ersichtlichen planaren Strukturen bilden, sichtbar zu machen. Mit dieser Methode wird aus der Verteilung der seismischen Ereignisse und weiterer ihrer Eigenschaften die Wahrscheinlichkeit der Lokation einer Kluft an einem bestimmten Ort berechnet. Das Ergebnis hat die Form eines sogenannten Pseudo Probabilistic Fracture Network (PPFN). Im Gegensatz zu anderen Methoden, die zum Ziel haben, Kluftnetzwerke in seismischen Wolken zu identifizieren, berücksichtigt das PPFN nicht nur die Hypozentren der seismischen Ereignisse, sondern auch deren Magnituden und Herdflächenlösungen, um einen engeren Zusammenhang mit den geophysikalischen Eigenschaften der Erdbeben zu erhalten. Das Grundprinzip der PPFN Identifizierung besteht darin, die Konnektivität zwischen einer beliebigen räumlichen Position in der seismischen Wolke und den einzelnen seismischen Ereignissen abzuschätzen. Dies geschieht auf der Grundlage der Entfernung jedes räumlichen Punktes zu jedem Ereignis, der minimalen Größe der Bruchfläche, die von der Magnitude der Ereignisse abgeleitet wird, und der Orientierung, die durch die Herdflächenlösungen bereitgestellt wird. Die Methode wird an synthetischen Datensätzen getestet, wobei gezeigt wird, dass sie in der Lage ist, Störungsflächen zu reproduzieren, die in einer Wolke zufällig verteilter seismischer Ereignisse liegen. Die PPFN Identifizierung wird dann auf die seismische Wolke angewendet, die

während der Stimulation der Bohrung GPK2 am Geothermiestandort Soultz-sous-Forêts induziert wurde. Das Ergebnis zeigt eine prominente Störung im tiefen, nördlichen Teil der seismischen Wolke, was in Übereinstimmung mit früheren Studien steht, sowie eine kleinere Struktur im südlichen oberen Bereich, die ein Zweig der Hauptstörung sein könnte.

Résumé

Les réseaux de fractures dans les réservoirs souterrains sont des voies importantes d'écoulement des fluides et donc un facteur décisif dans le développement des réservoirs géothermiques. Pourtant, ils sont difficiles à caractériser car ils ne sont généralement pas directement accessibles. Le sujet de cette thèse de doctorat est l'étude de la sismicité induite dans les systèmes géothermiques améliorés afin de caractériser le réseau de fractures souterraines. Les principaux objectifs sont de mieux comprendre les structures qui contrôlent l'écoulement des fluides et les processus responsables de la sismicité induite.

La première partie de ce travail se concentre sur l'étude de cas que constitue le réservoir géothermique profond de Rittershoffen. Il est démontré comment l'intégration de techniques de traitement avancées, telles que la détection par « template matching », la relocalisation relative et le regroupement de formes d'onde, peut conduire à une meilleure compréhension de la structure du système de failles et de sa réaction à l'injection répétée de fluide. Le puits GRT1 de Rittershoffen offre des conditions uniques pour une telle étude. Il a été soumis à une séquence de stimulation thermique, chimique et hydraulique, ce qui a permis d'effectuer un suivi détaillé de la réponse sismique des systèmes de failles aux injections de fluides avec différents dispositifs opérationnels. Grâce au traitement appliqué, la résolution spatio-temporelle a atteint un niveau de détail beaucoup plus élevé que celui des études précédentes sur la sismicité induite à Rittershoffen. Les résultats démontrent le développement progressif du réseau de failles activées au cours des étapes d'injection en retraçant l'influence des différentes stimulations et permettent d'analyser les mécanismes à l'origine de la sismicité induite. Deux segments de faille séparés dans l'espace sont devenus sismiquement actifs au cours de la séquence de stimulation, l'un pendant les injections elles-mêmes, l'autre à la toute fin de la stimulation hydraulique, puis à nouveau quatre jours après l'arrêt. La sismicité sur ces deux segments de faille présente des caractéristiques distinctes en termes de migration d'événements et de similarité

de formes d'onde, ce qui laisse supposer des mécanismes d'activation de la faille différents. La sismicité sur la première faille présente des caractéristiques similaires pour la stimulation thermique et hydraulique dans la zone active pendant les deux injections. La bonne connaissance des contextes géologique et opérationnel, combinée à l'analyse détaillée, a permis de mieux comprendre les interactions hydromécaniques dans le réservoir et a démontré un changement de l'état mécanique de la faille entre l'apparition de la sismicité pendant la stimulation thermique et pendant la stimulation hydraulique. Dans le cas de la sismicité induite à Rittershoffen, la relocalisation relative des événements a fait apparaître deux segments de faille planaire, dont les orientations et les étendues sont bien confinées. Cependant, il se peut qu'en dépit de la relocalisation précise des événements sismiques induits, les structures associées dans d'autres réservoirs souterrains restent floues car la sismicité forme un nuage spatial assez dense, ce qui rend les caractéristiques individuelles difficiles à détecter. C'est pourquoi, dans la deuxième partie de ce travail, une nouvelle méthode est proposée pour mettre en évidence le réseau de fractures dans les nuages sismiques qui ne forment pas de structures planes apparentes. Avec cette méthode, la probabilité d'avoir une fracture à un endroit donné est calculée à partir de la distribution des événements sismiques et de leurs paramètres à la source. Le résultat prend la forme de ce que j'ai appelé un réseau de fractures pseudo probabilistes (PPFN). Contrairement à d'autres méthodes qui tentent de mettre en évidence les réseaux de fractures dans les nuages sismiques, le PPFN prend en compte non seulement les hypocentres des événements mais aussi leurs magnitudes et leurs mécanismes au foyer, afin de garder un lien plus étroit avec les propriétés géophysiques des séismes. Le principe de base du PPFN est d'estimer la connectivité entre toute position spatiale dans le nuage sismique et les événements en se basant sur la distance de chaque événement, la taille minimale du plan de rupture dérivée de la magnitude de l'événement et l'orientation fournie par le mécanisme au foyer. Le PPFN est testé sur un ensemble de données synthétiques, où il est démontré que la méthode est capable de reproduire des plans de rupture placés dans un nuage d'événements répartis de manière aléatoire. Le PPFN est ensuite appliqué au nuage sismique induit pendant de la stimulation du puits GPK2, sur le site géothermique profond de Soultz-sous-Forêts. Il révèle une faille importante dans la partie nord et profonde du nuage sismique, ce qui corrobore les conclusions de précédents travaux, et une structure mineure dans la partie supérieure sud, qui pourrait être une branche de la faille principale.

Acknowledgements

Contents

III Closing Section 127

IV Appendix 161

List of Figures

List of Tables

Part I

Introduction and Theory

Chapter 1

Introduction

1.1 The role and potential of enhanced geothermal systems in the current energy market

The current energy markets of many countries worldwide aim at expanding the share of renewable energies to reduce CO2 emissions. In countries with suitable geological conditions, most importantly with areas of high heat flow near the surface in naturally permeable rocks, geothermal energy already contributes majorly to that goal. Iceland is already covering 90% of its space heating and 29% of its electricity demand by geothermal energy in 2019 (the remaining 71% of electricity is produced from hydro-energy) (Orkustofnun, 2020). The major advantage of geothermal energy to most other renewable energy sources is its potential to provide base load power without high fluctuations like wind or solar energy. Current geothermal plants operate with capacity factors of 0.5 to 0.9 (IEA, 2017). Yet, while geothermal energy is principally available everywhere on earth, its safe and economical extraction is still a challenge in most regions.

A look at the renewable energy statistics 2020 of the International Renewable Energy Agency (IRENA, 2020) shows that currently geothermal power plants worldwide have a total installed capacity of about 14 GWe, which is only 0.5% of the capacity supplied by renewable energies. A main reason for this is that the economically most viable and comparatively easy to harness hydrothermal systems are not found on earth in abundance. In countries without major hydrothermal resources, enhanced geothermal systems (EGS)

will have to play an important role to reach a significant increase in geothermal energy usage. EGSs aim at accessing hot brine in reservoirs with a natural permeability too low for direct extraction at economically sufficient flowrates. Therefore, permeability in the underground has to be increased artificially by reservoir engineering (Breede et al., 2013). This is a technically complex process that involves coupled hydro-mechanical-chemical processes between the wellbore, the reservoir rock and the brine that are still not fully understood and predictable. Research in this area is ongoing and experiences in the last decades have already lead to great advancements in this area and to a growing number of research but also commercially viable EGS sites.

The first research site that explored the feasibility of enhancing reservoir permeability is the Fenton Hill site in New Mexico, whose development started as early as 1974 (Brown, 2009). The project demonstrated the general technical feasibility of creating an underground fracture network, making thermal energy exploitable. One of the most important EGS sites worldwide is the Soultz-sous-Forêts site located in the French part of the Upper Rhine Graben. It was initiated as a research site in 1986 and a huge volume of scientific data on EGS has been gathered since (Genter et al., 2010). In 2009, a 1.5 MWe ORC power plant was commissioned and is in operation to date. The experiences gained at Soultz sparked the development of other EGS sites in the Upper Rhine Graben in France and Germany like Insheim (Küperkoch et al., 2018), Bruchsal (Herzberger et al., 2010), Landau (Vasterling et al., 2017) and Rittershoffen (Baujard et al., 2017) and the currently developed sites of Vendenheim (Sanjuan et al., 2020) and Illkirch (Glaas et al., 2020). In Iceland, at the Reykjanes site, EGS technology is explored in the DEEP-EGS project (Friðleifsson et al., 2019) to reach supercritical fluids at 5 km depth that may have the potential to generate 10 times more power than a traditional geothermal dry steam well (Fridleifsson et al., 2007).

However, there are also drawbacks in the development of EGS sites. The world's largest EGS power plant was scheduled to be operational in Habanero, Australia, by 2015 with 40 MWe installed in the first phase. While a 1 MWe demonstration plant went operational at the beginning of May 2013, the Habanero project was abandoned in 2015, due to unmet economic expectations (Hogarth and Holl, 2017). The development of the largest planned Asian EGS site in Pohang, Korea, had to be suspended because of a 5.5 magnitude earthquake that might be associated with the field development (Grigoli et al., 2018). The same fate suffered the EGS project at Basel that had to be stopped after a magnitude 3.4 earthquake (Häring et al., 2008). Only if such incidents can be mitigated in future projects, the EGS tech-

nology can exploit its full potential, which is quite large. Studies show that, on the European continent, the technical potential for EGSs in a depth up to 5 km and temperatures above 150°C is nearly 300 GWe (Chamorro et al., 2014). While this is only a rough estimate not considering specific geological conditions, it shows that there is considerable room for growth in the use of EGS in Europe. However, Olasolo et al. (2016), who analyzed specifically the economics of EGSs, came to the conclusion that significant technological improvements are required to make EGS facilities profitable and capable of competing financially with other renewable energy sources by 2030. Therefore, research has to be concentrated in making development of EGS systems on the one hand less expensive and on the other hand safer, especially in terms of induced seismicity.

1.2 Fracture dominated geothermal reservoirs

Many geothermal systems are located in fractured reservoirs (Vidal and Genter, 2018), characterizing fluid flow in fracture networks is therefore key in geothermal heat exploitation. Fractures in the subsurface develop in response to stresses in the rock mass and can be of various origins like lithostatic pressure, fluid pore pressure, tectonic forces or thermal stresses from heating and cooling. They vary in scale from microns to hundreds of kilometers and have a significant effect on flow and transport processes in the earth crust, acting as hydraulic pathways as well as barriers (NRC, 1996). However, not all fractures are equally hydraulically significant in flow systems. Often more critical to fluid flow than the amount of fractures is their connectivity and their inter-connection (Berkowitz, 2002). It has been observed that among a large number of fractures intersecting a well, only a few may actually transmit fluid (Evans et al., 2005b; Vidal et al., 2017). Parameters like fracture density, orientation, size and conductivity as well as the geometry of the overall network dictate the hydraulic and mechanical properties of the reservoir, making the assessment of the flow behavior of the geothermal fluid challenging.

For geothermal reservoirs, the success of the field development is highly dependent on a fracture network that enables subsurface fluid circulation. The intersection between the wells and the fracture system is crucial, making local fault zones often the main targets during exploration. In the Upper Rhine Graben, temperature data show a spatial link between high temperatures in the underground and local faults due to hydrothermal circulation

in the associated fracture networks (Baillieux et al., 2013; Pribnow and Schellschmidt, 2000). The higher the flowrate at which the fluids can be extracted and the higher the temperatures, the more geothermal power can be gained and the more economic the system. However, while too low permeability makes the system uneconomic, very high fracture transmissivities can also be problematic, since large, highly connected fractures can act as short circuits between production and injection wells (Brown et al., 1999). In such cases, reinjected fluids do not have enough residence time in the reservoir to absorb much heat.

Unlike hydrothermal systems, EGSs initially lack a conductive enough fracture network for economic operation. Therefore, the natural fracture network is enhanced by reservoir stimulation. These operations require knowledge about the subsurface stresses and the initial fracture geometry to be safe and efficient. For example, in the Upper Rhine Graben, fault zones are steeply dipping, therefore vertical wells have a low probability of ideally intersecting them and connection between fracture zones and wells may be weak (Vidal and Genter, 2018). The most recent wells drilled in the URG were deviated to reach higher intersection with the fracture system associated with the fault zone. These deviated wells show high hydraulic yields, even making reservoir stimulation unnecessary as observed at wells in Rittershoffen (GRT-2), Brühl (GT-1) or Insheim (GTI-2) (Vidal and Genter, 2018).

Over the course of reservoir development and exploitation, the stress state of the rock mass and the mechanical and hydraulic properties of the fracture network are perturbed by injection and extraction of fluids (Taron and Elsworth, 2010). These processes take place inevitably but are also used intentionally to influence the fracture network in stimulation operations of EGSs to increase rock permeability. However, processes during fluid extraction and injection are complex and not always predictable. Pore pressure changes, thermal effects and chemical reactions may cause movement on existing fractures, create new ones, lead to dissolution or precipitation of minerals and can over a lifetime of a reservoir lead to a net increase as well as decrease of the fracture network permeability depending on the specific conditions (André et al., 2006; Blöcher et al., 2016; Koh et al., 2011).

Fracture networks in underground reservoirs can be characterized by different approaches that each have advantages and disadvantages and provide different levels of detail. To get a direct, physical image of the fractures in the reservoir, the only way is the analysis of well-logs and cores (Dezayes et al.,

2004; Dezayes et al., 2010; Vidal et al., 2017). They provide an impression of fracture density, size, aperture and orientation and an indication of their connectivity. The major drawback is that logs and cores only provide a very limited spatial image in the direct vicinity of the well, not the 3D layout of the fracture network in the reservoir. Similar limitations has the mapping of outcrops as reservoir analogues (Cilona et al., 2016; Watkins et al., 2018). Here, the general pattern of fracture interconnection can be studied in 2D but outcrops can only be assumed to be representative of the underground conditions, which is not always the case (Howell et al., 2014; Watkins et al., 2015).

To analyse fluid flow in the reservoir, the fracture network properties estimated from logs, cores and/or outcrops can be used to build a fracture network model and simulate the hydraulic conditions. A huge amount of research has been performed in this domain (e.g. Kohl and Mégel, 2007; Tóth, 2010; Darcel et al., 2003b; Follin et al., 2014) but it is not subject of this thesis.

Instead, the focus is on the use of induced seismicity for reservoir imaging. Seismicity may be induced by activities like drilling, circulation and hydraulic stimulation of geothermal reservoirs (e.g. Maurer et al., 2020; Cuenot et al., 2008) due to shearing on fracture surfaces (Chapter 2). Therefore, the locations of induced earthquakes can be used to image the fracture network. This approach cannot provide a detailed map of the mesoscale fractures but it is able to image important fault zones across the 3D reservoir on a scale starting at several tens of meters. However, it has to be kept in mind that only seismogenic structures are highlighted, which may not represent the entirety on the fracture network.

1.3 Stimulation of enhanced geothermal systems and induced seismicity

Most environments do not provide ideal conditions for harnessing geothermal energy from the underground. A common obstacle is that the permeability of the fracture network in the potential reservoir is not high enough to allow fluid extraction at sufficient flowrates. In such a case, the reservoir might be stimulated by different approaches to increase the permeability by opening/widening fractures that act as fluid pathways. The geothermal system

is then considered an enhanced geothermal system (EGS) in contrast to hy-
drothermal systems that do not require permeability enhancement. The most
commonly used stimulation approach is hydraulic stimulation (Breede et al.,
2013), during which fluid at high pressures is injected into the underground to
induce shear movement on the fractures that leads to an increase in aperture
(McClure and Horne, 2014). In regions with very hot reservoir tempera-
tures like Iceland, thermal stimulation is a widely employed technique. The
high temperature differences between injected fluid and reservoir rock causes
widening of pre-existing fractures due to shrinkage of the rock mass as well
as creation of new fractures by thermal cracking (Axelsson et al., 2006). If
minerals are plugging the fractures, they can be dissolved by injecting special
chemicals in a chemical stimulation operation (Portier et al., 2009). Often
wells are stimulated several times, applying different stimulation techniques
to efficiently increase permeability of the fracture network.

Reservoir stimulation at EGS sites is regularly accompanied by induced
seismicity, especially hydraulic stimulation operations (Evans et al., 2012).
Small earthquakes are the expected and natural result of shearing on the
fracture surfaces that leads to enhanced permeability. The conditions under
which seismicity is induced depend on the local stress field in the underground
that is building up due to tectonic forces over geological time scales (Zang and
Stephansson, 2009). Natural earthquakes are one of the main mechanisms to
release these stresses when they exceed the strength of pre-existing planes of
weakness. Induced earthquakes follow the same principal, they occur when
either the local stress field is perturbed or the strength of the fracture is
reduced in a way that it is not stable anymore (Trifu, 2002). The initial
cause of the stress perturbation is in most cases assumed to be the increasing
pore pressure following fluid injection as also observed in other contexts like
wastewater disposal (Keranen et al., 2014), oil- and gas-recovery (Maxwell
et al., 2010) or CO2-sequestration (Rutqvist et al., 2016). Other processes
like temperature variations and chemical reactions in the reservoir can also
influence stress state and fault stability and lead to rock failure.

Seismicity at EGS sites is routinely monitored real-time to adjust the
injection scheme to the level of induced seismicity. The majority of seismic
events induced during development and exploitation of geothermal fields is
below magnitudes that would cause damage or can be felt by the population
(Evans et al., 2012). Still, induced seismicity can reach unexpectedly high
magnitudes and lead to the abandonment of a project. One such example
is the Basel Deep Heat Mining project where stimulation caused an event
of magnitude 3.4 after shut-in (Häring et al., 2008). The situation is even

more complicated and unpredictable when injection triggers seismicity on nearby fault structures that were not directly targeted. This happened likely at the Pohang geothermal site were a magnitude 5.5 earthquake occurred near the project site (Grigoli et al., 2018). That induced seismicity can be observed even after injection stopped or farther away from the project site is attributed to mechanisms like pore pressure diffusion, poro-elastic effects, aseismic stress transfer by slow movements or event-to-event triggering (Eyre et al., 2019; Fan et al., 2019; Mukuhira et al., 2017; Schoenball et al., 2012). The interactions between all these mechanisms cannot be easily traced or predicted.

Approaches to forecast induced seismicity are either based on the statistics of already monitored induced seismicity, on physical models of the geomechanical processes in the geothermal reservoir or the combination of both concepts (Gaucher et al., 2015b). Statistical models use the pattern of already monitored seismicity to predict changes of seismicity rate and magnitudes in relation to the stimulation operational parameters (e.g. Bachmann et al., 2011). Based on this approach, so called traffic-light systems have been developed to prevent large magnitude events during geothermal reservoir stimulation (e.g. Bommer et al., 2006). To date, for quantitative forecasts of induced seismicity during reservoir stimulation mostly statistical models are used. They are easy to implement, allow real-time application and have proven their ability to forecast induced seismicity during the main stimulation phase (e.g. Mena et al., 2013). However, they fail to predict large magnitude events during or after shut-in (Häring et al., 2008). The underlying reason for this limitation is the missing physical link between the processes at the origin of the induced seismicity and the seismic catalogue.

Such a link is provided by physics-based forecasting methods (e.g. Koh et al., 2011; Kohl and Mégel, 2007; McClure and Horne, 2014). They aim at predicting induced seismicity by modelling the underlying geomechanical processes during stimulation operations and therewith rely on an accurate description and parameterization of the reservoir conditions. Quantitative forecast based on physical models is still challenging due to the outlined complex processes that lead to induced seismicity. In hybrid models, the advantages of both, statistical and physics-based approaches, are combined (e.g. Shapiro et al., 2007; Shapiro and Dinske, 2009; Gischig and Wiemer, 2013; Goertz-Allmann and Wiemer, 2012), making them promising candidates for the use as reliable forecasting methods.

Since induced seismicity is a potential risk and one of the main reasons

for public rejection of EGS projects (Evans et al., 2012), it is important to advance prediction and mitigation of especially large magnitude event by getting a deeper understanding of the processes behind induced seismicity. Several factors can influence seismicity rate and event magnitudes like injection flowrate and pressure, total injected volume, injection depth, local stress field, rock type, natural seismicity in the area and proximity to faults (Gaucher et al., 2015a). Studies of induced seismicity at EGS projects have shown that the largest magnitude event cannot be reliably related to one single operational parameter like maximum injection pressure, injected volume or injection flowrate (Evans et al., 2012). This makes it difficult to predict the reaction of the reservoir to fluid injection and despite extensive research having been carried out in the last years in the field of induced seismicity, it is still not controllable to a sufficient degree to consider it a non-issue for future EGS projects.

While induced seismicity is a potential risk in the development and operation of EGS, it can also be a valuable tool for reservoir characterization (Cuenot et al., 2008; Deichmann et al., 2014; Lengliné et al., 2017). Since seismicity is induced on fractures whose permeability is enhanced during stimulation, the earthquake hypocenters can be used to image at least part of the underground fracture network that otherwise often remains highly speculative. The tempo-spatial distribution of induced seismicity in combination with the operational parameters during stimulation can also give insight into the mechanisms behind the induced seismicity (Maurer et al., 2020). Induced seismicity can therewith help to get a clearer picture of the pathways and processes that guide fluid flow in the reservoir.

1.4   Thesis overview

The objective of this thesis is to demonstrate how induced seismicity in enhanced geothermal systems can be used to characterize the underground fault network. The main points are to identify the geometry of the fault network and to understand its mechanical reaction during reservoir stimulation operations that lead to induced seismicity. The geometry of the fault network is a deciding factor for fluid flow in the reservoir and therefore the exploitation of hot brine, while induced seismicity is one of the main show-stoppers in the current development of EGSs. This thesis aims at contributing to a better understanding of these two key points to make development of EGSs safer and better predictable.

To get a theoretical understanding of why seismicity is induced during stimulation of enhanced geothermal systems and can be used for fault network characterization, Chapter 2 provides the geomechanical background of earthquake generation. Chapter 3 gives an overview over earthquake detection and location techniques to explain the choices in methodology made in this work. In Chapter 4, the two sites of the enhanced geothermal systems Rittershoffen and Soultz-sous-Forêts are introduced. The seismicity induced during the stimulation of the well GRT1, Rittershoffen, and GPK2, Soultz-sous-Forêts, is compared since the analysis that constitute this thesis are based on these two seismic catalogues.

In the main part of the thesis, two different cases of fault network characterization from induced seismicity are presented in two individual studies that are accepted for publication or submitted to international journals. The first study (Chapter 5) is a detailed interpretation of the seismicity induced over the injection sequence of thermal, chemical and hydraulic stimulation of the well GRT1 of the deep geothermal reservoir Rittershoffen. In this study, advanced methodologies like template matching detection, relative relocation and waveform clustering are integrated to obtain a comprehensive seismic catalogue. This catalogue is the basis for a detailed analysis of the tempo-spatial event distribution, the mechanical state of the fault and its changes over the injection sequence, and the processes behind the induced seismicity.

The second study (Chapter 6) presents a new method to highlight the geometry of the fault network in seismic clouds that do not exhibit obvious planar features even after precise event location. Instead of trying to infer the definite layout of the fault system, this method computes a measure of likelihood to have a fracture at a given location in the seismic cloud. For the computation, the spatial distribution of the event hypocenters, their magnitudes and their focal mechanisms are used, thus keeping a close link with the geophysical properties of the earthquakes. The method is applied to a set of synthetic datasets to demonstrate its feasibility and then to the seismicity induced during the stimulation of the well GPK2 of the Soultz-sous-Forêts geothermal site.

Chapter 2

Earthquake geomechanics

In this chapter, an introduction to basic principles of rock mechanics and earthquake generation as well as to the seismological foundations of earthquake source characterization is given. There exist various textbooks on these topics, the descriptions and explanations in this chapter follow mainly the monographs of Zoback (2010), Cornet (2015), Shearer (2019) and Aki and Richards (2009).

2.1   Stress in rock masses

Stress is the amount of force per unit area experienced by a material, e.g. the rock mass in the underground. Stresses in the underground rock mass are the result of different forces acting on it, like the overburden of overlying rocks causing lithostatic or confining stress equal from all directions and tectonic forces introducing deviatoric stresses or differential stresses that can be tensional, compressional or shear stresses (Fig. 2.1). The rock mass responds to the experienced stress with strain, which is a measure of deformation of the material.

Depending on several factors like pore pressure, strain rate, rock strength, temperature, stress intensity, time, and confining pressure the rock may respond with elastic deformation, ductile deformation or brittle deformation. Elastic deformation is reversible, meaning the rock mass returns to its original state when the stress would be removed. In this case, the experienced
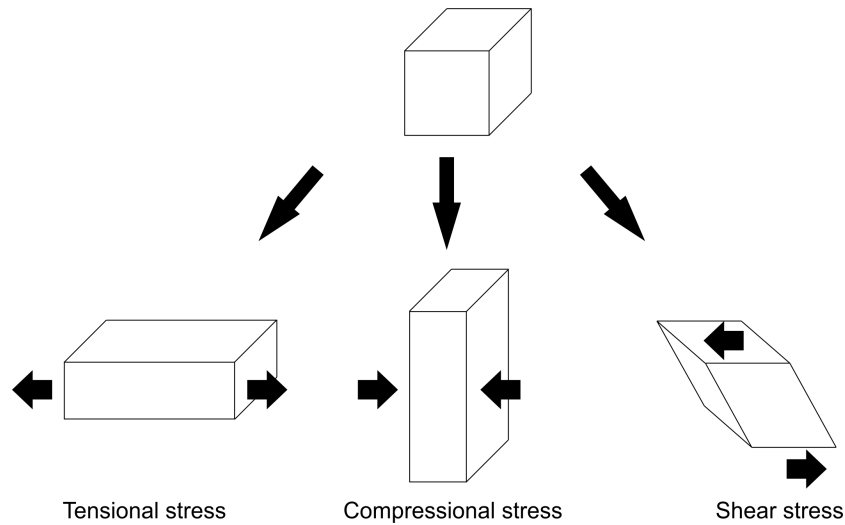
Figure 2.1 – Different types of differential stresses acting on a rock volume causing strain.

stress is lower than the yield strength of the rock. Ductile deformation and brittle deformation occur when the yield strength of the rock is surpassed by the applied stress and lead to permanent deformation. While during ductile deformation, the rock mass stays in one piece, during brittle deformation the rock breaks and a fracture is created (Fig. 2.2).

Shear stress released on such fractures by sliding rock masses is what causes earthquakes. This can be explained by the elastic rebound theory (Reid, 1910). When rock is strained to the point that it undergoes brittle deformation, it has already experienced a certain amount of elastic deformation during which energy is stored. Once rupture occurs, the rocks on both sides of the fault slip past each other to recover their original shape. This is called elastic rebound and releases the stored energy in form of heat and seismic waves (Fig. 2.3). After the rupture, the fault blocks may be locked together by friction and if stresses build up over time again, they can overcome the frictional resistance, the fault blocks slip again and the next earthquake occurs. In locations where the fault blocks are not locked, the applied stress causes continuous, gradual displacement between the fault blocks called fault creep.

Whether rock failure and slippage occur when stresses are applied to the rock mass in an underground reservoir is majorly dependent on the pre-existing stresses in the underground and therewith the local stress field as well as the orientation of pre-existing fractures. Stresses can be described by a so-
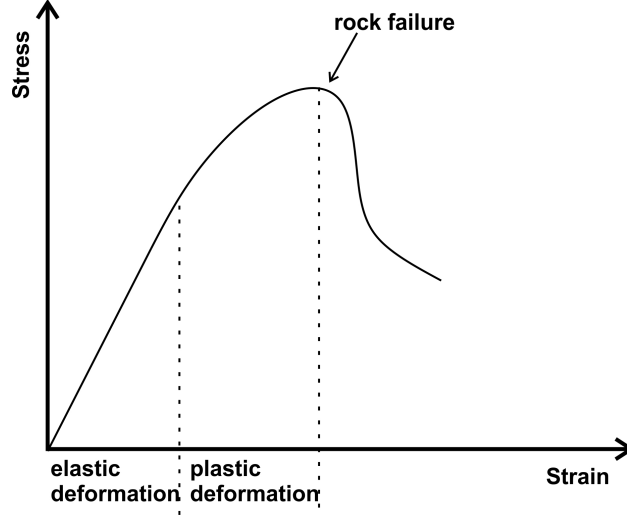
Figure 2.2 – Schematic stress-strain-diagram, indicating the different types of deformation with increasing stress and strain.
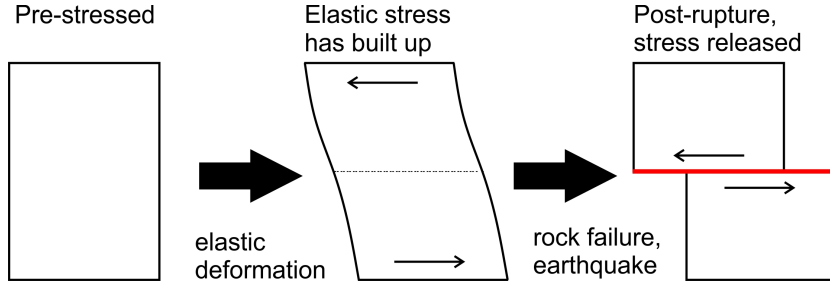
Figure 2.3 – Schematic of the earthquake-generation process. With increasing stress built-up, the rock mass first deforms elastically, then it ruptures and the stored elastic energy is released in form of seismic energy as an earthquake.

called stress tensor (Shearer, 2019). If an elementary volume in the rock mass is considered, stresses can act on every side of that volume in three directions x, y, z, resulting in three stress vectors for each side that can be summarized in form of a 2 dimensional tensor. This resulting stress tensor would consist of 9 components σ_{ij} with $i, j = 1, 2, 3$, with i denoting the direction of the plane normal on the elementary volume and j the direction in which the stress is acting (Fig. 2.4). The diagonal elements of the tensor, where $i = j$, are the normal stresses, meaning the stress is acting perpendicular to the plane. All other elements, where $i \neq j$, are shear stresses denoted by τ_{ij}.

Because the elementary volume is assumed to be in static equilibrium,
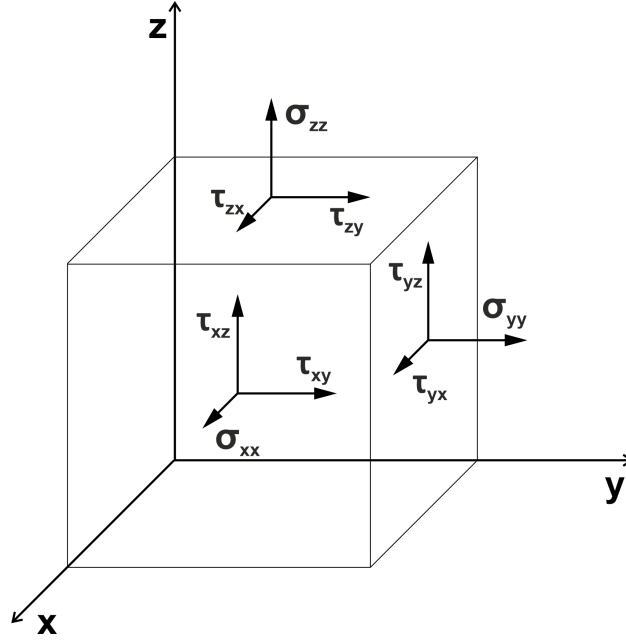
Figure 2.4 – Stress acting on an elementary volume in three different orientations on each surface, resulting in the nine components of the stress tensor.

angular momentum has to be conserved so that $\tau_{ij} = \tau_{ji}$. Therefore, the stress tensor is symmetric and consists of only six independent components that describe the stress state at each point in the rock mass:

$$\sigma = \begin{pmatrix} \sigma_{xx} & \tau_{xy} & \tau_{xz} \\ \tau_{xy} & \sigma_{yy} & \tau_{yz} \\ \tau_{xz} & \tau_{yz} & \sigma_{zz} \end{pmatrix} . \tag{2.1}$$

In any stress field, one can find a set of three orthogonal planes such that there are no shear stresses acting on these planes and the stress tensor thus takes a diagonal form:

$$\sigma = \begin{pmatrix} \sigma_1 & 0 & 0 \\ 0 & \sigma_2 & 0 \\ 0 & 0 & \sigma_3 \end{pmatrix} . \tag{2.2}$$

This transformation can be done by calculating the eigenvalues of the tensor. The corresponding eigenvectors are orthogonal and define the so-called principal stress axes of the stress field. In rock mechanics, the principal stresses
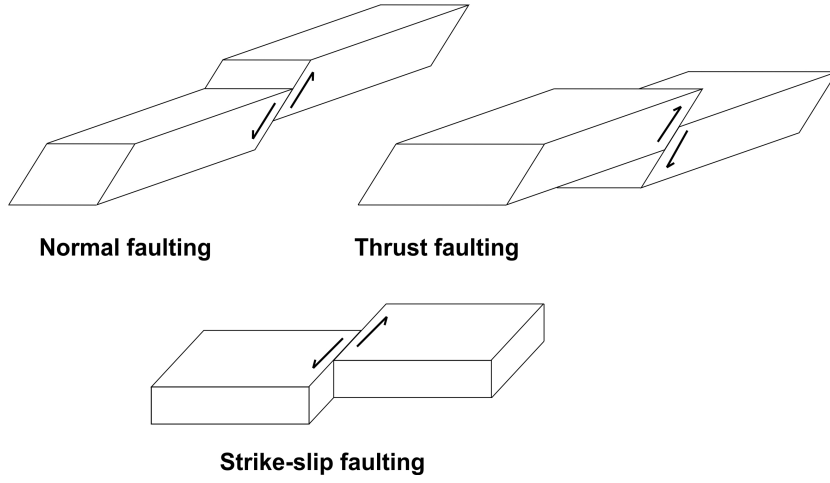
Figure 2.5 – Different modes of faulting, depending on the local stress regime.

are conventionally sorted in the following order:

$$\sigma_1 \geq \sigma_2 \geq \sigma_3 \,, \qquad\qquad (2.3)$$

where σ_1 and σ_3 are called the maximum and the minimum principal stress respectively.

In an underground reservoir, normally the vertical stress σ_v caused by the overburden is assumed to be one of the principal stresses (Andersonian stress system (Anderson, 1951)). The other two principal stresses would then be the maximum horizontal stress σ_H and the minimum horizontal stress σ_h. The stress magnitudes depend on the tectonic setting and determine the dominant mode of faulting in the area (Anderson, 1951). If $\sigma_v > \sigma_H > \sigma_h$, the expected faulting mode would be normal faulting, if $\sigma_H > \sigma_v > \sigma_h$, it would be strike-slip-faulting and if $\sigma_H > \sigma_h > \sigma_v$ it would be thrust or reverse faulting (Fig. 2.5). Conversely, the stress regime of a site can be deduced from observed faults.

2.2   Rock failure on fault planes

2.2.1   Mohr-Coulomb failure criterion

Whether slippage occurs on a fracture depends on the normal and shear stresses acting on it, which are again dependent on the fracture orientation relative to the local stress field. In the following, the case of an arbitrary x-y coordinate system in 2D space is discussed: A plane with angle θ to the direction σ_{xx} (that is relative to the x-axis), is subjected to the normal stress σ and the shear stress τ that can be described by the following relations:

$$\sigma = \frac{1}{2}(\sigma_{xx} + \sigma_{yy}) + \frac{1}{2}(\sigma_{xx} - \sigma_{yy})\cos(2\theta) + \tau_{xy}\sin(2\theta) \qquad (2.4)$$

$$\tau = \frac{1}{2}(\sigma_{yy} - \sigma_{xx})\sin(2\theta) + \tau_{xy}\cos(2\theta). \qquad (2.5)$$

Equations (2.4) and (2.5) are the parametric equations of the so-called Mohr-circle (Mohr, 1914), which is drawn in σ-τ space. The Mohr-circle visualizes the possible relationships between the normal and shear stresses acting on a plane of any orientation (see Fig. 2.6, left). Center and radius of the Mohr-circle can be derived by eliminating the parameter 2θ in Eqs. (2.4) and (2.5) and rearranging to:

$$\left[\sigma - \frac{1}{2}(\sigma_{xx} + \sigma_{yy})\right]^2 + \tau^2 = \left[\frac{1}{2}(\sigma_{xx} - \sigma_{yy})\right]^2 + \tau_{xy}^2. \qquad (2.6)$$

This can be seen as the equation of a circle with the general form:

$$(x - a)^2 + (y - b)^2 = r^2, \qquad (2.7)$$

with (a, b) the center of the circle and r the radius. The radius of the Mohr-circle therefore is

$$r = \sqrt{\left[\frac{1}{2}(\sigma_{xx} - \sigma_{yy})\right]^2 + \tau_{xy}^2} \qquad (2.8)$$

and the center is

$$(a, b) = \left(\frac{1}{2}(\sigma_{xx} + \sigma_{yy}), \ 0 \right), \tag{2.9}$$

putting the Mohr-circle on the σ-axis in the σ-τ diagram. The minimum and maximum normal stresses (left and right intersection of the Mohr-circle with the σ-axis) have $\tau = 0$ and are thus called the principal stresses:

$$\sigma_1 = \frac{1}{2}(\sigma_{xx} + \sigma_{yy}) + \sqrt{\left[\frac{1}{2}(\sigma_{xx} - \sigma_{yy}) \right]^2 + \tau_{xy}^2} \tag{2.10}$$

$$\sigma_2 = \frac{1}{2}(\sigma_{xx} + \sigma_{yy}) - \sqrt{\left[\frac{1}{2}(\sigma_{xx} - \sigma_{yy}) \right]^2 + \tau_{xy}^2}. \tag{2.11}$$

If the coordinate system is chosen such that the axes are parallel to the principal stresses, the τ_{ij} components become zero (see Eq. (2.2)) and therefore Eqs. (2.4) and (2.5) would become:

$$\sigma = \frac{1}{2}(\sigma_1 + \sigma_2) + \frac{1}{2}(\sigma_1 - \sigma_2)\cos(2\theta) \tag{2.12}$$

$$\tau = -\frac{1}{2}(\sigma_1 - \sigma_2)\sin(2\theta), \tag{2.13}$$

where θ is now the angle between maximum principal stress σ_1 and plane normal. In this principal coordinate system, center and radius of the Mohr-circle would be:

$$(a, b) = \left(\frac{1}{2}(\sigma_1 + \sigma_2), \ 0 \right) \tag{2.14}$$

$$r = \frac{1}{2}(\sigma_1 - \sigma_2). \tag{2.15}$$
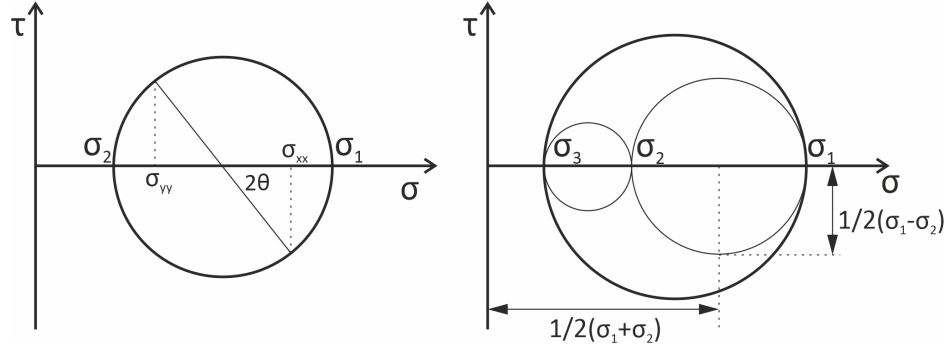
Figure 2.6 – Mohr-circles plotted in the σ-τ diagram. Left: in 2D space, the angle θ is the angle of the plane to the σ_1 direction. Right: in 3D space, the stress state of any plane lies within the radius of the σ_1-σ_3 circle but outside the σ_1-σ_2 and the σ_2-σ_3 circle.

The above equations are 2D representations for the x-y, or σ_1-σ_2 space but could just as well be set up for the σ_2-σ_3 and σ_1-σ_3 space. All three Mohr-circles are shown in Fig. 2.6. A full 3D treatment shows that normal and shear stress have to obey the following inequalities (Cornet, 2015):

$$
\tau^2 + \left[\sigma - \frac{1}{2}(\sigma_2 + \sigma_3)\right]^2 \geq \left[\frac{1}{2}(\sigma_2 - \sigma_3)\right]^2
$$
$$
\tau^2 + \left[\sigma - \frac{1}{2}(\sigma_1 + \sigma_3)\right]^2 \leq \left[\frac{1}{2}(\sigma_1 - \sigma_3)\right]^2
$$
$$
\tau^2 + \left[\sigma - \frac{1}{2}(\sigma_1 + \sigma_2)\right]^2 \geq \left[\frac{1}{2}(\sigma_1 - \sigma_2)\right]^2 . \tag{2.16}
$$

One can read these as relationships between σ, τ, the Mohr-radii $r_{ij} = \frac{1}{2}|\sigma_i - \sigma_j|$ and their circle centers $a_{ij} = \frac{1}{2}(\sigma_i + \sigma_j)$. In effect, only those points (σ, τ) which lie within the biggest but outside of the two smaller circles are valid configurations for normal and shear stress for any plane in 3D space (see Fig. 2.6).

To decide if a plane of a certain orientation would slip, a failure criterion can be applied that divides stable from unstable conditions. The plane slips when the shear stress on the plane is larger than the forces stabilizing the plane. One commonly applied failure criterion is the Coulomb failure

criterion (Coulomb, 1773). Failure is reached when:

$$\tau = \mu\sigma + c \qquad (2.17)$$

The forces stabilizing the plane have two different origins: On the one hand, shear movement is opposed by friction caused by the normal stress σ acting on the plane and the friction coefficient μ of the material. On the other hand, the material possesses a certain internal strength, expressed by its cohesion c. The Coulomb failure criterion can be plotted together with the Mohr-circle in the σ-τ diagram for the σ_1-σ_3 space (Fig. 2.7), since it assumes that failure is controlled by the maximum shear stress. If the Mohr-circle touches or crosses the failure criterion, faults with orientations in the area where the Mohr-circle lies above the failure criterion would slip in the present stress field, while planes with orientations below the failure line would be stable. The angle θ between a fault plane with an optimal orientation for failure and the σ_1-direction direction, that is the angle for which the failure criterion just touches the Mohr-circle, is dependent on the friction angle ϕ of the rock:

$$\theta = \frac{\pi}{4} + \frac{\phi}{2}\,, \qquad (2.18)$$

where $\phi = \arctan\mu$. If the rock was initially intact, this is the angle a newly created fracture will have relative to σ_1.

The Mohr-Coulomb criterion is the most commonly applied failure criterion to evaluate rock stability because it is simply and intuitive. However, other failure criteria exist, some of them also considering the influence of the intermediate stress σ_2 on rock strength (Zoback, 2010).

In the earth crust, fractures and faults exist in a stable state until an event or process changes the conditions in a way that the failure criterion is met. Looking at the Mohr-Coulomb criterion, this can either be due to a disturbance of the stress field, causing the effective stresses acting on the fault plane to decline, or a change in the mechanical rock properties, namely cohesion and friction coefficient. During stimulation operations in geothermal reservoirs, it is assumed that the most common cause for rock failure and therewith for induced seismicity is the applied fluid pressure. However, more and more research indicates that other effects may play an important role as well (Gaucher et al., 2015a).
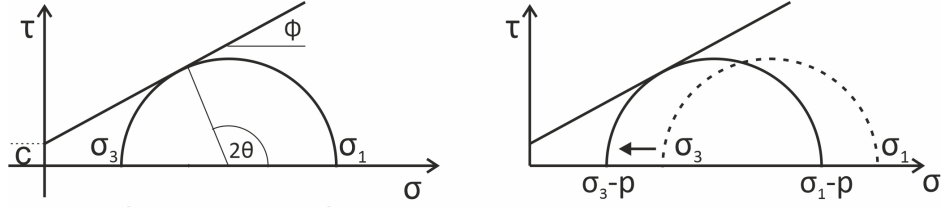
Figure 2.7 – Coulomb failure criterion (straight line) and Mohr circle. Left: the fault plane optimally oriented for failure has the angle θ to the σ_1 direction. c is the cohesion, ϕ is the friction angle of the rock. Right: the pore pressure p is reducing the total stresses and can move the Mohr-circle from stable to unstable conditions.

2.2.2   Pore fluid pressure

In the above section, the stress conditions under which rock breaks and slippage on a fracture occurs have been outlined. However, one important factor that has been neglected in this examination so far is the fluid present in the underground. Since geothermal energy production relies on circulation of fluids in the reservoir and stimulation operations involve the injection of fluids partly at high pressures, the influence of the fluid pressure on rock stability is a crucial factor. As already explained in the introduction, many geothermal reservoirs are fractured reservoirs and as such fluid flow is guided by the fractures and faults while flow in the rock matrix plays a minor role.

The flow rate Q of a fluid in a fracture is dependent on the fracture aperture a, the permeability k and the dynamic viscosity μ of the fluid and the pore fluid pressure p:

$$Q = -\frac{a \cdot k}{\mu} \cdot \nabla p \,. \tag{2.19}$$

The permeability k can be related again to the fracture aperture:

$$k \approx \frac{a^2}{12} \,. \tag{2.20}$$

This results in a cubic relationship between flowrate and fracture aperture, known as the cubic law (Snow, 1965). However, this relationship is an approximation strictly valid only for flow between parallel plates, the roughness

of the fracture surfaces or small-scale variations in the fracture aperture and orientation are not considered. Still, flow in the reservoir is highly dependent on fracture aperture and the fracture aperture can change under applied pressure, an effect which is used during reservoir stimulation.

When injecting fluid at high pressure, the fracture first reacts by an elastic response, resulting in widening of the fracture and therefore an increase in aperture. This makes more space available for the fluid, which in turn reduces the further build-up of fluid pressure if injection flowrate is not increased. The elastic stresses resulting from the widening of the fractures are distributed by diffusion into the reservoir away from the injection point (Biot, 1941; Wang, 2000).

When even higher fluid pressure is applied, the fracture approaches a critical state and slips, resulting in a displacement of the fracture walls against each other leading to a permanent increase of aperture and therewith reservoir permeability (Barton et al., 1985; Willis-Richards et al., 1996). The reason fractures slip under increased fluid pressure is that the pore fluid pressure in the reservoir is acting against the rock mass (Terzaghi, 1936). Therewith, pore pressure reduces the stress in the rock mass to the so-called effective stress:

$$\sigma_{i,eff} = \sigma_{i,tot} - p\,, \tag{2.21}$$

where the total stress σ_{tot} is the stress on the rock resulting from the local stress field and p is the pore fluid pressure. When investigating rock failure with the Mohr-Coulomb analysis, the effective stress has to be considered not the total stress. Since pore pressure reduces the effective stress, the rock might fail even if it would be stable if only the total stress would act on it (Fig. 2.7). This effect is used during hydraulic stimulation. The injection of fluid leads to an increase in pore pressure, the effective stresses acting on the rock are decreased and failure ensues, resulting in the creation of higher permeability.

2.2.3 Alternative causes for rock failure

In geothermal systems, the fluid transport is closely linked to heat transport processes and temperature changes also introduce stress perturbation in the

rock mass. Fluid and rocks react to the heating and cooling with expansion and contraction, leading to thermally induced stresses (Jeanne et al., 2017). Similar to pore pressure, a temperature decrease reduces the effective stress by the thermo-elastic effect. Rapid cooling of the rock mass can lead to thermal cracking due to contraction while the expansion of the fluid during heating can lead to an additional increase in pore pressure (Gens et al., 2007; Axelsson et al., 2006). Because the cold injected fluid during stimulation heats up quickly, it is assumed that thermal effects initially are restricted to the direct vicinity of the well, however, during long-term fluid circulation larger parts of the reservoir can be effected over time. Next to hydraulic and thermal effects, fluid injection can also lead to chemical reactions on the fracture surfaces. This is of course especially true for chemical stimulations (Portier et al., 2009) but the thermal perturbation alone during hydraulic or thermal stimulations can initiate chemical reactions like dissolution or precipitation. Such chemical reactions can cause changes in the mechanical properties of the fractures and may result in a reduction of cohesion and/or friction coefficient, bringing the fracture closer to failure.

Next to effects directly caused by the injection fluid, other mechanism can be provoked by the initial stress perturbation. This may also lead to induced seismicity in larger distances from the injection point than reached by the migrating fluid. As already explained, the initial reaction of the fractures to increased pore pressure is elastic opening. This leads to elastic stresses in the surrounding rock matrix that are distributed by poro-elastic stress transfer (Biot, 1962; Rice and Cleary, 1976). Poro-elastic stress transfer can result into failure on faults that would not slip due to increased pore fluid pressure alone (Fan et al., 2019). It can also cause seismicity on faults in large distances from the injection source where pore fluid pressure increase is minor and the elastic stress response can be much quicker than pore pressure diffusion if the permeability is low (Deng et al., 2016).

Another mechanism that may contribute to induced seismicity is static stress transfer and the related effect of event-to-event triggering. Resulting from slip on a fault plane, stresses are re-distributed in the surrounding rock mass. While stress is released along the fracture plane, stresses build up at the fracture tips. This stress re-distribution is analytically described for the simplified case of a homogeneous half-space by Okada (1992) and for more complex settings by Wang et al. (2003) and Wang et al. (2006). Static stress transfer can lead to failure on other previously near-critical fractures in the vicinity of the initial rupture plane and may cause further induced seismicity by event-to-event triggering, where the stress changes related to

one seismic event trigger another event and so on. This can lead to aftershock sequences following large earthquakes (King et al., 1994). The role of static stress transfer for seismicity induced during the stimulation of geothermal reservoirs is analyzed for example in Schoenball et al. (2012) or Lengliné et al. (2017).

Lately, aseismic slip has attracted much attention as possible stress transfer mechanism in geothermal reservoirs. Aseismic slip or creep describes the slow movement on fault planes without apparent seismicity. It may occur on faults with low frictional strength, where the fault blocks are not locked, or when low normal stresses are acting on the fault plane, which can also be a result of elevated pore-fluid pressure. Aseismic slip has been observed in the Soultz-sous-Forêts geothermal reservoir by several studies that show that the amount of slippage and stress release on the fractures cannot be explained by the induced seismicity alone (Cornet et al., 1997; Bourouis and Bernard, 2007; Calò et al., 2011). Such field observations are confirmed by experiments and numerical models evidencing that aseismic slip can play an important role for stress distribution and triggering induced seismicity. Schmittbuhl et al. (2014) investigated the link between aseismic slip and induced seismicity by conducting a laboratory experiment in which they tracked the evolution of an interfacial crack subjected to a load in time and space using optical and acoustic sensors. They showed that creep can trigger induced seismicity when heterogeneities exist along the fault and that seismic event occurrences in time and space are strongly related to the development of the aseismic motion. The models of Eyre et al. (2019) and Bhattacharya and Viesca (2019) evidence that the overpressure caused by fluid injection may activate aseismic slip over large distances and that the stress transfer resulting from aseismic slip can outpace the pore pressure diffusion front. All in all, there is ample evidence that aseismic stress transfer can be an important driver of induced seismicity in geothermal reservoirs.

2.3 Earthquake source characterization

2.3.1 Earthquake focal mechanism

The geometry of the source of an earthquake caused by rock failure can be described by the so-called focal mechanism or fault plane solution. It can be defined by strike ($0° \leq \varphi < 360°$), dip ($0° \leq \delta \leq 90°$) and rake
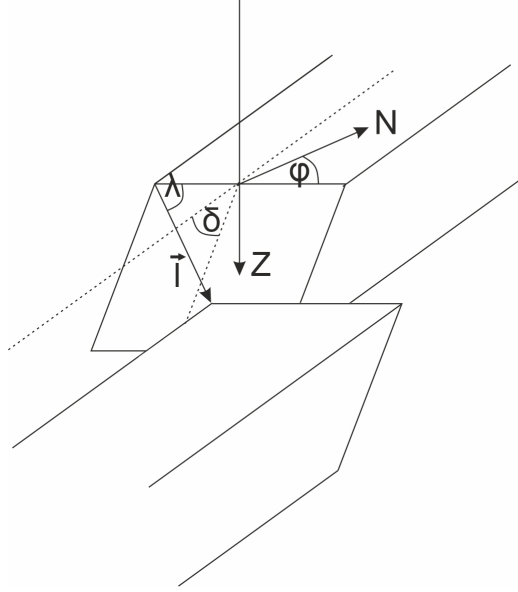
Figure 2.8 – Schematic of slip on a fault with slip vector $\vec{l}$, strike φ, dip δ and rake λ. N is the north-direction, Z is the depth-direction.

$(0° \leq \lambda < 360°)$, and the magnitude of the slip vector $\vec{l}$ (Fig. 2.8). Focal mechanisms are commonly derived either from the seismic moment tensor (e.g. Hingee et al., 2011) or from the pattern of first motion polarities of the seismic waves recorded at different seismic stations (e.g. Lentas, 2018).

The seismic moment tensor of an earthquake is the representation of the distribution of body forces resulting from the rupture (Shearer, 2019). The internal forces caused by slip on a fault plane must counteract each other to ensure conservation of momentum, resulting in two force vectors of the same magnitude and opposite orientation termed force couple. If the two vectors are separated by a distance perpendicular to their orientation, angular momentum has to be conserved by a second force couple of the same magnitude acting perpendicular to the first one. Such a pair of perpendicular force couples is termed double couple. In 3D space, nine different force couples M_{ij} pointing in direction i and separated in direction j can be defined (Fig. 2.9). They are summarized in the moment tensor M that consists of three double couples $M_{ij} = M_{ji}$ and three isotropic components with $i = j$:

$$M = \begin{pmatrix} M_{xx} & M_{xy} & M_{xz} \\ M_{yx} & M_{yy} & M_{yz} \\ M_{zx} & M_{zy} & M_{zz} \end{pmatrix} . \tag{2.22}$$
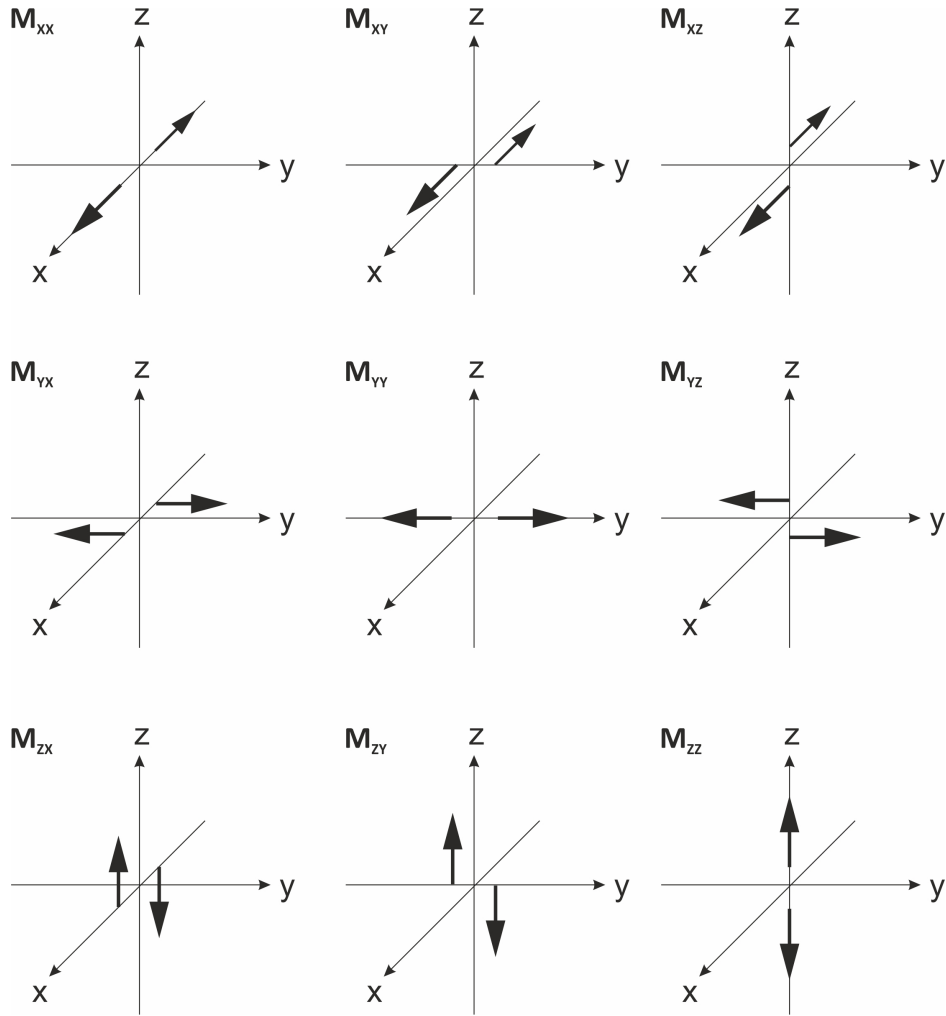
Figure 2.9 − The nine force double-couples of the moment tensor acting in three directions i separated in direction j. After Shearer (2019).

Although the moment tensor is an idealized representation of the internal forces acting at a point source, it can be used as an approximation for seismic sources that are small in comparison to the seismic wavelengths.

The moment tensor of an earthquake is characteristic for its focal mechanism. Strike φ, dip δ and rake λ of the rupture plane of a double-couple source are related to the components of the moment tensor (Aki and Richards, 2009):

$$
\begin{aligned}
M_{xx} &= -M_0 \left[\sin(\delta)\cos(\lambda)\sin(2\varphi) + \sin(2\delta)\sin(\lambda)\sin^2(2\varphi) \right] \\
M_{xy} &= M_0 \left[\sin(\delta)\cos(\lambda)\cos(2\varphi) + 0.5\,\sin(2\delta)\sin(\lambda)\sin(2\varphi) \right] \\
M_{xz} &= -M_0 \left[\cos(\delta)\cos(\lambda)\cos(\varphi) + \cos(2\delta)\sin(\lambda)\sin(\varphi) \right] \\
M_{yy} &= M_0 \left[\sin(\delta)\cos(\lambda)\sin(2\varphi) - \sin(2\delta)\sin(\lambda)\cos^2(\varphi) \right] \\
M_{yz} &= -M_0 \left[\cos(\delta)\cos(\lambda)\sin(\varphi) - \cos(2\delta)\sin(\lambda)\cos(\varphi) \right] \\
M_{zz} &= M_0 \left[\sin(2\delta)\sin(\lambda) \right].
\end{aligned}
\tag{2.23}
$$

The scalar seismic moment M_0 is a basic measure of earthquake strength and can be obtained from the moment tensor by:

$$
M_0 = \frac{1}{\sqrt{2}} \left[\sum_{ij} M_{ij}^2 \right]^{1/2}.
\tag{2.24}
$$

With the above relationships (2.23) and (2.24), the focal mechanism of an earthquake can be obtained by determining its moment tensor. The moment tensor is related to the displacement on the earth's surface that is measured in seismograms by the so-called Green's function (Jost and Herrmann, 1989). The Green's function describes the response of the rock mass to the seismic waves traveling through the earth from earthquake source to seismic station. From the Green's function and the measured seismogram, the moment tensor can be determined by moment-tensor inversion.

Even though the focal mechanism of a seismic source can be obtained by its moment tensor, routine waveform inversion techniques are usually mostly suitable for medium to large magnitude earthquakes that are detected by stations at teleseismic distances (Hingee et al., 2011; Ritsema and Lay, 1995). An alternative approach to obtain the focal mechanism of the source, e.g. for smaller earthquakes on a local scale, is to evaluate waveform first motion polarities (Schneider et al., 1987; Lentas, 2018). The polarity and the amplitude of the first arrival of a seismic wave recorded at a seismic station depend on the wave type, the position of the station relative to the earthquake source and the underlying focal mechanism (Bormann et al., 2012). Figure 2.10 shows the example of a left lateral shear displacement along a fault plane (mapview). At the stations aligned with the strike of the fault (stations 1 and 5), no P-wave will be recorded because its motion pattern has opposite polarities on both sides of the fault that cancel each other out. The station
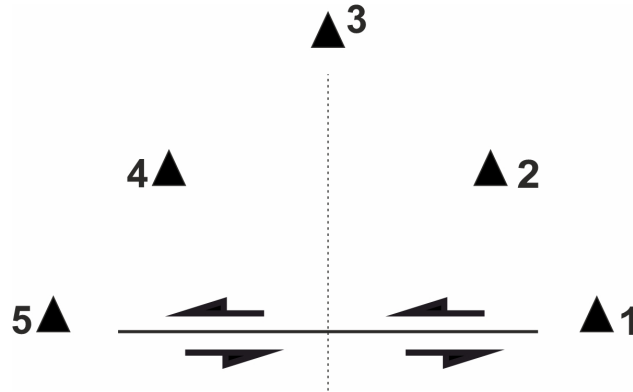
Figure 2.10 – Schematic of a left-lateral strike-slip fault and 5 seismic stations (black triangles) aligned with the fault (1 and 5), perpendicular to the fault (3) and in angles of 45° to the fault plane (2 and 4). After Bormann et al. (2012).

perpendicular to the fault (station 3) will also not receive a P-wave because the P-wave displacement acts only in direction of the wave propagation. Stations 2 and 4 on the other hand, positioned at a 45° angle to the fault, are receiving the P-wave arrivals at their maximum amplitudes but with opposite polarity. Therefore, by observing the P-wave polarities at various stations with high azimuthal coverage around the earthquake hypocenter, the fault plane solution of the earthquake can be obtained.

Fault plane solutions are usually depicted as graphical representations, the so-called beach balls (Fig. 2.11). The beach ball is representing the focal sphere, an arbitrarily small sphere around the seismic source. It can be divided into four quadrants separated by the nodal lines, which are the projections of the fault plane and its perpendicular auxiliary plane.

The P-wave polarity is the same in each quadrant but the amplitudes are large in the center and zero at the fault plane and the auxiliary plane. While opposite quadrants are characterized by the same P-wave polarity, adjunctive quadrants show polarities inverse to each other. How the quadrants are arranged on the focal sphere depends on the orientation of the fault (strike and dip) and on the slip direction (rake) (Bormann et al., 2012). This is illustrated by Fig. 2.11, which shows the beach ball representations for different types of faults. Black represents quadrants of positive P-wave polarity and resulting compressional stress and white represents quadrants of negative P-wave polarity and resulting tensional stress.

Due to the fact that the first-motion patterns are symmetric, which can
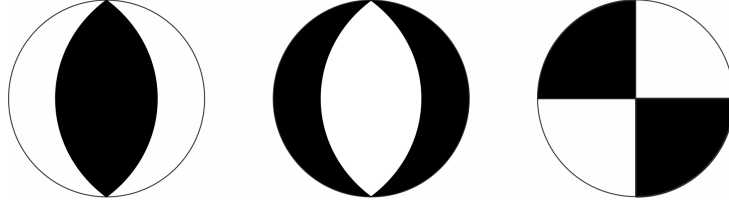
Figure 2.11 – Graphical representation (often referred to as beach balls) of the focal mechanisms of a thrust fault (left), normal fault (middle) and strike-slip fault (right).

be also seen in the seismic moment tensor, where $M_{ij} = M_{ji}$, there are always two fault planes with indistinguishable displacement fields and therefore the same focal mechanism representation. Discriminating between the real fault plane and the auxiliary plane for an obtained fault plane solution requires further geological constraints like knowledge about the local stress field and dominant fracture orientations in the region (Schoenball et al., 2014).

2.3.2   Earthquake strength and source size

The strength of an earthquake is most commonly given by its magnitude, which is an indirect approximation of the released energy. The first earthquake magnitude was introduced by Richter (1935) and is now called the local magnitude M_L. The local magnitude is determined from the maximum waveform amplitude and relies on calibration to a reference event. Therefore, it is only valid within a specific source region. While the transferability of the original local magnitude scale is limited since it has been specifically designed for southern California, the principal of deriving M_L can be transferred to other regions by defining appropriate calibration functions. Related to M_L is the coda magnitude (e.g. Suteau and Whitcomb, 1979), which is not derived from the maximum amplitude but from the amplitude of the scattered waves (the coda) following the first P and S arrivals (Shearer, 2019). Coda magnitudes are often more stable than M_L because they use an average over the radiation pattern instead of relying on a single value. Another local magnitude scale is the duration magnitude M_d, which is based on the signal duration of the earthquake (e.g. Castello et al., 2007). The signal duration can be determined by different means but is basically the time span from P-wave arrival to the point when the earthquake signal becomes indistinguishable from the seismic noise.

For teleseimic earthquakes, wave propagation in the deep earth is more regular than for shallower, local events, permitting the establishment of globally applicable magnitude scales like the body wave magnitude M_b and the surface wave magnitude M_s (Bormann et al., 2012). While M_b and M_s have been developed to be in agreement with M_L for seismicity in California as far as possible, alignment cannot be reached for the full range of event sizes (Utsu, 2002a). The reason is that the various magnitudes are calculated from different waveform periods and the frequency distribution of the earthquake source spectrum changes as a function of event size. Below a certain frequency, the so-called corner frequency f_c, there is a linear relationship between magnitude and seismic moment of an earthquake but at frequencies higher than f_c this linearity breaks down, causing a dealignment of the magnitude scale and the increasing source size (Shearer, 2019). The corner frequency moves to lower frequencies for larger events. When the event size exceeds a certain value, the corner frequency moves below the frequency used for determining the magnitude. Then, the magnitude is not increasing anymore in accordance with the event size, a phenomenon called magnitude saturation.

In contrast to the above described magnitude scales, the moment magnitude M_w is not derived from instrumental measurements but directly from the seismic moment M_0. The moment magnitude is therefore directly related to the source properties and not subjected to magnitude saturation. The scalar seismic moment is next to the moment tensor (see Eq. (2.24)) also related to the size of the rupture plane and the length of the displacement (Aki, 1966):

$$M_0 = GdA\,, \qquad (2.25)$$

where G is the shear modulus, d the average length of the fault displacement, and A the fault plane area. From the seismic moment, Kanamori (1977) defined the moment magnitude M_w:

$$M_w = \frac{\log(M_0)}{1.5} - 6.07\,, \qquad (2.26)$$

with M_0 measured in Nm.

The magnitude of an event is related to the size of its source, since the larger the source size, the larger the energy released during slip. This relationship is most obvious for the moment magnitude, which is directly derived

from the area of the rupture plane (Eq. (2.26)). However, the radius of a circular rupture plane can also be related to the corner frequency of an event:

$$r = \frac{k \cdot \beta}{f_c} \, , \tag{2.27}$$

where β is the S-wave velocity. k is a constant of different values for different models, e.g. 0.21 for Madariaga (1976) or 0.37 for Brune (1970). The corner frequency on the other hand can be empirically related to the local or duration magnitude of an event for a specific site (e.g. Charléty et al., 2007) and therefore a relationship between the measured magnitude and source size can be derived.

It can be observed for natural as well as induced seismicity that earthquakes of small magnitudes occur much more frequently than large magnitude earthquakes. Indeed, the relationship between event magnitude and frequency can be quantified by a power law that has been derived by Gutenberg and Richter (1954):

$$\log(N) = a - bM \, . \tag{2.28}$$

In this Gutenberg-Richter-relationship, N is the number of events with magnitudes $\geq M$ and a describes the overall seismic activity. The parameter b is referred to as the b-value and is a measure of the ratio between large and small earthquakes (Utsu, 2002b). The larger b, the more small magnitude events are present compared to large magnitude events. For natural seismicity, the b-value typically lies between 0.8 and 1.2 for regions worldwide and different ranges of magnitudes (El-Isa and Eaton, 2014). For seismicity induced by fluid injection, the b-value can be much higher in some cases, up to around 2.0, indicating a higher relative occurrence of small earthquakes (Bachmann et al., 2012).

Chapter 3

Earthquake detection and location

3.1 Detection techniques

Earthquakes are recorded by seismic stations, consisting mainly of a seismometer, a recording unit, a GPS antenna and a power supply. Simply speaking, a seismometer measures the ground-motion velocity or acceleration, which is recorded and displayed in form of a waveform in a seismogram (Shearer, 2019). Instruments may measure only vertical motion or motion in three perpendicular directions (commonly vertical, north-south, east-west). Usually a seismic station records continuously over time, so the earthquakes have to be identified in the continuous data stream that consists otherwise of natural and anthropogenic background noise. Earthquake detection could be done manually, by inspecting the continuous waveform in the seismogram and searching for spikes in the waveform amplitude marking the P- and/or S-wave arrivals of the earthquakes (Fig. 3.1). However, if more than a short time span is of interest, this is a very time consuming process and therefore not very practical for most applications. Instead, automatic detection algorithms are used to discriminate an earthquake signal from the background noise.

Widely used detection algorithms are based on so-called STA/LTA detection, also referred to as energy detectors. The basic principle is that the short-term-average (STA), so the average energy over a short time window
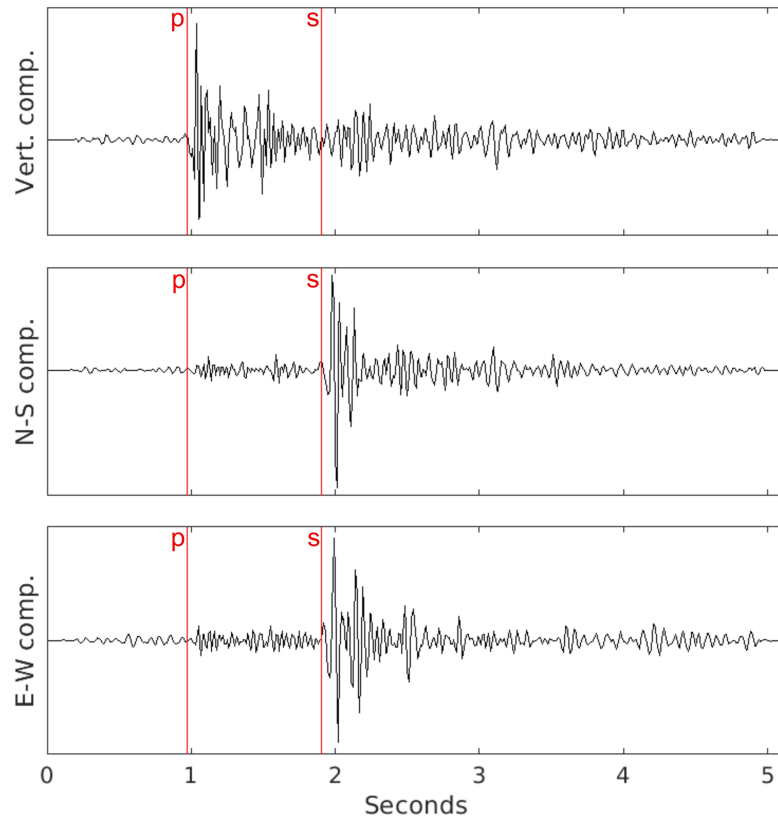
Figure 3.1 – Example of a seismogram from an earthquake induced during stimulation of the Rittershoffen reservoir. The P-wave arrives first and is most prominent on the vertical component, while the slower S-wave is more prominent on the two horizontal components.

of the waveform, is compared to the long-term-average (LTA), so the average energy over a longer time window. If the ratio between the two is significantly larger than one, this shows that a spike in amplitude exists in the short time window that could be caused by an earthquake, so a trigger is declared when a certain threshold is exceeded (Allen, 1982; Withers et al., 1998). This method has the advantage that it can be applied at any measurement site without much a priori knowledge about the expected seismic waveforms. In addition, STA/LTA detection algorithms are simple and computationally efficient, so in a short time, a high amount of data can be processed, which is ideal for real-time earthquake detection. STA/LTA detectors are able to identify earthquakes with prominent p-wave and s-wave arrivals, resulting in a high signal-to-noise ratio (SNR). Therefore, for general monitoring processes that aim at capturing the larger magnitude events to assess seismic

risk, STA/LTA detection may be considered sufficient and is widely applied. However, energy detectors have a limited detection capacity when it comes to small magnitude events or noisy environments. STA and LTA are not sufficiently different in such cases to trigger a detection. Furthermore, the P- and/or S-wave arrivals are often determined not very precisely and have to be manually corrected in order to obtain reliable locations of the earthquake hypocenters (see Chapter 3.2). Therefore, seismic catalogues generated by purely automatic STA/LTA detection may not be sufficient to answer specific research questions relying on a high data volume or precise earthquake locations and usually have to be manually post-processed (Maurer et al., 2020).

Over the last years, a second type of detector has become more widely applied, based on the so-called template matching or match-filtering technique (Lengliné et al., 2016; Shelly et al., 2007; Skoumal et al., 2015). Contrary to the STA/LTA detection, where only the energy of the earthquake is used, template matching exploits similarities in the shape of seismic waveforms. Therefore, template matching detection requires an initial database of known earthquakes, the so-called template events, providing a reference for possible event waveforms. During the detection process, these templates are compared with the continuous waveform signal in search for similar patterns that indicate additional events, working on the assumption that events with proximate hypocenters have similar waveforms. In practice, the detection algorithm computes the Pearson correlation coefficient CC between the template x and an equally sized time window of the continuous waveform data y with n samples:

$$\text{CC} = \frac{\sum\limits_{i=1}^{n} x_i y_i}{\sqrt{\sum\limits_{i=1}^{n} x_i^2}\sqrt{\sum\limits_{i=1}^{n} y_i^2}} \ . \tag{3.1}$$

The time window is sliding over the whole range of the continuous data in small time steps. If the correlation coefficient exceeds a specified threshold, a new detection is declared (Slinkard et al., 2014).

The advantage of template matching is the ability to detect events with a small SNR since the technique does not solely rely on the difference in amplitude between event and noise like during STA/LTA detection. Therefore, small magnitude events can be detected even in noisy environments (Gib-

bons and Ringdal, 2006; Schaff and Waldhauser, 2010). Furthermore, the arrival times of the seismic waves will be consistent for all events detected by one template, since they are picked always at the same position in the waveform. Of course, any imprecision in the arrival pick of the template will be also transferred to the new detections. Naturally, the final seismic catalogue generated by template matching detection is highly reliant on the initial template database. Only new events with waveforms similar enough to the templates are detected, creating a systematic bias favoring specific groups of events. It is essential that the template database is representative of the seismicity of interest and that it is reliable and does not e.g. contain accidental noise picks, otherwise the template matching algorithm will just detect more noise.

Other detection methods have been proposed that are based on principles similar to template matching, namely waveform cross correlation, but try to avoid the strong dependence on the template waveforms. One such example are subspace detectors (Barrett and Beroza, 2014; Harris, 2006). Instead of real earthquakes, subspace detectors use an artificial set of waveforms as templates that are created from a selection of the catalogue events. The singular value decomposition (SVD) of these selected events is calculated to find their orthonormal representation and extract the most important common features that are then used as templates. The idea is that since the artificial waveforms are more general, they may be able to detect a wider variety of waveforms not only those that are very similar to specific template events. Another, even more general approach based on waveform cross correlation would be autocorrelation, which does not require a-priori template waveforms (Brown et al., 2008). The continuous waveform data are partitioned into short, overlapping time windows and all of these windows are correlated among each other. Autocorrelation provides the high sensitivity of template matching detection and yet enables detection of events with previously unknown waveforms. The major drawback of the technique is that it is computationally highly intensive and therefore unfeasible for detecting earthquakes in larger data sets. This limitation has proposed to be overcome by locality-sensitive hashing (LSH) (Yoon et al., 2015). LSH allows to sort similar items into common 'buckets' and can therefore be used for data clustering. The comparison of dissimilar pairs is avoided and correlation is only performed for a shorter list of waveform pairs in each bucket that are likely to be similar with high probability.

Recently, the use of machine learning (ML) and artificial neural networks (ANN) for earthquake detection has been explored. Earthquake detection

can be seen as a pattern recognition problem and ML strategies have the potential to find unseen patterns in large datasets. A large range of ANN have been proposed for earthquake detection, employing assisted, semi-supervised or unsupervised learning (Rojas et al., 2019).

In Chapter 5 of this thesis, template matching detection is used to obtain a comprehensive catalogue of the seismicity induced during the stimulation of the Rittershoffen reservoir. As template database, the STA/LTA detected and manually revised catalogue presented in Maurer et al. (2020) is used. Template matching detection was chosen because it is an advanced yet well-established detection method with high detection sensitivity for small magnitude events in a noisy environment. It proofed to be indeed efficient in the case of the Rittershoffen stimulation, since the amount of detected events compared to the STA/LTA catalogue was tripled. Despite the fact that the STA/LTA template catalogue contains many events with very similar waveforms, the whole catalogue was used as template database to detect as many new events as possible. The basic steps of the template matching algorithm are shown in Fig. 3.2, details can be found in Chapter 5.2.2.

Lengliné et al. (2017) also applied detection based on waveform cross-correlation on the seismicity induced during the hydraulic stimulation at Rittershoffen but they used an approach comparable to subspace detection. They clustered the events of a STA/LTA detected catalogue into 13 clusters of similar waveforms and created an average waveform for each cluster. This results in a synthetic waveform comparable to using the first vector of the SVD of the clustered events. In the study of Lengliné et al. (2017), detection with these synthetic waveforms led to a doubling of the amount of events compared to the STA/LTA database and therefore to less new detections than with the template matching detection approach used in Chapter 5 of this thesis. It is likely that events uniquely similar to the original STA/LTA detected events are missed by using synthetic templates. While SVD or averaging waveforms captures the most common features among the events, it loses the specifics of the single templates.

The bias introduced by template matching that favors the detection of events belonging to always the same families also has advantages. The high waveform similarity can be exploited to obtain better constrained relative locations of the events (see Chapter 3.2) and to perform a waveform clustering analysis. Furthermore, the catalogue emphasizes structures that are repeatedly seismically active, so likely the dominant fault structures in the reservoir. The focus on structures with permanent seismic activity allows
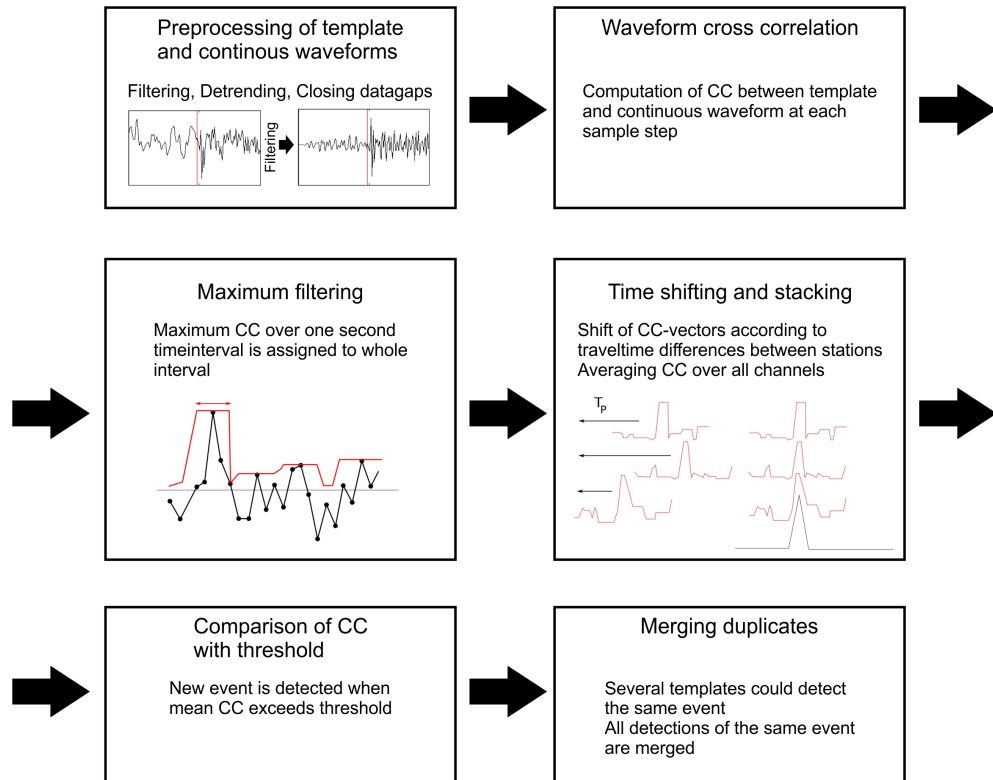
Figure 3.2 – Basic steps of the template matching detection algorithm applied to the seismicity induced at the Rittershoffen reservoir.

tracing their behavior over the different stimulation periods in the Rittershoffen study (Chapter 5).

3.2   Location techniques

The location of an earthquake usually referrers to its hypocenter, so the spatial position of energy release in the underground. Without knowing the earthquake hypocenter, other characteristics such as magnitude or focal mechanism of the event cannot be determined. The absolute event location is defined within a fixed geographic coordinate system, while the relative location is given as the distance to another spatial reference point, usually another earthquake. Basically, to locate an earthquake, the arrival times of the seismic waves at the seismic stations are needed, the coordinates of the seismic stations and a velocity model that specifies the wave-speeds in the sec-
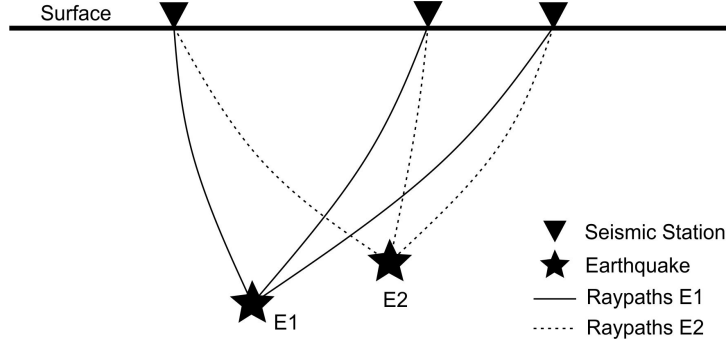
Figure 3.3 – Sketch of two earthquakes, a surface network of three seismic stations and the raypaths of the seismic waves travelling through the underground from source (earthquake) to receiver (seismic station).

tion of the underground that is travelled by the waves from source to receiver (Fig. 3.3) (Karasözen and Karasözen, 2020; Lomax et al., 2011). Ideally, velocity models represent the whole 3D velocity structure of the underground but to reach faster computation times or due to a lack of information, often 1D velocity models are used that represent only different velocity layers with depth but no lateral changes.

Earthquake location techniques can be classified based on the spatial type of the earthquake location (absolute or relative) that is obtained or the methodology applied to solve the location problem that can be grouped into linearized or nonlinear techniques (Karasözen and Karasözen, 2020). At its core, earthquake location is a nonlinear inverse problem with four unknowns: the hypocenter coordinates (x_0, y_0, z_0) and the origin time t_0. The origin $m_0 = (x_0, y_0, z_0, t_0)$ is determined by minimizing the residuals between observed and predicted arrival-times of the seismic waves (P- and/or S-waves) at N seismic stations. Predicted arrival-times are calculated by forward modeling in the given velocity model by assuming the origin m_0. The theory of earthquake location is described in textbooks on seismology (e.g. Shearer, 2019) or different studies on location techniques (e.g. Karasözen and Karasözen, 2020; Lomax et al., 2011). In the following, the basic steps are outlined.

Assuming an homogeneous medium with constant velocity v for a given wave type, the arrival-time t_i at the ith seismic station with coordinates

(x_i, y_i, z_i) for an earthquake with origin $m_0 = (x_0, y_0, z_0, t_0)$ is given by:

$$t_i = t_0 + \frac{1}{v}\sqrt{(x_i - x_0)^2 + (y_i - y_0)^2 + (z_i - z_0)^2}\,. \qquad (3.2)$$

Usually, the velocity varies spatially and the arrival-time is calculated by integration along the ray path of the wave. Since the travel-time is nonlinearly dependent on the source location (x_0, y_0, z_0), it becomes apparent that earthquake location is an inherently nonlinear problem.

The observed arrival times at each station t_i^{obs} can be related to the origin $m_0 = (x_0, y_0, z_0, t_0)$ of the earthquake by the function F:

$$t_i^{obs} = F_i(m_0)\,, \qquad (3.3)$$

where F is specific for the velocity model and the N locations of the seismic stations.

The goal is now to solve the inverse problem to find the origin m_0. Simplified, this can be done in a grid search by calculating predicted arrivals times t_i^{pre} for every possible origin m_0 on a grid using $F_i(m_0)$. The predicted arrival times are then compared with the observed arrivals times to find the minimal residuum between the two. Grid search algorithms have been one of the earliest earthquake location methods (Reid, 1910) and can potentially calculate the complete probabilistic solution to the inverse problem over the model space (Lomax et al., 2011). Yet, despite advancements in the computing power that made grid search methods more feasible for earthquake location (Husen et al., 2003; Lomax, 2005; Sambridge and Kennett, 1986), they are still computationally demanding for larger datasets. Therefore, linearized, iterative location methods are widely applied in routine earthquake location since they are easy to implement and computationally efficient. Based on the first linearized method proposed by Geiger (1910), various linearized location algorithms have been developed (Klein, 2002; Lahr, 1999; Lin and Shearer, 2006).

The linearization procedure starts with an initial guess for the origin:

$$m_{start} = \left(x_{start}, y_{start}, z_{start}, t_{start}\right). \qquad (3.4)$$

This initial guess is then perturbed by a small shift of the origin:

$$m = m_{start} + \Delta m \,, \tag{3.5}$$

with m being a new location at a small distance Δm from m_{start}. It is assumed that heterogeneities between the earthquake locations are sufficiently small that a linear approximation is valid.

The predicted arrival times at m are approximated using the first term in the Taylor series expansion for the predicted arrival times at m_{start}:

$$t_i^{pre}(m) = t_i^{pre}(m_{start}) + \frac{\partial t_i^{pre}}{\partial m_j}\Delta m_j \,, \tag{3.6}$$

with $j = 1, 2, 3, 4$ for the four parameters in $m = (x, y, z, t)$. The residuals between observed and predicted arrival times at the new location m are:

$$r_i(m) = t_i^{obs} - t_i^{pre}(m) = r_i(m_{start}) - \frac{\partial t_i^{pre}}{\partial m_j}\Delta m_j \,. \tag{3.7}$$

To minimize these residuals, Δm has to be chosen such that:

$$r_i(m_{start}) = \frac{\partial t_i^{pre}}{\partial m_j}\Delta m_j \quad \text{or} \quad r_i(m_{start}) = G\Delta m \,, \tag{3.8}$$

with G being the matrix of partial derivatives $G_{ij} = \frac{\partial t_i^{pre}}{\partial m_j}$, $i = 1, 2, \ldots, N$, $j = 1, 2, 3, 4$. Δm can be obtained by finding the least squares solution to Eq. (3.8). The model parameters are then updated iteratively, such that $m'_{start} = m_{start} + \Delta m$, until the location converges (Shearer, 2019).

The drawbacks of linearized methods are that they are highly sensitive to the initial guess of the location. If it is not sufficiently close to the true hypocenter, the linearized solution might converge to a local minimum of the residuals between observed and predicted arrival times, instead of the global minimum. If the dataset contains outliers or if there are strong variations in the velocity structure, the iteration process could be unstable and fail to converge (Karasözen and Karasözen, 2020). Also, contrary to nonlinear

methods, linearized methods usually do not represent a complete probabilistic solution over the whole area and only provide one optimized earthquake location (Lomax et al., 2011).

Earthquake locations are always subjected to errors, which are a combination of measurement and modeling errors resulting in location uncertainties and location inaccuracies (Kinnaert et al., 2016). Location uncertainties are mainly a result of uncertainties in the arrival times of the seismic waves, and, depending on the applied algorithm, could be estimated by taking into account known arrival time uncertainties during the location process (Lomax et al., 2011). Location inaccuracies on the other hand are the result of modeling errors due to effects that are not accounted for in solving the inverse problem. This can lead to a systematic bias in the computation of the earthquake location and a wrong positioning of the earthquake hypocenter. The most important cause for location inaccuracies is the use of a velocity model not representative of the real underground conditions due to unknown velocity heterogeneities or intentionally simplified velocity models (Bardainne and Gaucher, 2010; Kinnaert et al., 2016).

Relative earthquake location methods attempt to correct for relative location inaccuracies without actually solving for the velocity structure itself by taking advantage of the observation that the introduced bias tends to be nearly constant for spatially proximate earthquakes (Lin and Shearer, 2005). Therefore, it can be assumed that the difference between the travel-times of two events accounts only for their spatial offset. However, this assumption is only valid if the distance between two event hypocenters is small in comparison to the event-station distance and to the scale of velocity heterogeneities. While relative location methods effectively reduce the relative errors among nearby events, they cannot improve absolute location accuracy because this would again require knowledge of the true three-dimensional velocity structure.

Several relative relocation algorithm have been developed, among them the frequently used joint hypocenter determination (JHD), hypocentroidal decomposition (HD) and double-difference (DD) algorithms, which are compared in Lin and Shearer (2005). In the study on the seismicity induced at the Rittershoffen site presented in Chapter 5 of this thesis, the software HypoDD is used, which is based on a linearized double-difference approach. DD equations are similar to those for linearized location of single events. The difference is that instead of the residuals between observed and calculated travel-times t for each single event, the differences of the residuals between

all event pairs are computed, resulting in a double-difference dd. Therefore, Eq. (3.7) becomes for two earthquakes a and b at one station:

$$\mathrm{dd}_{ab} = (t_a - t_b)^{obs} - (t_a - t_b)^{pre}. \tag{3.9}$$

More technical details about the DD technique and the HypoDD software can be found in Waldhauser and Ellsworth (2000).

The DD technique has been chosen in Chapter 5 to re-locate the seismicity induced during the stimulation of the Rittershoffen reservoir for several reasons. To obtain high precision relative locations was essential for the study since it aims at detailing the geometry of the fault network, therefore, a relative location technique was the logical choice. Furthermore, the geological setting in the study area is complex, making errors introduced by heterogeneities in the velocity structure likely, which are mitigated by a relative location technique. The dataset is well suitable for relative location since it is a dense seismic cloud with limited spatial extent. The DD algorithm specifically was chosen because it allows the direct use of high-precision travel time differences obtained by waveform cross correlation of P- and/or S-waves, which can be easily obtained after performing template matching detection like in the Rittershoffen study.

Chapter 4

The Soultz-sous-Forêts and Rittershoffen geothermal sites

Soultz-sous-Forêts and Rittershoffen are two neighboring geothermal sites in the French part of the Upper Rhine Graben (URG). The URG is part of the Cenozoic rift system and formed in response to the NNE trending Alpine compression (Bourgeois et al., 2007). The faulted granitic basement is overlain by sedimentary layers of varying thickness, that were already well explored in the area around Soultz and Rittershoffen before geothermal exploration in the URG began because they host the Pechelbronn-Merkwiller oil field. Prior to 1970, more than 5000 oil wells were drilled and seismic surveys had been carried out, so the stratigraphy and structures in the sedimentary cover are well characterized (Brun and Wenzel, 1991). In several hundred of these wells temperature measurements were performed that highlighted thermal anomalies with high temperature gradients at Soultz and Rittershoffen as well as several other sites in the URG (Haas and Hoffmann, 1929; Pribnow and Schellschmidt, 2000). It could be observed that these thermal anomalies are linked to fault zones that compart the URG into horst and graben structures (Bächler et al., 2003; Baillieux et al., 2013).

4.1   Setting and development of the Soultz-sous-Forêts site

Soultz-sous-Forêts is the very first geothermal site that has been developed in the URG and one of the most important EGS sites worldwide. Its history and site characteristics are well documented (e.g. Baria et al., 1999; Genter et al., 2010; Schill et al., 2017). At Soultz, the crystalline basement that hosts the geothermal reservoir consists of highly fractured granites and is overlain by about 1.4 km of sedimentary cover (Fig. 4.1). Mesoscale fractures are ubiquitous in the granites but they are poorly connected and only have a minor contribution to the reservoir permeability. The dominant orientations vary from N175°E $\pm$ 30° with steep dips to the east or to the west (Dezayes et al., 2010). The main transmissive pathways are large scale fault zones of highly clustered fractures with thicknesses of up to 60 m and an average strike of N160°E $\pm$ 15° but other orientations are present as well. The average dip is higher than 60° dominantly to the west (Dezayes et al., 2010). These fault zones generally show a high level of hydrothermal alteration, while the rest of the granite is largely unaltered. The local stress field at Soultz is consistent with the URG setting. The minimum principle stress is horizontal but nearly equal to the vertical stress at reservoir depth. The maximum horizontal stress is oriented NNW-SSE. Studies have shown that many fractures are critically stressed in this local stress field, yet are stable up until a certain injection pressure, implying non-negligible cohesion on the fracture surfaces (Cornet et al., 2007). As already mentioned, the Soultz site is characterized by a heat anomaly. The temperature profile in the upper, sedimentary section down to 1 km depth shows a very high temperature gradient of about 110 °C/km. Below 1 km, the temperature gradient changes suddenly to a much lower value of about 5 °C/km, indicating a change in the dominant heat transport process from conduction to advection. The temperature gradient increases to 30 °C/km below 3.3 km, indicating again a conductive heat transport (Genter et al., 2010). This compartment of the geothermal gradient in three sections indicates significant fluid movement enabling advective heat transport in the depth range between 1 and 3.3 km.

Site development at Soultz started in 1987. In total four production / injection wells have been drilled, three of which reaching about 5 km depth and a reservoir temperature of about 200 °C (Fig. 4.1). The first well that was drilled, GPK1, initially reached 2002 m depth but was deepened in 1992 to 3590 m depth where it reached a temperature of about 170 °C. The second well GPK2, drilled in 1995, targeted the same depth at a lateral
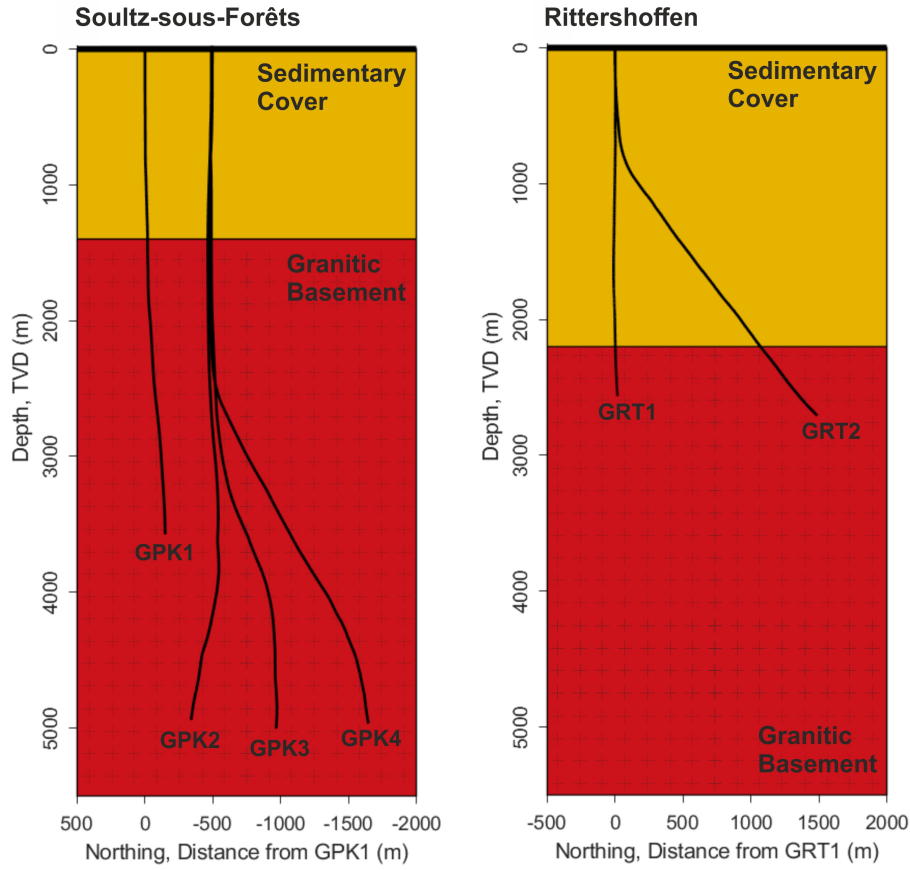
Figure 4.1 – Schematics of the Soultz-sous-Forêts (left) and Rittershoffen (right) reservoirs in North-Depth cross-sections. The black lines are the different wellpaths.

distance of 450 m to GPK1. Both wells were hydraulically stimulated and circulation was performed between them for 4 month (Baria et al., 1999). This first, shallower reservoir, was the first EGS that was constructed at Soultz. In 1999, GPK2 was deepened to 5000 m depth to reach a bottom hole temperature of 200 °C. Drilling of two more wells, GPK3 and GPK4, down to the same depth was finished in 2004, the bottom whole sections having a lateral distance of about 600-650 m to each other (Genter et al., 2010). All three deep wells underwent massive hydraulic stimulation that led to a significant improvement of injectivity/productivity for GPK2 and GPK4 but only a minor change for GPK3 (Schill et al., 2017). After the hydraulic stimulations, all three deep wells were subjected to chemical stimulations. All in all, injectivity/productivity increased for GPK2 from 0.02 L/s/bar to 0.5 L/s/bar, for GPK3 from 0.1 L/s/bar to 0.4 L/s/bar and for GPK4 from

0.01 L/s/bar to 0.5 L/s/bar (Portier et al., 2009).

The first circulation test between the three deep wells was conducted in 2005 for 5 month, revealing a good connectivity between GPK2 and GPK3 but a poor connection to GPK4 (Genter et al., 2010). In 2008, another circulation test was performed as part of the power-plant commissioning phase and in 2009, a 1.5 MWe Organic Rankine Cycle (ORC) power plant went operational. Since then it has been experimented with different production/injection schemes to optimize reservoir performance while preventing induced seismicity (Genter et al., 2012). In 2016, a new ORC unit went operational, whose capacity reaches 1.7 MWe for an annual electricity production of about 11 GWh/year (Ravier et al., 2019). Under the current set-up, GPK2 is used as the only production well, while GPK3 and GPK4 are used as re-injection wells. Geothermal brine is produced at a flowrate of 30 kg/s with a production temperature of 150 °C on the surface and an injection temperature of 70 °C.

4.2   Setting and development of the Rittershoffen site

The Rittershoffen geothermal site is located close to Soultz-sous-Forêts, about 6 km east. The reservoir has been accessed through the well doublet GRT1/GRT2, which targets a fault zone at 2.5 km depth and extracts hot brine of about 170° at a flow rate of 70 L/s to supply a near bio-refinery with 24 MWt (Baujard et al., 2017) (Fig. 4.1). At the Rittershoffen site, the transition from sedimentary cover to crystalline basement is located deeper than at the Soultz site at about 2200 m depth (Aichholzer et al., 2016). Like at Soultz, the rock units are intersected by the horst and graben structures prevalent in the Upper Rhine Graben, wherein the Rittershoffen site is situated in a lower compartment between two horsts. Similarly to the Soultz site, the crystalline basement consists of a partly highly altered and fractured granite, crossed by large scale fault zones (Baujard et al., 2017; Vidal et al., 2017). Specifically, the well doublet GRT1/GRT2 is designed to intersect the so-called Rittershoffen fault, a fault zone already characterized through reprocessed vintage seismic profiles available for the Rittershoffen area prior to the development of the geothermal site. The orientation of the Rittershoffen fault has been determined to be N355°E, becoming N-S at the well site, with a dip estimated between 45° and 83° to the west by different studies

(Baujard et al., 2017; Lengliné et al., 2017; Vidal et al., 2017; Vidal et al., 2016). The temperature profile is different from the one measured in Soultz but with the same characteristic of a high geothermal gradient in the upper depth section and a sudden change to a very low gradient in the lower depth section. From the surface down to the top of the Muschelkalk in 1650 m depth, the temperature gradient is constant with values of 85-87 °C/km for GRT1 and GRT2, so slightly lower than in Soultz. Below, the temperature profile changes to a low value of 3 °C/km for GRT1 and of 18 °C/km for GRT2 (Baujard et al., 2017).

The first well GRT1 has been drilled vertically down to 2580 m MD from September to December 2012. The open hole section of the well crosses clastic sandstones from the Buntsandstein and Permian before reaching the granitic basement at 2200 m TVD and intersecting the Rittershoffen fault just below. A series of hydraulic tests on GRT1 indicated a low initial productivity of about 0.45 L/s/bar at the nominal flowrate of 70 L/s. To enhance the productivity/injectivity of the well GRT1, a thermal, a chemical and a hydraulic stimulation were conducted. The GRT2 well was drilled from March to July 2014 to a final depth of 2707 m TVD. The well is deviated with an inclination of up to 37° directed to the north. Due to a high natural productivity of 2.8-3.5 L/s/bar the well was not stimulated (Baujard et al., 2017). Stimulation of the well GRT1 started with the thermal stimulation carried out from the 23th to the 25th of April 2013 for 62 hours, 20 minutes. A total volume of 4,230 m^3 brine, previously extracted from GRT1, with a temperature of 12 °C was injected at flow rates up to 25 L/s (Baujard et al., 2017; Maurer et al., 2020). The chemical stimulation was performed two month later from June 23rd to June 25th in three different depth intervals in 1922 to 2530 m MD (Baujard et al., 2017). The chemical stimulation was directly followed by the hydraulic stimulation on the 27th and 28th of June, lasting 26 hours, 20 minutes. The injection flowrate was increased stepwise to 80 L/s and then stepwise decreased until shut-in again. At the end of the stimulation, on the 28th of June 11:00 to 17:30, an injection test was performed at flowrates up to 60 L/s. In total, a volume of 3,180 m^3 brine had been injected during the hydraulic stimulation and 820 m^3 during the injection test (Baujard et al., 2017; Maurer et al., 2020). All three stimulation procedures leaded to a clear enhancement of the injectivity of GRT1 with a final injectivity index of about 2.5 L/s/bar (Baujard et al., 2017).

4.3   Seismicity induced at the Soultz-sous-Forêts and Rittershoffen sites

The hydraulic stimulations of the different wells at Soultz-sous-Forêts induced microseismic activity of thousands of earthquakes (Tab. 4.1). Seismicity was monitored by a combined downhole and surface network of seismic stations (Baria et al., 2004). While most events induced during reservoir stimulations at Soultz had low magnitudes, several exceeded magnitude 2 with the largest magnitude being 2.9, alarming the neighbouring population. Like observed at other EGS sites, the highest magnitude events tended to occur shortly after shut-in of the wells. The seismicity induced during the various hydraulic stimulations at Soultz has been thoroughly investigated. Several studies analysed the mechanisms behind induced seismicity including aseismic motion (Bourouis and Bernard, 2007; Calò et al., 2011; Cornet et al., 1997), poroelasticity (Schoenball et al., 2010) and triggering (Schoenball et al., 2012). Others focused on the analysis of the stress regime and faulting mechanisms (Cuenot et al., 2006; Horálek et al., 2010; Schoenball et al., 2014) on the hydraulic properties of the reservoir (Delépine et al., 2004; Shapiro et al., 1999) or on the fault network geometry (Evans, 2000; Evans et al., 2005a; Moriya et al., 2002; Moriya et al., 2003; Phillips, 2000). Charléty et al. (2007) analysed the characteristics of large magnitude earthquakes, Cuenot et al. (2008) concentrated on the link between induced seismicity and operational parameters and Dorbath et al. (2009) on the comparison of the seismicity induced during different stimulation operations.

During the thermal and hydraulic stimulation of the Rittershoffen GRT1-well, several hundred induced events have been detected by STA/LTA detection with magnitudes up to 1.6 (Maurer et al., 2020) and over 1000 for the hydraulic stimulation alone by template matching detection (Lengliné et al., 2017). Most notable is the observation that after four seismically

Table 4.1 – Overview over the seismicity induced during hydraulic stimulation operations at the Soultz reservoir.

Well	Date	Located events (surface network)	Highest magnitude	Reference
GPK1	9/10 1993	156	1.9	(Cornet et al., 1997)
GPK2	2000	7215	2.6	(Dorbath et al., 2009)
GPK3	2003	3253	2.9	(Dorbath et al., 2009)
GPK4	2004/2005	1341	2.7	(Dorbath et al., 2009)

quiet days following shut-in of the hydraulic stimulation seismicity suddenly raised again in a sudden burst of a few hundred events within two hours. The highest magnitude events belong to this delayed seismicity. In contrast to the wealth of studies on the seismicity induced at Soultz-sous-Forêts, seismicity induced during the stimulation at Rittershoffen has been addressed only by two studies so far, which are introduced in more detail in Chapter 5. One of these studies (Maurer et al., 2020) provides an overview over the seismicity induced during drilling and stimulation operations but relies on STA/LTA detection and absolute locations and does not provide enough detail for a thorough analysis of the fault system and mechanical processes in the reservoir. The other study by Lengliné et al. (2017) reaches a higher level of spatial detail by applying template matching detection and relative relocation but concentrates only on the hydraulic stimulation. Therefore, in Chapter 5, template matching detection and relative relocation is applied to the whole stimulation sequence of GRT1 and additionally a waveform clustering analysis is performed to get insight into the internal fault structure and mechanisms behind the induced seismicity. The aim is a detailed interpretation of the effects the stimulation sequence had on the fault network and ultimately to provide new insights on the Rittershoffen deep geothermal reservoir.

While the Rittershoffen case study demonstrates that relative relocation is a valuable technique for imaging underground fault systems, this approach may not be successful to image the fault network in all seismic clouds. The example of the seismicity induced during the stimulation of the well GPK2 at Soultz sous Forêts shows that even after advanced processing (Calò et al., 2011) a seismic cloud may not converge into sharp, spatial features. While the Rittershoffen seismic cloud clearly exhibits two separate fault segments with different shape and orientations (see Chapter 5), the internal structure of the GPK2 seismic cloud remained rather unclear despite a large data volume of over 7000 events and precise relative relocation. The cloud has been analysed in different studies by Cuenot et al. (2008), Dorbath et al. (2009) and Calò et al. (2011).

Cuenot et al. (2008) describe the GPK2 seismic cloud as a dense, flat ellipsoidal shape that is aligned in the direction of the maximum horizontal stress of the local stress field. They analyse the temporal evolution of the seismic cloud in relation to the injection flowrate during stimulation and note that the general direction of extension of the cloud is roughly in agreement with the geometrical pattern of the fault structures observed in the Soultz reservoir. Dorbath et al. (2009) also observe the seismicity induced during

the GPK2 stimulation as compact, homogenous cloud without visible internal structures. They relate the dense, homogeneous nature of the cloud to the observation that fracture zones in GPK2 are formed by complex clusters of medium-scale fractures surrounded by highly altered rock mass that was reactivated during stimulation. Calò et al. (2011) relocated the seismic events and simultaneously performed a 4D tomography with a double-difference tomography code. They also concentrated on the temporal development of the cloud and their observations largely agree with those of Cuenot et al. (2008) and Dorbath et al. (2009). For the late seismicity after shut-in they observe that the seismic cloud takes a Y shape in its northern part. They interpret this shape as two main internally active structures striking NW–SE to NNW–SSE.

However, none of these studies focused on deconstructing the internal structure of the cloud and except for a visual inspection of the event hypocenters no further processing is performed to highlight hidden features in the cloud. Therefore, in Chapter 6, a new method is proposed to deduce fracture networks from seismic clouds if precise relative relocation is not sufficient to highlight the underlying geometry. The method is described in detail and verified on a set of synthetic datasets before it is applied to the GPK2 seismic cloud.

Part II

Main Body

Chapter 5

Fault activation by repeated fluid injection: case study of the enhanced geothermal system at Rittershoffen, France

Authors: R. Koepke[1,2], O. Lengliné[2], E. Gaucher[1], J. Schmittbuhl[2] and T. Kohl[1]

[1]Karlsruhe Institute of Technology, Institute of Applied Geosciences, Division of Geothermal Research, Kaiserstr. 12, 76187 Karlsruhe, Germany

[2]University of Strasbourg/CNRS, IPGS/EOST, 5 rue René Descartes, 67084 Strasbourg, France

The underlying seismic catalogue used in this study as template database for the template matching detection is described and evaluated in Maurer et al. (2020). The author of this thesis is also co-author of this article. Both studies cover a similar topic but with different focus and based on a different methodology, therefore the following chapter contains a lot of references and comparisons to Maurer et al. (2020). For easier understanding the article of Maurer et al. (2020) is contained in Appendix A of this thesis.

Abstract

Induced seismicity in deep geothermal reservoirs can give valuable insight into the fault network and ongoing mechanical processes during fluid injection. The well GRT1 at the deep geothermal site Rittershoffen (France) underwent a sequence of thermal, chemical and hydraulic stimulation from April to June 2013 that was continuously seismically monitored. By an integrated approach of advanced methodologies like template matching detection, relative relocation and waveform clustering a high level of detail in the tempo-spatial resolution was derived. The results demonstrated the development of the successively activated fault network over the injection steps by tracing the influence of the different stimulations and allowed for an analysis of the mechanisms behind the induced seismicity. It could be shown that the same near-vertical, NNE-SSW striking fault was seismically active at a different spatial extent during the different stimulation periods. The events in fault areas activated during both stimulations could not be distinguished, both in terms of their location and their waveform. At the end of the hydraulic stimulation, a spatially separated N-S striking fault became seismically active, which then showed major activity again after a seismically quiet period of 4 days following shut-in. The waveform-clusters are pointing towards a transition of fault activation mechanisms with the majority of events on this second fault having waveforms very differently from the injection related seismicity. Our study shows that repeated fluid injections on the same fault plane produces an extension of the seismically active area, eventually triggering distant seismicity.

5.1   Introduction

In classical Enhanced Geothermal Systems (EGS), the initial natural productivity/injectivity of the deep fractured geothermal reservoir is too low to allow a sufficient fluid circulation for heat extraction at economic rates and minimum seismic risk (e.g. Lu, 2018). It is therefore a general requirement to increase the reservoir permeability to achieve higher flow rates. This can be accomplished by stimulation techniques based on either hydraulic, thermal or chemical methods (e.g. Axelsson et al., 2006; McClure and Horne, 2014; Portier et al., 2009) whereas hydraulic stimulation is most commonly used in EGS to date (Breede et al., 2013). The underlying mechanism of thermal and hydraulic stimulation is the enhancement of reservoir permeability

through mechanical processes like fracturing, aiming at the creation of new fractures, or shearing, whereby slip on existing fractures is induced (Jeanne et al., 2014; Norbeck et al., 2018). The common assumption for EGS is that stimulation occurs mainly through shearing with fracturing having a rather minor effect on the overall reservoir permeability. This contrasts Hot Dry Rock (HDR) systems that rely mostly on the generation of a new fracture network. In all cases, the knowledge of the in situ pre-existing stress field is crucial, since it determines the conditions under which rock failure can occur. For instance, shearing requires a differential stress field with a suitable orientation relative to the orientation of the fractures (e.g. Cornet et al., 2007). Fracturing/shearing is achieved in case of hydraulic stimulation by injecting fluids at high pressure and flow rates to increase pore pressure, whereas thermal stimulation foresees the injection of cold fluids to induce thermal stresses (Jeanne et al., 2017). Chemical stimulation on the other hand aims at dissolving minerals sealing fluid pathways and at changing their mechanical properties through alteration (Portier et al., 2009).

It is widely observed that stimulation operations at EGS sites may be accompanied by induced seismicity, especially during hydraulic stimulations (e.g. Dorbath et al., 2009; Zang et al., 2014). Induced seismicity should be controlled because of the potential risk it may pose to nearby infrastructure and population, but it gives valuable information on the geomechanical processes in the reservoir and highlights the fault structure (e.g. Cuenot et al., 2008; Eisner et al., 2010). In this context, seismic monitoring became a central task in the development and operation of EGS.

Herein, we use induced seismicity to follow the development of the fault system of the Rittershoffen deep geothermal reservoir caused by repeated fluid injection during different stimulation operations. The site is located in the French part of the Upper Rhine Valley and consists of the well doublet GRT1/GRT2 drilled down to 2.5 km depth. The targeted reservoir is located at the transition from the sedimentary cover to the granitic basement and is intersected by a major fault system. The site development and the hydraulic conditions have been thoroughly investigated (Baujard et al., 2017) and the regional stress field is well known due to extensive studies in the nearby Soultz-sous-Forêts geothermal site (Cornet et al., 2007; Evans et al., 2005a). In April to June 2013, GRT1 underwent a sequence of thermal, chemical and hydraulic stimulation. Since these individual injections were conducted in the same depth interval, they allow to trace the reaction of the fault system to each step. All operations have been continuously monitored by at least 12 seismic stations within 15 km distance from the wellheads (Lengliné et al.,

2017; Maurer et al., 2015; Maurer et al., 2020). The site therewith offers particularly suitable conditions to study the seismic response of the fault system in the reservoir to the sequence of different stimulation approaches.

A first study of the induced seismicity during the GRT1 hydraulic stimulation by Lengliné et al. (2017) applied template matching detection and relative relocation of the seismic events. Herein, we also use both methods but at a largely extended and completely new database accounting for the total GRT1 stimulation sequence in 2013. The advantage of template-matching is the high detection capability allowing to detail the development of the fault system over the different injection periods. Template-matching algorithms are exploiting waveform similarity of events generated under similar conditions, in close proximity to each other, by computing the correlation coefficient between a database of known events, i.e. the templates, and the continuous seismic signal. This technique is able to detect events up to one order of magnitude smaller than conventional energy detectors (Schaff and Waldhauser, 2010) and identifies events in data with low SNR (Schaff, 2008) in various geological settings, including mining-induced seismicity (Gibbons and Ringdal, 2006), earthquake swarms (Shelly et al., 2013), pre-eruptive seismicity in volcanic settings (Lengliné et al., 2016) and seismicity induced in hydrocarbon fields (Song et al., 2010). The template matching technique creates a systematic bias in the catalogue since only events with waveforms similar to the templates are detectable. However, this also means it focuses rather on structures with permanent seismic activity and thus allows to trace their behavior over the different stimulation periods in this study.

The recent work of Maurer et al. (2020) presents the seismicity induced during the whole stimulation sequence and the drilling operation of GRT1 and GRT2. They established a manually revised catalogue of events detected by an automatic STA/LTA system (Allen, 1982; Withers et al., 1998) and computed absolute earthquake locations. Maurer et al. (2020) present an overview on the seismicity but did not have the detection performance and location accuracy to analyse spatial specifics of the earthquake sequence.

In contrast, we focus on the details of the fault network development. The main topics analysed in this study are the mechanical state of the fault network and the associated variations over the course of the injection sequence, the characterization of the mechanisms behind the induced seismicity and the spatial and temporal distribution of the events. Small magnitude events likely to be missed by classical detection methods as used by Maurer et al. (2020) but grasped by template matching can help to discriminate the seismogenic

response of the fault system to the individual stimulation operations, especially in combination with high resolution relative re-location of the events. Seismicity onset, temporal development and spatial distribution of the events will be determined more precisely and may reveal additional details. Also, the extension of the catalogue will lead to a larger database for statistical analyses. The waveform similarities used in the template matching and relative relocation are further evaluated in a clustering analysis. Waveform clustering can highlight the internal structure of larger faults by pointing at repeated reactivation of the same fault patches. Different waveform clusters can also hint at different fault activation mechanisms.

In the following, the seismic data used in this study are introduced. Then, the applied template matching algorithm is described as well as the chosen relative relocation and the cluster analysis procedure. The following section describes the results obtained, focusing on the seismic response to the individual stimulations in terms of activated fault structures and tempo-spatial distribution as well as event clustering based on waveform similarities. The results are then jointly discussed.

5.2 Material and Methodology

5.2.1 Seismic monitoring network and database

The Rittershoffen geothermal site was monitored by several networks of seismic stations since the start of any drilling operations in 2012. Operating during all stages of the reservoir development and production is a permanent network composed of 6 seismic stations dedicated to the monitoring of the Rittershoffen field and 6 stations belonging to the monitoring network of the nearby Soultz-sous-Forêts geothermal site. Therefore, a total of 12 permanent stations are used for this study. During the thermal stimulation of GRT1, the permanent network was the only one operational (Maurer et al., 2020). In June 2013, 5 additional temporary stations were deployed to supplement the permanent stations and were operational during the chemical and hydraulic stimulations of GRT1. A map of the seismic networks operating during thermal and chemical/hydraulic stimulation is shown in Fig. 5.1.

The catalogue published and described in detail in Maurer et al. (2020)
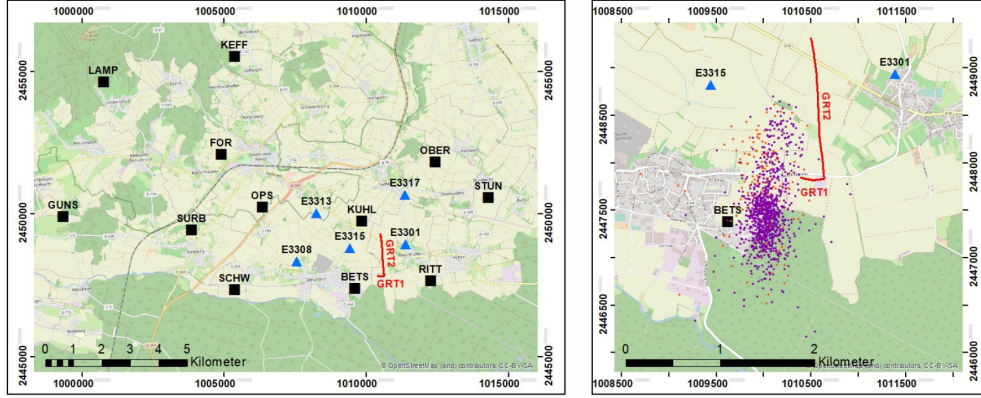
Figure 5.1 – Left: seismic monitoring network operational during thermal stimulation of GRT1 (black squares) and during chemical and hydraulic stimulation of GRT1 (additionally blue triangles). Right: Seismic catalogue used as template database for thermal stimulation (orange) and hydraulic stimulation (violet). The wellpaths of GRT1 and GRT2 are shown as red lines. Coordinates are in the Lambert II etendu (m) system.

forms the template database for this study. This catalogue was generated by automatic detection based on a STA/LTA method applied to the preprocessed vertical components of each station and manually checked. By this time-consuming process, false detections were disregarded, the automatic detected arrivals were repicked, and new arrivals were identified on further channels. For the thermal stimulation of GRT1, on the 24th and 25th of April 2013, the template catalogue contains 146 events. For the hydraulic stimulation of GRT1, the template catalogue contains 990 events in the time period from the 27th of June to the 4th of July, 2013. For the chemical stimulation, no seismic event is included in the catalogue (see Tab. 5.1).

5.2.2　Earthquake detection with template matching

Template matching detection uses a known signal, the template, to detect events with similar waveforms (Ross et al., 2019; Skoumal et al., 2015). This is done by computing the correlation coefficient between the template waveform and the continuous waveform at each time step of a given length. Because this technique uses the whole shape of the waveform, events can be potentially detected even if the signal to noise ratio is lower than 1. Since only events with waveforms similar to the template waveforms can be detected, the choice of the templates has to be well considered to minimize biased results.

The template matching algorithm employed in this study is similar to the one in Lengliné et al. (2017), but we decided to use all events in the previously introduced catalogue as templates instead of only selected representatives to minimize the chance of missed detections.The template windows for detection are 2.56 s (256 time samples) long and start 0.5 s (50 samples) before the P-wave pick.

Before correlation, the waveforms are preprocessed to improve the signal to noise ratio, remove data gaps, detrend and normalize the signal. All templates and continuous waveforms are resampled to 100 Hz and filtered with a 10-45 Hz bandpass filter. These values have been chosen after a comparative analysis of the power spectral density of the template waveforms and periods of noise for each channel. We built a list of all seismic stations ranked according to the number available P- and S-wave picks in the template catalogs. The correlation is computed on the first six channels of this list, when template waveforms and continuous waveforms are available e. g. because the current template could not be picked at that channel or due to the station being not operational. Since the seismic network changed between the thermal and the chemical and hydraulic stimulation, the list of channels is different for each period. The correlation procedure follows that of Lengliné et al. (2017) and returns the average Pearson correlation coefficient at each time step measured over these 6 channels. Then, the mean correlation coefficient has to exceed a given threshold for a new detection to be considered.

Tests on subsets of the data have shown that the distribution of the correlation values depends on the channels chosen for correlation and the templates themselves. Therefore, we decided to use a case adaptive approach similar to Slinkard et al. (2014) and Slinkard et al. (2016) to make an objective selection of the correlation threshold in order to achieve a given false alarm rate. Namely, we used a time-reversed and polarity reversed version of the template signal in order to obtain the statistics of false detection. The advantage of this approach is that the adaptive threshold takes into account the signal contained in a given template (i.e. the signal to noise ratio of the template waveform and its time-bandwidth product), the quality of the signal at each station where the detection is performed and the network quality (i.e. inter-station distance, geometry). The reversed signal is detrended and normalized and then correlated with the continuous waveforms as described above for the real templates. These correlation coefficients thus represent typical values when no event is present in the signal and can be used to infer a probability of false detection. Here we set the correlation threshold for each template and each day based on this distribution of correlation coefficients of

the flipped version. Each threshold is set such that the probability for each template to make a false detection is 1/10 000 per year.

Several events of the template catalogue are likely induced in close proximity to each other, on the same geological structures. Consequently, they may have similar waveforms and, when applying the waveform cross-correlation, this similarity could result in the detection of the same events by different templates. To prevent duplicate events in the final catalogue, the multiple detections of the same event should be discarded. Therefore, the detection times when the correlation exceeds the threshold for the different templates are compared. If they overlap or are separated by less than one second, the detections are merged and assigned to the template that detected the event with the highest correlation. Waveforms of the detected events are then extracted. Windows of 5.12 s starting 1 s before the assumed P-wave arrival are taken from all channels (including those not used for detection). They will be later used to compute the travel time differences between the events that are needed for the relative locations. The number of detected events for each period is given in Tab. 5.1.

5.2.3   Relative relocation of the detected events

Events detected by the same template have a strong waveform similarity. It implies that travel-time measurements from cross-correlation analysis can be achieved on these data with high precision. It is therefore conceivable that precise relative locations between the events can be obtained through relocation with a double-difference based algorithm. Travel time differences between the detected events are computed by correlation of the extracted waveforms of all channels filtered with a 10-45 Hz bandpass filter on 1.1 s long windows (110 samples). The windows are centered on the direct P-wave arrivals for the vertical components and the direct S-wave arrivals for the horizontal components, where the S-wave arrival times are estimated from the average Vp/Vs-ratio of 1.9 computed from the templates and the P-wave travel time. We chose a relatively short window length to ensure that the windows do not contain P- and S-wave arrival at once and too much noise before and after the arrivals. The obtained travel time differences are then filtered according to the following criteria: they must have been computed with a correlation coefficient higher than or equal to 0.5 and for the same event-pair this correlation coefficient must have been reached on at least 6 channels. This ensures that the relation of an event pair is stable and prevents

that outliers are given too much weight into the inversion. The relocation is performed with the software HypoDD (Waldhauser and Ellsworth, 2000) in the 1D velocity model used by Kinnaert et al. (2016). The initial locations of all the events for relocation are set on the wellpath of GRT1 at 2300 m depth, where hydraulic injection occurred. After the first relocation iteration, the result is filtered by removing events that are linked as defined above (correlation coefficient ≥ 0.5 on at least 6 channels) to less than 1% of all others. The second relocation iteration is performed without them.

For the relocated events relative magnitudes are computed from the magnitudes of the template event that detected each respective event based on the differences in maximum waveform amplitudes. The magnitudes of the template events are given in Maurer et al. (2020) and have been corrected for the new hypocenters after relative re-location.

5.2.4 Clustering analysis

To find clusters of similar waveforms among the events, we applied a modified k-means clustering algorithm (Arthur and Vassilvitskii, 2007; Lloyd, 1982). The k-means algorithm is a widely used approach to group large amount of data into clusters of similar properties by iteratively minimizing the within-cluster distances between each cluster member and the cluster center. The original k-means algorithm aims at partitioning n observations, where each observation is a d-dimensional real vector, into k clusters by minimizing the sum of squared Euclidean distances between each cluster member and the cluster mean, which is the within-cluster variance. However, other distance measures than the variance can be applied. The number k of clusters has to be specified beforehand and the cluster centers are adapted with each iteration to find the best cluster representation.

In the present case, we perform k-means clustering not on the correlation between two events but on the correlation pattern of each event with all other events. Thus, we use the cross-correlation matrix between all events, treating each row of the matrix as an observation belonging to a single event. As distance measure for the k-means clustering, we use the Pearson correlation distance (1-Pearson correlation coefficient), so we perform correlation between the pattern of correlation coefficients for each event with the pattern that represents the cluster center.

We consider this clustering approach less prone to the miss-assignment

of events without obvious cluster affiliation or to correlation of noisy signals. For example, if two waveforms would contain the same concise noise pattern, they could get a high correlation coefficient that is not based on the actual signal. Yet, it is unlikely that the same noise pattern is present over the 3000 event waveforms, so the overall correlation sequence in the correlation matrix between the noise-distorted events and all other events would be only slightly perturbed. Furthermore, using the correlation patterns instead of single correlations can help to highlight connections and especially distinctions between events that are otherwise ambiguous.

5.3   Results

5.3.1   Overview and detection statistics

In this study, we aim at following the development of the fault system in the reservoir over the course of the stimulation sequence applied to the well GRT1. Before going into details of spatial event distribution and waveform clustering, each stimulation period is introduced and an overview on the induced seismicity is given. The seismic catalogue derived using the described methodology that is the basis of the following analysis is presented in terms of available detections and event locations in Tab. 5.1.

The thermal stimulation was carried out from the 23th to the 25th of April 2013 for 62.5 hours. A total volume of 4,230 m^3 brine was injected at flow rates up to 25 L/s (Baujard et al., 2017; Maurer et al., 2020). During the thermal stimulation, 324 events could be detected with the template matching, where all events but 4 of the initial template database of 146 events have been recovered. Our final catalogue thereby contains 328 events for the thermal stimulation, new detections and templates together. Templates cannot be re-detected or new detections might be missed if they are too close in time to other detections. In that case, the algorithm does not discriminate between the events and we only recover the first one. The magnitudes of the events range from -1.2 to 0.3 with a magnitude of completeness of -0.7. Magnitude of completeness has been calculated by taking the magnitude bin with the highest event frequency in the non-cumulative frequency-magnitude-distribution with bins of 0.1 magnitude intervals. 285 of the detected events have been relocated, the remaining events did not meet the criteria we applied for the relative relocation.

Table 5.1 – For each stimulation, summary of the number of events in the template database, detected by the template matching algorithm (including recovered templates), in the final catalogue and number of relocated events. The percentage of recovered templates is also given.

Stimulation	Template events	Detections	% recovered	Final number	Relocated
Thermal stimulation	146	324	97.3	328	285
Chemical stimulation	-	2	-	2	-
Hydraulic stimulation	990	2910	92.9	2980	2824
Injection int. hyd. stim.	831	2443	91.8	2511	2386
Delayed int. hyd. stim.	159	467	98.7	469	439

The chemical stimulation was performed two months later from June 23rd to June 25th. The application of the template matching algorithm led to 2 detections, but there were also 3 detections the day prior to the chemical stimulation and 1 the day after, so the seismicity level is not distinguishable from the background noise. A manual inspection of these detections could not clearly confirm that they are indeed seismic events and not only noise detections. This is supported by the fact that no locations could be determined for these detections because the SNR is too low.

The chemical stimulation was directly followed by the hydraulic stimulation on the 27th and 28th of June, lasting 21 hours, 42 minutes. The injection flowrate was increased stepwise to 80 L/s and then stepwise decreased until shut-in. Directly after the stimulation, an injection test was performed at flowrates up to 60 l/s. In total, a volume of 3,180 m^3 brine had been injected during the hydraulic stimulation and 820 m^3 during the injection test (Baujard et al., 2017; Maurer et al., 2020). For the hydraulic stimulation 2910 events have been detected with the template matching, with a recovery of 92.9 % of the template database of 990 events. The recovery is noticeably lower than for the thermal stimulation, which is due to the higher seismicity rate: more events are occurring in the same time window. The final catalogue for the hydraulic stimulation therewith contains 2980 events, templates and new detections together. Among these events, 2824 have been relocated. The hydraulic stimulation can be divided into two intervals of high seismicity, one accompanying the stimulation itself, one four days after

shut-in. Events belonging to the injection related interval have magnitudes between -1.1 and 1.0 with a magnitude of completeness of -0.7, while events from the delayed seismicity interval have magnitudes between -1.0 and 1.6 and a magnitude of completeness of -0.1. Between these two intervals and after the second interval, there are also occasional seismic events.

The catalogue for the hydraulic stimulation of Lengliné et al. (2017) contains 1395 events and therefore about half the number of our final catalogue. The reasons for this are a smaller initial STA/LTA database (674 events) used in Lengliné et al. (2017) to obtain the templates and their approach to select only 13 templates representing different waveform families of these initial 674 events for the template matching detection. Compared to the catalogue of Maurer et al., 2020 we were able to triple the amount of detections and reduce the magnitude of completeness by about 0.1.

To give an overview over the development of the seismicity over the course of thermal and hydraulic stimulation, Fig. 5.2 shows flowrate, seismicity rate and wellhead pressure (WHP) over time. The time is the relative time since injection started, with thermal and hydraulic stimulation plotted over each other to ease the comparison of the seismicity development. During thermal stimulation, with each new injection step, the WHP reaches a maximum of 2.7-2.8 MPa and then declines. Onset of seismicity occured nearly 24 hours after injection start and about 1 hour after flowrate was increased to 20 L/s at a WHP of 2.7 MPa. Seismicity rate then remained constant at a low level before it increased after a short injection break. The maximum seismicity rate of 56 events/hour was reached at 25 L/s and a WHP of 2.8 MPa, before declining and reaching zero nearly 10 hours before injection stop.

The seismicity detected during the injection interval of the hydraulic stimulation starts at a flowrate of 26.5 L/s and WHP of 1.1 MPa (DHP = 1.5 MPa), 5.5 hours after injection started. WHP at the beginning of the hydraulic stimulation is much lower than during thermal stimulation, even when higher flowrates are reached. Contrarily to the thermal stimulation, after seismicity onset the seismicity rate follows closely the flowrate and pressure development over the injection steps up to a seismicity rate of 415 events/hour at maximum flowrate and pressure. During the subsequent injection test, only four events are detected. On the 2nd of July, after a four days quiet period following shut-in, seismicity raises again with a sudden burst of 399 events within two hours.
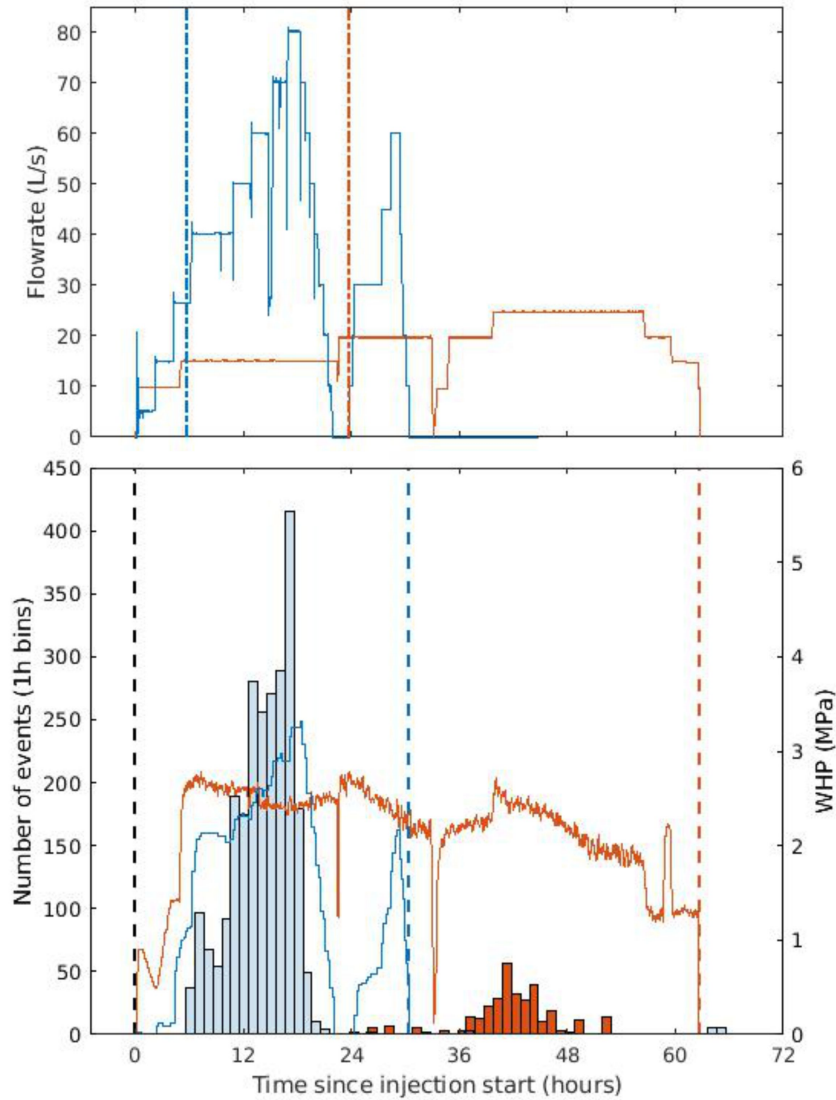
Figure 5.2 – Top: Injection flowrate during thermal stimulation (orange curve) and hydraulic stimulation (blue curve) plotted against time since injection start for each stimulation; The vertical blue dotted-dashed line marks the seismicity onset during hydraulic stimulation, the orange vertical dotted-dashed line marks the seismicity onset of thermal stimulation. Bottom: Seismicity rate in 1h bins for thermal stimulation (orange bars) and hydraulic stimulation injection interval (blue bars) plotted against time since injection start for each stimulation; The orange curve is the WHP during thermal stimulation and the blue curve is the WHP during hydraulic stimulation; The black vertical dashed line marks the injection start for both stimulations, the blue vertical dashed line marks the shut-in of the hydraulic stimulation and the orange vertical dashed line the shut-in of the thermal stimulation.

5.3.2   Spatial distribution of seismic events

The epicentre map after relative relocation (Fig. 5.3, top) shows that the seismic events induced during thermal stimulation are arranged in a SW-NE elongated cloud, extending over a distance of about 300 m. The position relative to the well for all events of both stimulations was fixed by putting the first event of the thermal stimulation at the well GRT1 at 2352 m depth (TVD), where a major fault had been observed in image logs (Vidal et al., 2017). For the hydraulic stimulation, the hypocenters of the majority of the events from the injection related seismic interval are clearly distinct from those of the delayed seismicity. Similar to the events of the thermal stimulation, they are forming a SW-NE elongated cloud partly occupying the same part of the reservoir previously active. Yet, the cloud is larger, extending farther south-eastward and to a broader width. A subset of 56 events from the injection related interval of the hydraulic stimulation is separated from the main cloud and co-located with the events from the delayed interval. The delayed events stretch north of GRT1 towards GRT2 with varying orientations from SW-NE to N-S. The north-depth cross-section (Fig. 5.3, bottom) shows that all three seismic clouds are horizontally aligned and located approximately in the same depth range between 2150 and 2400 m. While the depth range has to be treated with care because of the artificial placement of the first event after relative relocation, the seismic cloud seems to cover the whole range of the oxidized and hydrothermally altered granite, reaching about 50 m into the Buntsandstone at the upper horizontal limit and 50 m into the unaltered granite at the lower horizontal limit (Vidal et al., 2017).

While the spatial distribution of the seismic events obtained in this study and by Lengliné et al. (2017) are similar (for the hydraulic stimulation), the spatial distribution obtained by Maurer et al. (2020) is rather different. Contrary to the narrow depth range we obtained for the seismic clouds, in Maurer et al. (2020) the epicenters are distributed over a wide depth range of about 1 km, which they themselves consider rather unlikely in the present geological setting. They suspected their limitations in the absolute location process, especially the trade-off between depth determination and origin time. We performed relative relocation with different initial locations of the events, starting from the locations of the templates and from a single location in different depths, all leading to similar results. This suggests a certain robustness of the locations. However, it has to be acknowledged that the usage of a 1D instead of a 3D velocity model, especially in the complex geological setting at the boundary between granitic basement and

sedimentary cover intersected by a fault could distort the locations.

5.3.2.1 Activated fault structures

Since the seismic clouds show a clearly narrower extension in one dimension than the other two, they can be approximated by planar structures. To find the best fitting planes to the event clouds of thermal stimulation and injection related and delayed seismic intervals of hydraulic stimulation, the root mean square (RMS) of the orthogonal distance between each event and an assumed plane of any geometry is calculated for each cloud. The orientation associated with the smallest RMS is considered to be the orientation of the best fitting plane. The RMS for each orientation and the best fitting orientation is shown as stereoplot for each seismic interval in Fig. 5.4.

For the thermal stimulation and the injection interval of the hydraulic stimulation, the RMS distribution is similar, with best fitting orientations of N24°±7°E dipping 88°±6°W and N15°±9°E dipping 86°±8°W respectively. For the delayed interval of the hydraulic stimulation, orientations with a N-S strike and a steep dip have the lowest RMS values, with a minimum RMS at N5° ± 4°E dipping 80° ± 8°W. The mapview of the cloud of the delayed interval of the hydraulic stimulation though suggests that the strike of the structure is not constant over its whole length. Consequently, the calculated best fitting plane is to be seen as the average orientation of the structure.

According to the locations and the orientations of the event clouds of the thermal stimulation and injection interval of hydraulic stimulation, it is very likely that the same fault was seismically active, yet during the hydraulic stimulation a larger part of this fault. The second fault segment, mainly seismically active during the delayed interval of the hydraulic stimulation, may highlight an en-echelon fault structure (Lengliné et al., 2017). We assume that the fault activated during thermal and injection interval of hydraulic stimulation is the targeted Rittershoffen fault, whose orientation has been determined in previous studies by different means: from seismic profiles, which estimated a fault orientation of N175°E, dipping 45°W (Baujard et al., 2017), acoustic imaging (Vidal et al., 2016; Vidal et al., 2017) which gave an orientation of N170 − 175°E, dipping 55 − 65°W and two seismic studies by Maurer et al. (2020) and Lengliné et al. (2017). Maurer et al. (2020) determined a best fitting plane with orientation N5°E and vertical dip for the whole seismicity and Lengliné et al. (2017) a best fitting plane oriented N25°E dipping 70°W for the cloud induced during the injection interval
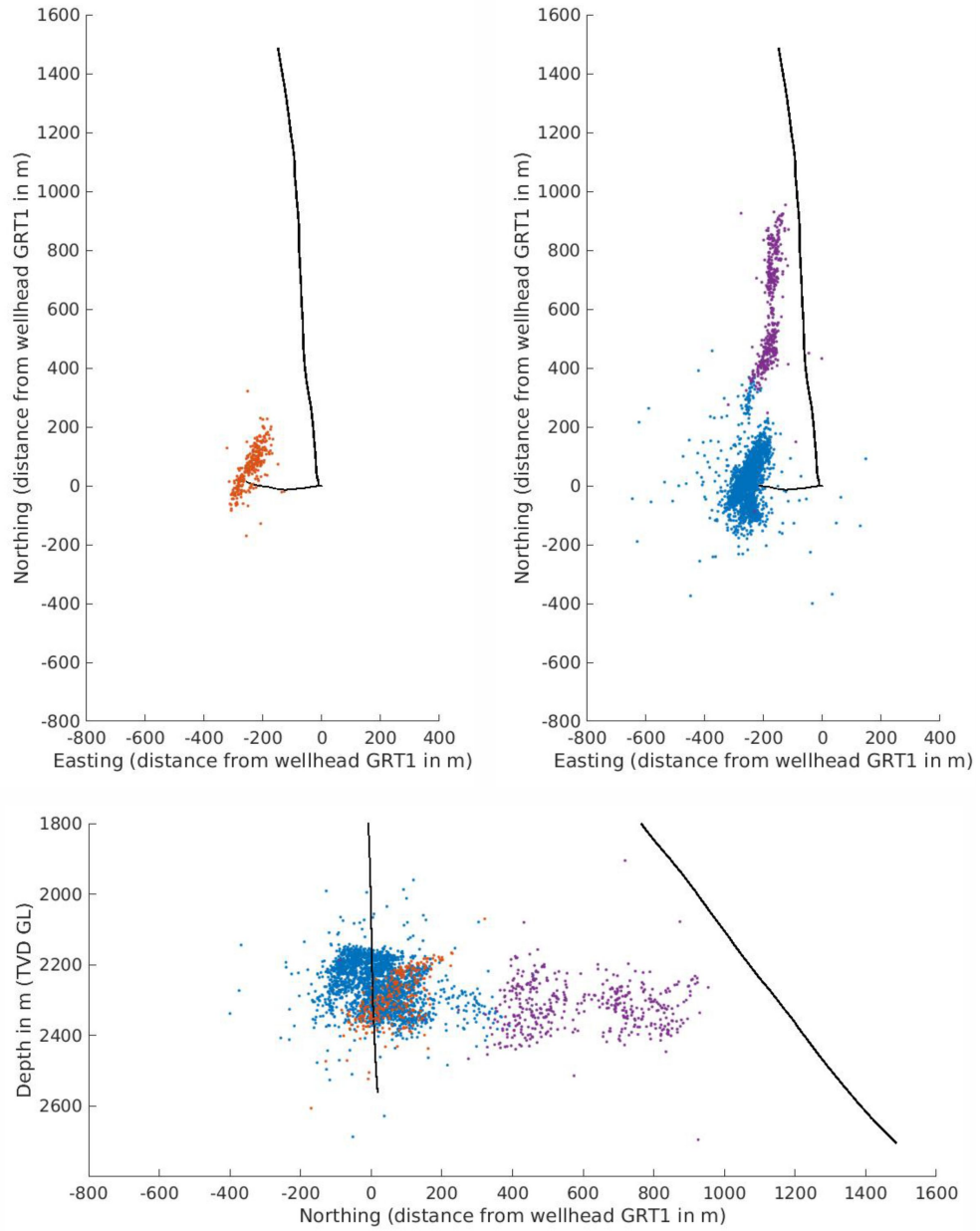
Figure 5.3 – Top: Mapview of the relocated events induced during thermal stimulation (left side, orange dots) and hydraulic stimulation (right side, the injection related seismic interval of the hydraulic stimulation is in blue, the delayed seismic interval in violet); Wellpaths GRT1 and GRT2 as black lines. Bottom: North-depth cross-section of the relocated events.
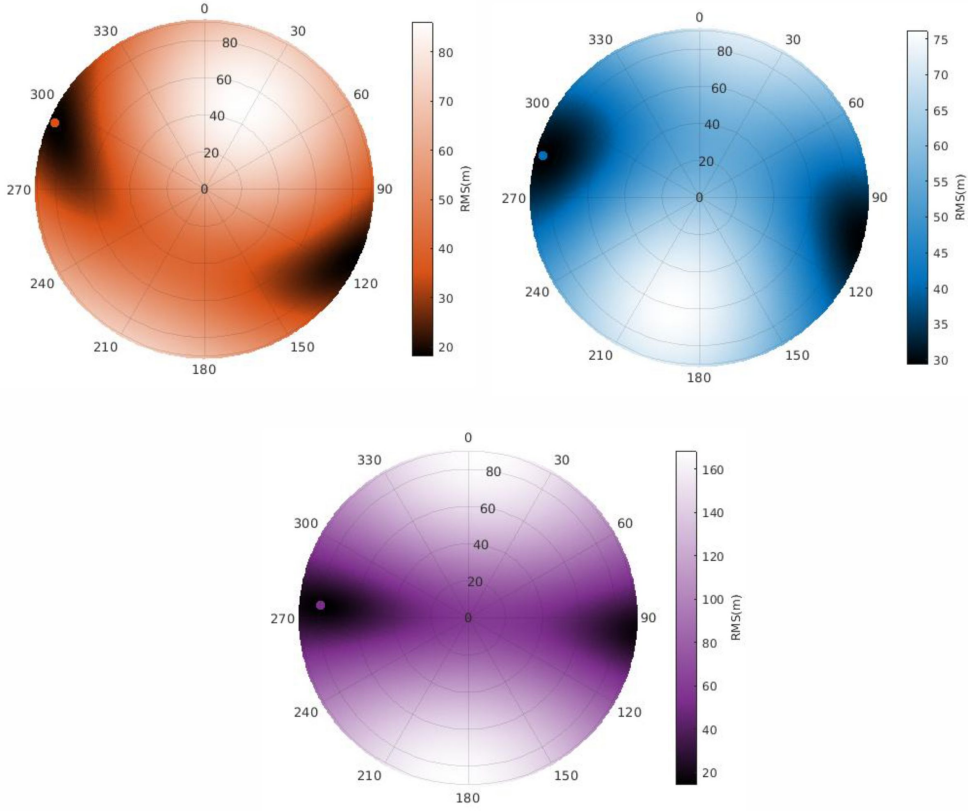
Figure 5.4 – Stereoplots showing the root mean square (RMS) of the orthogonal distance between the seismic events and a plane with varying orientation: dip from 0°to 90° and dip direction from 0° to 360°, in steps of 1°. Orange: thermal stimulation, blue: injection interval hydraulic stimulation, violet: delayed interval hydraulic stimulation. The small colored circles show the orientation with minimum RMS.

of the hydraulic stimulation. Our results are therewith in good agreement with the other studies on induced seismicity in the Rittershoffen reservoir. The orientation of the fault given by the seismic profile and acoustic imaging is rather NNW-SSE than NNE-SSW and the dip is not as steep. These discrepancies stem most likely from the different observation scales and the complexity of the fault zone geometry. As already observed in fault zones in the Soultz-sous-Forêts geothermal reservoir, small-scale fractures and larger scale fault zones do not necessarily have the same orientations (Dezayes et al., 2004; Dezayes et al., 2010). The orientation derived for the second fault cannot be verified by other studies since it was not calculated by Lengliné et al. (2017) and Maurer et al. (2020) and is not intersecting either well,

therefore being not captured by well-logging.

5.3.2.2   Reservoir volume active during both, thermal and hydraulic stimulation

Since part of the event cloud induced during the injection interval of the hydraulic stimulation is occupying the same reservoir volume as the event cloud induced during the thermal stimulation, we want to investigate whether inside that volume there is a distinction between the two sets of events. To quantify the overlap of the stimulated volumes during the thermal and hydraulic stimulation, we developed the following approach. The volume of the reservoir which is occupied by the seismic clouds of both stimulations is divided into regular cubes. The number of seismic events for both stimulations is calculated in each cube. The size of the cubes is chosen according to an estimation of the event location uncertainty. It corresponds to the scale for which a change in the dimensionality of the cloud is observed (Fig. 5.5). The assumption is that the events are induced on fault planes and therefore the seismic cloud should have a dimension of 2. However, owing to location uncertainties, the events may deviate at small scales from that planar structures and form a more 3-dimensional cloud. To find this transition from 3D to 2D in the dimension of the seismic cloud, we computed the correlation integral (Grassberger and Procaccia, 1983). More specifically, we calculated the cumulative number of pairs beneath a certain distance for all possible distances (Fig. 5.5, left). We indeed observe a transition between two simple euclidean geometries going from small to large scales: a line of slope 3 can be fitted for small inter-event distances and a line of slope 2 for large inter-event distances. The intersection of these lines gives an estimate of the distance where the dimensionality of the cloud changes and therewith of the location uncertainty. In the present case, this change happens at a distance of 15 m (Fig. 5.5, left). This value is not to be seen as an exact quantification of the location uncertainty but rather as an estimate of its order of magnitude. To overestimate the location error, we double this value to 30 m, and assign it to the cube size.

The whole volume between the minimum and maximum x, y and z-coordinates of the events of the thermal stimulation is divided into $30 \times 30 \times 30$ m cubes. The subset of events of the hydraulic stimulation falling inside the cubes is plotted in Fig. 5.5 (right) together with the events of the thermal stimulation. Out of the 122 cubes, 89 cubes contain events of both
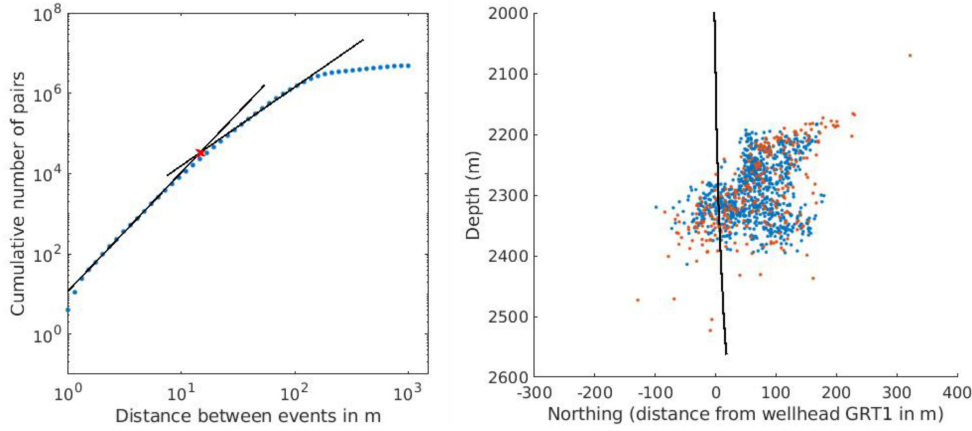
Figure 5.5 – Left: Estimation of the order of magnitude of the location uncertainty by investigation of the change in dimensionality of the whole seismic cloud; the cumulative number of all event pairs is plotted against the distance between the event pairs in double logarithmic scale (blue dots), the lower part of the curve can be fitted with a line of slope 3, the upper part with a line of slope 2 (black lines), the intersection (red cross) marks the change from an euclidean dimension of 3 to 2. Right: Close-up on the reservoir volume seismically active during thermal stimulation (orange dots) and hydraulic stimulation (blue dots).

stimulations and 33 cubes contain only events of the thermal stimulation. However, these 33 cubes are located at the edges of the investigated area and contain in total only 48 events, so in average little more than one event per cube. Therefore, it seems that inside the volume occupied by events from thermal and hydraulic stimulation, no clear spatial distinction between the two sets can be made. This shows that likely the same structures on the fault plane have been activated during both stimulation sequences, so both stimulations had a similar effect on the fault in this part of the reservoir.

5.3.2.3 Tempo-spatial event distribution

To link the spatial and temporal distribution of the seismic events, their order of appearance is shown projected on a vertical cross-section oriented along the best fitting plane for each of the seismic clouds (Fig. 5.6). For the thermal stimulation, no clear migration of the events with time can be observed (Fig. 5.6, top left). Overall, the event-distribution in time as well as space is quite homogenous without showing any clear development except a growing number of events in the same part of the fault over the course of the thermal stimulation.

For the injection related interval of the hydraulic stimulation, it can be observed that the earliest events also concentrate mostly in the volume previously activated by the thermal stimulation. This is especially true for the first 150 events, which are distributed exclusively in that part of the reservoir. Like already observed in Lengliné et al. (2017), later events migrate southeast- and upwards, into a region where the reservoir had been previously inactive but there are also still occurrences in the earliest active zone. The latest events of the main interval of the hydraulic stimulation are located either in the southeast-uppermost part of the cloud or separated from the main cloud north of GRT1, in the zone connected to the delayed seismicity (Fig. 5.6, top right).

For the delayed interval of the hydraulic stimulation we can confirm the observation of Lengliné et al. (2017) that the seismicity started in the middle of the cloud, at the edges of both spatial sub-clusters. Seismicity then migrated to the southeast towards GRT1, but without reaching the well, and to the northwest, creating a quasi-symmetrical pattern (Fig. 5.6, bottom).

5.3.3   Spatial and temporal waveform clustering

Template matching detection and relative relocation rely on waveform similarity between the events, when deploying these techniques it is therefore an assumption that there is a certain level of commonality among the events induced at one site. Yet, waveform similarity may vary among the events and can give insight on relations between them and substructures in the seismic cloud. To investigate these relations, we applied a modified k-means clustering algorithm as described in the methodology section.

K-means clustering requires an initial choice of the number of clusters (k). Since we do not know beforehand which number of clusters might represent best our current dataset, we performed clustering with $3 \leq k \leq 10$. With increasing values of k, the event clouds of thermal stimulation and injection interval of hydraulic stimulation are further partitioned into spatially separated clusters with relatively minor overlap, except for cluster 5, which is distributed over the whole area. For k = 8, the cluster that contains the events from the delayed interval of the hydraulic stimulation is split into two clusters, corresponding to the two spatial sub-clusters of the cloud (Fig. 5.7, top). We chose k = 8 as the maximum suitable number of clusters to represent the seismic clouds since for k = 9 and 10, new clusters contain only
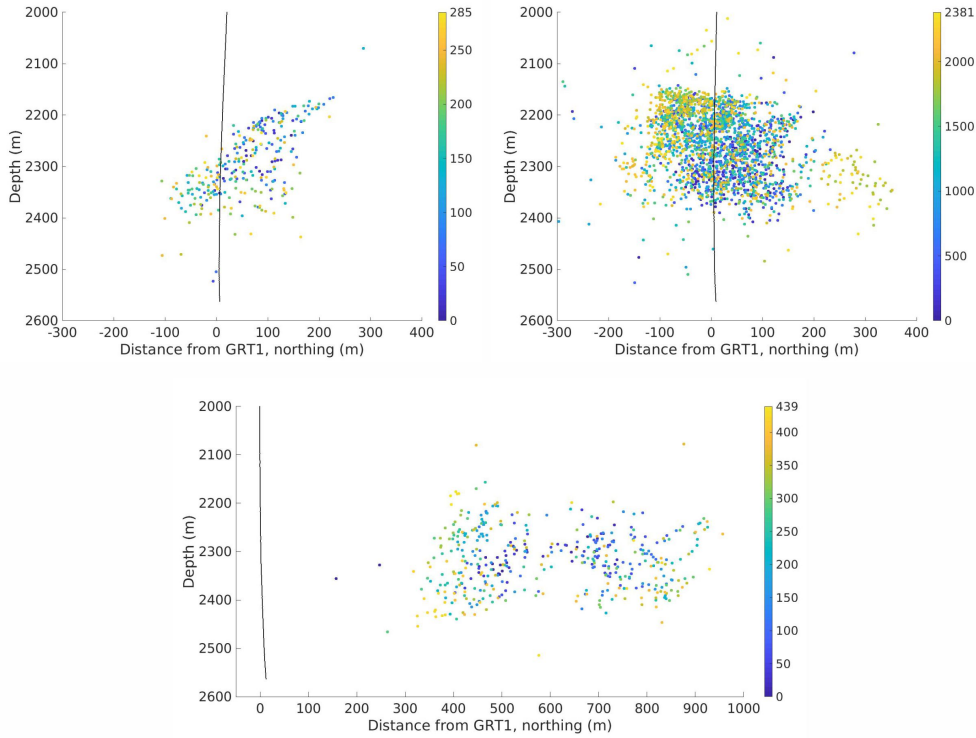
Figure 5.6 – Event cloud of the thermal stimulation (top left), main interval of hydraulic stimulation (top right) and delayed interval of hydraulic stimulation (bottom) projected on a vertical cross section oriented along the best fitting planes. The colors show the order of appearance, with dark blue for the earliest events and yellow for the latest ones.

few events that are distributed over the whole active fault area. That the event cloud can be partitioned into smaller and smaller spatial patches with increasing number of clusters shows that spatial proximity of the events seem to have a major influence on waveform similarity.

The temporal development of the cumulative number of events per cluster over the course of all seismic intervals shows that during thermal stimulation, the events belong mostly to clusters 1, 4 and 7 (Fig. 5.7, bottom). When looking closer at the seismicity onset during hydraulic stimulation, it can be seen that the first 150 events also belong to these three clusters. Then, clusters 2, 5 and 6 become additionally active. Cluster 3 and cluster 8 are mainly active during the delayed interval of the hydraulic stimulation, but cluster 3 already shows some activity at the end of the injection interval. Almost all events from the injection interval that belong to cluster 3 are part
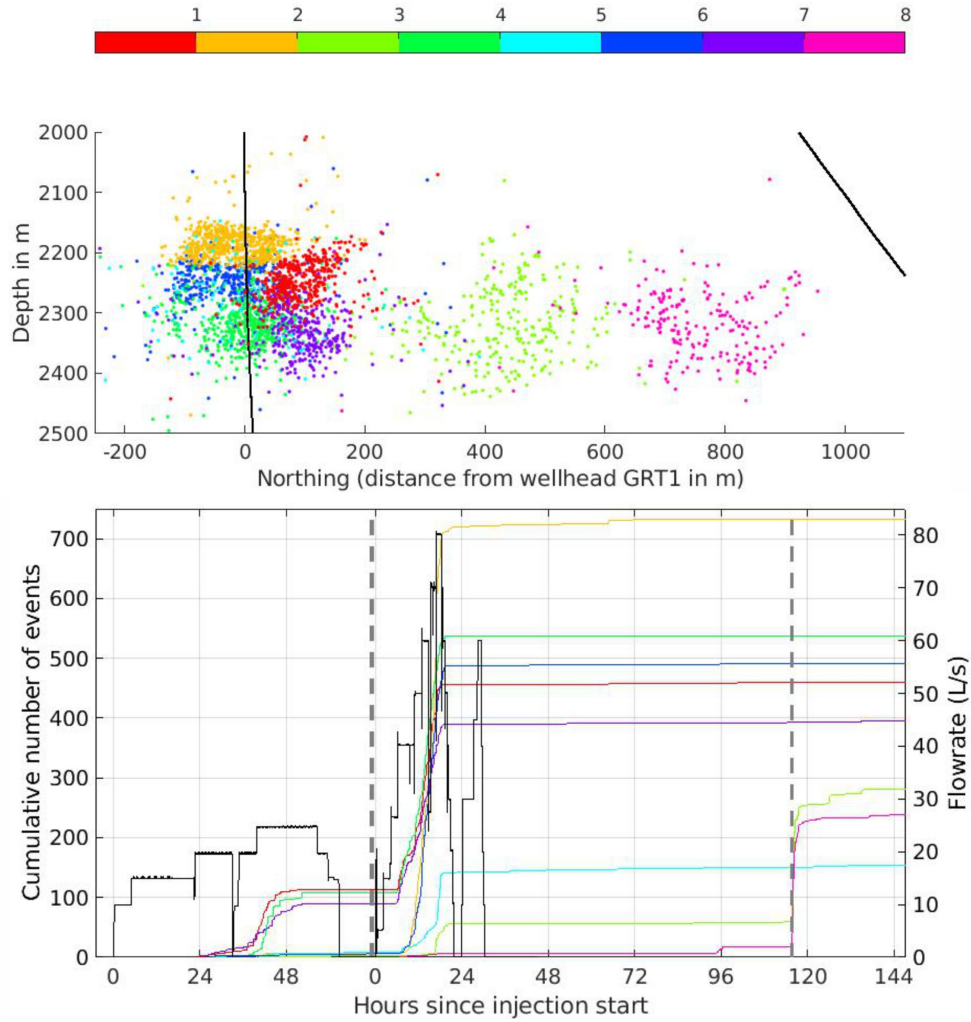
Figure 5.7 – Top: Spatial distribution of clusters for k = 8 clusters in North-Depth cross-section. Different clusters are represented in different colors according to the color bar. Bottom: Cumulative number of events per cluster (colored curves, color corresponds to cluster number shown in the color bar) in relation to flow rate (black curve) during thermal and hydraulic stimulation. The two grey dashed lines mark the beginning of the injection interval of the hydraulic stimulation and the beginning of the main activity of the delayed interval of the hydraulic stimulation. The time is shown as hours passed since injection started for the thermal stimulation up to the first grey dashed line and then as hours passed since injection started for the hydraulic stimulation.

of the subset of 56 events co-located with the delayed seismicity. On the other hand, not all of these 56 events belong to cluster 3, Fig. 5.7 (top) shows that few also belong to clusters 1, 5, 6 or 7.

Despite the time gap of two month and the chemical stimulation in between, the same waveform clusters active during thermal stimulation are re-activated during hydraulic stimulation. This shows that the mechanics of the fault patches during seismic slip remain largely the same and seem to be independent of time and applied stimulation operation. This is confirmed by the fact that clusters generally do not overlap each other significantly while events from thermal stimulation and injection interval of the hydraulic stimulation occupy the same reservoir volume.

5.4 Discussion

In this chapter, we combine the tempo-spatial development of the seismicity with the results of the clustering analysis and operational parameters to obtain an integrated analysis of the fault network development.

During the thermal and the hydraulic stimulation a fault with near-vertical dip and NNE-SSW strike was activated. It is evident from Figure 2 that during thermal stimulation, seismicity is starting at a WHP of 2.7 MPa at the 3rd injection step with a flowrate of 20 L/s (24 h after injection start, 1 h into the injection step). Under the common assumption that the WHP is causative for seismic slip, we present here a corresponding Mohr-Coulomb analysis. This requires adequate values of the stress state and the failure criterion. The local stress field was analysed in detail at the nearby Soultz-sous-Forêts geothermal site by Cornet et al. (2007) who give an overview on the different studies and have deduced a stress tensor of:

$$
\begin{aligned}
S_v &= 33.8 + 0.0255 \cdot (z - 1377) \\
S_h &= 0.54 \cdot S_v \\
P_f &= 0.9 + 0.0098 \cdot z \, ,
\end{aligned}
\tag{5.1}
$$

with S_v: vertical stress, S_h: minimum horizontal stress, P_f: pore fluid pressure, all in MPa, and z: depth in m.

Based on the findings of Lengliné et al. (2017) and Maurer et al. (2020), we assume strike-slip conditions with maximum horizontal stress S_H being slightly higher than S_v at reservoir depth: $S_H = 1.01 \cdot S_v$. The orientation of S_H at the injection depth is estimated by Cornet et al. (2007) to be $170° \pm 10°$. The resulting Mohr-circle for the stress state of the fault without fluid injection and for WHP = 2.7MPa is presented in Fig. 5.8. Assuming the friction coefficient μ of Cornet et al. (2007) for Soultz in the range of $0.8-0.96$, it becomes apparent that for an optimally oriented plane there has to be cohesion present on the fault, otherwise it would slip at much lower fluid pressure.

To better constrain the fault conditions, we look at seismicity onset during hydraulic stimulation. It can be seen in Fig. 5.2 that seismicity started at a WHP of 1.1 MPa (DHP = 1.5 MPa) and the Mohr circle for this DHP is also shown in Fig. 5.8. It becomes clear that, if the onset of seismicity is related to pore pressure, the failure criterion for the fault must have changed between both stimulations. Onset of seismicity during hydraulic stimulation could be explained with no cohesion on the fault using $\mu = 0.95$, which is in agreement with the value range proposed by Cornet et al. (2007). Assuming a constant friction coefficient, cohesion c would have to change over the course of the injection sequence by about $c = 1.1$ MPa between the thermal and the hydraulic stimulation on a fault optimally oriented in the stress field. For $\mu = 0.95$ the optimal orientation of a fault plane for failure would be N13° $\pm$ 10°E with vertical dip in the assumed stress field. If we alternatively assume a lower friction coefficient of $\mu = 0.85$, typical for rocks at low normal stress (Byerlee, 1978), cohesion would be overall higher: $c = 2.1$ MPa for the beginning of the thermal stimulation and $c = 1.1$ MPa for the beginning of the hydraulic stimulation. In this case the optimal orientation of a plane for failure would be N15° $\pm$ 10°E and therewith match exactly the orientation calculated for the best fitting fault plane for the injection interval of the hydraulic stimulation (N15° $\pm$ 9°E) and also for the thermal stimulation (N24° $\pm$ 7°E) within the uncertainty range. Thus, the criticality of the fault plane in the local stress field can be confirmed. The calculated initial cohesion of 1.1 to 2.1 MPa for $\mu = 0.95$ to 0.85 is in the lower range of what was proposed by Cornet et al. (2007) for Soultz.

In the above Mohr-Coloumb analysis for seismicity onset during thermal and hydraulic stimulation, it is assumed that the reached WHP at seismicity onset is initiating the seismicity. However, the thermal stimulation shows no obvious link between seismicity rate, pressure development and flowrate as illustrated in Fig. 5.2. We therefore analyse the different injection steps of
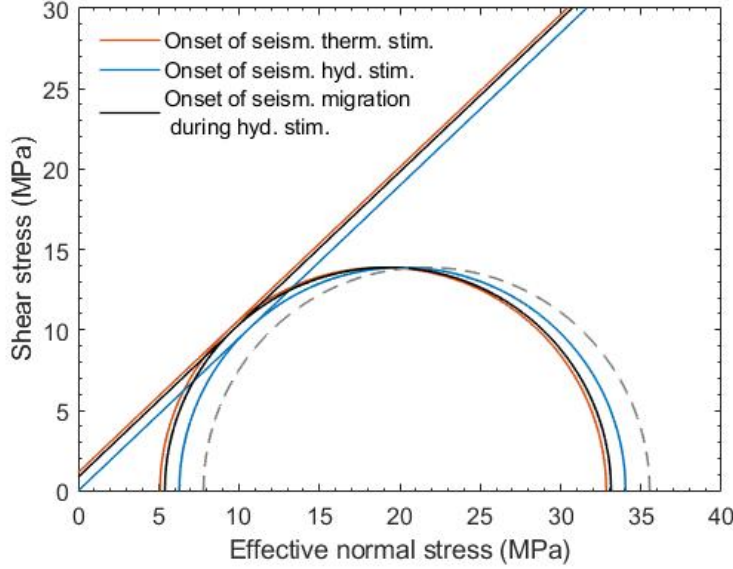
Figure 5.8 – Mohr-circles and failure criteria for seismicity onset during thermal stimulation (orange) at WHP = 2.7 MPa and c = 1.1 MPa, seismicity onset during hydraulic stimulation (blue) at DHP = 1.5 MPa and c = 0 MPa and after the first 150 events of the hydraulic stimulation (black) at DHP = 2.4 MPa and c = 0.9 MPa. The grey dashed circle shows the state of stress without fluid injection. The failure criteria have been calculated for a friction coefficient of 0.95.

the thermal stimulation more closely now.

The 1st injection step was carried out at 10 L/s with fluctuating WHP up to 1.5 MPa without being accompanied by any seismicity. At the 2nd injection step, the flowrate was increased to 15 L/s and WHP jumped to 2.8 MPa before slowly declining down to 2.3 MPa. Still, no seismicity was observed, despite the WHP remaining relatively high during the whole injection step. This suggests that the fluid was distributed into the reservoir through uncritical fractures that did not react strongly mechanically. The 3rd injection step at 20 L/s is divided by a short shut-in phase and seismicity shows distinct behavior before and after the injection break. Seismicity starts 1 h into the 3rd injection step at near maximum WHP of 2.7 MPa and remains at low level until the break. Afterwards, seismicity increases drastically. The increase of seismicity after the short shut-in shows that seismicity rate seems to react to the rate with which the flowrate is changed, so the length and magnitude of injection steps. This indicates that seismicity is lower when the system has time to adjust to the flowrate.

There are three possible routes of explanation for the upcoming seismicity at similar WHP compared to the seismically quiet 2nd injection step: 1) Criticality of fractures: The pressure front of the injected fluid has reached a more critically oriented fracture set or the initially uncritical fractures became critical due to changing mechanical properties in the previous steps. 2) Driving mechanism of induced seismicity: Instead of the WHP, seismicity is caused by thermal effects, increase in hydraulic energy (Baujard et al., 2014) or the structural load of the fluid mass on the fractures over a prolonged period. 3) The effective reservoir pressure is different from the measured WHP and actually higher during the 3rd than during the 2nd injection step.

At the fourth injection step, when flowrate is increased to 25 L/s, WHP reaches its peak value of 2.8 MPa again, accompanied by maximum seismicity rate before both subsequently decline. This time, the increase in injectivity is accompanied by a decrease in seismicity. This behaviour would be typical for a hydraulic stimulation: fractures slip seismically thereby increasing permeability, that leads to pressure decrease and consequently drop of the seismicity rate even at ongoing fluid injection. Overall, it remains unclear if the seismicity onset and development during thermal stimulation is related directly to pressure changes, to injection flowrate, to cumulative injected volume or to a combination of these factors. The calculated value for cohesion on the fault is only valid if the reached WHP caused the seismicity onset. However, even if this is not the case, it still gives a lower threshold for the mechanical stability of the fault regarding pore pressure since it did not seismically slip at lower WHP during the first 24 hours of injection.

The conditions of the thermal stimulation with flowrates below 25 L/s over 2.5 days are clearly different from the hydraulic stimulation with flowrates of up to 80 L/s over 22 hours. This is impacting also the induced seismicity. Fig. 5.2 shows that, contrary to the thermal stimulation, seismicity during hydraulic stimulation follows a pattern of increasing seismicity rate with increasing pressure. The different behaviour of the system during thermal and hydraulic stimulation suggests that either the mechanical state of the fault has changed between the two stimulations or that the relation between operational parameters and seismicity changes above a certain flowrate. Since during hydraulic stimulation seismicity rate and WHP develop in close correlation, a pressure related criterion for fault activation is not unlikely.

Baujard et al. (2017) report that injectivity during thermal stimulation was increased from 0.6 L/s/bar to 1.3 L/s/bar at a flowrate of 20 L/s and that

this injectivity increase was retained during the two month break before the chemical stimulation. This suggests that the fractures activated during thermal stimulation were then still open. The shear stress along the fault should have been reduced after the slippage during the thermal stimulation. The Kaiser-effect (Kaiser, 1950; Lavrov, 2003) claims that the fault should not be re-activated at a pressure level below the 2.8 MPa. However, seismicity was detected at less than half this WHP during the hydraulic stimulation. This suggests that the fractures were more critical before the hydraulic than prior to the thermal stimulation and that the value of cohesion has been impacted by the thermal and/or the chemical stimulation that took place immediately before the hydraulic stimulation. Seismicity could not be detected during this chemical stimulation despite a slightly decreased magnitude of completeness resulting from our method. The impact of the chemical treatment had however a clear impact on the well due to the increased injectivity (Baujard et al., 2017). Mineral reactions could have changed the mechanical state along parts of the fault, leading to a re-activation at lower pressure. The event locations show that within an approx. 200 m distance of the injection well, the initial, approx. 150 seismic events of the hydraulic stimulation and the events of the thermal stimulation are spatially indistinguishable. That means the same part of the fault got activated twice. This behaviour cannot be explained by a Kaiser-effect under the assumption of static mechanical parameters.

After the first phase of the hydraulic stimulation, the seismic cloud starts to migrate along the fault, about one hour after the increase of flowrate to 40 L/s at a DHP of 2.4 MPa. The detailed event re-location allows for a Mohr-Coulomb analysis of the onset of this migration along the hitherto seismically quiet part of the fault as shown in Fig. 5.8. It is characterized by a cohesion of 0.9 MPa for $\mu = 0.95$ or 1.8 MPa for $\mu = 0.85$, which is in correspondence to the determined cohesion of the fault at onset of seismicity during thermal stimulation. Above 40 L/s, Baujard et al. (2017) also observed a change of the state of the well by a linear increase of the downhole differential pressure with the flowrate. This is reflected in the described change of the tempo-spatial seismicity distribution: While during thermal and early hydraulic stimulation a whole part of the fault close to the well became seismogenic at once, after the flowrate increase to 40 L/s during the hydraulic stimulation, the events changed towards a directed migration along the fault. Reaching a final injectivity index of up to 2.5 L/s/bar, Baujard et al. (2017) concluded that the hydraulic stimulation of GRT1 led to a drastic enhancement of near-well hydraulic properties and the development of a good connection with the reservoir over a high-conductive feature. Our analysis confirms these

statements since seismicity and therewith pressure reached farther into the reservoir as evidenced by the larger activated fault-area.

The clustering analysis supports the above layout: There is largely a spatial division between clusters in both fault parts, the area activated during both stimulations closer to the well and the area becoming active only during hydraulic stimulation. Furthermore, the temporal development of the event clusters shows that the same fault patches are repeatedly activated over the whole duration of both stimulations. Noteworthy, the cluster activity is not linked to thermal or hydraulic stimulation. Thus, it is likely that the same fault activation mechanism took place.

A subset of 65 events induced at the end of the injection during the hydraulic stimulation is spatially separated from the rest of the cloud, situated on a second fault that became seismically active again four days later during the delayed seismic interval unrelated to on-site operations. The clustering analysis shows that 72% of the subset events belong to cluster 3 and their waveforms are therefore characteristic for the delayed interval. Despite being closely co-located, few events belong to cluster 1 (8%), 5 (3%), 6 (9%) and 7 (8%), having characteristic waveforms for the injection related interval. This confirms that location is not the only factor influencing the waveforms and may suggest that the fault activation mechanism plays a role. The co-location of events belonging to different clusters hints at the dynamic conditions in the reservoir with a transition of fault activation mechanisms taking place on the second fault.

The origin and mechanism for the delayed seismicity interval on the second fault segment is discussed in Lengliné et al. (2017), who proposes Coulomb stress transfer by aseismic slip followed by event-to-event triggering to be responsible. Aseismic movement could be favoured by clay minerals that are associated to the fault zones in the Rittershoffen reservoir (Vidal et al., 2018). Well tests and tracer tests between GRT1 and the later drilled well GRT2 give evidence of an existing pressure but a rather poor flow connection with a tracer breakthrough occurring only 12-14 days after tracer injection (Baujard et al., 2017; Sanjuan et al., 2016). These observations highlight the importance of stress transfer in the rock matrix. The existence of a good pressure connection may hint at poroelasticity as another possible driving mechanism of the delayed seismicity.

5.5 Conclusion

We derived a comprehensive seismic catalogue by template matching detection whose events were relocated by a relative relocation procedure and sorted into waveform clusters. This processing allowed for a detailed evaluation of the temporal and spatial distribution of the seismic events induced during the stimulation sequence of GRT1. The method yields reproducible and stable results. Specifically, a comparison with Lengliné et al. (2017) shows that the overall spatial distribution of events for hydraulic stimulation was reproduced from different initial template databases and velocity models. In comparison with the classical methods with STA/LTA detection and absolute locations (as used by Maurer et al. (2020)) our processing reveals more details, allowing us to highlight features of the reservoir that would otherwise remain invisible. In particular, the temporal development of the events over the injection steps and the shape and orientation of the different segments of the fault network is becoming evident. Overall, the amount of events has been tripled compared to the template catalogue, while the magnitude of completeness could be reduced by 0.1, making the catalogue only slightly more complete regarding the low-magnitude events.

Herein, we successfully applied this methodology to the seismicity induced during thermal and hydraulic stimulation of the well GRT1 of the Rittershoffen geothermal reservoir and characterized the development of the corresponding fault network. We detected two seismogenic fault segments in a depth range between 2150 and 2400 m, in the altered granite just below the transition from the Buntsandstein. Our high resolution re-location allows the conclusion that there is no direct and continuous migration of seismicity from one structure to the other and therewith stress transfer between the two faults had to be aseismic.

Our analysis has shown that GRT1 intersects a NNE-SSW striking fault that is highly critically oriented in the local stress field and was seismically activated during thermal and hydraulic stimulation. The multiple injection sequence on the same fault plane allows us to propose a scenario of progressive change of the fault condition. On the basis of the seismicity, the pressure conditions and the stress field, an initial cohesion of $\approx$1-2 MPa was derived under the assumption that the pore pressure is causative for the seismicity onset and a friction coefficient between 0.85 and 0.95. Other mechanisms that might have contributed are thermal effects, flowrate or the cumulative injected volume. The chemical stimulation did not cause seismicity but likely

affected the fracture network as evidenced by an increase of injectivity (Baujard et al., 2017). The thermal and/or chemical stimulation seemingly caused a reduction or even complete loss of cohesion, allowing seismic reactivation of the same part of the fault at lower fluid pressure during the hydraulic stimulation. Further indication for a change of the mechanical conditions can be seen in a detailed spatial comparison of the hypocentres of the thermal and the hydraulic stimulation showing that the locations are indistinguishable in the same reservoir volume. Also, the activated clusters show that the events from both stimulations in this part of the fault do not have distinct characteristics and therewith were most likely caused by the same fault activation mechanics. Seismicity started to migrate further into the reservoir and activated a new area of the fault and new clusters at flowrates > 40 L/s. The onset of the migration occurred at a similar pressure like onset of seismicity during thermal stimulation, confirming the obtained failure criterion for the unperturbed fault.

We identified a second fault with an orientation varying from NNE-SSW to N-S, situated north of the first one. It was primarily active during the delayed interval of seismicity four days after shut-in of the hydraulic stimulation but a subset of events induced during the late injection phase is also located on this fault. The delayed seismicity as well as most of the subset events belong to distinct clusters compared to the majority of the injection related events. This observation supports the hypothesis made by Lengliné et al. (2017) that the delayed seismicity was caused by a different mechanism than the injection related seismicity and is not directly related to fluid migration. However, a few of the late injection related events from the subset located on the second fault belong to waveform clusters active during the injection interval. This suggests that at the end of the injection a transition of fault activation mechanism took place. The triggering of a second fault after four days of quiescence shows that aseismic stress transfer plays an important role and can lead to unexpected seismicity on structures that may have not been targeted originally.

Our study provides new perspectives to understand the hydraulic processes in a faulted underground reservoir. The performed stimulation sequence at Rittershoffen gave us the opportunity to perform a detailed monitoring of the seismic response and therewith the mechanical state of a fault system to fluid injections with different operational set-ups. Especially our clustering analysis indicates the complexity and dynamics of the processes. The well-controlled setting in combination with our detailed integrated analysis allowed us to derive a deeper understanding of the hydro-mechanical

interactions in the reservoir and can thus contribute to the mitigation of seismicity in future operations and projects.

Acknowledgments

Chapter 6

Pseudo-probabilistic identification of fracture network in seismic clouds driven by source parameters

Authors: R. Koepke[1,2], E. Gaucher[1] and T. Kohl[1]

[1]Karlsruhe Institute of Technology, Institute of Applied Geosciences, Division of Geothermal Research, Kaiserstr. 12, 76187 Karlsruhe, Germany

[2]University of Strasbourg/CNRS, IPGS/EOST, 5 rue René Descartes, 67084 Strasbourg, France

Abstract

Fracture networks in underground reservoirs are important pathways for fluid flow and can therefore be a deciding factor in the development of such reservoirs for geothermal energy, oil and gas production or underground storage. Yet, they are difficult to characterize since they usually cannot be directly accessed. We propose a new method to compute the likelihood of having a fracture at a given location from induced seismic events and their source

parameters. The result takes the form of a so-called Pseudo Probabilistic Fracture Network (PPFN). In addition to the hypocenters of the seismic events used to image the fracture network, their magnitudes and focal mechanisms are also taken into account, thus keeping a closer link with the geophysical properties of the rupture and therefore the geology of the reservoir. The basic principle of the PPFN is to estimate the connectivity between any spatial position in the cloud and the seismic events. This is done by applying weighting functions depending on the distance between a seismic event and any location, the minimum size of the rupture plane derived from the event magnitude, and the orientation of the rupture plane provided by the focal mechanism. The PPFN is first tested on a set of synthetic datasets to validate the approach. Then, it is applied to the seismic cloud induced by the deep hydraulic stimulation of the well GPK2 of the enhanced geothermal site of Soultz-sous-Forêts (France). The application on the synthetic datasets shows that the PPFN is able to reproduce fault planes placed in a cloud of randomly distributed events but is sensitive to the free parameters that define the shape of the weighting functions. When these parameters are chosen in accordance with the scale of investigation, i.e. the typical size of the structures of interest, the PPFN is able to determine the position, size and orientation of the structure quite precisely. The application of the PPFN to the GPK2 seismic cloud reveals a large prominent fault in the deep-northern part of the seismic cloud, supporting conclusions from previous work, and a minor structure in the southern upper part, which could also be a branch of the main fault.

6.1   Introduction

Applications like geothermal energy, oil and gas production, wastewater disposal or gas storage that use the subsurface as reservoir or storage facility involve the extraction, injection and circulation of fluids. In many such reservoirs, especially when located in low porosity rocks, fracture networks can be the main pathways for the injection/extraction of these fluids (Gale et al., 2014; Vidal et al., 2018). They may, however, be a potential source of induced seismic events (Gellasch et al., 2013; Rutqvist et al., 2016). Consequently, the characterization of these fracture networks controlling the fluid flow is of major importance for a safe and efficient utilization (Aydin, 2000; Berkowitz, 2002). However, since they are typically located too far below direct access, such a characterization is challenging and has been addressed

by different approaches, including outcrop mapping, the evaluation of well-logs and drill-cores, stochastic and geomechanical modelling or, like in this study, analyzing induced seismicity. Each of these techniques has its own advantages and disadvantages (Lei et al., 2017):

The mapping of outcrops as reservoir analogues (Cilona et al., 2016; Watkins et al., 2018) or the evaluation of well-logs and drill-cores, which allow direct insight into the reservoir (Barthélémy et al., 2009; Aghli et al., 2016) have the advantage to provide a direct physical image of the fracture networks. However, they supply only limited, very localized data and logs and cores are potentially disturbed by the drilling process, whereas outcrops can only be assumed representative analogues of the underground conditions, an assumption which has its restraints (Howell et al., 2014; Watkins et al., 2015). Furthermore, these techniques basically only provide 1D and 2D information whereas knowledge about the 3D fracture network would be desirable.

Stochastic models may use such limited 1D/2D data sets to obtain a full 3D distribution of a fracture network in a reservoir (Kohl and Mégel, 2007; Tóth, 2010) with the fracture properties (i.e. location, density, size or orientation) following probability distributions (Darcel et al., 2003a; Follin et al., 2014). Another modelling approach is to simulate the formation of the fracture network under the geological and geomechanical conditions of the reservoir (Nick et al., 2011; Spence and Finch, 2014). However, due to the complexity of the geological processes, which are involved in fracture formation, a fully accurate representation is difficult to reach. All models, whether stochastic or geomechanical, can be only estimations of the actual fracture network in the reservoir, since a generic fracture network is created with characteristics aimed to be as similar as possible to the real fracture network instead of mapping the present underground conditions.

Herein, the imaging of the fracture network in the reservoir will be characterized by the induced seismicity resulting from changes in the stress field due to man-made activity like drilling, circulation and hydraulic stimulation (Maurer et al., 2020; Gaucher et al., 1998; Cuenot et al., 2008). This approach has the advantage that it provides 3D information directly about the reservoir. An implicit assumption is the spatial correlation of the seismic events with the distribution of at least some of the fluid pathways (Cornet and Scotti, 1993). To locate the induced seismicity as precisely as possible and describe their geometrical pattern is considered a promising way to image the 3D reservoir (Fehler et al., 2001). Many studies focus on the location

aspect, resulting in techniques, which allow location uncertainties as low as a few tens of meters. Those techniques include for example automatic refining of phase picking to reduce picking inconsistencies (Rowe et al., 2002), waveform cross correlation (Moriya et al., 2002; Lengliné et al., 2017) and event clustering (Phillips et al., 1997; Deichmann et al., 2014), multiplet relocation (Poupinet et al., 1985) double-difference relocation (Waldhauser, 2002; Poliannikov et al., 2013) and 4D tomography (Calò et al., 2011). Yet, despite the precise location of induced seismic events, the associated structures in the reservoir may remain unclear because the seismicity forms a rather dense spatial cloud of earthquakes, which makes individual features difficult to detect. Methods proposed to emphasize the fracture network from seismicity clouds are for example the three-point-method by Fehler et al. (1987) aiming at identifying major plane directions, the collapsing method by Jones and Stewart (1997) and the detection of structures in a point cloud by utilizing a 3D Hough transform (Sarti and Tubaro, 2002; Wang and AlRegib, 2014).

All of these methods assume that the seismicity should belong to planar structures but rely solely on the seismic event hypocenters and their location uncertainties in the case of Jones and Stewart (1997) to detect structures in the seismic cloud. However, seismic events possess other properties than just their locations such as their magnitudes and focal mechanisms, which describe the rupture geometry of the seismic source and thus can help to provide a stronger link to the geology in the reservoir and better define the fracture network. Eisner et al. (2010) used such additional information to create a discrete fracture network in a hydraulic fracturing case study in continental USA. They assigned a plane to each seismic event with an orientation derived from the source mechanism of the event and a size calculated from its seismic moment. In this work, we extend the approach of Eisner et al. (2010) by applying a probabilistic rather than a discrete approach and by including a criterion on the radius of influence of an event in addition to the hypocenter, magnitude and focal mechanism. As a consequence, a spatial probabilistic distribution of fracture planes will be associated to each event leading to a pseudo-probabilistic fracture network when all of them are jointly considered.

In the following, the new method, called pseudo-probabilistic fracture network identification (PPFN), is described in detail and its capability to detect and locate dominant structures in seismic clouds is demonstrated from synthetic datasets. On these synthetic datasets, the functionalities of the PPFN are evaluated and conclusions are drawn for the application to real-world datasets. In the next step, the PPFN is applied to the catalogue of

induced seismicity generated during the hydraulic stimulation of the well GPK2 of the enhanced geothermal site of Soultz-sous-Forêts (France). The subsequent discussion relates our results for the case study to other works, which analyzed the fracture network of the Soultz-sous-Forêts geothermal reservoir (Dezayes et al., 2004; Dezayes et al., 2010; Sausse et al., 2010) and gives recommendations for the application of the PPFN.

6.2 Pseudo probabilistic fracture network identification (PPFN)

We developed a method, which aims at detecting the spatial distribution of fractures in a seismic cloud by estimating the connectivity between any spatial position and the seismic events. The principle of the method is quite straight-forward and driven by the seismic source parameters, namely the event hypocenters, magnitudes and focal mechanism. The intrinsic assumption is that it is more likely that two events belong to the same structure when they are spatially closer than when they are farther apart. It is also assumed that the magnitude of an event is related to the size of its rupture plane and that two events whose rupture planes spatially intersect belong to the same structure. These assumptions are used to design weighting functions that assign decreasing weights with increasing distance from an event either by considering the distance from the event alone or by also taking into account their magnitudes. Both weighting schemes have a relatively similar distance weighting effect but the first one can be used in the absence of magnitude information. Lastly, the focal mechanisms of the events are used to gain information on the orientation of the structure an event originates from and thus connect events belonging to similar oriented planes. The combination of this information leads to a 3D map of weights, which shows where, in the seismic cloud, the dominant structures are located. Like all techniques based on seismic events, the method is conceptually limited to highlight only seismically active and connected structures, which may not reflect the entirety of the fracture network (Cornet and Scotti, 1993). Furthermore, the resolution of the method is limited by the location errors of the seismic events, so only structures larger than these location errors should be interpreted.
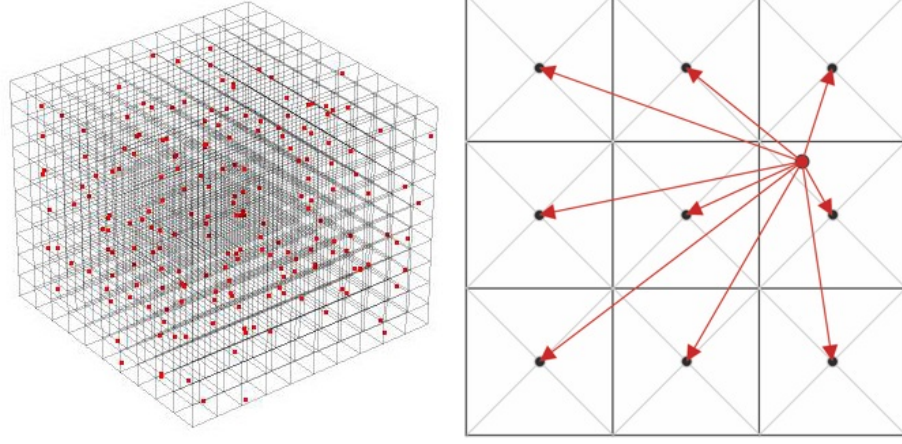
Figure 6.1 – Illustration of the first computation step of the PPFN: The area of the point cloud (red dots) is covered by a 3D grid of cubic cells (left side), then the connection vectors (red arrows) between each single point (red dot) and the center of each cell (black dots) are computed (right side).

6.2.1   Distance, magnitude and focal mechanism weighting

The first step of the methodology consists in meshing the seismic cloud volume with cubic cells. Then, the connection vector between each event and the center of each cell is calculated. The procedure is illustrated in Fig. 6.1: on the left-hand side, a hypothetic point cloud (red dots) is enclosed by a 3D mesh (in black) and on the right-hand side one sample event (red dot) and the center of each cubic cell (black dots), here in a 2D view, are connected by a vector (red arrows).

In case of the distance weighting, each cell is assigned a weight associated with each event, calculated according to a Gaussian distribution:

$$W_d = \exp\left(-\frac{d^2}{2 \cdot \sigma_d^2}\right),\tag{6.1}$$

where d is the length of the connection vector and the standard deviation σ_d a free parameter that affects the shape of the weight distribution. Equation (6.1) is comparable to a probability density function, except that it is not normalized and therefore we call this approach pseudo-probabilistic fracture network (PPFN) identification. The larger σ_d is chosen, the slower the

weighting function is declining with distance, such that events farther away from each other are connected more strongly. Thereby, it is possible to adjust the method to detect smaller or larger structures and to adapt it to geological conditions, if there is a priori knowledge about the scale of the fracture network of interest. With the weighting function for each cell, as many different values as events in the cloud are derived. All these values are then summed per cell, which gives a 3D distribution of weights W_d covering the investigated volume. Where the weights are high, the dominant structures are most likely located. In the following, the PPFN based on this weighting scheme is referred to as distance PPFN.

Other information than the inter-event distances can be included, depending on their availability. The weighting associated with the distance may be given an additional physical meaning when the size of the rupture is known. Indeed, for a given earthquake, we can consider that any cell within its source radius is fully connected and assigned these cells a weight of 1. Beyond this distance, a Gaussian-like weighting is applied similar to the distance weighting in Eq. (6.1) but with consideration of the event magnitude:

$$W_M = \exp\left(-\frac{d^2 - r^2(M)}{2 \cdot \sigma_M^2(M)}\right),$$ (6.2)

with

$$\sigma_M(M) = F \cdot r(M),$$ (6.3)

where d is again the length of the connection vector, $r(M)$ is the radius of the rupture plane of the event depending on the magnitude M and F a free parameter, which influences the shape of the curve. Thus, all cells within the radius of the rupture plane of the event are connected with certainty to the event and then the connection will be less likely or decrease as cells get farther away. Like for the distance weighting, the weights are calculated for each event and each cell and then are summed per cell to give a final 3D weight map. In the following, the weighting approach in Eq. (6.2) will be referred to as the magnitude PPFN because the magnitude will be used to estimate the source radius.

Several models could be used to estimate the earthquake source size under assumption of a circular rupture plane (Madariaga, 1976; Brune, 1970; Sato

and Hirasawa, 1973). The basic relationship in each case is:

$$r = \frac{k \cdot \beta}{f_c},$$
(6.4)

where k is a constant of different value for the different models, f_c is the corner frequency and β is the S-wave velocity. Depending on which model is used to compute the source radius, the radius of influence of an event could vary significantly, e.g. by a factor of 1.8 between Madariaga's ($k = 0.21$) and Brune's ($k = 0.37$) models. As can be seen from Eqs. (6.2) and (6.3), the source radius influences on the one hand site the range up to which a weight of 1 is assigned to a cell and on the other hand the steepness of the weighting function beyond that range. The larger the estimated radius, the larger is the area around an event that is assigned high weights. Furthermore, while Eq. (6.4) assumes a circular rupture plane, more complex slip geometry could be considered instead. Ide (2001) and Lanza et al. (1999) have shown spatial variability in the slip distribution of small earthquakes and Rubin and Gillard (2000) and Rubin (2002) found systematically elongated rupture planes along the strike direction in their studies about small aftershock events. In such cases, unilateral or bilateral Haskell (1964) models may be applied.

To calculate the source radius from the event magnitude, the corner frequency in Eq. (6.4) can be related to the magnitude of the event. However, this connection between corner frequency and magnitude is not universal and like the source rupture model should be always adapted to the seismological data under consideration. Independently from the definition of the PPFN itself, what matters is the reliability of the estimated source radius. If the confidence is low, the denominator of Eq. (6.2) could be increased to flatten the PPFN and decrease its value of information.

In the present work, we use the Soultz-sous-Forêts dataset as a case study and therefore assume the relationships between source radius, corner frequency and duration magnitude previously used for the same dataset by Charléty et al. (2007). They follow Abercrombie (1995) to relate corner frequency to source radius and consequently rely on the source rupture model of Madariaga (1976). Charléty et al. (2007) highlight a correlation between the event corner frequency f_c and its duration magnitude M_d for the Soultz dataset:

$$f_c = 35.06 - 8.20 \cdot M_d.$$
(6.5)

Using Eqs. (6.4) and (6.5), it is thus possible to estimate the event source radius r from its magnitude M_d. For the synthetic datasets we also use Madariaga's source rupture model and Eq. (6.5) to obtain the source radius, yet we also investigate how the weights calculated by the magnitude PPFN would change if we would apply Brune's model instead of Madariaga's.

The distance and the magnitude PPFN are connecting cells in all directions from the event, but the fault or fracture structure on which the event occurred is likely more or less planar. Consequently, there will be areas highlighted by high weights around the events, which are not lying in direction of the actual structure. It is now desirable to include also a directional information, to assign higher values to cells that are likely lying in the actual direction of the fault plane. This can be achieved by considering the focal mechanisms of the events if available. Again, a Gaussian-like weighting function is formulated, this time depending on the spatial angle α between the orientation of the fault plane given by the focal mechanism and the orientation of the connection vector between the event and each cell:

$$W_f = \exp\left(-\frac{\alpha^2}{2 \cdot \sigma_f^2}\right), \qquad (6.6)$$

where σ_f, the standard deviation, is a free parameter that affects the shape of the probability distribution and should be at least equal to the uncertainty of the focal plane orientation in degrees. To calculate the angle α, first the normal vector on the fault plane given by the focal mechanism is computed. Then the angle β between this normal vector and the connection vector between event and cell is calculated via the scalar product and then $\alpha = 90° - \beta$. By applying the directional weighting, cells along the rupture plane of an event are assigned higher weights than the others.

For a given event, the distance-/magnitude-weighting is direction independent and the focal mechanism-weighting is distance independent. These two types of information can be combined to constrain the areas of high weights around the events in size as well as orientation. This can be achieved by multiplying the distance PPFN/magnitude PPFN with the focal mechanism PPFN to assign each cell a weight reflecting distance and directional information. Once this multiplication is done, the results for all events are again summed for each cell to obtain the final PPFN map.

6.2.2   Normalization of the PPFN

In a last step, the weights resulting from the application of Eqs. (6.1), (6.2) or (6.6) are normalized to enable comparison of different PPFN results and to make them more meaningful. Specifically, after normalization, cells that show the presence of a fault should have weights larger than zero to allow easy identification. The PPFN is based on the concept that weights are higher in areas with expected faults than in areas where the events are randomly distributed. If the events would be randomly distributed among the whole area the cloud covers, the weights for the cells should be smaller than if a fault would be present. This can lead to the following inequalities:

$$\frac{W}{W_s} > \frac{W_r + \text{SF}}{W_{rs}} \quad \text{or} \quad \frac{W \cdot W_{rs}}{W_s} > W_r + \text{SF} \,, \tag{6.7}$$

where W is the weight of each cell after applying the PPFN to the actual dataset, W_s the sum of W over all cells, W_r the mean weight of each cell after applying the PPFN to 100 random datasets W_{rs} the sum of W_r over all cells and SF a scaling factor to account for variations in the randomly distributed point clouds.

Therefore, normalization can be performed by subtracting the term on the right hand side of Eq. (6.7) from the term on the left hand side, meaning the background noise resulting from randomly distributed events is removed, leaving only increased weights due to the presence of a fault:

$$W_n = \frac{W \cdot W_{rs}}{W_s} - W_r - \text{SF} \,. \tag{6.8}$$

Then, cells with $W_n > 0$ are expected to belong to faults. To calculate W_r and W_{rs}, the PPFN is applied to 100 random datasets and the mean weight of these 100 datasets is calculated for each cell. To design these random datasets, the volume of the actual event cloud is divided into cubes and the same amount of points per cube is randomly distributed in each cube, with the overall number of points being the same as the number of seismic events in the actual cloud. In case the number of points cannot be distributed evenly on the cubes, the remaining points are distributed again randomly among the cubes. The size of the cubes has to be small enough to approximate the shape of the actual seismic cloud but not too small to prevent from having many

(empty) cells that would unnecessarily increase the computation time. The PPFNs for 100 of these randomly distributed point clouds are calculated and then averaged, resulting in the value W_r. We chose a number of 100 datasets to ensure the distribution is not dominated by accidental accumulation of events in single random datasets. Higher numbers can be used to further mitigate this effect but the higher the number of datasets, the longer the computation time.

The scaling factor SF in Eq. (6.8) has to be high enough to account for fluctuations in the weight distribution over the cells for randomly distributed point clouds due to random accumulation of points in certain areas or the overall shape of the cloud. If the normalized PPFN is applied to a random dataset, Eq. (6.8) should only result in weights smaller than zero because no faults are present. Therefore it must be:

$$\text{SF} > \frac{W \cdot W_{rs}}{W_s} - W_r \qquad (6.9)$$

and SF can be determined by the following procedure: the PPFNs for the 100 random point clouds are calculated and normalized according to Eq. (6.8) with SF = 0. The weights for each of the resulting PPFNs will naturally vary and to capture the maximum weight produced by the random noise the maximum weight among all the weights is taken from each of the 100 resulting normalized PPFNs. Then the distribution of these maximum weights for the 100 random point clouds is calculated. This distribution represents the maximum noise, which is still present after normalizing a random distribution of points and therefore a value, which has to be additionally subtracted from the PPFN for the actual dataset. The factor SF is calculated from this distribution as:

$$\text{SF} = W_{mr} + D \cdot s_{mr} \,, \qquad (6.10)$$

with W_{mr} the mean of the distribution of maximum weights after the normalization of the 100 random point clouds, s_{mr} the standard deviation of this distribution and D a factor to weight the standard deviation, here chosen to be $D = 5$. At last, after the normalization of the actual dataset, every weight value larger than zero indicates an area where a preferred structure is located.

6.3 Assessment of the PPFN on synthetic datasets

6.3.1 Synthetic datasets

Three sets of synthetic datasets are created to confirm that the PPFN is working as intended and to test the influence of the parameters σ_d for the distance PPFN and F for the magnitude PPFN. The synthetic datasets do not have the purpose to simulate real seismicity clouds, they are merely designed to be sufficient to evaluate whether the methods work technically as expected. For this purpose, a simple geometry is favorable because it is more robust to design errors, easy to manipulate and leads to clear results easy to verify.

The datasets consist each of 500 points distributed randomly within a sphere of 1000 m radius, except for a subset of points distributed on one or two rectangles assumed to represent fault planes. The point cloud is placed in a 3D Cartesian coordinate system, with the three axis defined to represent northing, easting and depth (with 0/0/0 being the uppermost, southernmost and westernmost corner) to be consistent with the description of the orientation of geological fault planes in real-world settings. Dataset 1 contains one rectangle of length 1000 m and width 500 m located in the middle of the cloud and orientated 45°/180° (dip/dip direction), meaning the plane is dipping 45° to the south, having a E-W strike. Out of the 500 points, this rectangle is defined by 100 points in dataset 1a, by 50 points in dataset 1b and by 25 points in dataset 1c. Dataset 2 contains two parallel rectangles close to opposite margins of the cloud (Fig. 6.2) of length 500 m and width 250 m and are both orientated 45°/180°. They are each defined by 50 of the 500 points for dataset 2a, 25 points for dataset 2b and 15 points for dataset 2c. Finally, dataset 3 has the same characteristics as dataset 2, but the rectangles are orthogonal, orientated 45°/180° and 45°/270°. The characteristics of the synthetic datasets are summarized in Tab. 6.1.

Testing magnitude and focal mechanism PPFN requires to artificially assign a magnitude and a focal mechanism to each event of the clouds. The magnitudes are simulated by real numbers, with one decimal, between 0 and 2.5 following a distribution according to the Gutenberg-Richter magnitude-frequency power law with a generic b-value of 1, and are randomly assigned to the points. The value of 2.5 is chosen here because this is the maxi-
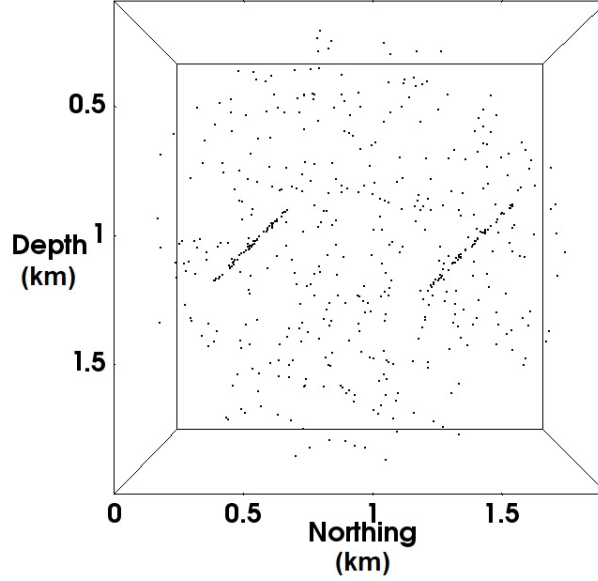
Figure 6.2 – Synthetic dataset 2a: Spheric cloud of 1 km radius consisting of 400 randomly distributed points and two rectangles of size 500 mx250 m oriented 45/180 (dip/dip direction) consisting of 50 points each.

mum magnitude for the real dataset of the hydraulic stimulation of GPK2 in the Soultz reservoir that is later used to apply the PPFN to a field case. Higher values for the magnitudes could be chosen, there is no theoretical limit in the method. To simulate the focal mechanisms random orientations are assigned to all points except the points on the planes, which are assigned the orientation of the plane they are forming. We test the PPFN first for all synthetic datasets using the distance- and magnitude-weighting only and then we combine distance and magnitude PPFN with the focal mechanism-weighting. The size of the cubic cells of the grid when meshing the cloud volume should be chosen according to the location error of the events in the seismic cloud. For the application of the PPFN to the synthetic cases, a cube side of 50 m is used because 50 m is the average location error of the events in the GPK2 seismic dataset, so this will be also the grid resolution we use for the applied case.

6.3.2   Application of the PPFN to the synthetic datasets

The scaling free parameters σ_d, F and σ_f are playing a central role when applying the PPFN. They determine the shape of the Gaussian weighting

Table 6.1 – Characteristics of the three groups of synthetic datasets for the evaluation of the PPFN.

Group	Size (length (m) x width (m)); Orientation (dip/dip direction in degree)	Set	Number of events per plane/ total number of events
Group 1: 1 plane	1000 x 500; 45/180	1a 1b 1c 1d	100/500 50/500 25/500 15/500
Group 2: 2 parallel planes	Plane 1: 500 × 250; 45/180 Plane 2: 500 × 250; 45/180	2a 2b 2c	50x2/500 25x2/500 15x2/500
Group 3: 2 orthogonal planes	Plane 1: 500 × 250; 45/180 Plane 2: 500 × 250; 45/270	3a 3b 3c	50x2/500 25x2/500 15x2/500

functions and therefore how many points may connect. Since it is the goal to connect the points on each plane but not too many points beyond, it is sensible to relate the choice of σ_d and F to the size of the plane that has to be detected. Since the distance and magnitude weightings connect points in all directions, we choose as reference length for the Gaussian distributions half the size of the larger dimension of the plane, which is in our test cases also the size of the smaller dimension of the plane. In the following, three cases are tested. For the distance weighting, σ_d is chosen to be 1/2 length, 1/4 length and 1/6 length of the larger dimension of the plane, which means for dataset 1 $\sigma_d = 500$ m, 250 m and 125 m and for the datasets 2 and 3 $\sigma_d = 250$ m, 125 m and 83 m. For the magnitude weighting, the distribution depends not only on the parameter F but also on the magnitude of the event (see Eq. (6.3)). To still relate the weighting to the size of the plane, the scaling free parameter F is calibrated for the mean magnitude of the events, so that $\sigma_M(\overline{M}) = 1/2$ length, 1/4 length or 1/6 length of the larger dimension of the plane. For events with magnitudes smaller than the mean magnitude, the weighting function will decline steeper whereas for events with magnitudes larger than the mean magnitude, the weighting function will be flatter. Yet, as discussed in the previous section, for the magnitude PPFN next to the parameter F also the choice of the source rupture model can influence the weighting function. However, due to the calibration of F such that $\sigma_M(\overline{M})$
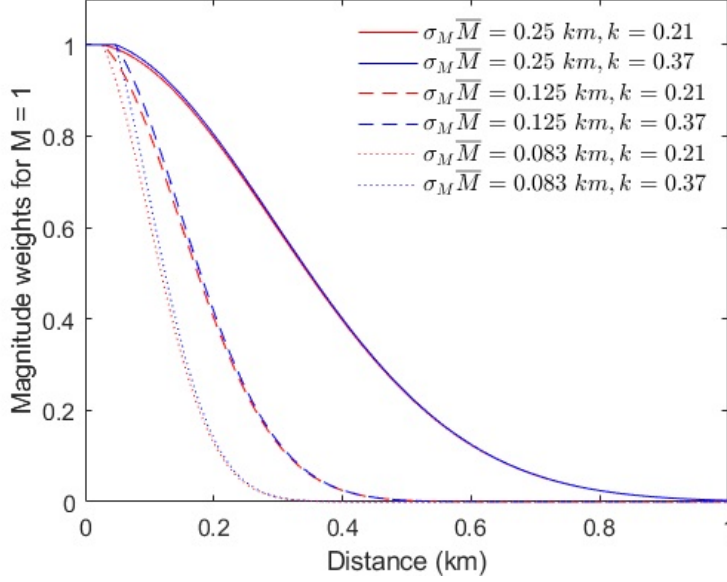
Figure 6.3 – Influence of σ_M and k on the weighting function: Red: weighting functions for k = 0.21 (Madariaga, 1976), blue: weighting functions for k = 0.37 (Brune, 1970), straight line: $\sigma_M(\overline{M}) = 250$ m, dashed line: $\sigma_M(\overline{M}) = 125$ m, dotted line: $\sigma_M(\overline{M}) = 83$ m. Weighting functions are shown for an event with magnitude 1.

is a fixed value related to the fault size, F also becomes dependent on r and in return $\sigma_M(M)$ becomes independent of k. Therefore, k only determines the cut-off point but not the shape of the weighting function, giving it as a whole a rather minor influence as shown for an event of magnitude 1 in Fig. 6.3. In the following, therefore k is fixed to 0.21 according to the model of Madariaga (1976) and in agreement with the Soultz case study performed in the next chapter. To quantify the performance of the different values for σ_d and $\sigma_M(\overline{M})$, the center of mass, the orientation derived from principal component analysis and the dimensions of the detected structures are computed and compared with the actual features of the planes.

The results of the application of the distance and magnitude PPFN for dataset 2a are presented in Fig. 6.4. The two planes dipping 45° south are made visible by weights larger than zero. Figure 6.4 shows, as color distribution, the PPFN for $\sigma_d = 250$ m and $\sigma_M(\overline{M}) = 250$ m and the thresholds of positive weights for $\sigma_d = 250$ m, $\sigma_d = 125$ m and $\sigma_d = 83$ m and $\sigma_M(\overline{M}) = 250$ m, $\sigma_M(\overline{M}) = 125$ m, $\sigma_M(\overline{M}) = 83$ m. The planes themselves are plotted as white rectangles. It becomes apparent that the higher

σ_d and $\sigma_M(\overline{M})$ are chosen, the larger is the area of positive weights around the planes. Consequently, it is more difficult to precisely determine size and orientation of the plane for high values of σ_d and $\sigma_M(\overline{M})$. For $\sigma_d = 250$ m and $\sigma_M(\overline{M}) = 250$ m the deviation of the determined dip from the dip of the designed rectangle is $6°$ and $8°$ respectively for one of the planes, the deviation of the dip direction $25°$ and $38°$. For $\sigma_d = 83$ m and $\sigma_M(\overline{M}) = 83$ m on the other hand, the deviation of the dip for this plane is about $1°$ for both, distance and magnitude PPFN, and of the deviation of the dip direction close to $0°$. The size of the same plane has been determined to be 640 m/ 650 m/600 m (length/width/height) for $\sigma_d = 250$ m and 600 m/550 m/600 m for $\sigma_M(\overline{M}) = 250$ m. For $\sigma_d = 83$ m and $\sigma_M(\overline{M}) = 83$ m the dimensions of the structure could be determined much more precisely but might be slightly underestimated with length/width/height being 420 m/350 m/210 m for both weighting methods. Appendix B Tab. B.1 summarizes the characteristics of the detected structures for quantification of the results.

The results for the magnitude and the distance weighting are very similar. The differences between the two weighting functions, which lie in the fact that the cells inside the radius of the rupture plane are assigned a weight of 1 and that the decline of weights with distance also depends on the magnitude not only on the scaling factor for the magnitude weighting, has only a minor influence. This is due to the fact that the assigned magnitudes are rather small. Even for the highest magnitude of 2.5, the radius is only 147 m. At this distance, the distance weight is still 0.84 for $\sigma_d = 250$ m.

In the next step, the distance- and magnitude-PPFN are combined with the focal mechanism PPFN to test whether adding directional information can improve the identification of planar structures. For σ_f, we chose the value $5°$ to be very restrictive on the directional weighting, since we assume that the orientation of the rupture plane is known from the focal mechanism and we want to heavily take it into account. The results for the combination of magnitude and focal mechanism PPFN are shown in Fig. 6.5 for $\sigma_M(\overline{M}) = 250$ m and $\sigma_M(\overline{M}) = 83$ m. The PPFNs are shown as color distributions cut at the zero threshold. It can be seen that the orientation of the planes becomes much more obvious now compared to the distance/magnitude PPFN alone, but for $\sigma_d = 250$ m and $\sigma_M(\overline{M}) = 250$ m the size of the planes is highly overestimated. This is confirmed by a quantification of the results (Appendix B Tab. B.1): The combination with focal mechanism weighting leads to a deviation in dip of not more than $1°$ and in dip direction of not more than $2°$ from the actual orientation all values of σ_d and $\sigma_M(\overline{M})$ considered. On the other hand, for $\sigma_d = 250$ m and $\sigma_M(\overline{M}) = 250$ m, plane
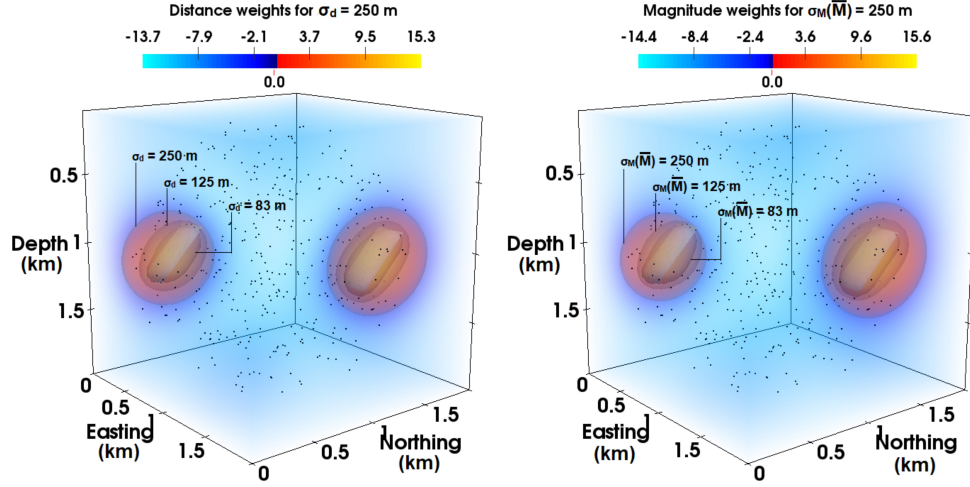
Figure 6.4 − Distance and Magnitude PPFN applied to the dataset 2a:Left: Distance PPFN, right: Magnitude PPFN. The color map shows the weight distribution for σ_d and $\sigma_M(\overline{M}) = 250$ m, the synthetic fault planes are plotted in white. The thresholds for W_d and $W_M = 0$ are plotted as contours for σ_d and $\sigma_M(\overline{M}) = 250$ m, σ_d and $\sigma_M(\overline{M}) = 125$ m, σ_d and $\sigma_M(\overline{M}) = 83$ m.

dimensions are overestimated in length more than 2 times and in width even up to nearly 4 times. Only the height of the structures is better constrained now compared to the distance/magnitude PPFN alone, letting the structures better be recognized as planar features. The overestimation of length and width of the planes leads also to an imprecise determination of the center up to nearly 200 m away from the real center.

The application of the different weighting methods on the synthetic datasets 3a and 1a leads to the same conclusions as for dataset 2a. The results for σ_d and $\sigma_M(\overline{M}) = 83$ m combined with the focal mechanism weighting are overall the most precise considering the combination of position, size and orientation of the planes. For the higher values of σ_d and $\sigma_M(\overline{M})$, the dimensions of the planes are overestimated and much more when the focal mechanism weighting is combined with the distance/magnitude weighting. The center of the planes can be determined quite precisely with distance/magnitude weighting alone but the orientation cannot be determined reliably. When combined with the focal mechanism weighting, it is the other way round: The orientation can be determined precisely but the size and center of the structures may be way of from those of the actual planes.

When applied to the datasets 1b, 2b and 3b and the datasets 1c, 2c
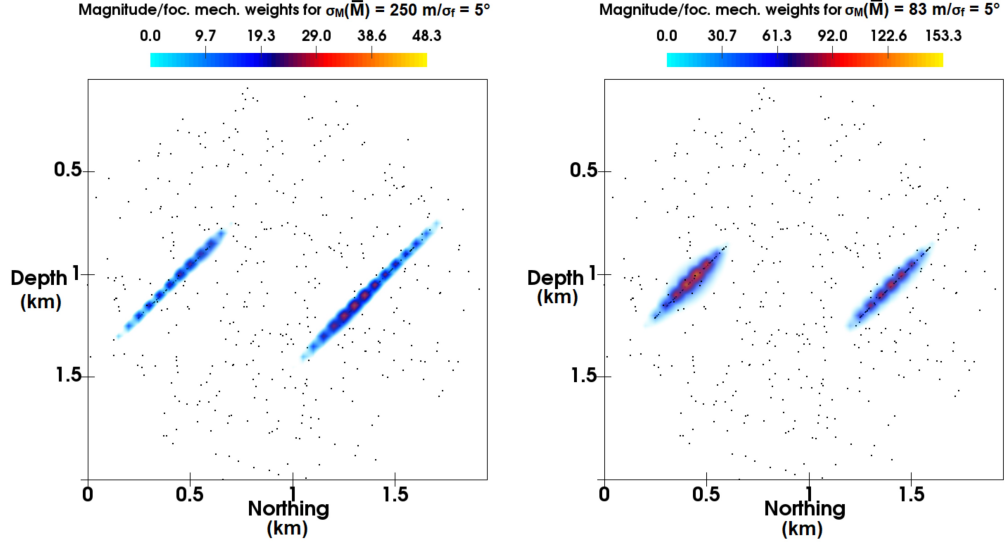
Figure 6.5 – Magnitude combined with focal mechanism PPFN applied to dataset 2a: The color maps show the weight distribution above the threshold weight of $W_{M/f} = 0$ for the combined magnitude and focal mechanism PPFN with the parameters $\sigma_M(\overline{M}) = 250$ m and $\sigma_f = 5°$ on the left and with the parameters $\sigma_M(\overline{M}) = 83$ m and $\sigma_f = 5°$ on the right.

and 3c a second effect becomes clear: when the point density on the planes is getting lower only areas of the plane with a locally higher point density are highlighted, especially for small values of σ_d and $\sigma_M(\overline{M})$. This can be seen in Fig. 6.6 for datasets 1a, 1b and 1c with the combined magnitude and focal mechanism weighting for $\sigma_M(\overline{M}) = 83$ m. The actual plane is outlined by the black rectangle, the zero weight threshold for dataset 1a as pale yellow, for dataset 1b as orange and for dataset 1c as red shape. In such cases with low point density the best results, that is with center, dimensions and orientation closest to the actual planes, are achieved by the combined distance/magnitude and focal mechanism weighting for σ_d and $\sigma_M(\overline{M}) = 250$ m. For the datasets 2c and 3c and $\sigma_d = 83$ m, only one of the planes can be detected at all, at this low point density (15 points per plane) the detection capacity of the method is reached.
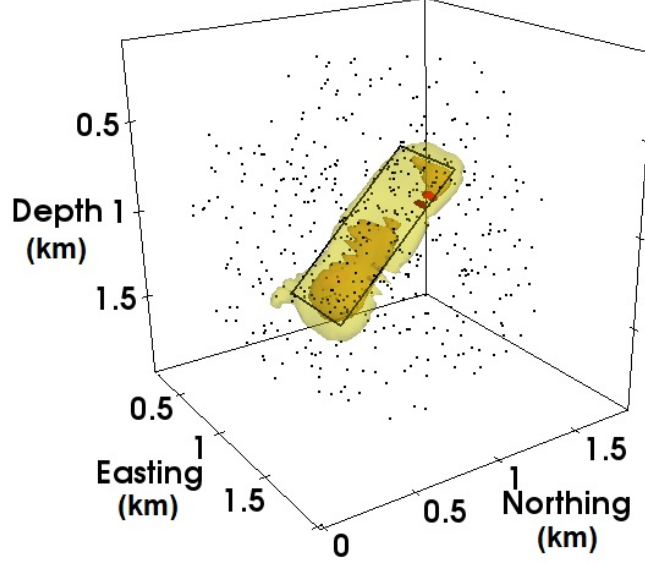
Figure 6.6 − Magnitude combined with focal mechanism PPFN for datasets 1a, 1b and 1c: Black outline: predefined size of the synthetic fault plane of the datasets 1a,b,c; light yellow shape: $W_{M/f} = 0$ threshold for the combined magnitude and focal mechanism PPFN with $\sigma_M(\overline{M}) = 83$ m and $\sigma_f = 5°$ applied to dataset 1a (100 points on the plane); orange shape: $W_{M/f} = 0$ threshold for the same parameters applied to dataset 1b (50 points on the plane); red shapes: $W_{M/f} = 0$ threshold for the same parameters applied to dataset 1c (25 points on the plane).

6.3.3 Influence of uncertainties on the focal mechanism and random choice between nodal planes

To take into account the focal mechanisms of seismic events, we first designed a case where all events on a plane have focal mechanisms oriented exactly like this plane. For σ_f a low value of 5° was chosen, which would correspond to an assumed uncertainty of the orientation of the focal mechanism of 5°. This ideal scenario was chosen to highlight the differences between the use of only distance related information, i.e. distance and magnitude PPFN, and the combined use of distance and directional information. It was demonstrated that the consideration of focal mechanism can lead to a more precise determination of the fault plane orientation. However, in reality, the determination of focal mechanism is a complex process and the quality of the results may be lower because of sparse or not ideally distributed seismic stations or high noise on the seismic signals. Furthermore, additional information like inde-

pendent estimations of the stress field or dominating fracture orientations are necessary to discriminate the fault plane from the auxiliary plane (Schoenball et al., 2014). If no such additional information are available, both nodal planes are equally likely to represent the fault plane.

To test the influence of higher uncertainty of the focal mechanisms we distributed dip and direction for the events on the planes (according to a Gaussian distribution) with a mean equal to the orientation of the plane and a standard deviation of 5°, 10° and 20° respectively. We chose σ_f to be 5°, 10° and 20° accordingly, so that the weighting function for the focal mechanism PPFN reflects the uncertainty on the focal mechanism. The results are shown in Fig. 6.7, left column, for the combined magnitude and focal mechanism PPFN for $\sigma_M(\overline{M}) = 250$ m applied to dataset 2a. In a second step, we chose randomly between the two nodal planes for all three cases (focal mechanism uncertainties and σ_f of 5°, 10° and 20°) to reflect the situation when no additional information to choose the fault plane are available. The results are shown in Fig. 6.7, right column, for the combined magnitude and focal mechanism PPFN for $\sigma_M(\overline{M}) = 250$ m applied to dataset 2a. The quantification of the results shown in Fig. 6.7 is summarized in Appendix B, Tab. B.2.

It can be seen that an increase of the uncertainty of the focal mechanisms by 5° or 10° can lead to less overestimating length and width of the planes compared to the ideal focal mechanisms that are oriented exactly like the planes. For the ideal focal mechanisms the length of the two planes is overestimated partly more than twice, width even up to four times. For uncertainties of 5° and 10°, the size of the planes is still overestimated but with a range of 640 m to 810 m for the length and 600 m to 800 m for the width not as strongly as for the ideal focal mechanism. This effect, that the size of the plane is better restrained for slightly larger uncertainties in the focal mechanisms, is due to the interaction of the magnitude and the focal mechanism PPFN. The smaller σ_f is chosen and the more the orientations of all the points on the plane are aligned, the stronger is the focal mechanism PPFN focused in one direction and dominates the shape of the area of high weights in the whole grid. Therewith, high weights are assigned to cells relatively far away from the plane as long as they are aligned with the orientation of that plane, despite the influence of the magnitude weighting that should restrict high weights to the close surrounding of the planes. When the orientation of the focal mechanisms on the planes vary and σ_f is chosen larger, the concentration of the focal mechanism PPFN in one direction decreases and is restricted by the magnitude PPFN to cells closer to the plane. So, for
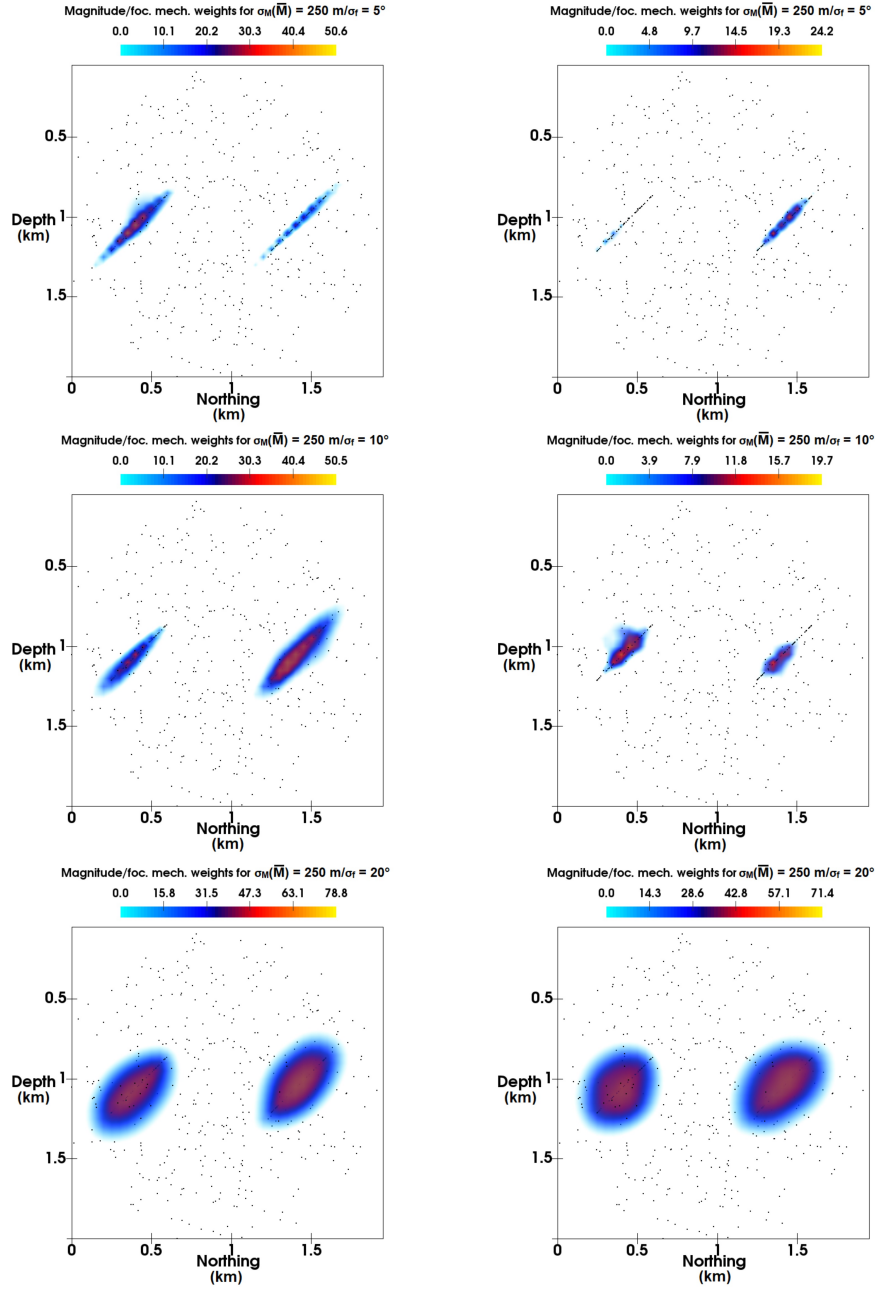
Figure 6.7 – Combined magnitude and focal mechanism PPFN for $\sigma_M(\overline{M}) = 250$ m and different values of σ_f and with and without random choice of the nodal plane: Left column: always correct nodal plane is used, right column: orientation is chosen randomly between the two nodal planes. Top row: $\sigma_f = 5°$, middle row: $\sigma_f = 10°$, bottom row: $\sigma_f = 20°$.

a small uncertainty on the focal mechanisms, the effects of the directional weighting and the distance/magnitude weighting are more balanced than for a perfect alignment of the focal mechanism. When the uncertainty of the focal mechanism is increased to 20°, the reverse effect can be observed: The magnitude PPFN starts to dominate the shape of the area of high weights around the plane because the focal mechanism PPFN is spreading too much and especially the height (dimension perpendicular to the plane) of the structure becomes less constrained (Fig. 6.7). For a random distribution of focal mechanism on the planes, the focal mechanism PPFN would add no additional information to the distance/magnitude PPFN. For very high values of σ_f, the combined directional and distance PPFN would therefor become similar to the distance/magnitude PPFN alone.

In a second step, we chose randomly between fault plane and auxiliary plane keeping all other parameters as described above. For an uncertainty of 5°, one of the planes can be barely detected and for an uncertainty of 10°, only part of both planes is highlighted (Fig. 6.7). Only few cells on these planes show values larger than zero after normalization, leading to an underestimation of the length of the planes. For an uncertainty of 20° on the other hand, both planes are clearly identified albeit with a near-circular shape around them that leads to an imprecise determination of the plane orientation. This shows again that the combined magnitude and focal mechanism PPFN is dominated by the directional weighting for low uncertainties and low values of σ_f and by the magnitude weighting for high uncertainties and values of σ_f. In the first case, the two strong but contradicting preferred orientations lead to a cancellation effect even though the magnitude PPFN alone can identify the plane. For $\sigma_f = 20°$ however, the directional information becomes so diffuse that it only slightly influences the shape of the area of high weights around the planes compared to the magnitude PPFN alone.

To summarize, a variation of the orientation of the focal mechanisms on the planes by 5° to 10° and the corresponding choice of σ_f does not lead to an overall drop in performance of the PPFN. While the orientation of the planes may be determined with slightly less precision length and width of the planes are less overestimated than with ideal focal mechanisms because the alignment in one direction is not so strong. When the variation becomes higher, the influence of the focal mechanism PPFN becomes less pronounced and the results similar to the magnitude PPFN alone. When the choice between the two nodal planes is random, this can lead, for low values of σ_f, to the effect that the two strong perpendicular orientations cancel each other out and that the planes cannot be clearly identified. For large values of σ_f,

this effect again decreases and the result gets closer to the one produced by the magnitude PPFN alone. We also tested the different values of σ_f and the random choice between the nodal planes for $\sigma_M(\overline{M}) = 83$ m. Qualitatively, similar effects like with $\sigma_M(\overline{M}) = 250$ m can be observed although much less pronounced. Since for $\sigma_M(\overline{M}) = 83$ m, the results of the magnitude weighting alone and with combination of the focal mechanism PPFN with ideal focal mechanism are already similar, adding uncertainty or choosing randomly between the nodal planes has only a minor influence.

6.3.4   Conclusions on the synthetic datasets

It has to be kept in mind, that the setting in the synthetic datasets is rather unnatural. The planes are clearly separated from each other, while in a real fracture network, the planes may intersect each other and have changing orientations, which will make the detection more difficult.

Yet, the results for the synthetic datasets are promising. The distance and magnitude weighting lead to the identification of a PPFN, which is in good agreement with the actual planes present in our synthetic cases. The precision with which the center, the dimensions and the orientation of the planes can be determined depends on the parameter setting. The combination with a focal mechanism weighting leads to a more precise determination of the orientation of the planes but can lead to an overestimation of their dimensions. The choice of the parameters σ_d and F depends on the size of the plane and the density of points on the plane. In any case, σ_d and $\sigma_M(\overline{M})$ should be smaller than the size of the plane to prevent from connecting points outside the plane and consequently overestimate the plane size. For high point density on the plane, low values of σ_d and $\sigma_M(\overline{M})$, in the range of 1/6 dimension of the plane, lead to relatively precise results whereas for low point densities higher values, in the range of half the plane dimension, should be chosen to connect a sufficient amount of points to detect the plane. Also, σ_d and $\sigma_M(\overline{M})$ should be chosen at least as large as the cell size of the grid and therewith the location error, since smaller distances cannot be resolved by the PPFN anyway. For the focal mechanism PPFN, σ_f should be chosen according to the uncertainties of the focal mechanism. If there are large uncertainties of more than 10° on the focal mechanisms, the focal mechanism PPFN likely brings no additional asset to the magnitude/distance PPFN. The choice of the wrong nodal plane could lead to the effect that a structure is not detected unless the associated uncertainties are large.

The PPFN derived from magnitude weighting is designed to connect events with overlapping rupture area and then to decline at larger distances depending on the magnitude itself and the parameter F. For the current synthetic dataset and the choice of $\sigma_d = \sigma_M(\overline{M}) = 1/2$, $1/4$ and $1/6$ length of the plane, the magnitude weighting leads to a quite similar PPFN like the distance weighting. However, in a real application, the dimension of the faults is probably not known. The advantage of the magnitude weighting in this case is that a priory information about the fracture size is available from the relation between magnitude and size of the rupture plane. The magnitude can therefore give an indication of the minimum size of the fractures. Based on that assumption, an alternative approach for the magnitude weighting would be to not assume a fracture size at all to set the parameter F. Since $\sigma_M(M)$ is directly related to the radius r(M) of the rupture plane anyway (Eq. (6.3)), F could be seen as factor to set the multiples of r(M) with which the weighting should decline. For F = 0, there would be a clear cut after the radius is reached, assigning each cell within the radius a weight of 1 and each cell outside a weight of 0. However, since the radii are minimum estimates of the fault size, it seems reasonable to choose F in a way that cells outside the radius but still close are assigned a value larger than 0. For example, F = 1/2 would mean that the cells closer than r(M) are connected to the event for sure but cells in a distance of 1.5 r(M) would still lie in the 1σ-range of the weighting function and thus get relatively strongly connected to the event. Given the rather small magnitudes of the present datasets, this approach would lead to a very steep decline of the weighting function, which has the advantage that the fault size will not be overestimated and a detailed layout of the fracture distribution can be potentially highlighted if the event density is high enough. On the other hand, if the event density is low, this approach will not be suitable to detect the faults as indicated for the synthetic datasets with low point densities on the planes and small values for $\sigma_M(M)$. This second approach of applying the magnitude weighting will be tested for different values of F directly on the real dataset of the GPK2 seismic cloud, which is a very dense seismic cloud and therewith suitable for this approach.

6.4 Application of the PPFN to the seismicity induced during the stimulation of GPK2, Soultz-sous-Forêts

6.4.1 The Soultz-sous-Forêts geothermal site

After evaluating the PPFN on synthetic datasets, the method will be applied on a well-known real dataset to discuss the value of the techniques. For this purpose, the induced seismicity cloud recorded during the hydraulic stimulation of the well GPK2 of the Soultz-sous-Forêts deep geothermal reservoir is chosen. The Soultz-sous-Forêts geothermal site is located in the Upper Rhine Valley in Alsace, France, and is one of the most studied enhanced geothermal systems worldwide (Genter et al., 2010). It consists of four main wells, GPK1 with a depth of 3.6 km and GPK2, GPK3 and GPK4 reaching nearly 5 km depth. All wells have been stimulated to enhance their injectivity/productivity by developing the naturally present fracture network (Schill et al., 2017).

During the years, a huge amount of data has been collected on the Soultz reservoir, so the conditions there are well known compared to other geothermal systems. The granitic basement that hosts the deep reservoir is covered by a 1.4 km sedimentary section and can be roughly divided into two different units along the wells. Down to about 4.5 km depth a grey porphyritic monzo-granite is dominating, below a grey, fine-grained two-mica granite (Genter et al., 2000; Hooijkaas et al., 2006). The granitic basement is penetrated by individual small scale fractures scattered pervasively throughout the granite but also by larger fault zones of highly clustered fractures, which extend from several tens to several hundred meters or even a few kilometers. These fracture arrangements have been studied by analyzing drill-cores and well-logs (Dezayes et al., 2004; Dezayes et al., 2010). Additionally, vertical seismic profiles (Sausse et al., 2010) and induced seismicity (Evans et al., 2005a; Cuenot et al., 2008; Dorbath et al., 2009) have been studied to image at least the major structures farther from the wells. Sausse et al. (2010) created a 3D structural model of the reservoir to visualize the spatial distribution of the fault zones by combining all available information. We will use their work later, in the discussion part, to evaluate our own findings.

6.4.2 Seismicity induced during the hydraulic stimulation of GPK2

For this study, the seismicity induced during the hydraulic stimulation of the well GPK2 in June-July 2000, described in detail in Cuenot et al. (2008) is used. During the 6 days of stimulation, a total volume of $23,400\text{m}^3$ water was injected in three steps: 30 L/s for 24 h, 40 L/s for 27 h and 50 L/s for 90 h (Weidler et al., 2002). The operation was monitored by a seismic network consisting of five downhole stations and four permanent as well as 14 temporary surface stations deployed around the geothermal site. The recorded seismicity was processed and is described by Cuenot et al. (2008). The resulting dataset consists of 7215 located seismic events with a maximum moment magnitude MW of 2.5. The hypocenter locations were recomputed by Calò et al. (2011), in the course of a 4D tomographic inversion, resulting in location errors of about $+/-30$ m horizontally and $+/-50$ m vertically. This dataset is in the following referred to as the large dataset. Additionally, focal mechanisms have been computed by Schoenball et al. (2012) for a subset of the large dataset (Cuenot et al., 2008) that was used in the study of Dorbath et al. (2009) containing 715 events with MW > 1, in the following referred to as the small dataset. Figure 6.8 shows both seismic clouds, where the large dataset is represented in black and the small dataset in red.

The choice of the nodal plane, which is assumed to be the fault plane, is described in Schoenball et al. (2014). It is based on a combination of two types of information: the orientation of fractures in the reservoir measured from well-logs and a hydromechanical constraint associated with injection pressure during stimulation. With both, Schoenball et al. (2014) estimated a probability for each nodal plane to be the fault plane. The focal mechanism catalogue contains the nodal planes with the higher probability to be the fault plane. Figure 6.9 shows the distribution of the orientations of the focal mechanisms on a stereoplot presented on a brown-scale from light-brown for a 50% probability to black for a 100% probability that the chosen nodal plane is the fault plane. It can be seen that the orientations can be divided into two sets: one scattered over SSW to NW orientations dipping 40° to 90° and the other one over NNE to SE orientations and dip values between 40° and 90°. However, the second set shows a concentration between 30° and 90° dip direction and 50° and 70° dip. While two sets of preferred orientations can be seen, the orientations are spread over a relatively wide range, which might impede their usefulness for the focal mechanism PPFN.
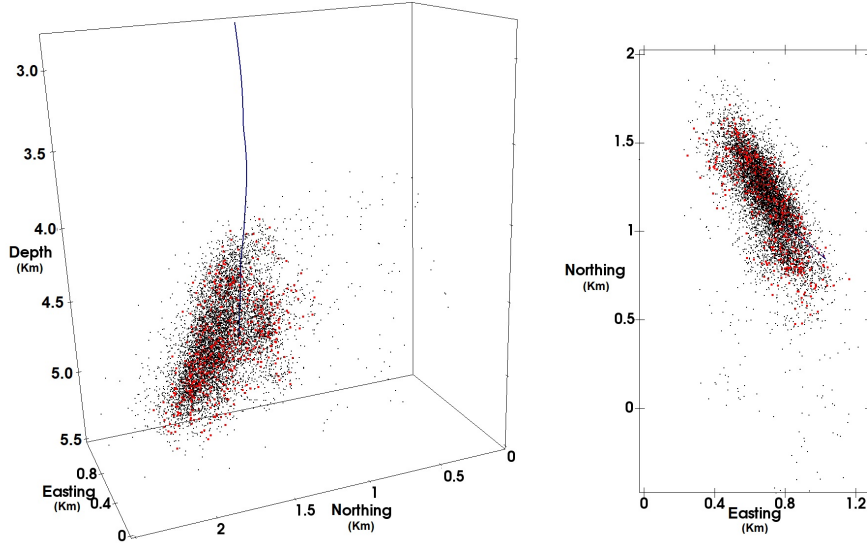
Figure 6.8 – Cloud of seismic events induced during hydraulic stimulation of GPK2, Soultz-sous-Forêts: Black dots: 7215 seismic events forming the large dataset; red dots: 715 seismic events with magnitude larger than 1 forming the small dataset; black line: wellpath GPK2. Left: 3D view of the seismic cloud. Right: Map view of the seismic cloud.

To apply the distance PPFN to the GPK2 datasets, we have to assume a fault size to make a sensible parameter choice for σ_d. As reference, we take the fracture model of the Soultz reservoir by Sausse et al. (2010) who estimate a typical fault size of 300 m for the majority of the faults. Like for the synthetic case, the distance PPFN is applied to the large and the small dataset with $\sigma_d = 1/6$, $1/4$ and $1/2$ of the fault size, giving $\sigma_d = 50$ m, 75 m and 150 m. For the small dataset, the same approach is used for the magnitude PPFN, so $\sigma_M(\overline{M}) = \sigma_d$. The large dataset has a very high event density, which makes it a promising candidate for the application of the magnitude PPFN without assuming any prior fault size and only starting from the size of the rupture plane given by the magnitudes themselves. To test again a range of parameters, the magnitude PPFN is applied with F = 1/2, F = 1 and F = 2, meaning the standard deviation of the weighting function beyond the cells within the radius itself is half the radius, the radius or two times the radius of the fracture plane.

For the small dataset, focal mechanisms are available, so the combined distance and focal mechanism PPFN and the combined magnitude and focal mechanism PPFN are applied. For the application of the focal mechanism PPFN, we consider the probabilities for the focal mechanisms to represent
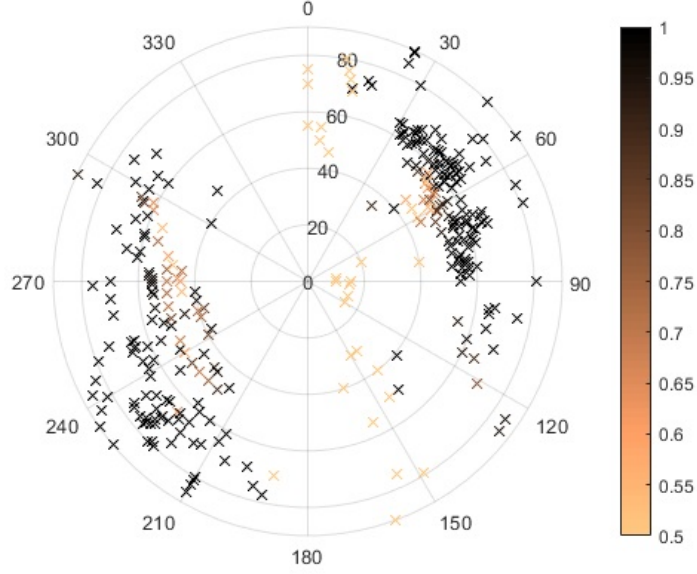
Figure 6.9 – Stereoplot of the focal mechanism of the small GPK2 dataset: Dip is 0° at the center and 90° at the outer most circle, Dip direction ranges from 0° (North) over 90° (East), 180° (South), 270° (West) back to 0° around the circle. Each focal mechanism is shown as a cross in a brown shade between light brown and black according to the probability that this orientation is the correct nodal plane (light brown: 50%, black: 100%). Focal mechanisms adopted from Schoenball et al. (2014))

the fault plane given by Schoenball et al. (2014) by multiplying the focal mechanism PPFN with a scaled factor ranging from 0 for a probability of 50% to 1 for a probability of 100%. Therewith, focal mechanisms with low probability are not or very weakly considered contrarily to high-probability focal mechanisms. For σ_f, we chose a value of 5° because the uncertainty of the focal mechanism is given to be 4.05° by Schoenball et al. (2014). The size of the grid cells is chosen to be 50x50x50 m^3 to reflect the size of the location error.

6.4.3 Application of the PPFN on the GPK2 seismic cloud

Before applying the PPFN, we remove events from the datasets, which are sparsely distributed. To do so, when meshing the seismic cloud with cubic

cells of 100 m side length, all events falling in cubes with less than a specified amount of events are discarded from the analysis. For the large dataset, 3 events are chosen as the threshold, for the small dataset, 2. Following this is a pre-processing step, the finer mesh (50 m side length) is generated to calculate the PPFN. This data filtering prevents from having many close to empty cells in the final PPFN mesh, which would unnecessarily slow down the computation process and make the normalization unstable.

The distance PPFN applied to the large dataset shows that the highest weights are concentrated in the deeper-northern part of the event cloud. The detected fault structure is dipping steeply towards WSW. Figure 6.10 (top) shows the contour at the $W_d = 0$ threshold for $\sigma_d = 50$ m, 75 m and 150 m and the color map for $\sigma_d = 50$ m. Like for the synthetic datasets, the area of high weights is the smallest for the smallest value of σ_d (50 m) and the largest for the largest value of σ_d (150 m). In fact, for $\sigma_d = 150$ m nearly the whole cloud is included in the $W_d = 0$ threshold. For $\sigma_d = 50$ m, the PPFN is more differentiated than for the higher values of σ_d, showing that in the lower northern part, the area of weights above $W_d = 0$ is forming a narrow ellipsoid that becomes wider towards the upper southern part while the values of W_d become lower. The overall orientation of this deformed ellipsoid is 83°/249° (dip/dip direction).

The magnitude PPFN, which was applied without a-priori assumption on the fault size, is in this case more suitable than the distance PPFN to distinguish different features in the cloud. While the results for F = 2 are similar to the distance weighting with $\sigma_d = 50$ m, for F = 1 and F = 1/2, smaller features of high weights emerge from the volume already highlighted by the distance PPFN. Figure 6.10 (bottom) shows the results for the magnitude PPFN as contour at the threshold for $W_M = 0$ for all values of F and as color map for F = 1/2. For F = 1, the main structure with the highest weights in the deeper northern part splits into two sup-structures with lower weights in the southern part of the cloud. For F = 1/2, only the upper of this two sub-structures is connected as a narrower branch to the deep main part while the lower one only contains small, isolated areas of high weights exceeding the $W_M = 0$ threshold.

To better see the strike of the structure and the changes in depth, Fig. 6.11 (bottom) displays three depth sections of the magnitude PPFN for F = 1/2 as color map and the distance PPFN for $\sigma_d = 50$ m as contour at the $W_d = 0$ threshold. The position of the depth slices is indicated in Fig. 6.11 (top), they are lying in 4900 m, 5150 m and 5350 m depth. The up-
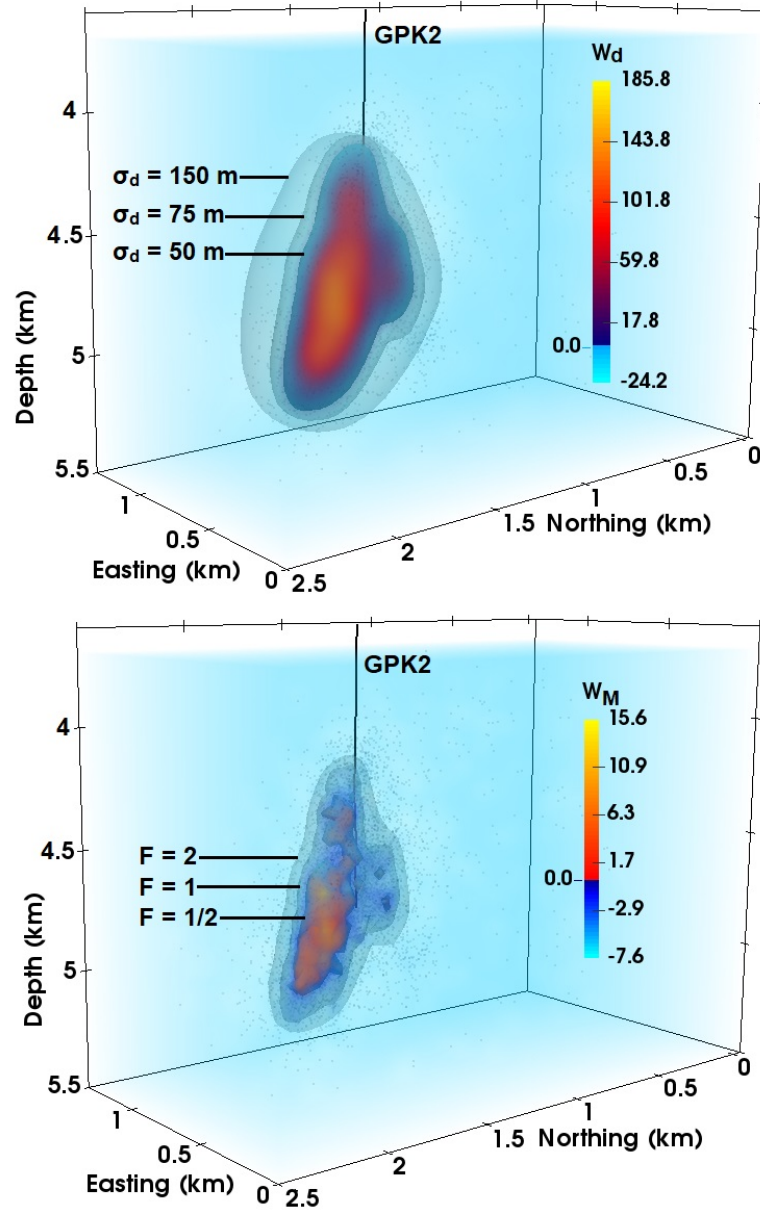
Figure 6.10 – Distance PPFN (top) and magnitude PPFN (bottom) applied to the large GPK2 dataset for varying values of σ_d and F: Top: Distance PPFN for $\sigma_d = 50$ m as color map and contour for the $W_d = 0$ threshold, distance PPFN for $\sigma_d = 75$ m as contour for $W_d = 0$ and distance PPFN for $\sigma_d = 150$ m as contour for $W_d = 0$. Bottom: Magnitude PPFN for F $= 1/2$ as color map and contour for $W_d = 0$, magnitude PPFN for F $= 1$ as contour for $W_d = 0$ and magnitude PPFN for F $= 2$ as contour for $W_d = 0$. Wellpath GPK2 as black line.

permost section shows that in the upper part, the fault highlighted by the PPFN is striking NW-SE with the northwestern part directly at the well GPK2. In the second depth section, the fault stretches farther north and south and is oriented more NNW-SSE. While the distance PPFN shows a continuous contour, the magnitude PPFN shows several small, disconnected patches aligned in the NNW-SSE strike. The deepest section shows for the distance PPFN approximately the same size and extension of the fault as in the middle section. For the magnitude PPFN, a large area in the northern part is highlighted while the southern part is not marked as part of the fault. The cross sections confirm that there is a main fault stretching from the upper southern to the lower northern part of the seismic cloud getting more pronounced in the lower part. In the middle section of the magnitude PPFN, there is an isolated area in the south, which may be a substructure of the main fault.

The results obtained for the small dataset are similar to the large one. Since the seismic cloud is much less dense, the magnitude PPFN was applied with $\sigma_M(\overline{M}) = \sigma_d = 50$ m, 75 m and 150 m. Like for the synthetic datasets, the results are quite similar for both weighting approaches. The results for the magnitude PPFN are shown in Fig. 6.12 (left), as contours for all parameters at the $W_M = 0$ threshold and as color map for $\sigma_M(\overline{M}) = 50$ m. The distance PPFN and the magnitude PPFN are producing an asymmetric ellipsoid of high weights in the deeper-northern part of the cloud for $\sigma_M(\overline{M}) = \sigma_d = 50$ m with an orientation of 83°/248°, very much like for the large dataset. Like for the large dataset, the shallower southern part of the cloud is also highlighted by elevated weights, but here, this area is detached from the main structure in the northern part. For $\sigma_M(\overline{M}) = 75$ m, the two areas get connected and a second area in the lower southern part gets highlighted and connected to the main structure. For $\sigma_M(\overline{M}) = 150$ m, the ellipsoid around the main structure gets larger and encloses the whole lower part of the cloud, yet, unlikely for the large dataset, not the upper part.

Since there are focal mechanisms available for the small dataset, the distance and the magnitude PPFN are now combined with the focal mechanism PPFN for the same values of σ_d and $\sigma_M(\overline{M})$ as before. To take into account the difficulty to distinguish between the two nodal planes, before combining the distance/magnitude PPFN with the focal mechanism PPFN, the latter is multiplied with an additional weighting according to the probability given by Schoenball et al. (2014) that the selected nodal plane is indeed the fault plane (as explained earlier). In both cases, the joint PPFN shows different results than for the distance and magnitude PPFN alone, but the results with and
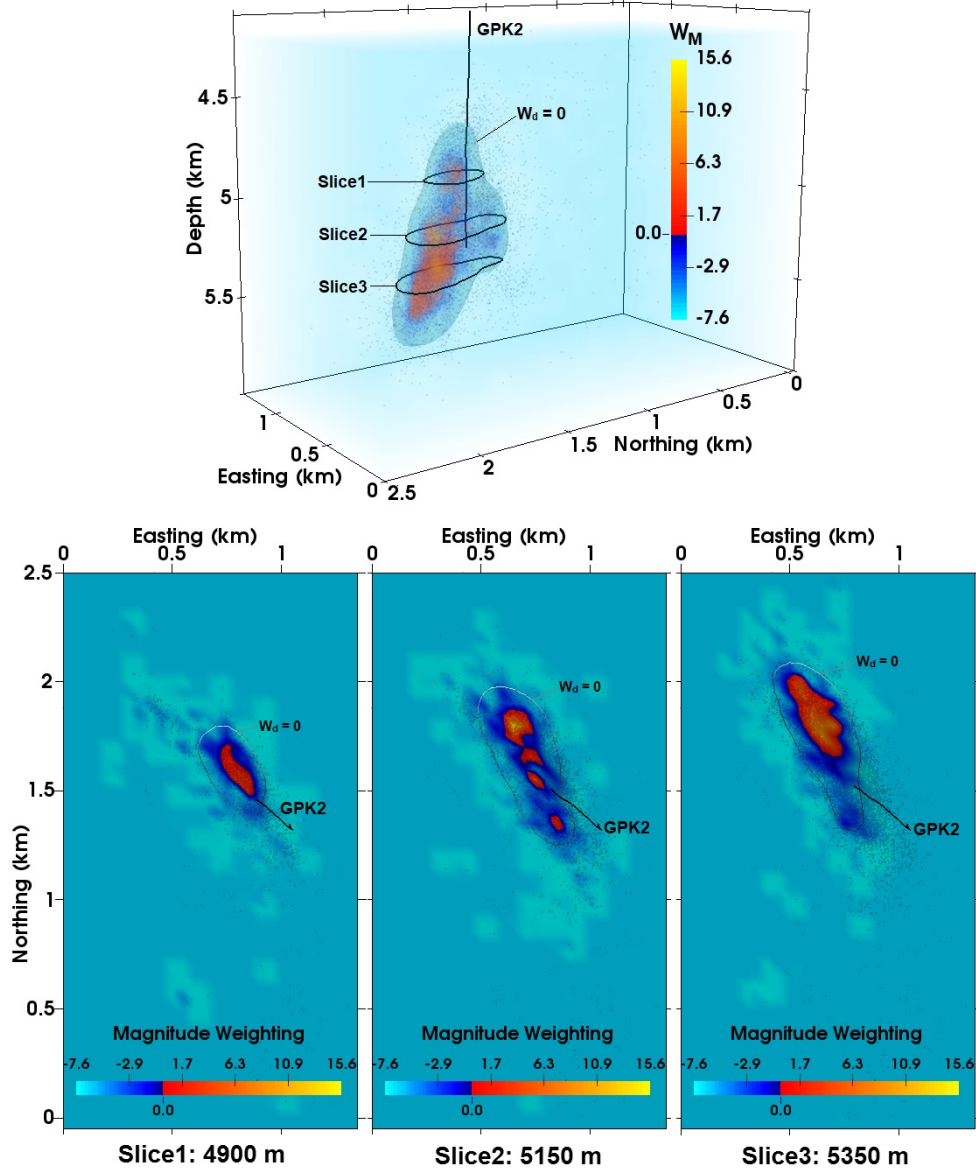
Figure 6.11 − Distance and Magnitude PPFN applied to the large dataset of the GPK2 seismic cloud: The color map shows the weights for the magnitude PPFN applied with F = 1/2; The distance PPFN with $\sigma_d = 50$ m is shown as contour for the $W_d = 0$ threshold. Black dots: seismic events, black line: wellpath GPK2. Top: 3D view, the three black outlines around the contour indicate the depths of the slices in the bottom. Bottom: Three slices at different depth sections indicated in the 3D view.
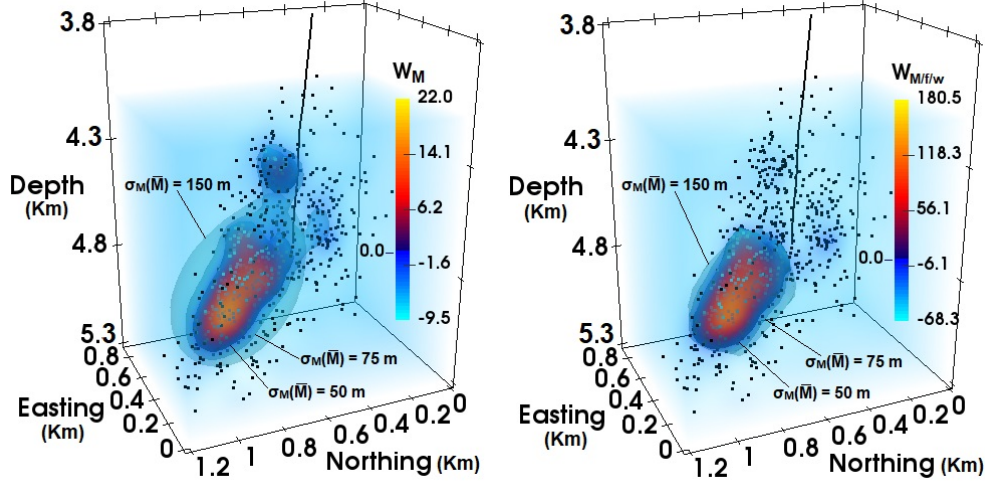
Figure 6.12 – Magnitude PPFN and combined magnitude-focal mechanism PPFN with additional weighting according to the probability that the chosen nodal plane is the fault plane applied to the small dataset of the GPK2 seismic cloud: Left: The color map shows the weight distribution for the magnitude PPFN with $\sigma_M(\overline{M}) = 50$ m and the contours above the threshold value $W_d = 0$ for $\sigma_M(\overline{M}) = 50$m, 75 m and 150 m. Right: Combined magnitude and focal mechanism PPFN with additional nodal plane weighting for different values for $\sigma_M(\overline{M})$: The color map shows the weight distribution for $\sigma_M(\overline{M}) = 50$ m, The $W_d = 0$ threshold is shown as contour for $\sigma_M(\overline{M}) = 50$ m, $\sigma_M(\overline{M}) = 75$ m and $\sigma_M(\overline{M}) = 150$ m.

without the additional probability weighting of the focal mechanism PPFN are very much the same. The orientation of the ellipsoid of high weights in the deeper-northern part of the cloud has changed slightly compared to the distance/magnitude PPFN alone to 87°/247°. Moreover, the area in the southern part of the cloud is now not highlighted any more. The results are presented for the combined magnitude and focal mechanism PPFN including the additional weighting for the focal plane probability in Fig. 6.12 (right) for all values of $\sigma_M(\overline{M})$ (50 m, 75 m and 150 m) as contour at the $W_{M/f/W} = 0$ threshold and for $\sigma_M(\overline{M}) = 50$ m as color map. It can be seen that again the area of high weights is the largest for $\sigma_M(\overline{M}) = 150$ m, but here the effect is not as pronounced as for the large dataset.

6.5   Discussion

6.5.1   Evaluation of the PPFN from the results obtained for synthetic and real datasets

The PPFN uses event locations, inter-event distances, magnitudes and focal mechanism to determine the spatial distribution of fracture networks in seismic clouds. Applied to synthetic datasets, the PPFN showed promising results: location, size and orientation of rectangles representing fault planes placed in a random point cloud have been successfully identified. However, it became apparent that the choice of the weighting method and the scaling free parameters σ_d and F have a strong influence on the results and have to be chosen carefully and appropriately for the specific case and scientific question. Focal mechanisms should be considered only when the uncertainties are relatively low, otherwise the focal mechanism PPFN brings no additional constraint to the distance/magnitude PPFN. Furthermore, only focal mechanisms with relatively certain fault plane should be considered because the use of the wrong nodal plane could reduce the detection capability of the method. For the application on the two datasets of the GPK2 seismic cloud, different values for σ_d and $\sigma_M(\overline{M})$ were tested and the results from the synthetic datasets could be confirmed: the larger σ_d and $\sigma_M(\overline{M})$ are chosen, the larger get the areas of weights above the $W = 0$ threshold until nearly the entire point cloud is included. The smaller the values, the more differentiated the area becomes. The synthetic as well as the applied case therefore highlight the influence of the weighting-scheme and parameter choice.

When the magnitude PPFN is applied like the distance PPFN by assuming a fault size and choosing the parameters σ_d and $\sigma_M(\overline{M})$ accordingly both weighting methods yield to very similar results. The distance PPFN and the magnitude PPFN calibrated to an a priori assumed fracture size can connect events, which are farther away from each other and therefore detect large, primary structures. Here, the parameters σ_d and $\sigma_M(\overline{M})$ should be chosen smaller than the desired investigation length of structures in the range of half the investigation length for sparse clouds and 1/6 of the investigation length for dense clouds. Although the real extent of the faults activated during the stimulation of GPK2 is unknown, we consider $\sigma_d = \sigma_M(\overline{M}) = 50$ m as the most reasonable parameter choice for the following reasons: the synthetic cases show that especially for a high event density it is more likely to overestimate than to underestimate the size of the structures, therefore

small values for σ_d and $\sigma_M(\overline{M})$ should be preferred. The study of Sausse et al. (2010) gives for most faults in the Soultz reservoir a size of about 300 m. This gives a starting point for the parameter choice, leading to σ_d and $\sigma_M(\overline{M}) = 50$ m since 50 m would be $1/6$ of the fault size. Smaller values should not be chosen because the location error and therewith the mesh size of 50 m imposes a limit to the resolution. Tests with larger values have not resulted in useful information since just the whole inner part of the cloud is detected as fault.

Another approach for the magnitude PPFN is to start from the size of the rupture plane given by the magnitude itself. In this case the magnitude PPFN is far more restricted to the direct surrounding of an event than the distance PPFN. In this second case, mainly events with overlapping rupture planes get connected and hence requires either a very dense event cloud or high magnitudes to work as intended. For such a case, quite detailed structures in the cloud potentially get visible. For the large GPK2 seismic cloud, which is quite local and dense, the distance PPFN with $\sigma_d = 50$ m already connected so many events, that only one large ellipsoidal structure could be identified. Therefore, we applied the magnitude PPFN with F = $1/2$, 1 and 2. For F = 2, the results are similar to the distance weighting with $\sigma_d = 0.05$ but the magnitude PPFN applied with F = $1/2$, while highlighting overall a similar area, reveals more details of the inner structure of the fault.

The application of the PPFN to the seismic cloud of the GPK2 hydraulic stimulation, with the parameters we consider the best for this case ($\sigma_d = \sigma_M(\overline{M}) = 50$ m for the small dataset, $\sigma_d = 50$ m and F = $1/2$ for the large dataset), revealed a major structure in the lower-northern part of the cloud, which steeply dips WSW, and a less prominent feature in the southern part of the cloud. For the large dataset and the distance PPFN, these two features are connected with each other and form one large, deformed ellipsoid, narrow in the north and getting wider towards south. For the magnitude PPFN, the structure forms one slim branch from the upper south to the lower north and a few small, disconnected patches in the lower southern part of the ellipsoid. For the small dataset, the main structure in the lower northern part is separated from the southern upper part. So, while the results are overall consistent, the structures detected in the seismic cloud are more or less pronounced, connected or separated from each other and varying in size, shape and slightly in orientation. This may be because the different features are part of a larger structure, which is differentiated into several sub-structures, depending on the chosen parameters.

Including directional information in the form of focal mechanism greatly enhanced the results for the synthetic datasets regarding the orientation of the planes and reducing the dimension orthogonal to the plane. For the GPK2 small dataset, including the focal mechanism PPFN slightly changed the orientation of the main structure. Additionally, the southern structure was not highlighted anymore. This may indicate that the seismic cloud there presents a large variability of rupture plane orientations as defined by the focal mechanisms and cannot enhance a preferred direction. The distribution of the focal mechanism in Fig. 6.9 shows a relative high dispersion in their orientation. Additionally, the orientation of the main structure is dipping steeply WSW while the highest concentration of focal mechanisms is ENE with intermediate dip. As shown for the synthetic case for the random choice of nodal plane, a mismatch in the orientation of the fault plane and the focal mechanisms can lead to the effect that the fault is not detected anymore.

Another parameter, which controls the detection capability of the PPFN besides the weighting scheme, is the cube size of the grid that is used to mesh the area of the seismic cloud. The cube size sets a lower limit to the resolution of fault structures by the PPFN approach. It should be chosen according to the uncertainty of the event hypocenters, for this study: 50 m. This means that the precision of the PPFN can be enhanced by using event locations with low uncertainties as input, which can be obtained e.g. by double difference relocation techniques or clustering analysis.

6.5.2 Comparison with other studies

In a final step, we compare these results with previous investigations on the fracture and fault networks in the Soultz-sous-Forêts geothermal reservoir. The orientation of fractures and fault zones is well known in the vicinity of the wells due to the analysis of drill-cores, BHTV and UBI logs (Dezayes et al., 2004; Dezayes et al., 2010). Unfortunately, for GPK2 UBI-logs are not available beneath a depth of 3800 m. Yet, since the orientations of fractures in the granite are relatively consistent in the other wells, it can be assumed that they are similar in GPK2 as well (Dezayes et al., 2004). Overall, the reservoir granite is dominated by two conjugated fracture sets. These fracture sets have an average orientation of N170°E varying mostly from N160°E to N180°E with nearly vertical dips to the east and to the west (Dezayes et al., 2004; Dezayes et al., 2010). The distribution of fracture orientation with depth shows that the eastward dip direction is more prominent in the upper

part of the granite, the westward dip direction in the lower part (Dezayes et al., 2004). These observations come from the analysis of mesoscale fractures scattered throughout the granite (Dezayes et al., 2004; Dezayes et al., 2010). Yet, the granite is also crossed by fracture zones, where the fractures are locally very concentrated over 0.5 to 60 m thickness intervals (Dezayes et al., 2010). In GPK2, Dezayes et al. (2010) identified eight such fracture zones by the analysis of temperature- and flow-logs, four of them in the depth interval relevant to our study. Unfortunately, their orientation has not been determined because of the missing UBI-log. All wells considered, the fracture zones in the granite have an average orientation of N160°±15°E and are dipping westward with angles steeper than 60° (Dezayes et al., 2010). Hence, the mean orientation of the fracture zones fits perfectly the orientation of the major structure obtained with the PPFN, which is dipping $83 - 87°$ in a $247 - 249°$ dip direction.

Sausse et al. (2010) combined the fracture zones detected by Dezayes et al. (2010) from well logs with VSP-data and induced seismicity analysis to gain a 3D fracture model of the Soultz-sous-Forêts geothermal reservoir. To compare their model with our results, only the part of the reservoir relevant to our study is described, which contains five known fracture zones. The fracture zone GPK3-FZ4770 has been observed in GPK3 at 4775 m measured depth and is supposed to fit with the fracture zone GPK2-FZ3900 observed in GPK2 at 3900 m measured depth. The orientation of GPK3-FZ4770 has been measured to be 64°/234°, whereas the orientation of GPK2-FZ3900 could not be measured and is therefore assigned the same orientation by Dezayes et al. (2010). Sausse et al. (2010) corrected the orientation of GPK3-FZ4770 to 71°/234° by fitting the plane to some major seismic events from the GPK3 stimulation. They assigned the fault zone a minimum radius of 3 km. Additionally, Dezayes et al. (2010) detected three deep fault zones crossing GPK2 at 4760 m, 4890 m and 5060 m measured depth, whose orientations could not be measured and were assigned a generic orientation of 65°/250° by the authors. Sausse et al. (2010) assigned these fracture zones radii of 400 m, 300 m and 400 m respectively. These three planes, GPK2-FZ3900 and GPK3-FZ4770 are plotted in Fig. 6.13 as green and grey planes together with our results from the distance PPFN for $\sigma_d = 0.05$ as contour at the $W_d = 0$ threshold and from the magnitude PPFN for F = 1/2 as color map applied to the large dataset. They are shown as 3D view as well as sections in the same three depth intervals like used in Fig. 6.11.

To include in their model information in addition to the fracture zones derived from well-logs, Sausse et al. (2010) performed a clustering analysis
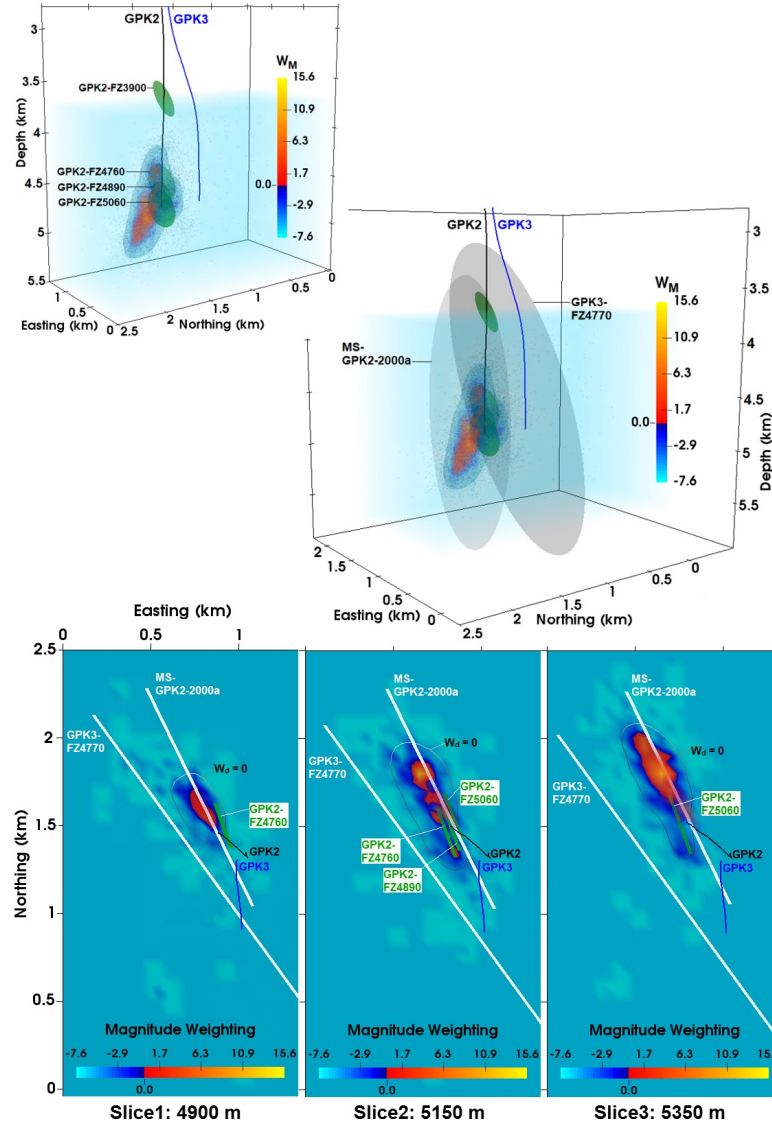
Figure 6.13 – Magnitude PPFN and distance PPFN applied to the large dataset of the GPK2 seismic cloud and fracture zones intersecting GPK2: Top left: Magnitude PPFN with F = 1/2 as color map, distance PPFN for $\sigma_d = 50$m as contour at the $W_d = 0$ threshold and 4 fracture zones from flow logs as green planes. Middle right: best fitting plane MS-GPK2-2000a from cluster analysis performed by Sausse et al. (2010) of the seismic cloud as grey plane added and fracture zone GPK3-FZ4770 as large grey plane added. Bottom: three slices at the same depth sections as in Fig. 6.11, fault planes as green and white lines. Black dots: seismic events, black line: wellpath GPK2; blue line: wellpath GPK3. Position, orientation and size of the fracture planes from Sausse et al. (2010)

on 718 events of the GPK2 seismic cloud with magnitudes larger than 1 with 3D regular grid (voxet) functions available in the GOCAD software. They detected two clusters. The larger cluster contains the majority of the seismic events and its corresponding major plane, also plotted in Fig. 6.13, is oriented 86°/244°. This is in good agreement with the orientation of $83° - 87°/247° - 249°$ we determined with the PPFN for the major structure in the lower-northern part of the seismic cloud. Sausse et al. (2010) propose that the seismic clusters they detected belong to the huge fault zone, which is observed as GPK3-FZ4770 in GPK3 and as GPK2-FZ3900 in GPK2. However, especially the depth sections in Fig. 6.13 (bottom) show that this structure crosses the GPK2 seismic cloud rather peripheral. Of cause, it may well be that the orientation of the fault does not remain constant between the two wells. A curved shape of the structure with steeper and more westward dip in the deep part of GPK2 would be necessary for the fault zone to go through the main part of the GPK2 seismic cloud, intersect GPK2 at 3900 m and GPK3 at 4775 m measured depth.

On the other hand, the three smaller fracture zones that cross GPK2 at 4760 m, 4890 m and 5060 m measured depth fall in the depth range where the GPK2 seismic cloud is the closest to the well. These three structures plotted as green planes in Fig. 6.13 fit quite well the southern part of the seismic cloud in orientation and position. Since their size is only restrained by flow anomalies and the distance to the neighboring wells (Sausse et al., 2010) it may well be possible that one, two or all of these fracture zones extend farther north and downwards in the main area of the seismic cloud and become more seismically active. They would then fit with the steeply westward dipping main structure we detected with the PPFN.

6.6 Conclusion

We proposed a new method to visualize faults in an induced seismicity cloud as 3D pseudo-probabilistic fracture networks. Herewith, not only event locations but also inter-event distances, magnitudes and focal mechanisms can be included in the reservoir characterization. These parameters provide a link with the physical rupture characteristics supporting the events. Tests on synthetic datasets showed the potential of the PPFN: it works well to identify size, orientation and location of planes in a point cloud if there is a sufficient fracture density and if the scaling parameters are chosen in accordance with the scale of investigation. With the distance PPFN, large structures can be

identified in clouds with low event density, with the magnitude PPFN detailed structures in dense clouds. The focal mechanism PPFN additionally brings consistency between the network and the rupture plane orientations, hence offers the perspective to carry out analyses consistent with geomechanical information. The application of the different PPFNs to the two GPK2 datasets gave an overview of the main features in the seismic cloud, which consist of a dominating connected structure in the deeper northern part of the cloud and a secondary feature located in the upper southern part, which may be connected to the northern main structure. The main fault structure in the lower-northern part of the cloud also coincides with a major seismic cluster detected by Sausse et al. (2010) from the GPK2 seismic cloud with a clustering analysis.

Acknowledgments

Part III

Closing Section

Chapter 7

Conclusion and Perspectives

7.1 Conclusion

Reservoir stimulation operations in enhanced geothermal systems are usually accompanied by induced seismicity (Breede et al., 2013). These reservoirs are predominantly located in fractured rocks where matrix porosity only plays a minor role for reservoir permeability. The main pathways for fluid flow are fault zones, which comprise of highly clustered small scale fractures (Vidal and Genter, 2018). The seismicity induced during stimulation operations is an expression of the reaction of such fault zones to the injection of fluids. The increased pore pressure disturbs the stress state in the reservoir and leads to rock failure mostly on favorably oriented pre-existing faults (Cornet et al., 2007). Other effects may also contribute to rock failure but pore pressure increase is usually the dominating effect during reservoir stimulation in enhanced geothermal systems (Gaucher et al., 2015a). Due to the fact that induced seismicity originates from slipping faults, it can be used as an imaging tool to highlight such seismogenic faults in the reservoir and to deduce their mechanical state (e.g. Lengliné et al., 2017). Induced seismicity can also help to understand how different stimulation set-ups influence the reservoir and in return to design stimulation schemes to mitigate especially large magnitude events. This is of key importance since induced seismicity is still a major concern in the development of deep geothermal systems as contributors to the green energy mix.

In this thesis, two concepts of fault network characterization from in-

duced seismicity analysis and their application to two different EGS sites in the URG have been presented. The first study focuses on applying an optimized workflow consisting of template matching detection, relative relocation and waveform clustering analysis to obtain a comprehensive seismic catalogue for a thorough reservoir interpretation (Chapter 5). The procedure has been applied to the stimulation sequence of thermal, chemical and hydraulic stimulation of the well GRT1 of the Rittershoffen reservoir and has proven to be effective to highlight the fault network and give insight into geomechanical processes in the reservoir. The interpretation of the obtained catalogue led to a better understanding of the effects the different stimulation steps had on the fault network and new insights on how reservoir stimulation can effect the reservoir beyond the initially targeted fault.

The comparison with the study of Maurer et al. (2020) highlights the importance of the application of advanced processing for a detailed as well as reliable reservoir interpretation. In comparison to the seismic catalogue obtained by STA/LTA detection (Maurer et al., 2020) the newly generated catalogue by template matching detection contains thrice as many events. This allowed for a more precise analysis of the temporal development of the induced seismicity and especially for a more exact determination of the onset of seismicity. This is of major importance for determining the rock failure criterion and revealed a major drop of cohesion on the fault between seismicity onset during thermal and hydraulic stimulation on the same fault. The application of relative relocation compared to absolute event locations gave a much clearer view on the geometry of the fault network. It revealed two spatially separated seismogenic fault segments between which aseismic stress transfer took place at the end of the hydraulic stimulation, triggering delayed seismicity on the second fault segment four days after shut-in. The performed clustering analysis allowed to draw the conclusion that the processes behind the induced seismicity seem to be similar during thermal and hydraulic stimulation since the same waveform clusters were activated during both stimulations. The delayed seismicity on the other hand showed very distinct waveforms, suggesting a different fault activation mechanism and confirming the hypothesis that seismicity during the delayed interval is rather triggered than induced. This shows that aseismic stress transfer can lead to unexpected seismicity on structures that may not have been targeted originally. All these conclusions could not be drawn from the STA/LTA generated catalogue with absolute locations of Maurer et al. (2020). Without a comprehensive database, meaningful interpretation of the induced seismicity is seriously impeded and may even produce misleading results.

This also suggests that it could be worthwhile to apply template matching detection as a real-time monitoring tool during the development of geothermal reservoirs instead of STA/LTA detection, which is mostly used to date. Vasterling et al. (2017) implemented a real-time cross-correlation detector as a SeisComP3 module, however, it is currently not routinely applied for reservoir monitoring. The results from the Rittershoffen study show that many additional information can be gained from template matching detection especially when coupled with relative relocation. This would allow the operators to adapt their stimulation schedules more precisely to the situation in the reservoir and could give earlier warning of a potential seismic risk. One difficulty when implementing template matching for real time detection is the needed template database. In case of the algorithm of Vasterling et al. (2017), initial template events are needed before the template matching detection can be applied. They demonstrated the capability of template matching for real time detection on the induced seismicity of the geothermal reservoirs Landau and Insheim with one template for each of the reservoirs. An alternative approach would be to couple the template matching directly to STA/LTA detection to obtain a subsequently updated template database. A potential drawback could be that, if the template database becomes too large, this could slow down the detection to a point were it could not be considered real-time anymore. Considering the pay-off of a much more comprehensive view on the induced seismicity the route of template matching for real-time detection should be pursuit further.

The second study in this thesis shows a possible way to go forward if the above described procedure does not lead to conclusive results and the fracture network geometry remains unclear despite precise event locations (Chapter 6). This can happen when the seismic cloud has a rather compact, dense shape instead of being aligned in planar features like for the stimulation of the well GPK2 of the Soultz-sous-Forêts reservoir in 2000 (Cuenot et al., 2008). The reason for this may be that the induced seismicity is generated from a complex, widely distributed network of mesoscale fractures instead of one dominating fault zone. However, it is still likely that such a network has an internal structure and that one or several structures are majorly responsible for the induced seismicity. The PPFN is a new pseudo-probabilistic method developed to uncover this internal structure from the seismic cloud and has proven to be successful on synthetic datasets as well as the GPK2 seismic cloud.

Contrarily to other methods used for fracture network identification from seismic clouds (e.g. Jones and Stewart, 1997), the PPFN uses not only event

locations but also magnitudes and focal mechanisms to derive a 3D map of weights in the area covered by the seismic cloud. High weights indicate where the dominant seismogenic structures are located within the cloud. The PPFN works well to identify planes in a synthetic point cloud but the result depends highly on the choice of the parameters for the weighting functions. They should be chosen appropriately for the approximate fracture size in the reservoir, otherwise the size of structures might be highly overestimated. In the Soultz-case, the reservoir was already thoroughly studied, therefore this information on the approximate fracture size was available. The PPFN was able to detect a dominating structure in the deeper northern part of the cloud and a secondary feature located in the upper southern part, which may be connected to the northern main structure. This is in agreement with previous studies on the reservoir (Sausse et al., 2010).

Besides the possibility to directly combine distance and directional information in the PPFN and therewith to keep a close link to the earthquake source characteristics, another unique feature of the PPFN is its probabilistic character. Other methods give one specific proposal for the fracture network, maybe with an error estimate on fault orientation. The PPFN provides a full representation of the 3D space covered by the seismic cloud by giving an estimate of the likelihood a fracture is present at any location. This allows for a more comprehensive view on the seismic cloud and a better understanding of the reliability of the proposed fracture network. While the weights are not actual probabilities, they can give a sense of the certainty of the derived result.

To refine the PPFN further, a synthetic dataset that is more complex and representative of real seismic clouds should be designed. Such a dataset would be key to get a better understanding of the strengths and limits of the method and for a better calibration of the weighting parameters. However, the design of a realistic, synthetic seismic cloud is not an easy task in itself. It should be representative of seismicity induced by fluid injection into a real fracture network and the underlying fracture network should be easy to control and modify to test different fracture network layouts. Maybe such a cloud could be designed by modelling the seismic response of an artificially created and therewith controllable fault network. The PPFN should also be tested on other case studies to verify its applicability.

The two presented studies on the Soultz and Rittershoffen reservoirs have shown that it is possible to improve the knowledge about the underground fracture network gained from induced seismicity analysis with the appropriate

methodology. It has to be kept in mind though that this imaging capability is limited to large-scale seismogenic structures, so only part of the fracture network is highlighted. Highly conductive faults may not show a seismic response when stimulation is applied since not enough pore pressure will build up in such faults to induce slip. Sealing faults without any fluid flow remain also invisible but may be important in guiding the underground fluid flow as barriers. However, induced seismicity highlights those faults that are strongly affected by the reservoir stimulation operations and are likely majorly responsible for any injectivity/productivity increase. These faults are also the structures, which pose the highest risk to generate earthquakes and therefore the ones the operators of the reservoir have to be aware of to mitigate major seismic events.

7.2 Perspectives

Induced seismicity during stimulation operations is a widely discussed topic because here the main seismic activity is expected. This thesis also focused on stimulation induced seismicity. However, successful geothermal systems are ideally operated for many years and the continuous fluid circulation will also effect the underground fault network. Indeed, seismicity has been observed also during reservoir operation (Genter et al., 2012; Vasterling et al., 2017) and the analysis of this seismicity would help to get a better understanding on the implications of long-term fluid circulation for the fault network and may help to make predictions on the future reservoir behavior.

Induced seismicity at the Rittershoffen reservoir is continuously monitored since start of the reservoir development in 2012. The application of template matching detection to the period from July 2013 to the end of 2017 revealed over 5000 induced events (Fig. 7.1). Preliminary processing indicates that the induced seismicity is not distributed equally over this time period. From July 2013 to June 2016 the seismicity rate stayed below 50 events per week with an average of 10 events per week, except for the 26th of March and the 19th of June 2014 when 269 and 79 events were detected respectively that are linked to the drilling of GRT2. In the second half of June 2016 the overall seismicity rate started to increase considerably to an average of 52 events per week. This change in seismicity rate coincidences with the time when the power plant went operational (Baujard et al., 2017). However, the detected seismicity has not been revised for false detections yet and the analysis of the seismicity during chemical stimulation of GRT1
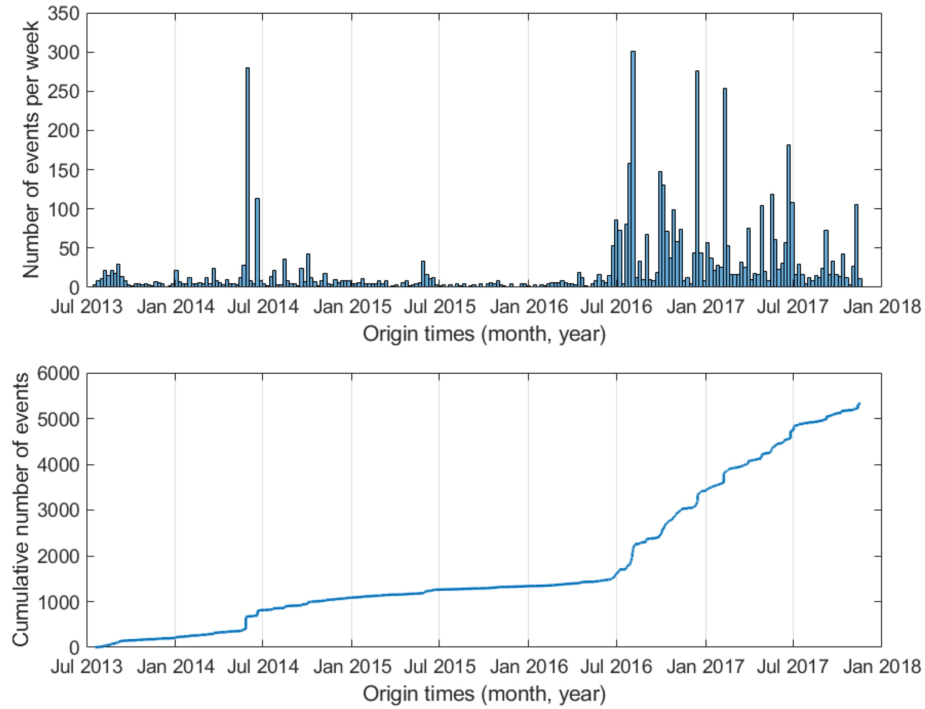
Figure 7.1 − Seismicity rate during the time period July 2013 to December 2017 of the Rittershoffen geothermal reservoir. Top: seismicity rate in bins of one week. Bottom: cumulative number of seismic events.

indicates that about 1-2 false detections per day might occur (Chapter 5). Such a false detection rate is rather insignificant for the analysis of hundreds of events within hours like during stimulation operations but becomes important for periods of low seismicity. The next steps would be to compare the development of the seismicity rate with on-site operations, to relocate the seismic events and perform the waveform clustering analysis to derive results comparable to the ones obtained for the stimulation sequence. Applying the same processing to the operation period will show if the same faults continue to get re-activated, seismicity migrates further into the reservoir and if previously inactive fault segments may become active. Since the conditions during operation are more stable in terms of flowrate/pressure than during stimulation, the analysis of operation induced seismicity could provide an additional viewpoint on the geomechanical processes in the reservoir and help to improve the understanding of the mechanisms behind induced seismicity.

Further steps to improve the seismicity analysis at the Rittershoffen reservoir would be the determination of location uncertainties and the computa-

tion of focal mechanisms. The location uncertainties have been estimated to be around 30 m from the change of dimensionality of the seismic cloud. However, a more precise determination of location uncertainties would help to quantify the reliability of the derived geometry of the fault network. This is especially important to confirm the spatial gap between the two seismogenic fault segments. Focal mechanisms of the induced seismic events would give information on the dominating faulting mode and show if the orientations of the earthquake sources are in agreement with the determined overall orientation of the fault segments.

The Rittershoffen case study has shown that induced seismicity has the potential to reveal effects of stimulation operations that are not restricted to the targeted fault zone. An even more extreme example is the seismicity induced at the Vendenheim geothermal reservoir near Strasbourg that is currently under development. Here, seismicity was triggered on a fault 4-5 km away from the injection well, the largest event having a local magnitude of 3.0 (Schmittbuhl et al., 2020). Without induced seismicity, the fact that the reservoir stimulation operations had an effect on the underground way beyond the targeted reservoir would remain unknown. Induced seismicity is a unique means to follow the stress propagation in the underground over larger distances. However, while induced seismicity on distant faults makes it clear that stress induced by stimulation operations may travel large distances, from seismic observations alone it is difficult to deduce the exact mechanisms of this stress transfer. This is especially true when the stress transport itself is aseismic over a larger distance like in the Vendenheim case. To investigate the mechanisms behind the triggering of seismicity on faults not directly targeted by the injection, it would be worthwhile to combine the seismicity analysis with a reservoir modeling of fluid flow and stress transfer to get a better understanding of the geomechanical processes.

References

Abercrombie, R. E. (1995). "Earthquake source scaling relationships from -1 to 5 ML using seismograms recorded at 2.5-km depth." In: *Journal of Geophysical Research: Solid Earth* 100 (B12), pp. 24015–24036. DOI: `10.1029/95JB02397`.

Aghli, G., B. Soleimani, R. Moussavi-Harami, and R. Mohammadian (2016). "Fractured zones detection using conventional petrophysical logs by differentiation method and its correlation with image logs." In: *Journal of Petroleum Science and Engineering* 142, pp. 152–162. DOI: `10.1016/j.petrol.2016.02.002`.

Aichholzer, C., P. Duringer, S. Orciani, and A. Genter (2016). "New stratigraphic interpretation of the Soultz-sous-Forêts 30-year-old geothermal wells calibrated on the recent one from Rittershoffen (Upper Rhine Graben, France)." In: *Geothermal Energy* 4.13. DOI: `10.1186/s40517-016-0055-7`.

Aki, K. (1966). "Estimation of earthquake moment, released energy, and stress-strain drop from G wave spectrum." In: *Bulletin of the Earthquake Research Institute* 44, pp. 73–88.

Aki, K. and P. Richards (2009). *Quantitative Seismology, Theory and Methods*. 2nd edition. Mill Valley: University Science Books.

Allen, R. (1982). "Automatic phase pickers: Their present use and future prospects." In: *Bulletin of the Seismological Society of America* 72.6, pp. 225–242.

Anderson, E. M. (1951). *The Dynamics of Faulting and Dyke Formation with Applications to Britain*. Oliver and Boyd. 224 pp.

André, L., V. Rabemanana, and F.-D. Vuataz (2006). "Influence of water–rock interactions on fracture permeability of the deep reservoir at Soultz-sous-Forêts, France." In: *Geothermics* 35.5, pp. 507–531. DOI: 10.1016/j.geothermics.2006.09.006.

Arthur, D. and S. Vassilvitskii (2007). "k-means++: the advantages of careful seeding." Presented at: *Proceedings of the eighteenth annual ACM-SIAM symposium on Discrete algorithms*. USA, pp. 1027–1035.

Axelsson, G., S. Thórhallsson, and G. Björnsson (2006). "Stimulation of geothermal wells in basaltic rock in Iceland." Presented at: ENGINE Workshop 3, Stimulation of reservoir and microseismicity. Zürich, Switzerland.

Aydin, A. (2000). "Fractures, faults, and hydrocarbon entrapment, migration and flow." In: *Marine and Petroleum Geology* 17.7, pp. 797–814. DOI: 10.1016/S0264-8172(00)00020-9.

Bächler, D., T. Kohl, and L. Rybach (2003). "Impact of graben-parallel faults on hydrothermal convection—Rhine Graben case study." In: *Physics and Chemistry of the Earth, Parts A/B/C* 28.9, pp. 431–441. DOI: 10.1016/S1474-7065(03)00063-9.

Bachmann, C. E., S. Wiemer, B. P. Goertz-Allmann, and J. Woessner (2012). "Influence of pore-pressure on the event-size distribution of induced earthquakes." In: *Geophysical Research Letters* 39.9, n/a–n/a. DOI: 10.1029/2012GL051480.

Bachmann, C. E., S. Wiemer, J. Woessner, and S. Hainzl (2011). "Statistical analysis of the induced Basel 2006 earthquake sequence: introducing a probability-based monitoring approach for Enhanced Geothermal Systems." In: *Geophysical Journal International* 186.2, pp. 793–807. DOI: 10.1111/j.1365-246X.2011.05068.x.

Baillieux, P., E. Schill, J.-B. Edel, and G. Mauri (2013). "Localization of temperature anomalies in the Upper Rhine Graben: insights from geophysics and neotectonic activity." In: *International Geology Review* 55.14, pp. 1744–1762. DOI: 10.1080/00206814.2013.794914.

Bardainne, T. and E. Gaucher (2010). "Constrained tomography of realistic velocity models in microseismic monitoring using calibration shots." In: *Geophysical Prospecting* 58.5, pp. 739–753. DOI: 10.1111/j.1365-2478.2010.00912.x.

Baria, R. et al. (2004). "Microseismic Monitoring of the World's Largest Potential HDR Reservoir." Presented at: Twenty-ninth workshop on geothermal reservoir engineering, Stanford University. Stanford, California.

Baria, R., J. Baumgärtner, A. Gérard, R. Jung, and J. Garnish (1999). "European HDR research programme at Soultz-sous-Forêts (France) 1987–1996." In: *Geothermics* 28.4, pp. 655–669. DOI: `10.1016/S0375-6505(99)00036-X`.

Barrett, S. A. and G. C. Beroza (2014). "An Empirical Approach to Subspace Detection." In: *Seismological Research Letters* 85.3, pp. 594–600. DOI: `10.1785/0220130152`.

Barthélémy, J.-F., M. L. Guiton, and J.-M. Daniel (2009). "Estimates of fracture density and uncertainties from well data." In: *International Journal of Rock Mechanics and Mining Sciences* 46.3, pp. 590–603. DOI: `10.1016/j.ijrmms.2008.08.003`.

Barton, N., S. Bandis, and K. Bakhtar (1985). "Strength, deformation and conductivity coupling of rock joints." In: *International Journal of Rock Mechanics and Mining Sciences & Geomechanics Abstracts* 22.3, pp. 121–140. DOI: `10.1016/0148-9062(85)93227-9`.

Baujard, C., A. Genter, E. Dalmais, V. Maurer, R. Hehn, R. Rosillette, J. Vidal, and J. Schmittbuhl (2017). "Hydrothermal characterization of wells GRT-1 and GRT-2 in Rittershoffen, France: Implications on the understanding of natural flow systems in the rhine graben." In: *Geothermics* 65, pp. 255–268. DOI: `10.1016/j.geothermics.2016.11.001`.

Baujard, C., M. Schoenball, T. Kohl, and L. Dorbath (2014). "Large magnitude events during injections in geothermal reservoirs and hydraulic energy: A heuristic approach." In: *Geothermics* 52, pp. 140–152. DOI: `10.1016/j.geothermics.2014.07.002`.

Berkowitz, B. (2002). "Characterizing flow and transport in fractured geological media: A review." In: *Advances in Water Resources* 25.8, pp. 861–884. DOI: `10.1016/S0309-1708(02)00042-8`.

Bhattacharya, P. and R. C. Viesca (2019). "Fluid-induced aseismic fault slip outpaces pore-fluid migration." In: *Science* 364.6439, pp. 464–468. DOI: `10.1126/science.aaw7354`.

Biot, M. A. (1962). "Mechanics of Deformation and Acoustic Propagation in Porous Media." In: *Journal of Applied Physics* 33.4, pp. 1482–1498. DOI: `10.1063/1.1728759`.

Biot, M. A. (1941). "General Theory of Three-Dimensional Consolidation." In: *Journal of Applied Physics* 12.2, pp. 155–164. DOI: `10.1063/1.1712 886`.

Blöcher, G. et al. (2016). "Hydraulic history and current state of the deep geothermal reservoir Groß Schönebeck." In: *Geothermics* 63, pp. 27–43. DOI: `10.1016/j.geothermics.2015.07.008`.

Bommer, J. J., S. Oates, J. M. Cepeda, C. Lindholm, J. Bird, R. Torres, G. Marroquín, and J. Rivas (2006). "Control of hazard due to seismicity induced by a hot fractured rock geothermal project." In: *Engineering Geology* 83.4, pp. 287–306. DOI: `10.1016/j.enggeo.2005.11.002`.

Bormann, P., S. Wendt, and D. DiGiacomo (2012). "Chapter 3. Seismic Sources and Source Parameters." In: *Manual of Seismological Observatory Practice (NMSOP-2)*. Ed. by Bormann, P. Potsdam: IASPEI, GFZ German Research Centre for Geosciences. DOI: `10.2312/GFZ.NMSOP-2 _CH3`.

Bourgeois, O., M. Ford, M. Diraison, C. Le Carlier de Veslud, M. Gerbault, R. Pik, N. Ruby, and S. Bonnet (2007). "Separation of rifting and lithospheric folding signatures in the NW-Alpine foreland." In: *International Journal of Earth Sciences* 96.6, pp. 1003–1031. DOI: `10.1007/s00531-0 07-0202-2`.

Bourouis, S. and P. Bernard (2007). "Evidence for coupled seismic and aseismic fault slip during water injection in the geothermal site of Soultz (France), and implications for seismogenic transients." In: *Geophysical Journal International* 169.2, pp. 723–732. DOI: `10.1111/j.1365-246X.2 006.03325.x`.

Breede, K., K. Dzebisashvili, X. Liu, and G. Falcone (2013). "A systematic review of enhanced (or engineered) geothermal systems: past, present and future." In: *Geothermal Energy* 1.4. DOI: `10.1186/2195-9706-1-4`.

Brown, D., R. DuTeaux, P. Kruger, D. Swenson, and T. Yamaguchi (1999). "Fluid circulation and heat extraction from engineered geothermal reservoirs." In: *Geothermics* 28.4, pp. 553–572. DOI: `10.1016/S0375-6505(9 9)00028-0`.

Brown, D. W. (2009). "Hot Dry Rock Geothermal Energy: Important Lessons from Fenton Hill." Presented at: Thirty-Fourth Workshop on Geothermal Reservoir Engineering, Stanford University. Stanford, California.

Brown, J. R., G. C. Beroza, and D. R. Shelly (2008). "An autocorrelation method to detect low frequency earthquakes within tremor." In: *Geophysical Research Letters* 35.16. DOI: 10.1029/2008GL034560.

Brun, J. P. and F. Wenzel (1991). "Crustal-scale structure of the southern Rhinegraben from ECORS-DEKORP seismic reflection data." In: *Geology* 19.7, pp. 758–762. DOI: 10.1130/0091-7613(1991)019<0758:CSSOTS>2.3.CO;2.

Brune, J. N. (1970). "Tectonic stress and the spectra of seismic shear waves from earthquakes." In: *Journal of Geophysical Research (1896-1977)* 75.26, pp. 4997–5009. DOI: 10.1029/JB075i026p04997.

Byerlee, J. (1978). "Friction of Rocks." In: *Rock Friction and Earthquake Prediction.* Ed. by Byerlee, J. D. and Wyss, M. Basel: Birkhäuser, pp. 615–626. DOI: 10.1007/978-3-0348-7182-2_4.

Calò, M., C. Dorbath, F. Cornet, and N. Cuenot (2011). "Large-scale aseismic motion identified through 4-D P-wave tomography: Temporal subsetting of the stimulation period." In: *Geophysical Journal International* 186.3, pp. 1295–1314. DOI: 10.1111/j.1365-246X.2011.05108.x.

Castello, B., M. Olivieri, and G. Selvaggi (2007). "Local and Duration Magnitude Determination for the Italian Earthquake Catalog, 1981–2002." In: *Bulletin of the Seismological Society of America* 97.1, pp. 128–139. DOI: 10.1785/0120050258.

Chamorro, C. R., J. L. García-Cuesta, M. E. Mondéjar, and A. Pérez-Madrazo (2014). "Enhanced geothermal systems in Europe: An estimation and comparison of the technical and sustainable potentials." In: *Energy* 65, pp. 250–263. DOI: 10.1016/j.energy.2013.11.078.

Charléty, J., N. Cuenot, L. Dorbath, C. Dorbath, H. Haessler, and M. Frogneux (2007). "Large earthquakes during hydraulic stimulations at the geothermal site of Soultz-sous-Forêts." In: *International Journal of Rock Mechanics and Mining Sciences* 44.8, pp. 1091–1105. DOI: 10.1016/j.ijrmms.2007.06.003.

Cilona, A., A. Aydin, J. Likerman, B. Parker, and J. Cherry (2016). "Structural and statistical characterization of joints and multi-scale faults in an alternating sandstone and shale turbidite sequence at the Santa Susana Field Laboratory: Implications for their effects on groundwater flow and contaminant transport." In: *Journal of Structural Geology* 85, pp. 95–114. DOI: 10.1016/j.jsg.2016.02.003.

Cornet, F. H., J. Helm, and H. Poitrenaud (1997). "Seismic and Aseismic Slips Induced by Large-scale Fluid Injections." In: *Pure and Applied Geophysics* 150, pp. 563–583.

Cornet, F. H., T. Bérard, and S. Bourouis (2007). "How close to failure is a granite rock mass at a 5km depth?" In: *International Journal of Rock Mechanics and Mining Sciences* 44.1, pp. 47–66. DOI: 10.1016/j.ijrmms.2006.04.008.

Cornet, F. H. and O. Scotti (1993). "Analysis of induced seismicity for fault zone identification." In: *International Journal of Rock Mechanics and Mining Sciences & Geomechanics Abstracts* 30.7, pp. 789–795. DOI: 10.1016/0148-9062(93)90024-8.

Cornet, F. H. (2015). *Elements of Crustal Geomechanics*. Cambridge University Press. 479 pp.

Coulomb, C. (1773). "Application des règles de maxima et minima à quelques problèmes de statique relatifs à l'Architecture." In: *Mémoires de Mathématiques et de Physiques présentés à l'Académie Royale des Sciences* 7, pp. 343–382.

Cuenot, N., J. Charléty, L. Dorbath, and H. Haessler (2006). "Faulting mechanisms and stress regime at the European HDR site of Soultz-sous-Forêts, France." In: *Geothermics* 35.5, pp. 561–575. DOI: 10.1016/j.geothermics.2006.11.007.

Cuenot, N., C. Dorbath, and L. Dorbath (2008). "Analysis of the Microseismicity Induced by Fluid Injections at the EGS Site of Soultz-sous-Forêts (Alsace, France): Implications for the Characterization of the Geothermal Reservoir Properties." In: *Pure and Applied Geophysics* 165.5, pp. 797–828. DOI: 10.1007/s00024-008-0335-7.

Darcel, C., O. Bour, and P. Davy (2003a). "Cross-correlation between length and position in real fracture networks." In: *Geophysical Research Letters* 30.12. DOI: 10.1029/2003GL017174.

Darcel, C., O. Bour, P. Davy, and J. R. de Dreuzy (2003b). "Connectivity properties of two-dimensional fracture networks with stochastic fractal correlation." In: *Water Resources Research* 39.10. DOI: 10.1029/2002WR0 01628.

Deichmann, N., T. Kraft, and K. F. Evans (2014). "Identification of faults activated during the stimulation of the Basel geothermal project from cluster analysis and focal mechanisms of the larger magnitude events." In: *Geothermics* 52, pp. 84–97. DOI: 10.1016/j.geothermics.2014.04 .001.

Delépine, N., N. Cuenot, E. Rothert, M. Parotidis, S. Rentsch, and S. A. Shapiro (2004). "Characterization of fluid transport properties of the Hot Dry Rock reservoir Soultz-2000 using induced microseismicity." In: *Journal of Geophysics and Engineering* 1.1, pp. 77–83. DOI: 10.1088/1742-2132/1/1/010.

Deng, K., Y. Liu, and R. M. Harrington (2016). "Poroelastic stress triggering of the December 2013 Crooked Lake, Alberta, induced seismicity sequence." In: *Geophysical Research Letters* 43.16, pp. 8482–8491. DOI: 10.1002/2016GL070421.

Dezayes, C., A. Genter, and S. Gentier (2004). "Fracture Network of the EGS Geothermal Reservoir at Soultz-sous-Forêts (Rhine Graben, France)." In: *Geothermal Resources Council Transactions* 28, pp. 213–218.

Dezayes, C., A. Genter, and B. Valley (2010). "Structure of the low permeable naturally fractured geothermal reservoir at Soultz." In: *Comptes Rendus Geoscience* 342.7, pp. 517–530. DOI: 10.1016/j.crte.2009.10.002.

Dorbath, L., N. Cuenot, A. Genter, and M. Frogneux (2009). "Seismic response of the fractured and faulted granite of Soultz-sous-Forêts (France) to 5 km deep massive water injections." In: *Geophysical Journal International* 177.2, pp. 653–675. DOI: 10.1111/j.1365-246X.2009.04030.x.

Eisner, L., S. Williams-Stroud, A. Hill, P. Duncan, and M. Thornton (2010). "Beyond the dots in the box - Microseismicity-Constrained Fracture Models for Reservoir Simulation." In: *The Leading Edge* 29, pp. 326–333. DOI: 10.1190/1.3353730..

Evans, K. F., H. Moriya, H. Niitsuma, R. H. Jones, W. S. Phillips, A. Genter, J. Sausse, R. Jung, and R. Baria (2005a). "Microseismicity and permeability enhancement of hydrogeologic structures during massive fluid

injections into granite at 3 km depth at the Soultz HDR site." In: *Geophysical Journal International* 160.1, pp. 388–412. DOI: `10.1111/j.1365-246X.2004.02474.x`.

Evans, K. F. (2000). "The Effect of the 1993 Stimulations of Well GPK1 at Soultz on the Surrounding Rock Mass: Evidence for the Existence of a Connected Network of Permeable Fractures." Presented at: World Geothermal Congress, 2000. Kyushu - Tohoku, Japan.

Evans, K. F., A. Genter, and J. Sausse (2005b). "Permeability creation and damage due to massive fluid injections into granite at 3.5 km at Soultz: 1. Borehole observations." In: *Journal of Geophysical Research: Solid Earth* 110 (B04203). DOI: `10.1029/2004JB003168`.

Evans, K. F., A. Zappone, T. Kraft, N. Deichmann, and F. Moia (2012). "A survey of the induced seismic responses to fluid injection in geothermal and CO2 reservoirs in Europe." In: *Geothermics* 41, pp. 30–54. DOI: `10.1016/j.geothermics.2011.08.002`.

Eyre, T. S., D. W. Eaton, D. I. Garagash, M. Zecevic, M. Venieri, R. Weir, and D. C. Lawton (2019). "The role of aseismic slip in hydraulic fracturing–induced seismicity." In: *Science Advances* 5.8, eaav7172. DOI: `10.1126/sciadv.aav7172`.

Fan, Z., P. Eichhubl, and P. Newell (2019). "Basement Fault Reactivation by Fluid Injection Into Sedimentary Reservoirs: Poroelastic Effects." In: *Journal of Geophysical Research: Solid Earth* 124.7, pp. 7354–7369. DOI: `10.1029/2018JB017062`.

Fehler, M., L. House, and H. Kaieda (1987). "Determining planes along which earthquakes occur: Method and application to earthquakes accompanying hydraulic fracturing." In: *Journal of Geophysical Research* 92 (B9), pp. 9407–9414. DOI: `10.1029/JB092iB09p09407`.

Fehler, M., A. Jupe, and H. Asanuma (2001). "More Than Cloud: New techniques for characterizing reservoir structure using induced seismicity." In: *The Leading Edge* 20.3, pp. 324–328. DOI: `10.1190/1.1438942`.

Follin, S., L. Hartley, I. Rhén, P. Jackson, S. Joyce, D. Roberts, and B. Swift (2014). "A methodology to constrain the parameters of a hydrogeological discrete fracture network model for sparsely fractured crystalline rock, exemplified by data from the proposed high-level nuclear waste repository

site at Forsmark, Sweden." In: *Hydrogeology Journal* 22.2, pp. 313–331. DOI: 10.1007/s10040-013-1080-2.

Fridleifsson, G. O., A. Albertsson, B. Stefansson, and H. Adalsteinsson (2007). "Deep Unconventional Geothermal Resources: a major opportunity to harness new sources of sustainable energy." Presented at: 20th World Energy Congress 2007. Rome, Italy.

Friðleifsson, G. Ó., A. Albertsson, A. Stefánsson, G. Þórólfsson, K. G. Mesfin, K. Sigurðsson, Ó. Sigurðsson, and Þ. Gíslason (2019). "The Reykjanes DEEPEGS Demonstration Well – IDDP-2." Presented at: European Geothermal Congress 2019. Den Haag, The Netherlands.

Gale, J. F., S. E. Laubach, J. E. Olson, P. Eichhuble, and A. Fall (2014). "Natural Fractures in shale: A review and new observations." In: *AAPG Bulletin* 98.11, pp. 2165–2216. DOI: 10.1306/08121413151.

Gaucher, E., F. H. Cornet, and P. Bernard (1998). "Induced Seismicity Analysis for Structure Identification and Stress Field Determination." Presented at: SPE/ISRM Rock Mechanics in Petroleum Engineering. DOI: 10.2118/47324-MS.

Gaucher, E., M. Schoenball, O. Heidbach, A. Zang, P. A. Fokker, J. D. V. Wees, and T. Kohl (2015a). "Induced Seismicity in Geothermal Reservoirs: Physical Processes and Key Parameters." Presented at: World Geothermal Congress 2015. Melbourne, Australia.

Gaucher, E., M. Schoenball, O. Heidbach, A. Zang, P. A. Fokker, J.-D. van Wees, and T. Kohl (2015b). "Induced seismicity in geothermal reservoirs: A review of forecasting approaches." In: *Renewable and Sustainable Energy Reviews* 52, pp. 1473–1490. DOI: 10.1016/j.rser.2015.08.026.

Geiger, L. (1910). "Herdbestimmung bei Erdbeben aus den Ankunftszeiten." In: *Nachrichten von der Gesellschaft der Wissenschaften zu Göttingen, Mathematisch-Physikalische Klasse 1910* 4, pp. 331–349.

Gellasch, C. A., K. R. Bradbury, D. J. Hart, and J. M. Bahr (2013). "Characterization of fracture connectivity in a siliciclastic bedrock aquifer near a public supply well (Wisconsin, USA)." In: *Hydrogeology Journal* 21.2, pp. 383–399. DOI: 10.1007/s10040-012-0914-7.

Gens, A., J. Vaunat, B. Garitte, and Y. Wileveau (2007). "In situ behaviour of a stiff layered clay subject to thermal loading: observations and inter-

pretation." In: *Géotechnique* 57.2, pp. 207–228. DOI: `10.1680/geot.200`
`7.57.2.207`.

Genter, A., N. Cuenot, X. Goerke, M. Bernd, B. Sanjuan, and J. Scheiber
(2012). "Status of the Soultz geothermal project during exploitation be-
tween 2010 and 2012." Presented at: 37th Workshop on Geothermal Reser-
voir Engineering, Stanford University. Stanford, California.

Genter, A., K. Evans, N. Cuenot, D. Fritsch, and B. Sanjuan (2010). "Contri-
bution of the exploration of deep crystalline fractured reservoir of Soultz
to the knowledge of enhanced geothermal systems (EGS)." In: *Comptes
Rendus Geoscience* 342.7, pp. 502–516. DOI: `10.1016/j.crte.2010.01`
`.006`.

Genter, A., H. Traineau, B. Ledésert, B. Bourgine, and S. Gentier (2000).
"Over 10 years of geological investigations within the HDR Soultz project,
France." Presented at: World Geothermal Congress 2000. Kyushu-Tohoku,
Japan.

Gibbons, S. J. and F. Ringdal (2006). "The detection of low magnitude seis-
mic events using array-based waveform correlation." In: *Geophysical Jour-
nal International* 165.1, pp. 149–166. DOI: `10.1111/j.1365-246X.2006`
`.02865.x`.

Gischig, V. S. and S. Wiemer (2013). "A stochastic model for induced seis-
micity based on non-linear pressure diffusion and irreversible permeabil-
ity enhancement." In: *Geophysical Journal International* 194.2, pp. 1229–
1249. DOI: `10.1093/gji/ggt164`.

Glaas, C., P. Patrier, J. Vidal, D. Beaufort, J.-F. Girard, and A. Genter
(2020). "Hydrothermal Alteration in the New Deep Geothermal Well GIL-
1 (Strasbourg Area, France)." Presented at: World Geothermal Congress
2020. Reykjavik, Iceland.

Goertz-Allmann, B. P. and S. Wiemer (2012). "Geomechanical modeling of
induced seismicity source parameters and implications for seismic hazard
assessment." In: *Geophysics* 78.1, KS25–KS39. DOI: `10.1190/geo2012-0`
`102.1`.

Grassberger, P. and I. Procaccia (1983). "Characterization of Strange At-
tractors." In: *Physical Review Letters* 50.5, pp. 346–349. DOI: `10.1103`
`/PhysRevLett.50.346`.

Grigoli, F. et al. (2018). "The November 2017 Mw 5.5 Pohang earthquake: A possible case of induced seismicity in South Korea." In: *Science* 360.6392, pp. 1003–1006. DOI: `10.1126/science.aat2010`.

Gutenberg, B. and C. F. Richter (1954). *Seismicity of the Earth and Associated Phenomena.* 2nd edition. Princeton University Press.

Haas, I. O. and C. R. Hoffmann (1929). "Temperature Gradient in Pechelbronn Oil-Bearing Region, Lower Alsace: Its Determination and Relation to Oil Reserves." In: *AAPG Bulletin* 13.10, pp. 1257–1273. DOI: `10.1306/3D932884-16B1-11D7-8645000102C1865D`.

Häring, M. O., U. Schanz, F. Ladner, and B. C. Dyer (2008). "Characterisation of the Basel 1 enhanced geothermal system." In: *Geothermics* 37.5, pp. 469–495. DOI: `10.1016/j.geothermics.2008.06.002`.

Harris, D. B. (2006). *Subspace Detectors: Theory.* Report: UCRL-TR-222758. Lawrence Livermore National Laboratory. DOI: `10.2172/900081`.

Haskell, N. A. (1964). "Total energy and energy spectral density of elastic wave radiation from propagating faults." In: *Bulletin of the Seismological Society of America* 54.6, pp. 1811–1841.

Herzberger, P. et al. (2010). "The Geothermal Power Plant Bruchsal." Presented at: World Geothermal Congress 2010. Bali, Indonesia.

Hingee, M., H. Tkalčić, A. Fichtner, and M. Sambridge (2011). "Seismic moment tensor inversion using a 3-D structural model: applications for the Australian region." In: *Geophysical Journal International* 184.2, pp. 949–964. DOI: `10.1111/j.1365-246X.2010.04897.x`.

Hogarth, R. and H.-G. Holl (2017). "Lessons Learned from the Habanero EGS Project." In: *Geothermal Resources Council Transactions* 41.

Hooijkaas, G. R., A. Genter, and C. Dezayes (2006). "Deep-seated geology of the granite intrusions at the Soultz EGS site based on data from 5km-deep boreholes." In: *Geothermics* 35.5, pp. 484–506. DOI: `10.1016/j.geothermics.2006.03.003`.

Horálek, J., Z. Jechumtálová, L. Dorbath, and J. Šílený (2010). "Source mechanisms of micro-earthquakes induced in a fluid injection experiment at the HDR site Soultz-sous-Forêts (Alsace) in 2003 and their temporal and spatial variations." In: *Geophysical Journal International* 181.3, pp. 1547–1565. DOI: `10.1111/j.1365-246X.2010.04506.x`.

Howell, J. A., A. W. Martinius, and T. R. Good (2014). "The application of outcrop analogues in geological modelling: a review, present status and future outlook." In: *Geological Society, London, Special Publications* 387.1, pp. 1–25. DOI: 10.1144/SP387.12.

Husen, S., E. Kissling, N. Deichmann, S. Wiemer, D. Giardini, and M. Baer (2003). "Probabilistic earthquake location in complex three-dimensional velocity models: Application to Switzerland." In: *Journal of Geophysical Research: Solid Earth* 108 (B2). DOI: 10.1029/2002JB001778.

Ide, S. (2001). "Complex source processes and the interaction of moderate earthquakes during the earthquake swarm in the Hida-Mountains, Japan, 1998." In: *Tectonophysics* 334.1, pp. 35–54. DOI: 10.1016/S0040-1951(01)00027-0.

IEA (2017). *Geothermal Power Report 2017*. International Energy Agency. URL: https://iea-gia.org/publications-2/working-group-publications/#Annex-X (visited on 10/26/2020).

IRENA (2020). *Renewable Energy Statistics 2020*. The International Renewable Energy Agency, Abu Dhabi.

El-Isa, Z. H. and D. W. Eaton (2014). "Spatiotemporal variations in the b-value of earthquake magnitude–frequency distributions: Classification and causes." In: *Tectonophysics* 615-616, pp. 1–11. DOI: 10.1016/j.tecto.2013.12.001.

Jeanne, P., J. Rutqvist, and P. F. Dobson (2017). "Influence of injection-induced cooling on deviatoric stress and shear reactivation of preexisting fractures in Enhanced Geothermal Systems." In: *Geothermics* 70, pp. 367–375. DOI: 10.1016/j.geothermics.2017.08.003.

Jeanne, P., J. Rutqvist, P. F. Dobson, M. Walters, C. Hartline, and J. Garcia (2014). "The impacts of mechanical stress transfers caused by hydromechanical and thermal processes on fault stability during hydraulic stimulation in a deep geothermal reservoir." In: *International Journal of Rock Mechanics and Mining Sciences* 72, pp. 149–163. DOI: 10.1016/j.ijrmms.2014.09.005.

Jones, R. H. and R. C. Stewart (1997). "A method for determining significant structures in a cloud of earthquakes." In: *Journal of Geophysical Research: Solid Earth* 102 (B4), pp. 8245–8254. DOI: 10.1029/96JB03739.

Jost, M. L. and R. B. Herrmann (1989). "A Student's Guide to and Review of Moment Tensors." In: *Seismological Research Letters* 60.2, pp. 37–57. DOI: `10.1785/gssrl.60.2.37`.

Kaiser, J. (1950). "Untersuchung über das Auftreten von Geräuschen beim Zugversuch." Dissertation. Technische Universität München.

Kanamori, H. (1977). "The energy release in great earthquakes." In: *Journal of Geophysical Research (1896-1977)* 82.20, pp. 2981–2987. DOI: `10.1029/JB082i020p02981`.

Karasözen, E. and B. Karasözen (2020). "Earthquake location methods." In: *GEM - International Journal on Geomathematics* 11.13. DOI: `10.1007/s13137-020-00149-9`.

Keranen, K. M., M. Weingarten, G. A. Abers, B. A. Bekins, and S. Ge (2014). "Sharp increase in central Oklahoma seismicity since 2008 induced by massive wastewater injection." In: *Science* 345.6195, pp. 448–451. DOI: `10.1126/science.1255802`.

King, G. C. P., R. S. Stein, and J. Lin (1994). "Static stress changes and the triggering of earthquakes." In: *Bulletin of the Seismological Society of America* 84.3, pp. 935–953.

Kinnaert, X., E. Gaucher, U. Achauer, and T. Kohl (2016). "Modelling earthquake location errors at a reservoir scale: a case study in the Upper Rhine Graben." In: *Geophysical Journal International* 206.2, pp. 861–879. DOI: `10.1093/gji/ggw184`.

Klein, F. W. (2002). *User's guide to HYPOINVERSE-2000, a Fortran program to solve for earthquake locations and magnitudes*. Open-File Report 02-171. U.S. Geological Survey.

Koh, J., H. Roshan, and S. S. Rahman (2011). "A numerical study on the long term thermo-poroelastic effects of cold water injection into naturally fractured geothermal reservoirs." In: *Computers and Geotechnics* 38.5, pp. 669–682. DOI: `10.1016/j.compgeo.2011.03.007`.

Kohl, T. and T. Mégel (2007). "Predictive modeling of reservoir response to hydraulic stimulations at the European EGS site Soultz-sous-Forêts." In: *International Journal of Rock Mechanics and Mining Sciences* 44.8, pp. 1118–1131. DOI: `10.1016/j.ijrmms.2007.07.022`.

Küperkoch, L., K. Olbert, and T. Meier (2018). "Long-Term Monitoring of Induced Seismicity at the Insheim Geothermal Site, GermanyLong-Term Monitoring of Induced Seismicity at the Insheim Geothermal Site, Germany." In: *Bulletin of the Seismological Society of America* 108.6, pp. 3668–3683. DOI: 10.1785/0120170365.

Lahr C., J. (1999). *HYPOELLIPSE: A Computer Program for Determining Local Earthquake Hypocentral Parameters, Magnitude, and First-Motion Pattern.* Open-File Report 99-23. U.S. Geological Survey, 119pp.

Lanza, V., D. Spallarossa, M. Cattaneo, D. Bindi, and P. Augliera (1999). "Source parameters of small events using constrained deconvolution with empirical Green's functions." In: *Geophysical Journal International* 137.3, pp. 651–662. DOI: 10.1046/j.1365-246x.1999.00809.x.

Lavrov, A. (2003). "The Kaiser effect in rocks: principles and stress estimation techniques." In: *International Journal of Rock Mechanics and Mining Sciences* 40.2, pp. 151–171. DOI: 10.1016/S1365-1609(02)00138-7.

Lei, Q., J.-P. Latham, and C.-F. Tsang (2017). "The use of discrete fracture networks for modelling coupled geomechanical and hydrological behaviour of fractured rocks." In: *Computers and Geotechnics* 85, pp. 151–176. DOI: 10.1016/j.compgeo.2016.12.024.

Lengliné, O., M. Boubacar, and J. Schmittbuhl (2017). "Seismicity related to the hydraulic stimulation of GRT1, Rittershoffen, France." In: *Geophysical Journal International* 208.3, pp. 1704–1715. DOI: 10.1093/gji/ggw490.

Lengliné, O., Z. Duputel, and V. Ferrazzini (2016). "Uncovering the hidden signature of a magmatic recharge at Piton de la Fournaise volcano using small earthquakes." In: *Geophysical Research Letters* 43.9, pp. 4255–4262. DOI: 10.1002/2016GL068383.

Lentas, K. (2018). "Towards routine determination of focal mechanisms obtained from first motion P-wave arrivals." In: *Geophysical Journal International* 212.3, pp. 1665–1686. DOI: 10.1093/gji/ggx503.

Lin, G. and P. Shearer (2005). "Tests of relative earthquake location techniques using synthetic data." In: *Journal of Geophysical Research: Solid Earth* 110 (B4). DOI: 10.1029/2004JB003380.

Lin, G. and P. Shearer (2006). "The COMPLOC Earthquake Location Package." In: *Seismological Research Letters* 77.4, pp. 440–444. DOI: 10.1785/gssrl.77.4.440.

Lloyd, S. (1982). "Least squares quantization in PCM." In: *IEEE Transactions on Information Theory* 28.2, pp. 129–137. DOI: 10.1109/TIT.1982.1056489.

Lomax, A. (2005). "A Reanalysis of the Hypocentral Location and Related Observations for the Great 1906 California Earthquake." In: *Bulletin of the Seismological Society of America* 95.3, pp. 861–877. DOI: 10.1785/0120040141.

Lomax, A., A. Michelini, and A. Curtis (2011). "Earthquake Location, Direct, Global-Search Methods." In: *Extreme Environmental Events: Complexity in Forecasting and Early Warning*. Ed. by Meyers, R. A. New York, NY: Springer, pp. 230–254. DOI: 10.1007/978-1-4419-7695-6_16.

Lu, S.-M. (2018). "A global review of enhanced geothermal system (EGS)." In: *Renewable and Sustainable Energy Reviews* 81, pp. 2902–2921. DOI: 10.1016/j.rser.2017.06.097.

Madariaga, R. (1976). "Dynamics of an expanding circular fault." In: *Bulletin of the Seismological Society of America* 66.3, pp. 639–666.

Maurer, V., N. Cuenot, E. Gaucher, M. Grunberg, J. Vergne, H. Wodling, M. Lehujeur, and J. Schmittbuhl (2015). "Seismic Monitoring of the Rittershoffen EGS Project (Alsace, France)." Presented at: Proceedings World Geothermal Congress 2015. Melbourne.

Maurer, V., E. Gaucher, M. Grunberg, R. Koepke, R. Pestourie, and N. Cuenot (2020). "Seismicity induced during the development of the Rittershoffen geothermal field, France." In: *Geothermal Energy* 8.1, p. 5. DOI: 10.1186/s40517-020-0155-2.

Maxwell, S. C., J. Rutledge, R. Jones, and M. Fehler (2010). "Petroleum reservoir characterization using downhole microseismic monitoring." In: *Geophysics* 75.5, 75A129–75A137. DOI: 10.1190/1.3477966.

McClure, M. W. and R. N. Horne (2014). "An investigation of stimulation mechanisms in Enhanced Geothermal Systems." In: *International Journal of Rock Mechanics and Mining Sciences* 72, pp. 242–260. DOI: 10.1016/j.ijrmms.2014.07.011.

Mena, B., S. Wiemer, and C. Bachmann (2013). "Building Robust Models to Forecast the Induced Seismicity Related to Geothermal Reservoir Enhancement." In: *Bulletin of the Seismological Society of America* 103.1, pp. 383–393. DOI: `10.1785/0120120102`.

Mohr, O. (1914). *Abhandlungen aus dem gebiete der technischen mechanik.* Berlin: Ernst & Sohn.

Moriya, H., K. Nakazato, H. Niitsuma, and R. Baria (2002). "Detailed Fracture System of the Soultz-sous-Forêts HDR Field Evaluated Using Microseismic Multiplet Analysis." In: *Pure appl. geophys.* 159, pp. 517–541.

Moriya, H., H. Niitsuma, and R. Baria (2003). "Multiplet-Clustering Analysis Reveals Structural Details within the Seismic Cloud at the Soultz Geothermal Field, France." In: *Bulletin of the Seismological Society of America* 93.4, pp. 1606–1620. DOI: `10.1785/0120020072`.

Mukuhira, Y., C. Dinske, H. Asanuma, T. Ito, and M. O. Häring (2017). "Pore pressure behavior at the shut-in phase and causality of large induced seismicity at Basel, Switzerland." In: *Journal of Geophysical Research: Solid Earth* 122.1, pp. 411–435. DOI: `10.1002/2016JB013338`.

Nick, H. M., A. Paluszny, M. J. Blunt, and S. K. Matthai (2011). "Role of geomechanically grown fractures on dispersive transport in heterogeneous geological formations." In: *Physical Review E* 84.5. DOI: `10.1103/PhysRevE.84.056301`.

Norbeck, J. H., M. W. McClure, and R. N. Horne (2018). "Field observations at the Fenton Hill enhanced geothermal system test site support mixed-mechanism stimulation." In: *Geothermics* 74, pp. 135–149. DOI: `10.1016/j.geothermics.2018.03.003`.

NRC (1996). *Rock Fractures and Fluid Flow: Contemporary Understanding and Applications.* National Academies Press. 568 pp.

Okada, Y. (1992). "Internal deformation due to shear and tensile faults in a half-space." In: *Bulletin of the Seismological Society of America* 82.2, pp. 1018–1040.

Olasolo, P., M. C. Juárez, J. Olasolo, M. P. Morales, and D. Valdani (2016). "Economic analysis of Enhanced Geothermal Systems (EGS). A review of software packages for estimating and simulating costs." In: *Applied Ther-*

mal Engineering 104, pp. 647–658. DOI: `10.1016/j.applthermaleng.2016.05.073`.

Orkustofnun (2020). *Orkustofnun Data Repository*. OS-2020-T006-01 and OS-2020-T008-01.

Phillips, W. S. (2000). "Precise Microearthquake Locations and Fluid Flow in the Geothermal Reservoir at Soultz-sous-Forêts, France." In: *Bulletin of the Seismological Society of America* 90.1, pp. 212–228.

Phillips, W. S., L. S. House, and M. C. Fehler (1997). "Detailed joint structure in a geothermal reservoir from studies of induced microearthquake clusters." In: *Journal of Geophysical Research: Solid Earth* 102 (B6), pp. 11745–11763. DOI: `10.1029/97JB00762`.

Poliannikov, O. V., M. Prange, A. Malcolm, and H. Djikpesse (2013). "A unified Bayesian framework for relative microseismic location." In: *Geophysical Journal International* 194.1, pp. 557–571. DOI: `10.1093/gji/ggt119`.

Portier, S., F.-D. Vuataz, P. Nami, B. Sanjuan, and A. Gérard (2009). "Chemical stimulation techniques for geothermal wells: experiments on the three-well EGS system at Soultz-sous-Forêts, France." In: *Geothermics* 38.4, pp. 349–359. DOI: `10.1016/j.geothermics.2009.07.001`.

Poupinet, G., J. Fréchet, W. L. Ellsworth, M. J. Frèmont, and F. Glangeaud (1985). "Doublet analysis: improved accuracy for earthquake prediction studies." In: *Earthq. Predict. Res.* 1.1, pp. 81–93.

Pribnow, D. and R. Schellschmidt (2000). "Thermal tracking of upper crustal fluid flow in the Rhine graben." In: *Geophysical Research Letters* 27.13, pp. 1957–1960. DOI: `10.1029/2000GL008494`.

Ravier, G., O. Seibel, A. S. Pratiwi, J. Mouchot, A. Genter, R. Ragnarsdóttir, and X. Sengelen (2019). "Towards an optimized operation of the EGS Soultz-sous-Forêts power plant (Upper Rhine Graben, France)." Presented at: European Geothermal Congress 2019. The Hague, The Netherlands.

Reid, H. F. (1910). *The California Earthquake of April 18, 1906, Volume II: The Mechanics of the Earthquake*. Report of the State Earthquake Investigation Commission. Carnegie Institution of Washington.

Rice, J. R. and M. P. Cleary (1976). "Some basic stress diffusion solutions for fluid-saturated elastic porous media with compressible constituents."

In: *Reviews of Geophysics* 14.2, pp. 227–241. DOI: `10.1029/RG014i002 p00227`.

Richter, C. F. (1935). "An instrumental earthquake magnitude scale." In: *Bulletin of the Seismological Society of America* 25.1, pp. 1–32.

Ritsema, J. and T. Lay (1995). "Long-period regional wave moment tensor inversion for earthquakes in the western United States." In: *Journal of Geophysical Research: Solid Earth* 100 (B6), pp. 9853–9864. DOI: `10.10 29/95JB00238`.

Rojas, O., B. Otero, L. Alvarado, S. Mus, and R. T. Tous (2019). "Artificial Neural Networks as Emerging Tools for Earthquake Detection." In: *Computación y Sistemas* 23.2, pp. 335–350–350. DOI: `10.13053/cys-23-2-3 197`.

Ross, Z. E., D. T. Trugman, E. Hauksson, and P. M. Shearer (2019). "Searching for hidden earthquakes in Southern California." In: *Science* 364.6442, pp. 767–771. DOI: `10.1126/science.aaw6888`.

Rowe, C. A., R. C. Aster, W. S. Phillips, R. H. Jones, B. Borchers, and M. C. Fehler (2002). "Using Automated, High-precision Repicking to Improve Delineation of Microseismic Structures at the Soultz Geothermal Reservoir." In: *Pure appl. geophys.* 159, pp. 563–596.

Rubin, A. M. (2002). "Aftershocks of microearthquakes as probes of the mechanics of rupture." In: *Journal of Geophysical Research: Solid Earth* 107 (B7), ESE3/1–ESE3/16. DOI: `10.1029/2001JB000496`.

Rubin, A. M. and D. Gillard (2000). "Aftershock asymmetry/rupture directivity among central San Andreas fault microearthquakes." In: *Journal of Geophysical Research: Solid Earth* 105 (B8), pp. 19095–19109. DOI: `10.1029/2000JB900129`.

Rutqvist, J., A. P. Rinaldi, F. Cappa, P. Jeanne, A. Mazzoldi, L. Urpi, Y. Guglielmi, and V. Vilarrasa (2016). "Fault activation and induced seismicity in geological carbon storage – Lessons learned from recent modeling studies." In: *Journal of Rock Mechanics and Geotechnical Engineering* 8.6, pp. 789–804. DOI: `10.1016/j.jrmge.2016.09.001`.

Sambridge, M. S. and B. L. N. Kennett (1986). "A novel method of hypocentre location." In: *Geophysical Journal International* 87.2, pp. 679–697. DOI: `10.1111/j.1365-246X.1986.tb06644.x`.

Sanjuan, B., G. Negrel, M. Le Lous, E. Poulmarch, F. Gal, and P.-C. Damy (2020). "Main geochemical characteristics of the deep geothermal brine at Vendenheim (Alsace, France) with constraints on temperature and fluid circulation." Presented at: *World Geothermal Congress 2020*. Rekjavik, Iceland.

Sanjuan, B., J. Scheiber, F. Gal, S. Touzelet, A. Genter, and G. Villadangos (2016). "Inter-well chemical tracer testing at the Rittershoffen geothermal site (Alsace, France)." Presented at: *European Geothermal Congress 2016*. Strasbourg, France.

Sarti, A. and S. Tubaro (2002). "Detection and characterisation of planar fractures using a 3D Hough transform." In: *Signal Processing* 82.9, pp. 1269–1282. DOI: 10.1016/S0165-1684(02)00249-9.

Sato, T. and T. Hirasawa (1973). "Body Wave Spectra from Propagating Shear Cracks." In: *Journal of Physics of the Earth* 21.4, pp. 415–431. DOI: 10.4294/jpe1952.21.415.

Sausse, J., C. Dezayes, L. Dorbath, A. Genter, and J. Place (2010). "3D model of fracture zones at Soultz-sous-Forêts based on geological data, image logs, induced microseismicity and vertical seismic profiles." In: *Comptes Rendus Geoscience* 342.7, pp. 531–545. DOI: 10.1016/j.crte.2010.01.011.

Schaff, D. P. (2008). "Semiempirical Statistics of Correlation-Detector Performance." In: *Bulletin of the Seismological Society of America* 98.3, pp. 1495–1507. DOI: 10.1785/0120060263.

Schaff, D. P. and F. Waldhauser (2010). "One Magnitude Unit Reduction in Detection Threshold by Cross Correlation Applied to Parkfield (California) and China Seismicity." In: *Bulletin of the Seismological Society of America* 100.6, pp. 3224–3238. DOI: 10.1785/0120100042.

Schill, E., A. Genter, N. Cuenot, and T. Kohl (2017). "Hydraulic performance history at the Soultz EGS reservoirs from stimulation and long-term circulation tests." In: *Geothermics* 70, pp. 110–124. DOI: 10.1016/j.geothermics.2017.06.003.

Schmittbuhl, J., O. Lengliné, S. Lambotte, M. Grunberg, C. Doubre, J. Vergne, F. Cornet, and F. Masson (2020). "A triggered seismic swarm below the city of Strasbourg, France in November 2019." Presented at: European Geothermal Workshop 2020. Strasbourg, France.

Schmittbuhl, J., O. Lengliné, F. Cornet, N. Cuenot, and A. Genter (2014). "Induced seismicity in EGS reservoir: the creep route." In: *Geothermal Energy* 2.1, p. 14. DOI: 10.1186/s40517-014-0014-0.

Schneider, J. F., W. D. Pennington, and R. P. Meyer (1987). "Microseismicity and focal mechanisms of the intermediate-depth Bucaramanga Nest, Colombia." In: *Journal of Geophysical Research: Solid Earth* 92 (B13), pp. 13913–13926. DOI: 10.1029/JB092iB13p13913.

Schoenball, M., C. Baujard, T. Kohl, and L. Dorbath (2012). "The role of triggering by static stress transfer during geothermal reservoir stimulation." In: *Journal of Geophysical Research: Solid Earth* 117 (B9). DOI: 10.1029/2012JB009304.

Schoenball, M., T. M. Müller, B. I. R. Müller, and O. Heidbach (2010). "Fluid-induced microseismicity in pre-stressed rock masses." In: *Geophysical Journal International* 180.2, pp. 813–819. DOI: 10.1111/j.1365-246X.2009.04443.x.

Schoenball, M., L. Dorbath, E. Gaucher, J. F. Wellmann, and T. Kohl (2014). "Change of stress regime during geothermal reservoir stimulation." In: *Geophysical Research Letters* 41.4, pp. 1163–1170. DOI: 10.1002/2013GL058514.

Shapiro, S. A. and C. Dinske (2009). "Scaling of seismicity induced by nonlinear fluid-rock interaction." In: *Journal of Geophysical Research: Solid Earth* 114 (B9). DOI: 10.1029/2008JB006145.

Shapiro, S. A., C. Dinske, and J. Kummerow (2007). "Probability of a given-magnitude earthquake induced by a fluid injection." In: *Geophysical Research Letters* 34.22. DOI: 10.1029/2007GL031615.

Shapiro, S. A., P. Audigane, and J.-J. Royer (1999). "Large-scale in situ permeability tensor of rocks from induced microseismicity." In: *Geophysical Journal International* 137.1, pp. 207–213. DOI: 10.1046/j.1365-246x.1999.00781.x.

Shearer, P. M. (2019). *Introduction to Seismology.* 2nd edition. Cambridge, UK: Cambridge University Press. 443 pp.

Shelly, D. R., G. C. Beroza, and S. Ide (2007). "Non-volcanic tremor and low-frequency earthquake swarms." In: *Nature* 446.7133, pp. 305–307. DOI: 10.1038/nature05666.

Shelly, D. R., D. P. Hill, F. Massin, J. Farrell, R. B. Smith, and T. Taira (2013). "A fluid-driven earthquake swarm on the margin of the Yellowstone caldera." In: *Journal of Geophysical Research: Solid Earth* 118.9, pp. 4872–4886. DOI: `10.1002/jgrb.50362`.

Skoumal, R. J., M. R. Brudzinski, and B. S. Currie (2015). "Distinguishing induced seismicity from natural seismicity in Ohio: Demonstrating the utility of waveform template matching." In: *Journal of Geophysical Research: Solid Earth* 120.9, pp. 6284–6296. DOI: `10.1002/2015JB012265`.

Slinkard, M., D. Schaff, N. Mikhailova, S. Heck, C. Young, and P. G. Richards (2014). "Multistation Validation of Waveform Correlation Techniques as Applied to Broad Regional Monitoring." In: *Bulletin of the Seismological Society of America* 104.6, pp. 2768–2781. DOI: `10.1785/0120140140`.

Slinkard, M., S. Heck, D. Schaff, N. Bonal, D. Daily, C. Young, and P. Richards (2016). "Detection of the Wenchuan Aftershock Sequence Using Waveform Correlation with a Composite Regional Network." In: *Bulletin of the Seismological Society of America* 106.4, pp. 1371–1379. DOI: `10.1785/0120150333`.

Snow, D. T. (1965). "A parallel plate model of fractured permeable media." Dissertation. University of California, Berkeley.

Song, F., H. S. Kuleli, M. N. Toksöz, E. Ay, and H. Zhang (2010). "An improved method for hydrofracture-induced microseismic event detection and phase picking." In: *GEOPHYSICS* 75.6, A47–A52. DOI: `10.1190/1.3484716`.

Spence, G. H. and E. Finch (2014). "Influences of nodular chert rhythmites on natural fracture networks in carbonates: an outcrop and two-dimensional discrete element modelling study." In: *Geological Society, London, Special Publications* 374.1, pp. 211–249. DOI: `10.1144/SP374.18`.

Suteau, A. M. and J. H. Whitcomb (1979). "A local earthquake coda magnitude and its relation to duration, moment Mo, and local Richter magnitude ML." In: *Bulletin of the Seismological Society of America* 69.2, pp. 353–368.

Taron, J. and D. Elsworth (2010). "Coupled mechanical and chemical processes in engineered geothermal reservoirs with dynamic permeability." In: *International Journal of Rock Mechanics and Mining Sciences* 47.8, pp. 1339–1348. DOI: `10.1016/j.ijrmms.2010.08.021`.

Terzaghi, K. (1936). "The shearing resistance of saturated soils and the angle between planes of shear." In: *Proceedings of the First International Conference on Soil Mechanics and Foundation Engineering*. Cambridge, Massachusetts: Harvard University Press, pp. 54–56.

Tóth, T. M. (2010). "Determination of geometric parameters of fracture networks using 1D data." In: *Journal of Structural Geology* 32.7, pp. 878–885. DOI: `10.1016/j.jsg.2009.04.006`.

Trifu, C. I. (2002). *The Mechanism of Induced Seismicity*. Springer Science & Business Media. 632 pp.

Utsu, T. (2002a). "Relationships between magnitude scales." In: *International Handbook of Earthquake and Engineering Seismology, Part A*. Ed. by Lee, W. H. San Diego: Academic Press, pp. 733–746.

Utsu, T. (2002b). "Statistical features of seismicity." In: *International Handbook of Earthquake and Engineering Seismology, Part A*. Ed. by Lee, W. H. San Diego: Academic Press, pp. 719–732.

Vasterling, M., U. Wegler, J. Becker, A. Brüstle, and M. Bischoff (2017). "Real-time envelope cross-correlation detector: application to induced seismicity in the Insheim and Landau deep geothermal reservoirs." In: *Journal of Seismology* 21.1, pp. 193–208. DOI: `10.1007/s10950-016-9597-1`.

Vidal, J., A. Genter, and F. Chopin (2017). "Permeable fracture zones in the hard rocks of the geothermal reservoir at Rittershoffen, France." In: *Journal of Geophysical Research: Solid Earth* 122.7, pp. 4864–4887. DOI: `10.1002/2017JB014331`.

Vidal, J. and A. Genter (2018). "Overview of naturally permeable fractured reservoirs in the central and southern Upper Rhine Graben: Insights from geothermal wells." In: *Geothermics* 74, pp. 57–73. DOI: `10.1016/j.geothermics.2018.02.003`.

Vidal, J., A. Genter, F. Chopin, and E. Dalmais (2016). "Natural fractures and permeability at the geothermal site Rittershoffen, France." Presented at: European Geothermal Congress 2016. Strasbourg, France.

Vidal, J., P. Patrier, A. Genter, D. Beaufort, C. Dezayes, C. Glaas, C. Lerouge, and B. Sanjuan (2018). "Clay minerals related to the circulation of geothermal fluids in boreholes at Rittershoffen (Alsace, France)." In:

Journal of Volcanology and Geothermal Research 349, pp. 192–204. DOI: `10.1016/j.jvolgeores.2017.10.019`.

Waldhauser, F. (2002). "Fault structure and mechanics of the Hayward Fault, California, from double-difference earthquake locations." In: *Journal of Geophysical Research* 107 (B3). DOI: `10.1029/2000JB000084`.

Waldhauser, F. and W. L. Ellsworth (2000). "A Double-Difference Earthquake Location Algorithm: Method and Application to the Northern Hayward Fault, California." In: *Bulletin of the Seismological Society of America* 90.6, pp. 1353–1368. DOI: `10.1785/0120000006`.

Wang, H. F. (2000). *Theory of Linear Poroelasticity with Applications to Geomechanics and Hydrogeology.* Princeton University Press. 314 pp.

Wang, R., F. Lorenzo-Martín, and F. Roth (2003). "Computation of deformation induced by earthquakes in a multi-layered elastic crust—FORTRAN programs EDGRN/EDCMP." In: *Computers & Geosciences* 29.2, pp. 195–207. DOI: `10.1016/S0098-3004(02)00111-5`.

Wang, R., F. Lorenzo-Martín, and F. Roth (2006). "PSGRN/PSCMP—a new code for calculating co- and post-seismic deformation, geoid and gravity changes based on the viscoelastic-gravitational dislocation theory." In: *Computers & Geosciences* 32.4, pp. 527–541. DOI: `10.1016/j.cageo.2005.08.006`.

Wang, Z. and G. AlRegib (2014). "Automatic fault surface detection by using 3D Hough transform." In: *SEG Technical Program Expanded Abstracts 2014, Denver, Colorado*, pp. 1439–1444. DOI: `10.1190/segam2014-1590.1`.

Watkins, H., C. E. Bond, D. Healy, and R. W. Butler (2015). "Appraisal of fracture sampling methods and a new workflow to characterise heterogeneous fracture networks at outcrop." In: *Journal of Structural Geology* 72, pp. 67–82. DOI: `10.1016/j.jsg.2015.02.001`.

Watkins, H., D. Healy, C. E. Bond, and R. W. Butler (2018). "Implications of heterogeneous fracture distribution on reservoir quality; an analogue from the Torridon Group sandstone, Moine Thrust Belt, NW Scotland." In: *Journal of Structural Geology* 108, pp. 180–197. DOI: `10.1016/j.jsg.2017.06.002`.

Weidler, R., A. Gerard, R. Baria, J. Baumgaertner, and R. Jung (2002). "Hydraulic and micro-seismic results of a massive stimulation test at 5 km depth at the european hot-dry-rock test site Soultz, France." Presented at: Workshop on Geothermal Reservoir Engineering Stanford University. Stanford,California.

Willis-Richards, J., K. Watanabe, and H. Takahashi (1996). "Progress toward a stochastic rock mechanics model of engineered geothermal systems." In: *Journal of Geophysical Research: Solid Earth* 101 (B8), pp. 17481–17496. DOI: 10.1029/96JB00882.

Withers, M., R. Aster, C. Young, J. Beiriger, M. Harris, S. Moore, and J. Trujillo (1998). "A comparison of select trigger algorithms for automated global seismic phase and event detection." In: *Bulletin of the Seismological Society of America* 88.1, pp. 95–106.

Yoon, C. E., O. O'Reilly, K. J. Bergen, and G. C. Beroza (2015). "Earthquake detection through computationally efficient similarity search." In: *Science Advances* 1.11. DOI: 10.1126/sciadv.1501057.

Zang, A., V. Oye, P. Jousset, N. Deichmann, R. Gritto, A. McGarr, E. Majer, and D. Bruhn (2014). "Analysis of induced seismicity in geothermal reservoirs – An overview." In: *Geothermics* 52, pp. 6–21. DOI: 10.1016/j.geothermics.2014.06.005.

Zang, A. and O. Stephansson (2009). *Stress Field of the Earth's Crust.* Springer Science & Business Media. 327 pp.

Zoback, M. D. (2010). *Reservoir Geomechanics.* Cambridge University Press. 505 pp.

Part IV

Appendix

Appendix A

Seismicity induced during the development of the Rittershoffen geothermal field, France

↻ **Geothermal Energy**

RESEARCH   **Open Access**

Seismicity induced during the development of the Rittershoffen geothermal field, France

Vincent Maurer[1*] ⓘ, Emmanuel Gaucher[2], Marc Grunberg[3], Rike Koepke[2], Romain Pestourie[3] and Nicolas Cuenot[1]

*Correspondence:
vincent.maurer@es.fr
[1] ES-Geothermie, 5 rue
de Lisbonne, Le Belem,
67300 Schilitigheim, France
Full list of author information
is available at the end of the
article

Abstract

The development of the Rittershoffen deep geothermal field (Alsace, Upper Rhine Graben) between 2012 and 2014 induced unfelt seismicity with a local magnitude of less than 1.6. This seismicity occurred during two types of operations: (1) mud losses in the Muschelkalk formation during the drilling of both wells of the doublet and (2) thermal and hydraulic stimulations of the GRT-1 well. Seismicity was also observed 4 days after the main hydraulic stimulation, although no specific operation was performed. During chemical stimulation, however, no induced seismicity was detected. In the context of all field development operations and their injection parameters (flow rates, overpressures, volumes), we detail the occurrence or lack of seismicity, its magnitude distribution and its spatial distribution. The observations suggest the presence of the rock stress memory effect (Kaiser effect) of the geothermal reservoir as well as uncritically stressed zones connected to the GRT-1 well and/or rock cohesion. A reduction of the seismic rate concurrent with an increase of injectivity was noticed as well as the reactivation of a couple of faults, including the Rittershoffen fault, which was targeted by the wells. These results are derived from the homogeneous and consistent catalogue of more than 1300 local earthquakes that is provided. This reference catalogue is based on a standard detection method, whose output was manually verified and improved. The given absolute locations have been computed in a calibrated, geologically realistic 3D velocity model. Our work builds on previous analyses addressing the seismicity induced by the GRT-1 hydraulic stimulation and places the results into a historical context, thus considering the full dynamics of the observed phenomena. This paper also complements existing descriptions of the hydrothermal characteristics of the deep reservoir by providing insights separate from the wells.

Keywords: Seismic monitoring, Induced seismicity, Geothermal system, Stimulation, Upper Rhine Graben

Introduction

The Upper Rhine Graben (URG) currently hosts several enhanced geothermal system (EGS) plants that are in the exploitation phase, such as those in Rittershoffen and Soultz-sous-Forêts in France (Baujard et al. 2017; Genter et al. 2018), Landau and Insheim in Germany (Ganz et al. 2013; Küperkoch et al. 2018) and Riehen in Switzerland. Other EGS projects in France are in the drilling phase (Vendenheim and Illkirch-Graffenstaden) or

in an earlier stage (Eckbolsheim, Hurtigheim, Wissembourg), demonstrating the growing interest and viability in utilizing deep geothermal resources in the current energy mix. All of these EGS fields exploit hot local geothermal brine that is circulating in fracture and fault networks of Triassic sediments and the underlying granitic fractured basement. The geological context of this extensional basin hosts many faults bounding local horst and graben structures (Schumacher 2002), and the high geothermal gradient observed (Baillieux et al. 2013) strongly contributes to the geothermal development of this area.

EGS technology consists of increasing the low natural hydraulic performance of deep geothermal reservoirs by thermal, chemical and/or hydraulic stimulations. These stimulations aim to improve the connection of the wells with the nearby formation and increase the permeability in a reservoir, allowing the geothermal brine to be produced or reinjected at economically viable flow rates (Baujard et al. 2017; Nami et al. 2008; Portier et al. 2009; Schindler et al. 2010). In the course of these stimulations, seismicity is often induced (Majer et al. 2007; Zang et al. 2014), which, on the one hand, provides insight into the reservoir properties but, on the other hand, must be mitigated to prevent harmful effects on the population and goods, and on the project sustainability and acceptability (Deichmann and Giardini 2009; Gaucher et al. 2015). Seismicity can also be temporarily or continuously induced during the exploitation itself, i.e., during the inter-well circulation of the geothermal fluid (Baujard et al. 2018; Cuenot and Genter 2015; Evans et al. 2012; Megies and Wassermann 2014).

Worldwide, approximately 30 EGS sites have been or are being developed, and far fewer sites are active. This observation calls for continuous investigations of existing geothermal sites and an extensive description of any new site to increase the maturity level of such a technology, especially from a seismic risk perspective. Our work intends to contribute to this effort: we detail the occurrence or lack of seismicity, its magnitude distribution and its spatial distribution, in the light of all field operations and their injection parameters (flow rates, over-pressures, volumes). Thus, detailed description of the microseismic activity in parallel with the geothermal operations is presented for the first time for the Rittershoffen geothermal site. This paper complements the hydrothermal characterization of the Rittershoffen deep reservoir, performed by Baujard et al. (2017), and the seismicity analysis of Lengliné et al. (2017), by considering all reservoir operations, in addition to the hydraulic stimulation of the first well.

In this paper, first, we discuss the context of the Rittershoffen deep geothermal field. Then, the seismic networks implemented to monitor the field are described, as well as the processing, which was applied to the continuous records. Finally, the local seismicity identified during the major development phases (drillings, stimulations), which covers the period December 2012–June 2014, is characterized and discussed in the context of the field operational parameters.

Geothermal field context

Upper Rhine Graben geological setting

The deep geothermal field of Rittershoffen is located on the western margin of the NE–SW-striking central segment of the URG. The URG is a 300-km-long, 40-km-wide rift zone with an azimuthal extension averaging N20° E between Mainz (Germany) and Basel (Switzerland) (Fig. 1) (Ziegler 1992). It is associated with the Rhine valley, which is

Fig. 1 Simplified geological map of the Upper Rhine Graben indicating the geothermal gradients and status of current deep geothermal fields (modified from the final report of the GeORG Project INTERREG IV 2013)
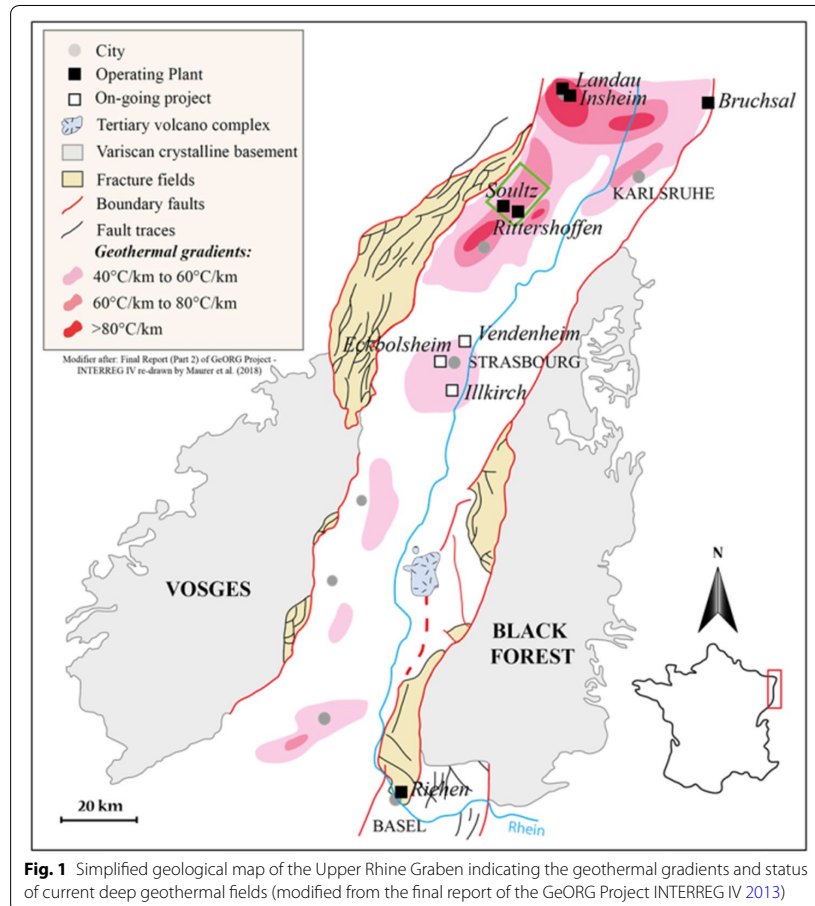
structurally bounded in the south by the folded Jura, in the west by the low-relief Vosges mountain range, in the east by the Black Forest massif and in the north by the Vogelsberg volcanic massif.

Tectonically, the western and the eastern edge of the URG are limited by major normal faults. A regional extension began 40 My ago, which is at the origin of the spacing between the Western and Eastern Rhine faults. Moreover, in the center of the graben, the sedimentological filling of the basin is syn-tectonic. The sedimentary cover is also affected by numerous normal faults, which also contributed to the opening of the URG.

Very favorable temperature gradients, higher than 60 °C/km, may be encountered at relatively shallow depths, and strong high-temperature anomalies also exist (Baillieux et al. 2013). Typically, from the surface to the top of the Middle Triassic (Muschelkalk), a conductive zone is observed, which is located above a multi-kilometric convective zone into which the geothermal fluid circulates (Fig. 2). The natural permeability in the convective zone is shown to be governed by the natural fracture system embedded in an approximately impermeable matrix (Baujard et al. 2017; Dezayes

Fig. 2 a East–West simplified vertical section of the Rhine Graben crossing the Soultz-sous-Forêts GPK–2 and the Rittershoffen GRT-1 wells (from Edel et al. 2018); **b** temperature logs, at equilibrated thermal conditions, for the Soultz-sous-Forêts GPK-2 well (from Genter et al. 2010) and for the Rittershoffen GRT-1 well (from Baujard et al. 2017) (vertical scale is in MD)
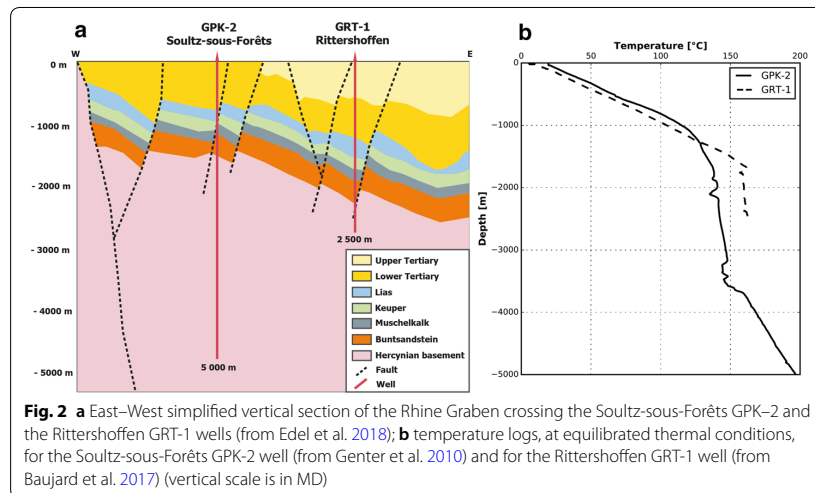
et al. 2010; Genter et al. 2010; Sanjuan et al. 2016). Consequently, natural faults play a major role in geothermal reservoir circulation and are the primary targets for exploitation. Therefore, almost all projects in the URG exploit the deep, fractured reservoirs located within the Triassic sediments and/or the crystalline basement (Soultz-sous-Forêts, Landau, Insheim, Rittershoffen) (Fig. 2).

Rittershoffen geothermal site development

Rittershoffen is located in northern Alsace, ~ 7 km southeast of Soultz-sous-Forêts. Designed for direct use of geothermal heat, the deep geothermal plant of Rittershoffen is one of very few plants of that kind currently operating in Europe. The plant currently produces a thermal power of 24 MWth, with a production temperature of 170 °C and a production flow rate of 70 L/s. The geothermal heat is provided to a biorefinery located in the city of Beinheim, 15 km away from the geothermal plant, through a specific transport loop.

The historic exploitation of oil and gas in the area highlighted the high-temperature anomalies at the Rittershoffen site. Furthermore, the reprocessing of 2D vintage seismic reflection profiles provided a preliminary structural model of the subsurface and revealed a major fault that affects the entire sedimentary cover and propagates into the granitic basement at a relatively shallow depth (~ 2.2 km below surface). Accordingly, Rittershoffen was selected for the development of a geothermal site and the Rittershoffen normal fault selected as target for the geothermal wells.

The first well, GRT-1, reached a final measured depth (MD) of 2580 m at the end of December 2012 (Fig. 3). Its open-hole section crosses the Buntsandstein sandstone and the fractured Paleozoic granite (Duringer et al. in press). Various logs and hydraulic tests were performed throughout the year 2013. Because the initial well injectivity index was low, a strategy was defined to enhance the connection of the well to the reservoir and the fracture system. Stimulation operations were applied in two

Fig. 3 Timeline of the operations performed during the development of the Rittershoffen deep geothermal field. The seismogenic periods of interest (during GRT-1 drilling, thermal and hydraulic stimulations and GRT-2 drilling) are indicated by black triangles
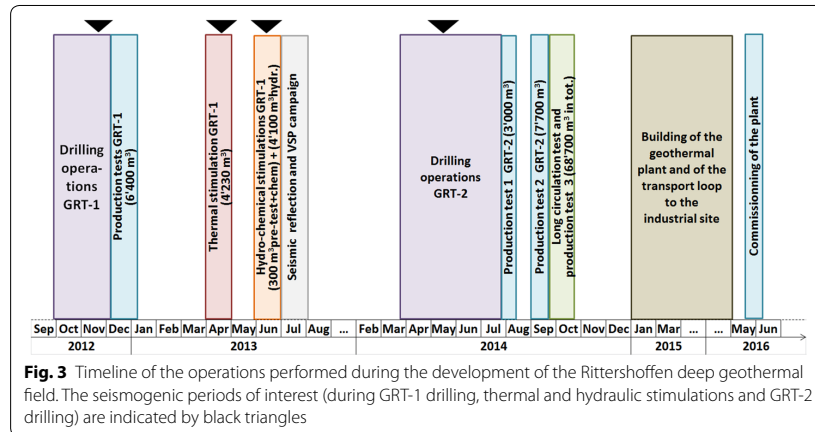
sequences: first in April 2013, with a thermal stimulation and, second in June 2013, with both chemical and hydraulic stimulations.

The injection temperature being similar in thermal and hydraulic stimulations (about 10 °C), the main difference lies in the injection flow rate. In a thermal stimulation, fluid injection is performed under reduced flow rate, which is expected to predominantly activate thermo-mechanical effects to enhance the reservoir permeability. On the contrary, higher flow rates are applied during hydraulic stimulation to activate hydro-mechanical effects.

After successful stimulation, which increased the initial injectivity index by a factor of five (Baujard et al. 2017), an active 2D seismic survey was performed. The main purpose was to define the trajectory of the second well of the doublet, GRT-2, and to improve the structural model of the underground (see subsection "Velocity model"). Thus, the drilling of GRT-2 started in March 2014 and ended in August 2014. GRT-2 is a deviated well, 3200 m in length, that reaches 2707 m TVD GL.

Production and circulation tests were performed after the drilling phase. No reservoir enhancement was necessary because production tests revealed that the initial productivity index was high enough, between 2.8 and 3.5 L/s/bar for the expected exploitation flow rate (Baujard et al. 2017). The year 2015 was dedicated to constructing the heat transport loop and the geothermal plant, which was commissioned in May 2016 and has been continuously operating since.

Six months prior to any field operation, seismicity was monitored by several networks (see subsection "Seismic monitoring"). No seismicity (natural or induced) was detected during this period. Four main seismogenic periods were later identified (Maurer et al. 2015): first, during the drilling of the first well, GRT-1; second, during the thermal stimulation of GRT-1; third, during the hydraulic stimulation; and fourth, during the drilling of GRT-2. This paper focuses on these four seismogenic periods.

Velocity model

In such a geological context, using a 1D velocity model is not the best method to accurately locate the seismicity induced at the Rittershoffen site. Moreover, the fault

identified as the most permeable zone in the area and targeted by the geothermal doublet exhibits ~ 350-m offset (~ 200-m vertically). Accordingly, a 3D velocity model was developed for the area. This model is based on the active seismic interpretation and the geological and geophysical logs acquired in GRT-1.

First, the numerous vintage seismic lines were reprocessed to better represent the deep formations. Following the June 2013 active seismic survey, two seismic lines, centered on Rittershoffen and oriented NNW–SSE and W–E, were added to the 3D seismic processing flow. Hence, five main seismic horizons were identified: the top of the "Fish shale" (Oligocene top), the top of the Lias (Jurassic top), the marl–calcareous lithological transition (Keuper or Trias top), the calcareous–sandstone lithological transition (top of the Buntsandstein) and the altered crystalline basement (top of the basement). In addition to the horizon selection, many faults were identified and incorporated for interpretation. Time-to-depth conversion of the horizons was constrained using vertical seismic profiles (VSPs), available sonic logs or check-shots. In the Rittershoffen zone, only the VSP data associated with the GRT-1 well were available and thus used. The five main horizons could be accurately positioned in depth at and around the GRT-1 well. With this active seismic interpretation, a regional model covering ~ 250 km^2 was obtained (Maurer et al. 2016).

In the second step, the VSP, the sonic log and the stratigraphic interpretation of GRT-1 (Aichholzer et al. 2016; Duringer et al. in press) were compared to better constrain the velocity model near GRT-1. As a result, two interfaces exhibiting noticeable velocity contrasts were added to the five main seismic interfaces. One corresponds to the bottom of the weathered zone, positioned 80 m below the surface. Its topography was assumed to follow the ground surface topography. The second interface corresponds to the top of the Muschelkalk formation, which is located between the Keuper and Buntsandstein formations. The top of the Buntsandstein surface was considered to be representative of the top of the Muschelkalk formation.

Once the underground layers were defined, the VSP data were used again to compute P-wave interval velocities (Vp) for each formation. Although the velocity is computed along GRT-1, it is assumed to be representative of the entire Rittershoffen area.

To develop the S-wave velocity (Vs) model, the full sonic log was used. From this log, average Vp/Vs ratios were calculated for the identified layers, thus providing interval S-wave velocities. Because the full sonic log was acquired below ~ 450 m MD, the Vp/Vs ratio was fixed to 2.12 for the two shallowest formations, i.e., until the top of the "Fish shale". This ratio corresponds to the median value measured at the top of the "Fish shales".

The final Vp, Vs and Vp/Vs values for each formation of the final 3D model are provided in Table 1. Figure 4 shows the corresponding profiles along GRT-1 with the entire sonic log. As observed, the P-wave velocity derived from the VSP (red curve) is consistent with the P-wave velocity derived from the full sonic log (dark gray curve). Furthermore, the main interfaces considered in the final model correspond to noticeable velocity contrasts in the sonic log. Figure 4 also shows as background a vertical South–North section of the 3D P-wave velocity model, next to GRT-1 and GRT-2 wells (red curves).

Table 1 Interval seismic velocities applied in the 3D velocity model

Interface	Depth in GRT1 (m TVD MSL)	Vp (m/s)	Vs (m/s)	Vp/Vs
Surface (at GRT1)	− 151	1300	613	2.12
Bottom of weathered zone	− 71	2315	1092	2.12
Top of "Fish shales"	272	2961	1544	1.92
Top of Lias	1023	3332	1778	1.87
Top of Keuper	1298	4307	2413	1.78
Top of Muschelkalk	1504	5236	2821	1.86
Top of Buntsandstein	1649	4818	2858	1.69
Top of unaltered granite	2209	5951	3351	1.78

The velocity parameters apply below the depth of the mentioned interfaces, which is given along GRT1

Fig. 4 Vertical profile of the 3D velocity model along GRT-1 overlaying a vertical South–North section of the 3D P-wave velocity model next to GRT-1 and GRT-2 wells (red curves). The red velocity profile indicates the Vp derived from the VSP, the blue velocity profile indicates the Vs derived from the VSP and the Vp/Vs ratio of the full sonic (see text for further explanations). The Vp and Vs measured by the full sonic log are presented for comparison in dark and light gray, respectively

To locate induced seismicity, this 3D velocity model is discretized with a 20-m side cubic mesh.

Seismic monitoring

Permanent monitoring network

To detect any seismicity induced by the Rittershoffen field operations, a permanent seismic network, of four surface stations, was deployed 6 months before any drilling operation, which was in compliance with the French mining authorities. This network completed the eastern part of the network dedicated to the surveillance of the Soultz-sous-Forêts geothermal plant, composed of eight surface stations in operation since

2002. Thus, since 2012, the micro-seismic activity of the Rittershoffen geothermal project has been monitored by a permanent seismic network of 12 surface stations (Fig. 5).

The Soultz-sous-Forêts network is composed of 1-Hz short-period seismometers, consisting of one or three components (L4C/L4C-3D), deployed at the surface. Signals are digitized on site, sampled at 150 Hz and transmitted to a central site. At the central site, a SeisComp3 (Hanka et al. 2010) plugin enables the *École et Observatoire des Sciences de la Terre* of the University of Strasbourg (EOST) to get the data in real-time via an internet connection. The Rittershoffen network is also composed of 1-Hz, short-period, three-component seismometers (L4C-3D) deployed at the surface. The signals were initially digitized at a sampling rate of 100 Hz that was increased to 200 Hz beginning of 2014. The digital data are sent in real-time to a central site where a SeisComp3 server allows EOST to access them via an internet connection.

This permanent seismic network was the only one actively monitoring prior to the chemical and hydraulic stimulation of GRT-1 in June 2013 (Fig. 5 and Table 4).

Temporary monitoring network

In addition to the permanent network, several temporary surface stations were deployed in June 2013, using equipment belonging to the Geophysical Instrument Pool Potsdam

Fig. 5 Map of the location of the 43 seismological stations monitoring the Rittershoffen geothermal field. The 12 permanent stations are indicated with black squares; these were active during all development operations. The five temporary stations recording from the start of GRT-1 chemical and hydraulic stimulation are displayed as black inversed triangles. The 26 temporary stations added before GRT-2 drilling commenced are displayed as black triangles. The trajectories of the Rittershoffen and Soultz-sous-Forêts geothermal wells are also indicated in red

(GIPP) of the GFZ German Research Centre for Geosciences (Gaucher et al. 2018). The primary objective was to improve the detection and location capabilities of the seismic monitoring during the field development operation (i.e., well tests; chemical and hydraulic stimulations of GRT-1; drilling, stimulation, and production tests of GRT-2; and further circulation tests). A secondary objective was to apply and test several processing techniques based on dense seismic networks (Gaucher et al. 2013). Hence, a dense network lay-out was designed as a large antenna focusing on the geothermal wells and providing homogeneous coverage. It consisted of three circles centered on the wellheads with radius up to 5 km (i.e., about twice the depth of the geothermal reservoir) and a distance between the stations ranging between 1.5 and 2 km. Consequently, 31 three-component seismometers were added temporarily to the permanent network. Short-period, 1-Hz seismometers (L4C-3D) were selected because microseismicity was the main focus. The signals were digitized, sampled at 300 Hz and stored as miniSEED files. Several stations periodically uploaded the files to the SeisComp3 server at EOST, thus providing shortly delayed seismograms complementing the permanent network data.

During the chemical and hydraulic stimulations of GRT-1—the third seismogenic phase of the project (June 2013)—a total of 17 seismic stations (12 permanent, five temporary) were monitoring (Fig. 5 and Table 4). From April to November 2014—the fourth and final seismogenic phase of the project—all temporary stations were operational and recording. Thus, during that period, which includes the GRT-2 drilling, 43 stations were continuously monitoring the area.

Figure 5 shows the location of all seismic stations constituting the monitoring network installed between 2012 and 2014 around the Rittershoffen geothermal field. The dense part of the network centered around GRT-1 and GRT-2 is clearly visible as well as the relatively regular spacing between the stations. The periods during which the stations were active are also indicated in Table 4: Appendix provides the exact location of the stations and their operational periods.

Data processing

During real-time monitoring, the SeisComp3 automatic detection parameters were changed over time, as knowledge was gained from the identified seismicity. These changes led to inhomogeneous detection capabilities hence an inconsistent seismological catalogue over time. To correct from this bias, all continuous waveforms acquired around the seismogenic periods were processed again using a homogeneous automatic detection procedure based on the SeisComp3 toolbox. This detection procedure combined the grid-search method of the "scautoloc" module with the density-based clustering algorithm (Ester et al. 1996) of the "scanloc" module (Clinton et al. 2018; Grigoli et al. 2017). The latter can use S-picks and performs generally better than the former. The scanloc detection parameters were tuned using a parameter sweep method, on an initial database that contained all induced earthquakes identified by manual and systematic review of the data recorded during the first 6 h of the GRT-1 hydraulic stimulation. The recovery rate of the final automatic system applied to this initial database reached 96%. This re-processing stage guarantees homogeneous detection capabilities over the period of interest. Once applied, all events detected automatically were manually controlled. For the local earthquakes, correction or addition of the P- and S-wave onset

times with the associated uncertainties was done and, when possible, the peak-to-peak amplitude of the P-wave on the vertical component and the associated half-period were measured. Then, the earthquakes were located in the 3D velocity model (see subsection "Velocity model") using the NonLinLoc software (Lomax et al. 2000, 2009; Lomax 2018) with the application of the Bayesian inversion approach proposed by Tarantola and Valette (1982) and the oct-tree importance sampling algorithm (Lomax and Curtis 2001). The location provides the earthquake hypocenter together with its uncertainty given as a 3D uncertainty ellipsoid (Lomax 2018). For simplicity, in the following, the location uncertainty will be quantified by one parameter only: the largest half-length of the major axis of the uncertainty ellipsoid.

Although the velocity model is relatively well defined from prior data, a major source of location error still lies in the S-wave velocity value of the superficial layers (see subsection "Velocity model"). To decrease the impact of such an unknown and to increase the hypocenter accuracy, the velocity model was calibrated using a seismic event recorded while drilling the GRT-2 well. On May 26, 2014, the drill bit became stuck in the GRT-2 at a depth of 1862 m MD (the total depth was 2123 m MD at that time), in the Middle Muschelkalk formation (Trias). During one of the attempts to free the bottom-hole assembly, the mud pressure increased, resulting in mud losses and induced seismicity. Interestingly, the drilling of this well section was performed with a rate of penetration that was higher than in the previous and next depth intervals, which supports the existence of a weak or fractured zone at this depth and could well explain the adherence of the bottom-hole assembly and the subsequent mud losses and induced seismicity. Consequently, we can reasonably assume that the initial seismicity occurred at the well at that depth. Hence, one of the first recorded earthquakes associated with this incident was positioned at 1862 m MD in GRT-2 and used as a "calibration shot" (event 2014-05-26T13:33:24.622974Z). This event was chosen because 73 seismic phases were picked, among which were 38 P-waves; thus, both phases were observed on almost all 43 stations of the network. The event location was determined using the 3D velocity model and only the P-wave arrivals to avoid contamination from the unconstrained S-wave velocity in the first 450 m of the model and because the network coverage at that time was sufficiently homogeneous. Hence, the earthquake origin time could be estimated and used to compute the observed travel times of both P- and S-waves to the seismic stations. After subtracting the latter from the theoretical travel times computed between the 1862 m MD reference point in GRT-2 and the stations, time differences at each station for both phase types were obtained. By adding the time differences to the corresponding observed wave arrivals, the calibration shot could be perfectly relocated to its expected position. Finally, such a time correction was systematically applied to the picked arrival times prior to locating any identified earthquake and compensates, to a certain extent, for the inadequacy of the 3D velocity model in the superficial layers.

Once the earthquake hypocenter was obtained, the magnitude determined at the station KUHL was assigned to the earthquake. Usually, the event magnitude is estimated from the average magnitude obtained at the different stations of the network. However, this procedure was not applied for three reasons. First, the coverage and the number of stations of the seismological network changed over time, which would lead to changing average magnitude for a similar event. Second, the KUHL station is a permanent

station that was operating during all seismogenic periods. It is located approximately 2.5 km NNW from the well pad (Fig. 5) and shows a good signal-to-noise ratio around the P-wave arrival, also for weak events. Therefore, a local magnitude at this station could be estimated for 95% of the located earthquakes, which was not the case for any other station of the network. Finally, the seismic focal mechanisms inverted for the different seismogenic periods (see subsection "Spatial distribution") show similar rupture geometry when the latter is well determined, or, at least, consistent polarities at the measured stations, when many solutions may fit. So, the radiation coefficient to station KUHL may be considered relatively constant over time. Consequently, the magnitude determined at the single permanent station KUHL is the most consistent over time and will allow comparisons between the four seismogenic periods. (When the P-wave amplitude could be measured at a station different from KUHL, its associated magnitude was computed. This showed that, on average, the difference in magnitude between the KUHL station and the other station remained consistent for all processed events.) To calculate the magnitude, the formula of Bakun and Joyner (1984) was applied using their default parameters. The approach using the P-wave peak-to-peak amplitude and the corresponding half-period, measured on the vertical component of KUHL, was selected because it is less sensitive to high low-frequency noise that may contaminate a weaker higher-frequency seismic arrival. This is particularly noticeable for small magnitude local earthquakes, for which magnitude determination is always critical (Kendall et al. 2019).

To estimate the magnitude of completeness of the seismic catalogue, or part of it, and the *b*-value for the corresponding earthquake set, we applied the goodness-of-fit approach, as described by Wiemer and Wyss (2000) and Aki (1965), which assumes that the frequency–magnitude distribution of the seismic events follows a Gutenberg–Richter power law (see subsection "Magnitude distribution").

Results

The processing procedure was applied to the continuous seismic data recorded during and around all major development operations: GRT-1 drilling, stimulations and testing; and GRT-2 drilling (Fig. 3). The result is a reference seismic catalogue, which is available as Additional file 1. Geographical coordinates are given in "Lambert II étendu" and the reference selected for depths is the mean sea level (MSL). The altitude of the geothermal platform is 149 m. This catalogue is more exhaustive and consistent than the preliminary catalogue presented by Maurer et al. (2015).

Table 2 summarizes the characteristics of the observed seismicity in parallel with the primary characteristics of the reservoir development operations.

In total, 1348 earthquakes were detected: 26 during GRT-1 drilling, 146 during GRT-1 thermal stimulation, 992 during hydraulic stimulation of the same well and 184 during GRT-2 drilling. Thus, the hydraulic stimulation of GRT-1 was the most seismogenic operation.

The local magnitude of the seismicity ranged between -1.5 and 1.6 and the magnitude of completeness was estimated to be between -0.65 and 0.05 (see next subsections for details). None of the induced events was felt by the population.

Table 2 Summary of the seismicity observed during the development of the Rittershoffen geothermal reservoir

First event Last event	N_{EVT}	M_{MIN} to M_{MAX}	ΔDepth (m TVD MSL)	Q_{MAX} (L/s)	WHP_{MAX} (MPa)	Volume (m³)	Duration (h)	Productivity and injectivity indices (L/s/bar)
Drilling of GRT-1								
2012-11-29T22:23:33 2012-11-29T22:51:42	26	− 1.3 to 0.6	1200–2000	–	–	–	–	$P = 0.45$
GRT-1 production test								
None	–	–	–	–	–	6400	216	$P = 0.6$
Thermal stimulation of GRT-1								
2013-04-24T07:24:05 2013-04-25T09:44:28	146	− 1.5 to 0.3	1300–3050	25	2.8	4135	62.6	$I = 0.9$
Pre-stimulation test and chemical stimulation of GRT-1								
None	–	–	–	27 + 5	2.5 +/	357 + 269	6.5 + 14.2	$I = 1.7$
Hydraulic stimulation of GRT-1 and injection test								
2013-06-27T15:23:38 2013-07-01T00:19:11	831	− 1.4 to 0.9	1200–2000	80 + 60	3.3 + 2.2	3180 + 820	21.7 + 6.5	$I = 2.5$
2013-07-02T04:46:15 2013-07-12T22:14:23	161	− 0.9 to 1.6	1300–2050	–	–	–	–	–
Drilling of GRT-2								
2014-05-26T12:18:06 2014-05-26T23:43:55	184	− 1.5 to 1.0	1250–1850	–	–	–	–	$P = 2.8$ to 3.5

For each period, N_{EVT} represents the number of located events, M_{MIN} and M_{MAX} are the minimum and maximum observed magnitudes, respectively, and ΔDepth is the depth interval containing 80% of the events. Finally, Q_{MAX}, WHP_{MAX}, Volume and Duration correspond to the maximum flow rate, maximum wellhead pressure, total injected or produced volume and duration of the stimulation operations, respectively. The productivity or injectivity indices have been measured following the associated operations

In the following subsections, the seismicity, which was recorded during GRT-1 drilling, GRT-1 thermal, chemical and hydraulic stimulations and during GRT-2 drilling is described in greater detail. Interpretation of these results and comparison of the seismogenic behaviors between these different phases is presented in the "Discussion" section.

Seismicity during GRT-1 and GRT-2 drilling

During the drilling of the GRT-1 well, seismicity was induced and was most likely due to circulation losses while setting the 9–5/8″ pipe in the 12″1/4 open-hole section, between 1029 and 1773 m TVD MSL. The mud parameters had a flow rate of 17 L/s and an injection pressure of 4.8 to 6 MPa. A total of 26 earthquakes were recorded on November 29, 2012, within a period of 30 min (between 22:23 and 22:51 UTC). The magnitude ranged between − 1.3 and 0.6.

Figure 6 shows the location of these events. As observed, the hypocenters are generally oriented in a South–North direction. However, as emphasized by the depth sections,

Fig. 6 Epicenter map (left) and South–North vertical projection (right) of the seismicity recorded during the GRT-1 drilling (magenta circles) and GRT-2 drilling (blue circles)

Fig. 7 GRT-2 drilling. Seismic rate, per 15 min, and local magnitudes of the recorded earthquakes
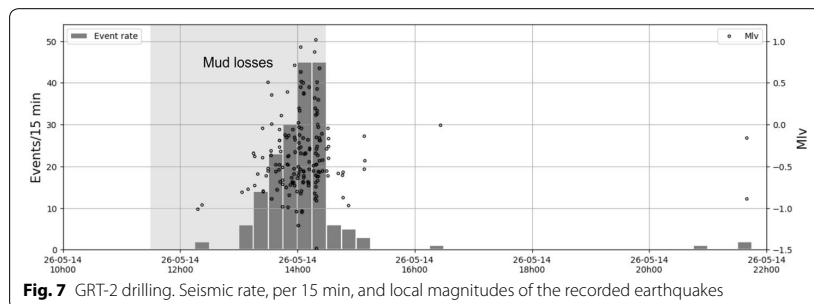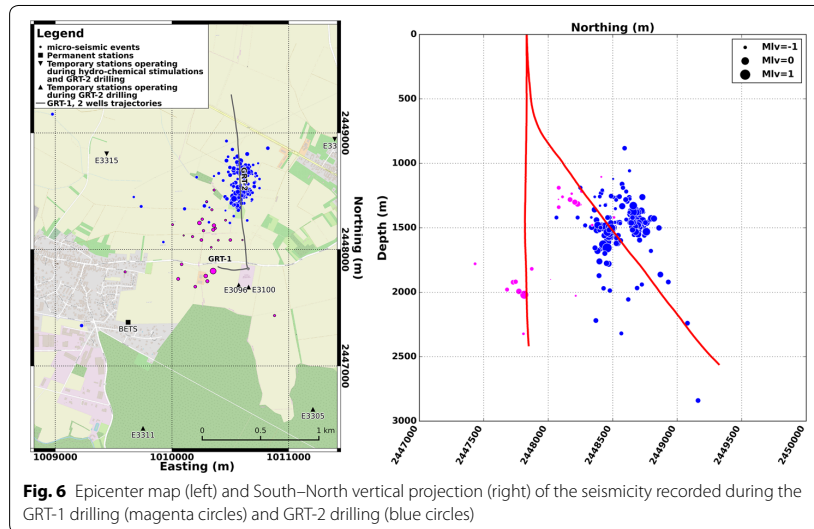
they are divided into two clusters: a northern one between 1200 and 1400 m and a southern one between 1800 and 2000 m that is near GRT-1. The low number of events and their weak magnitudes prevent a reliable interpretation of the associated hypocenters. Furthermore, the network configuration may bias the results as explained in the subsection "Spatial distribution" of "Discussion".

As previously mentioned (see section "Data processing"), earthquakes were also induced on May 26, 2014 during GRT-2 drilling operations (Fig. 7). A total of 184 earthquakes were detected, 177 within 3 h (between 13:00 and 16:00 UTC) (Fig. 7. However, most of the seismicity occurred within approximately 1 h, between 13:30 and 14:30 UTC). The maximum seismic rate was 45 events in 15 min. The magnitude range of these local earthquakes was between -1.5 and 1.

As observed in Fig. 6, the first hypocenters are centered on GRT-2 at the depth of the mud losses (1517 m TVD MSL), as expected from the location calibration procedure (see subsection "Data processing"). However, the seismicity later divided into two clusters, about 200 m apart, one to the south and one to the north of the well. They are

aligned in a N7° E direction and both are approximately at the same depth interval in the Muschelkalk. During GRT-2 drilling, 80% of the hypocenters exhibited uncertainties between ±20 m and ±200 m, with a median of ±55 m. Therefore, the location uncertainties cannot affect the observation of the two clusters that may be associated with real geological features.

Seismicity during GRT-1 thermal stimulation

The first significant induced seismicity occurred during GRT-1 thermal stimulation in April 2013, which was 4 months after drilling (Fig. 8). A total of 146 induced earthquakes were detected and located. The stimulation consisted of injecting reservoir fluids, previously discharged from GRT-1, at an ambient temperature of 10 °C into the open-hole section of the well (1773 to 2431 m TVD MSL) that was drilled into sandstone and granite (silicate rocks), which had a temperature of approximately 160 °C. Thus, between April 23 and 25, 2013, over the course of 62.6 h, 4135 m^3 of brine were injected. The initial injection flow rate of 10 L/s was increased stepwise by 5 L/s, up to 25 L/s, and then decreased stepwise to 15 L/s before ending. The wellhead pressure (WHP) quickly increased to 2.8 MPa at 15 L/s; the pressure subsequently remained below that level but was generally above 1.8 MPa, regardless of the injection rate. No downhole pressure gauge was available during GRT-1 thermal stimulation.

The first detected induced event occurred 26 h after the beginning of the injection. Considering the WHP, this event occurred 21 h after a first raise of the WHP to the maximum value of 2.8 MPa, at 15 L/s, or 3 h after the WHP reached its maximum value again at 20 L/s. However, the majority of the seismic activity occurred 39 h after the start of injection, when the flow rate reached 20 L/s, then 25 L/s, with a maximum rate of approximately one event per minute. Interestingly, the seismic rate decreased strongly while the injection was on-going at 25 L/s, whereas the WHP decreased from 2.7 to 2.2 MPa. A last burst of seismicity was observed at 25 L/s (1.9 MPa). These events occurred 4 h before the decrease of the injection rate from 25 to 20 L/s or 11 h before the injection was stopped.

In total, 146 events were detected and located, with magnitudes ranging from −1.5 to 0.3. Most of the seismicity occurred between 22:00 and 06:00 local time, which explains the ability of the system to detect small magnitude earthquakes, as low as Mlv = − 1.5.

As presented in Fig. 8, most of the earthquakes are clustered around and north of the GRT-1 well. After removal of the outliers, the best plane fitting the hypocenter distribution (least-squares criterion) has a N3° E direction, dipping 86° W. The length of the primary cloud is ~ 1500 m along its main direction and is ~ 500 m wide. Eighty percent (between the 10th and 90th percentiles) of the hypocenters are located between 1300 and 3050 m depth (the deepest events are not visible in Fig. 8) and have location uncertainties between ±80 m and ±250 m, with a median of ±135 m. The shallowest events are the northernmost and the deepest are the southernmost. Deeper and to the south of the primary seismic cloud, earthquakes along the main direction are observed.

Seismicity during GRT-1 chemical and hydraulic stimulations

In June 2013, additional stimulations were performed in GRT-1 (Fig. 9). Following a pre-stimulation test on June 22, chemical treatments of three different sections of the open-hole isolated by packers were performed on June 23, 24 and 25. In total, 269 m^3

Fig. 8 GRT-1 thermal stimulation: epicenter map (**a**) and South–North vertical projection (**b**) of the seismicity recorded (red circles); injection flow rate and wellhead pressure over time (**c**) in parallel with the seismic rate per 15 min and the local magnitude (**d**)
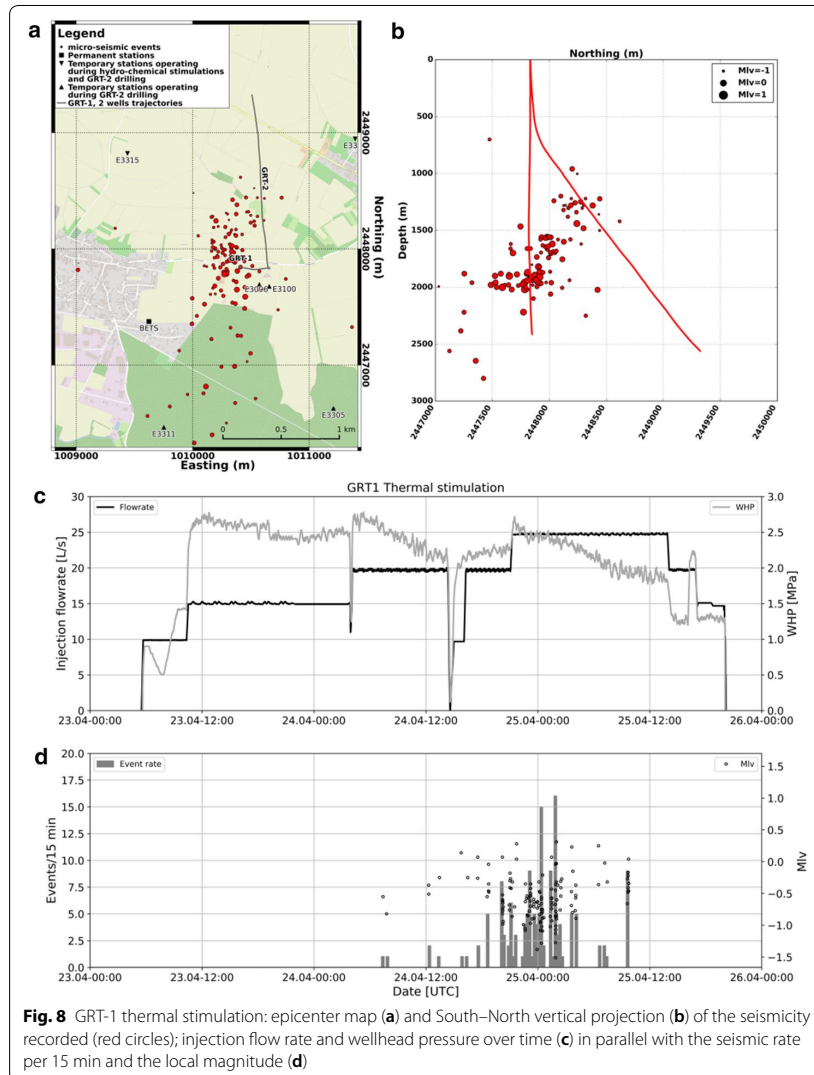
of fluid, of which 216 m^3 were biodegradable acids, were injected (Baujard et al. 2017). No seismic activity was detected during these operations (Fig. 9).

On June 27 and 28, 2013, hydraulic stimulation of the GRT-1 open-hole section was performed, followed by a short injection test (Fig. 10). During hydraulic stimulation, the injection flow rate was raised stepwise from 5 to 80 L/s and then decreased stepwise. Approximately 3180 m^3 of brine were injected within approximately 21.7 h. The maximum WHP was 3.3 MPa, and the maximum downhole overpressure (DHP) was 3.0 MPa, both of which were reached at the end of the highest injection rate period (80 L/s). During the post-stimulation test, 820 m^3 of brine were injected at a specified flow rate, which was also increased stepwise up to 60 L/s and then decreased

Fig. 9 GRT-1 pre-stimulation test, chemical and hydraulic stimulations. Injection flow rate and wellhead pressure (top) in parallel with the seismic rate per hour and local magnitude (bottom)
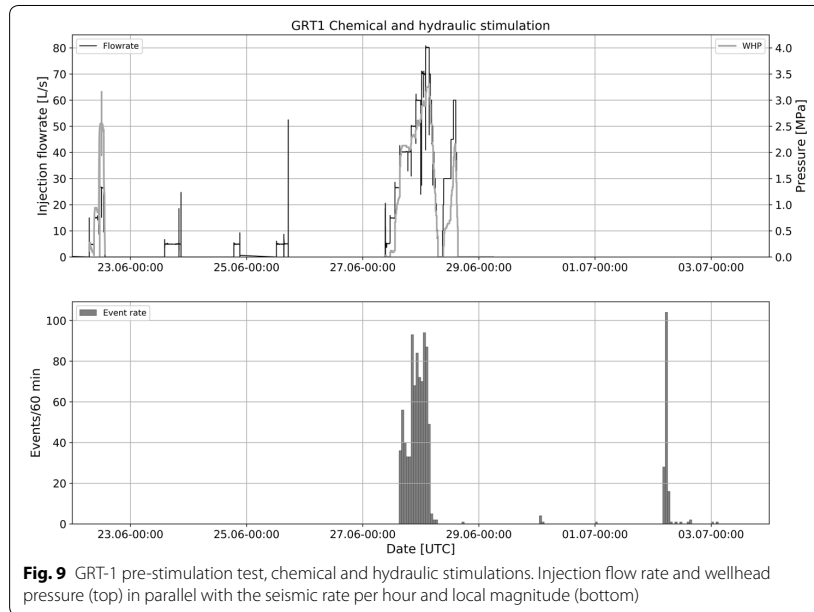
stepwise. The post-stimulation test began 2 h after the hydraulic stimulation for a total duration of approximately 6.5 h. The maximum WHP and DHP were both equal to 2.2 MPa.

In total, 824 earthquakes were detected and located during the hydraulic stimulation. The seismic activity began 6 h after injection began, when the flow rate changed from 26.5 to 40 L/s and the WHP reached 1.5 MPa (DHP = 1.8 MPa). Then, seismicity occurred continuously with an increase of the seismic rate. Starting with an average of 40 events per hour, the rate reached an average of 80 events per hour. The maximum observed rate was 50 events per 15 min, which was observed at the time the flow rate increased from 40 to 50 L/s and the WHP reached 2.2 MPa (DHP = 2.4 MPa). Seismicity observed during the injection for the most part stopped during the injection step down, when the rate was back to 50 L/s and WHP = 2.2 MPa (DHP = 2.4 MPa), i.e., 2.5 h before injection stopped. The magnitude of the observed events ranged between −1.4 and 0.9, and the largest event occurred during the time of the highest injection rate of 80 L/s.

During the short injection test, no seismicity was recorded, even if the flow rate was raised as high as 60 L/s with a WHP = 2.2 MPa (DHP = 2.4 MPa). However, one event was recorded 1.5 h later.

In addition to the six earthquakes recorded on the June 30 and July 1, 2 days after injection (34 h), the most striking observation was a burst of seismicity on July 2, 4 days after injection (425 h) and in the absence of any on-site operation (Fig. 10). Within approximately 1.5 h, 146 earthquakes were recorded with a magnitude range between −0.9 and 1.6.

The earthquakes observed during the hydraulic stimulation were located around GRT-1 and extended to the north (Fig. 10). The cloud they formed was approximately

Fig. 10 GRT-1 hydraulic stimulation: epicenter map (**a**) and South–North vertical projection (**b**) of the seismicity recorded during GRT-1 hydraulic stimulation (yellow circles), including the following crisis of July (green circles); injection flow rate, wellhead pressure and downhole overpressure over time (**c**) in parallel with the seismic rate per 15 min and the local magnitude (**d**); seismic rate per 15 min and local magnitude of the earthquakes recorded during the July crisis while no injection operation was on-going (**e**)

1800 m long and less than 500 m wide. The best least-squares fitting plane passing through the hypocenters is oriented N1° E, dipping 89° W, i.e., almost vertical. Most of the hypocenters were located between 1200 and 2000 m depth. The events at approximately 2000-m depth were located near the injection depth, whereas shallower events were located North of the injection. The earthquakes associated with the July 2013 burst extended the main stimulation cloud further NNE, in a N13° E direction, and a slight overlap between the hypocenters of both sequences was observed. This burst of seismicity was concentrated at two different depth intervals, between 1300 and 1500 m in the sedimentary layers, above the Muschelkalk, and between 1900 and 2100 m near the interface between the basement and sedimentary cover.

During the hydraulic stimulation, 80% of the hypocenters exhibited uncertainty between ± 35 m and ± 255 m, with a median of ± 95 m, whereas during the burst, 80% of the hypocenters exhibited uncertainty between ± 35 m and ± 180 m, with a median of ± 60 m.

Discussion

Occurrence of seismicity

Despite the injection temperature being similar in thermal and hydraulic stimulations (about 10 °C), the main difference lies in the injection flow rate. In a thermal stimulation, the flowrate is reduced to predominantly activate thermal effects contrarily to hydraulic stimulation that would enhance permeability to elevated pore pressure and shear slip of pre-existing fractures. According to Vidal et al. (2016), thermal stimulation is typically performed to enhance the near-well field permeability, which may have been reduced by drilling (cuttings and mud clogging feed zones), and thus this stimulation is generally performed immediately after drilling. As modeled by Gentier et al. (2004), during cold injection, thermal microcracking of quartz within the fractured zone is observed, which creates preferential flow paths and thus leads to preferential cooling in these fractures. At Rittershoffen, all identified permeable fractures are associated with quartz veins, which could enhance the thermal effect of cold reinjection through the fractured zones (Vidal et al. 2019). This technique is not usually applied to EGS geothermal wells in the URG, but has produced satisfactory results in high-temperature systems in volcanic environments.

During the GRT-1 thermal stimulation, seismicity started 26 h after the beginning of the injection, or 21 h after the WHP reached 2.8 MPa at 15 L/s (Fig. 8). Interestingly, this WHP was the largest observed over the entire operation and was also measured immediately after the 15 to 20 L/s and the 20 to 25 L/s injection steps. The lack of seismicity at the beginning of injection indicates that uncritically stressed zones connected to the open-hole existed and/or that rock cohesion was present. In the first case, it means that substantial pore pressure increase is needed to reach the Coulomb failure envelop, the latter meaning that the rock can sustain shear stress even though effective normal stress is null. From another perspective, the seismicity began 3 h following constant injection at 20 L/s and when the WHP was decreasing, which is evidence of increased injectivity and enhanced fluid circulation in the formation. This observation suggests that neither the flow rate nor the pressure observed when the first event occurred were at the origin of the seismicity, but rather delayed

(thermo-) mechanical effects on the rock mass due to the earlier part of the injection. Most of the seismicity occurred at the end of the 20-L/s injection plateau, when the WHP was increasing, and during the first half of the 25-L/s injection plateau. Then, the seismic rate decreased significantly while the injection was on-going at 25 L/s but the WHP was decreasing again. Finally, a last burst of seismicity was observed 11 h before injection ended. Thus, seismicity occurred only during a relatively short period of the injection.

Two months after thermal stimulation, the pre-stimulation test, chemical stimulation, hydraulic stimulation and injectivity test were conducted (Fig. 9). The seismic activity associated with these operations began only 6 h after start of the hydraulic stimulation, when the flow rate increased from 26.5 to 40 L/s, and the WHP reached 1.5 MPa (DHP = 1.8 MPa). Therefore, no seismicity was recorded during the pre-stimulation test, neither during the chemical stimulation nor during the injectivity test. The first two operations involved a limited volume of injected fluid, 626 m^3, which represents approximately 1/6 of the volume injected during thermal stimulation. Moreover, the injections were conducted at a maximum flow rate of 27 L/s and WHP of 2.5 MPa, which are levels not exceeding those observed during thermal stimulation, and under an injectivity index that was similar to that observed when the thermal stimulation ended (1.2 L/s/bar). Aware of the stimulation history, we would interpret the delayed seismicity to be a rock stress memory effect rather than a result of aseismic slips or creeping as suggested by Lengliné et al. (2017). Nonetheless, the latter cannot be excluded, especially for the first part of the thermal stimulation and if we consider that clay in fractured zones due to hydrothermal alteration could favor creeping rather than shearing (Meller and Kohl 2014). The rock stress memory effect implies that repeated loading of a rock mass generates seismicity only when and where maximum stress previously experienced is exceeded. Also known as the "Kaiser effect" (Kaiser 1950; Lavrov 2003), this characteristic has been observed in many EGS sites during forced fluid injection operations, e.g., Soultz-sous-Forêts (Dorbath et al. 2009), Cooper Basin—Australia (Baisch et al. 2015) and Berlín—El Salvador (Kwiatek et al. 2014). Nonetheless, in the present case, seismicity began only once the injection flow rate exceeded the largest rate applied (27 L/s) but at a WHP that was lower than previously measured (1.5 MPa vs. 2.8 MPa), which strictly differs from the Kaiser effect. This observation may be an evidence that the chemical stimulation was effective by creating new fluid pathways, not hydraulically stimulated yet.

Once seismicity began during the hydraulic stimulation, it continuously occurred and exhibited increasing seismic rates in correlation with increasing flow rates, except when the 60 to 70 L/s step was preceded by a 20-min injection at 27 L/s. A decrease in the seismicity rate was also observed during the 40-L/s injection plateau and when the WHP (and DHP) began to decrease, implying an increase of well injectivity, which was also observed at the end of the thermal stimulation. Thus, the decrease in seismicity is linked to an increase in injectivity throughout the course of the injection. Furthermore, seismicity almost vanished once the injection step-down phase began, which was also the case for the thermal stimulation, and no event was identified during the injectivity test following the hydraulic stimulation (except a single episode

approximately 1.5 h after injection stopped). These observations could also be interpreted as evidence of the Kaiser effect.

Figure 11 presents the distribution of the number of earthquakes above a minimum magnitude as a function of the injected volume for the thermal and hydraulic stimulations. The lowest minimum magnitude applied in both cases corresponds to the estimated magnitude of completeness (Fig. 12). For the hydraulic stimulation, the isolated burst of seismicity in July 2013 is not considered in the plot. As observed, there is no linear relation between both parameters during the thermal stimulation. During hydraulic stimulation, however, a linear tendency is observed after the first 500 m^3 are injected. This change in behavior may reflect an initialization phase of the main physical processes that induce seismicity and/or are a result of the previously conducted thermal stimulation. Deviation from the linear tendency was also observed and was expected; we noticed previously that seismicity decreased with increasing injectivity, and the seismicity rate increased with the injection steps, which implies hydro-mechanical coupling. Thus, the seismogenic index concept proposed by Shapiro et al. (2007) may not be applicable in a simple manner to the present case and that the underlying hypotheses are not fully satisfied. Specifically, it is questionable whether the pressure front diffusion in an infinite and homogeneous medium would be the mechanism responsible for controlling the seismicity occurrence (Cornet 2000).

Magnitude distribution

Figure 12 presents the frequency–magnitude distribution of the seismicity, which was identified during the GRT-1 thermal stimulation (145 events), the hydraulic stimulation (781 events), the following burst (152 events), and the drilling of GRT-2 (168 events). Given the low number of earthquakes recorded during the drilling of GRT-1, they are not considered in this analysis. As observed, a Gutenberg–Richter power law can explain more than 95% of the frequency–magnitude distribution of the seismic events at the given magnitudes of completeness (M_C). The M_C for these periods is very similar,

Fig. 11 Distribution of the number of earthquakes above a minimum magnitude (M_{Min}) as a function of the injected volume for the thermal stimulation (left) and hydraulic stimulation (right)

Fig. 12 Frequency–magnitude distribution of induced earthquakes: cumulative number (black circles) and histogram (gray bars), and an estimate of the magnitude of completeness and b-values. The results are given for the GRT-1 thermal stimulation (top left), GRT-2 drilling (bottom left), GRT-1 hydraulic stimulation—June (top right) and July burst (bottom right). The axis scales are different among the plots

approximately $M_C = -0.6$, except for the seismicity burst in July 2013, where $M_C = 0.05$. The occurrence of the seismicity during the seismicity burst, primarily between 7:00 and 9:00, which is when anthropogenic noise is relatively high, may explain the higher observed M_C value.

During the thermal stimulation and hydraulic stimulation, the *b*-values were estimated to 1.53 ± 0.15 and 1.16 ± 0.05, respectively. These are significantly higher than the typical tectonic value of 1, although only 42 events were used to calculate the *b*-value during the thermal stimulation (against 107 for the hydraulic stimulation). However, such high values are very common in injection-induced seismicity (Bachmann et al. 2011; Cuenot et al. 2008; Dorbath et al. 2009) and may be interpreted as the creation or reopening of small cracks and fractures in the rock mass due to high stress variation near the injection interval (El-Isa and Eaton 2014; Scholz 1968; Zang et al. 2014). Furthermore, the larger *b*-value measured during thermal stimulation may indicate relatively higher volumetric effects than the hydraulic stimulation, if not due to the low number of event used to calculate it. Thermal stimulation is supposed to activate thermomechanical effects and, to a lesser extent, hydro-mechanical effects, thus resulting in different rock responses.

In particular, the variable thermal properties of the minerals constituting the stimulated rock would lead to greater homogeneous breakdown of the matrix near the cold front. In the granite, fractures filled with secondary euhedral quartz (Glaas et al. 2018a, b) could be prone to thermal cracking (Wang et al. 1989). The event burst in July 2013 and the events induced by GRT-2 drilling, conversely, exhibit b-values of 0.92 ± 0.08 and 0.96 ± 0.07, respectively, which is more consistent with the reactivation of existing faults. In these periods, 61 and 75 events, respectively, could be used to calculate these values. These measurements corroborate the variation in the b-value between the hydraulic stimulation and the subsequent burst that was mentioned by Lengliné et al. (2017). They also highlight that different structures of different scales were activated by the hydraulic stimulation.
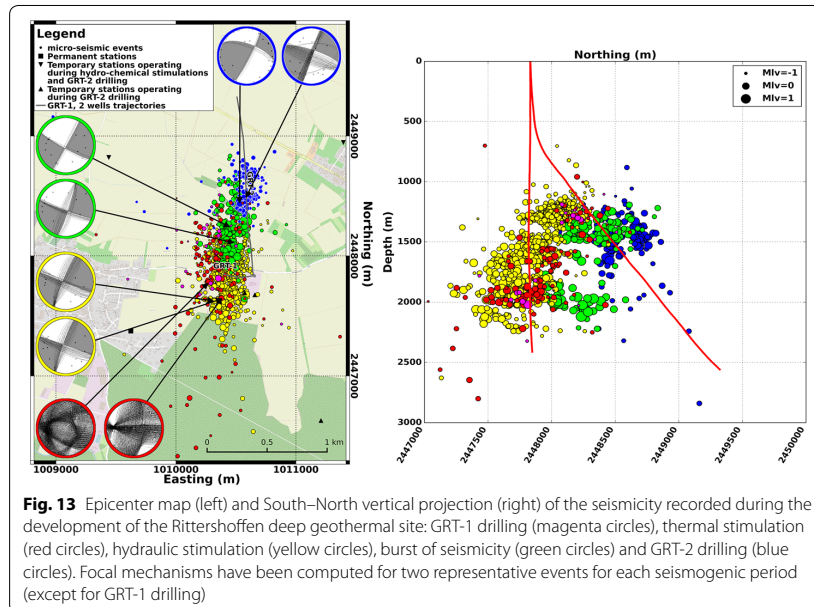
During the GRT-1 thermal and hydraulic stimulations, there was no tendency for higher magnitude events to occur as the stimulation was on-going.

Finally, the largest magnitude earthquakes observed during the thermal stimulation were much weaker than those of the hydraulic stimulation. Both stimulations involved the same amount of injected fluid; however, when considering the hydraulic stimulation as being complementary of the thermal stimulation (and chemical stimulation), this observation is in accordance with the general idea that the largest induced earthquake is related to the injected volume (Galis et al. 2017; McGarr 2014). However, this argument will not be further investigated because previously discussed observations suggest that the seismogenic response is more complex than the assumptions made in these modeling approaches.

Spatial distribution

In Fig. 13, the epicenter map shows that the cloud of seismicity associated with the thermal and hydraulic stimulations of GRT-1, as well as the July 2013 burst of seismicity, extends from the injection depth up to the GRT-2 well (which did not exist at that time) along an approximately N5° E vertical plane. The depth range of the cloud is relatively large. The deepest part roots in the granite and at the Buntsandstein–granite interface, which also corresponds to the intersection of the Rittershoffen fault with the well. Thus, the events clustered at approximately ~2000-m depth and extending to the north possibly occurred on the Rittershoffen fault, as also proposed by Lengliné et al. (2017). The shallowest part of the cloud reaches the 1300- to 1500-m depth interval, in the Keuper formation above the Muschelkalk. Thus, overall, the cloud appears to highlight a major vertical structure. Nonetheless, the observed vertical extension is questionable. First, this extension from more than 500 m cannot be a consequence of the location uncertainties, which are smaller than ± 255 m for more than 80% of the events. Second, the vertical distance to the injection point is relatively large, of the same order as the horizontal distance to the injection point. Such a development of seismicity is not in accordance with the expected normal- to strike–slip faulting regime of the region (Azzola et al. 2019; Cornet et al. 2007; Hehn et al. 2016), which favors a horizontal (rather than vertical) extension of seismicity. Third, the observed vertical distribution does not follow the dip of the Rittershoffen fault and would require the presence of another fault that was not identified, neither from drilling logs nor from active seismic processing. Fourth, the Keuper formation is not suspected to be very seismogenic because it is predominantly

Fig. 13 Epicenter map (left) and South–North vertical projection (right) of the seismicity recorded during the development of the Rittershoffen deep geothermal site: GRT-1 drilling (magenta circles), thermal stimulation (red circles), hydraulic stimulation (yellow circles), burst of seismicity (green circles) and GRT-2 drilling (blue circles). Focal mechanisms have been computed for two representative events for each seismogenic period (except for GRT-1 drilling)
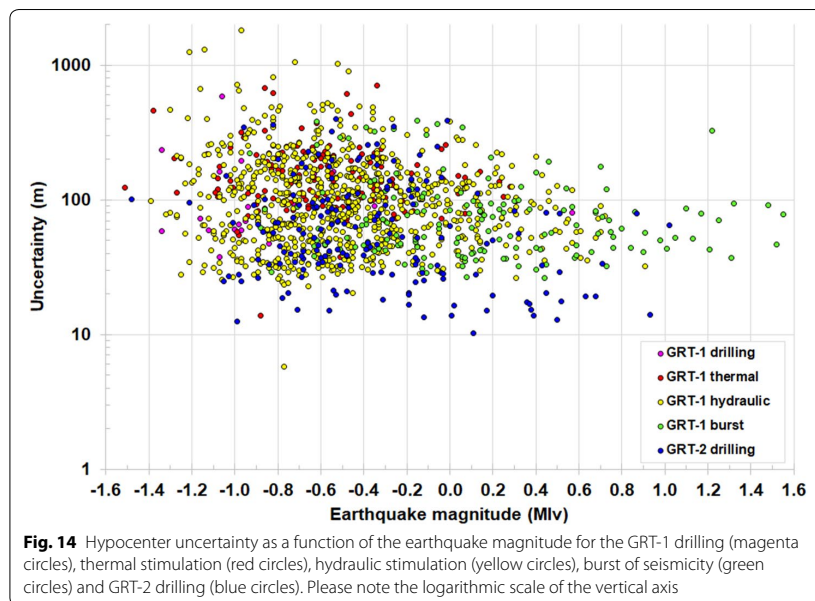
composed of evaporates and clays, which have a rather rheological ductile behavior. Moreover, it is noteworthy that, first, absolute locations are considered, even though being calibrated until the Muschelkalk. Second, the seismic network was composed of the permanent stations during the thermal stimulation with a few additional temporary stations: five stations during the hydraulic stimulation and eight stations during the July burst. All stations were exclusively located in the northern part of the GRT-1 well (Fig. 5). As discussed by Kinnaert et al. (2016), a large coverage gap may lead to strong uncertainties in the location and, interestingly, the average inclination of the seismic clouds (especially during hydraulic stimulation) is consistent with the location uncertainty direction. Further investigations highlighted a tendency of the hypocenters to belong to the deeper cluster when the number of seismic phases selected to locate an event was larger. Thus, the combined northern and vertical extension of the seismic events located south of the network may be, to some extent, a trade-off between depth and time resolution of the hypocenters due to the approximately exclusive northern coverage of the network prior to the GRT-2 drilling. (Such a trade-off could also explain both clusters associated with GRT-1 drilling.) Although relative earthquake location by double-differences (Poliannikov et al. 2013; Waldhauser and Ellsworth 2000) are beyond the scope of this paper, they may minimize or remove such effects by adding more constraints in the likelihood function of the earthquake hypocenters and origin times (Poliannikov et al. 2013). Consequently, the apparent vertical extension of the "GRT-1 cloud", especially up to 1300 m, and its apparent connection with the seismicity recorded during GRT-2 drilling should be further investigated before providing any definitive conclusions.

The suspected Kaiser effect highlighted by the occurrence of seismicity during stimulations should be supported by the location of the associated hypocenters. The Kaiser

Maurer *et al. Geotherm Energy*   (2020) 8:5

Page 24 of 31

effect is clearly observed between the seismicity occurring during the hydraulic stimulation and the following burst of seismicity (Fig. 13). Indeed, the July burst of seismicity is exclusively located at the northern rim of the seismicity induced during the hydraulic stimulation itself. However, the relatively widespread cloud of events associated with the thermal stimulation appears to cover a volume similar to the seismogenic zone of the hydraulic stimulation. Indeed, no evolution of the hypocenter distance to the well as a function of time was observed in this study. Yet, without relative location of the seismicity, detailed spatio-temporal interpretation is limited because the absolute hypocenter uncertainties can range between ± 20 m and ± 250 m. Figure 14 shows the hypocenter uncertainty as a function of the earthquake magnitude, for each period. As seen, the seismicity induced during thermal stimulation is less certain (median of ± 135 m) than seismicity induced during hydraulic stimulation (median of ± 95 m). This is first due to the smaller seismic network monitoring the thermal stimulation and second to lower magnitude events induced during that period (see Fig. 12). One can also note that the smallest hypocenter uncertainties are associated with earthquakes recorded during GRT-2 drilling (blue circles), that is when the monitoring network was the most complete. As expected, Fig. 14 highlights that the less certain hypocenters are associated with small magnitude events. However, small magnitude events do not necessarily lead to large hypocenter uncertainties because the seismic background noise also affects the imprecision of the P- and S-phase picking.

Focal mechanisms

Focal mechanisms were determined for earthquakes, which occurred during the thermal and hydraulic stimulations, the July burst and the GRT-2 drilling. They were assumed double-couples and were determined using FOCMEC (Snoke 2017) with

Fig. 14 Hypocenter uncertainty as a function of the earthquake magnitude for the GRT-1 drilling (magenta circles), thermal stimulation (red circles), hydraulic stimulation (yellow circles), burst of seismicity (green circles) and GRT-2 drilling (blue circles). Please note the logarithmic scale of the vertical axis

Maurer *et al. Geotherm Energy*   *(2020) 8:5*

Page 25 of 31

the polarity of the P-wave arrivals. Relative weighting of the polarities was applied to allow possible polarity mismatch close to the focal planes. Two earthquakes per seismogenic period were considered. To maximize the chances of determining the focal mechanism on the relatively noisy data, the earthquakes with the highest number of P-wave picks and the highest magnitudes were preselected. Then, the earliest and latest events of the sequence were chosen to form the pair assuming the chance that the focal mechanisms would differ higher. Table 3 gives the characteristics of the eight inverted mechanisms and the corresponding earthquake. Among all focal plane solutions, the solution associated with the median plane dip is given on the lower hemisphere in gray in Fig. 13, as well as all other possible solutions (with a maximum of 500 solutions).

As seen, all earthquakes induced during and after hydraulic stimulation and during drilling of GRT-2 have sinistral strike–slip focal mechanisms. The network coverage for the earthquakes induced during thermal stimulation is clearly too small and prevents determining the rupture geometry unambiguously. However, sinistral strike–slip is one of the numerous possible solutions.

These results show that a common rupture with strike, dip and rake in the intervals 195 to 210° N, 85 to 90° and −5 to 20°, respectively, could be attributed to the earthquakes associated with the stimulation operations, at least for the strongest ones. Interestingly, Azzola et al. (2019) identified a maximal horizontal stress direction of N15° in the Buntsandstein, which is consistent with the observed strike range and the earthquake depths. The corresponding focal plane is relatively consistent with the earthquake distribution as well as the Rittershoffen fault orientation. Hence, during thermal and hydraulic stimulations, the Rittershoffen fault was undoubtedly activated

Table 3 Characteristics of the earthquakes for which focal mechanism was determined

Period	Origin time	Easting (m)	Northing (m)	Depth (m TVD MSL)	Mlv	N_{POL}	Dip (°)	Strike (°)	Rake (°)
Thermal stimulation	2013-04-25 01:59:33	2,447,782	1,010,272	1960	0.31	5	–	–	–
Thermal stimulation	2013-04-25 03:38:00	2,447,649	1,010,380	1901	0.23	6	–	–	–
Hydraulic stimulation	2013-06-27 23:25:59	2,447,636	1,010,372	1993	0.69	14	80	199	− 3
Hydraulic stimulation	2013-06-28 01:45:44	2,447,624	1,010,312	1860	0.54	12	80	202	3
July burst	2013-07-02 04:53:52	2,448,243	1,010,448	2023	1.21	14	87	29	− 10
July burst	2013-07-02 05:11:18	2,448,113	1,010,473	1480	1.31	12	81	188	− 5
GRT-2 drilling	2014-05-26 13:33:25	2,448,495	1,010,587	1517	0.01	18	87	200	− 9
GRT-2 drilling	2014-05-26 14:18:29	2,448,456	1,010,532	1656	1.02	31	80	28	39

The column N_{POL} gives the number of P-wave polarities used to determine the focal mechanism. The focal plane angles follow the standard convention (Aki and Richards 1980)

189

beside other smaller faults or fractures as suggested by the *b*-values higher than 1. The seismicity recorded in July would belong exclusively to that structure, which is supported by the *b*-value of 0.92. These results also indicate that the hypothesis of attributing the local magnitude calculated at the KUHL station to the earthquakes is reasonable. Moreover, P-wave polarity at station KUHL is always negative (dilation) and supports this hypothesis in case of undetermined focal mechanism.

Conclusion

We presented and discussed the seismicity associated with the Rittershoffen field development, its occurrence, its magnitude distribution and its spatial distribution in the light of all field operations and their injection parameters. The development of the Rittershoffen geothermal reservoir was associated with unfelt seismicity. More than 1300 earthquakes were processed. Mud losses in the Muschelkalk formation, in the course of the drilling of both wells of the doublet, led to several tens (GRT-1) to several hundreds (GRT-2) of events located near the wells, all with local magnitudes smaller than 1.0.

Most of the recorded seismicity, 85%, was induced directly or indirectly by the GRT-1 stimulations. The initial 2.5-day thermal stimulation was the first operation that induced substantial seismicity. The latter, however, was recorded more than 1 day after the beginning of the injection and did not coincide with an abrupt change of the injection flow rate, nor the maximum injection flow rate (25 L/s), nor a WHP peak, nor the maximum WHP (2.8 MPa), showing that uncritically stressed zones connected to the open-hole may exist or/and that rock cohesion should be considered. Furthermore, a reduction of the seismic rate related to an increase of injectivity was observed during thermal and hydraulic stimulations. There was no clear evidence of a linear relationship between the number of recorded earthquakes and the injected volume.

Several observations are interpreted as a typical signature of the rock stress memory effect, or "Kaiser" effect, e.g., the lack of seismicity recorded during the pre-stimulation test of GRT-1 (the first injection following the thermal stimulation), during the chemical stimulations, for the first 6 h of the hydraulic stimulation and during the final injection test. This Kaiser effect signature was difficult to further support based on the earthquake hypocenters obtained from absolute location methods that are not sufficiently accurate, with the exception of the earthquakes associated with the burst of seismicity, which were located to the north of the previously active zone.

During stimulations, *b*-values were larger than 1.1, which may be interpreted as the creation or reopening of small cracks and fractures in the rock mass due to high stress variation near the injection. However, *b*-values decreased to 0.9 during the burst of seismicity following the hydraulic stimulation, which is interpreted as the reactivation of an existing major structure—possibly the Rittershoffen fault. During the seismicity burst, the largest event induced at Rittershoffen, $Mlv = 1.6$, occurred and the events typically had larger magnitudes than previously observed.

The absolute location of the seismicity as well as the determination of a few focal mechanisms support the idea that pre-existing faults were reactivated above the intersection between the Rittershoffen fault and the GRT-1 well, in the Buntsandstein–basement interface during the thermal and the hydraulic stimulations. The limited coverage of the seismic network before GRT-2 drilling, however, prevents strong conclusions

from being made on the veracity of the depth extension of the stimulated zone up to the Keuper formation, thus necessitating further investigations. The relative locations of future earthquakes will minimize systematic bias and will improve the geometrical interpretation of induced seismicity to understand better the development and the behavior of the Rittershoffen geothermal reservoir.

Supplementary information

Supplementary information accompanies this paper at https://doi.org/10.1186/s40517-020-0155-2.

> **Additional file 1.** Reference catalogue of the 1348 earthquakes discussed in the paper. For each event, it contains the following parameters, in the following order: origin date and time (UTC time), northing and easting of epicenter location (Lambert II extended coordinate system, meters), depth (true vertical depth below sea level, meters), local magnitude (vertical component), azimuth and dip of the small uncertainty axis (Az1, Dip1, degrees), azimuth and dip of the middle uncertainty axis (Az2, Dip2, degrees), smallest-, middle- and largest-uncertainties (Len1, Len2 and Len3, meters) and the recorded period: 0–GRT-1 drilling, 1–GRT-1 thermal stimulation, 20–GRT-1 hydraulic stimulation, 21–GRT-1 burst of seismicity and 3–GRT-2 drilling. See text for more details on how these values were calculated.

Abbreviations
ANR: French National Research Agency (Agence Nationale pour la Recherche); DCF: Deutschland longwave signal transmitted by station Mainflingen near Frankfurt am Main; DHP: downhole pressure; ECOGI: Operating company of the Rittershofen geothermal field (Exploitation de la Chaleur d'Origine Géothermale pour l'Industrie); EGS: enhanced geothermal system; EOST: École et Observatoire des Sciences de la Terre (Earth Science School and Observatory); ESG: ES-Géothermie; GFZ: German Research Centre for Geosciences; GIPP: Geophysical Instrument Pool Potsdam; GL: ground level; M_C: magnitude of completeness; MD: measured depth at ground Level; Mlv: vertical local magnitude; MSL: mean sea level; MWth: thermal megawatt; My: million years; STA/LTA: short time average over long time average; TVD: true vertical depth; URG: Upper Rhine Graben; UTC: coordinated universal time; Vp: P-wave velocity; Vs: S-wave velocity; VSP: vertical seismic profile; WHP: wellhead pressure.

Authors' contributions
All authors worked to generate the reference seismological catalogue presented in this paper. VM and EG analyzed the data and wrote the initial manuscript. MG completed the seismic monitoring and processing sections. All authors contributed to the final manuscript. All authors read and approved the final manuscript.

Availability of data and materials
The referenced seismic catalogue analyzed during this study is included in this published article as an Additional file 1. The raw seismic files acquired using the temporary seismic monitoring network are available upon request from the Geophysical Instrument Pool Potsdam of the GFZ German Research Centre for Geosciences by referencing the Scientific Technical Report of Gaucher et al. (2018).

Competing interests
The authors declare that they have no competing interests.

Author details
[1] ES-Geothermie, 5 rue de Lisbonne, Le Belem, 67300 Schilitigheim, France. [2] Division of Geothermal Research, Institute of Applied Geosciences, Karlsruhe Institute of Technology, Kaiserstraße 12, 76131 Karlsruhe, Germany. [3] Université de Strasbourg, CNRS, EOST UMS 830, 67000 Strasbourg, France.

Maurer *et al. Geotherm Energy*   (2020) 8:5

Page 28 of 31

Appendix
See Table 4.

Table 4 Seismic station locations (in the extended Lambert II Cartesian coordinate system) and associated recording periods: *P*1: from beginning of monitoring; *P*2: from GRT-1 chemical and hydraulic stimulation; and *P*3: before GRT-2 drilling

Network	Station	Easting (m)	Northing (m)	Depth (m MSL)	*P*1	*P*2	*P*3
Permanent	BETS	1,009,624.3	2,447,374.9	− 146	1	1	1
	FORA	1,004,921.7	2,452,089.6	− 156	1	1	1
	GUNS	999,344.6	2,449,908.1	− 224	1	1	1
	KEFF	1,005,387.2	2,455,522.6	− 208	1	1	1
	KUHL	1,009,871.8	2,449,753	− 176	1	1	1
	LAMP	1,000,768.6	2,454,636.3	− 257	1	1	1
	OBER	1,012,458.4	2,451,824.5	− 177	1	1	1
	OPS	1,006,369.1	2,450,232.9	− 198	1	1	1
	RITT	1,012,306.7	2,447,654.7	− 138	1	1	1
	SCHW	1,005,375.8	2,447,345.1	− 143	1	1	1
	STUN	1,014,315.6	2,450,563.5	− 146	1	1	1
	SURB	1,003,874.7	2,449,430.3	− 203	1	1	1
Temporary	E3022	1,005,972.5	2,448,936.6	− 182	0	0	1
	E3024	1,007,780.7	2,443,765.9	− 156	0	0	1
	E3025	1,009,739.1	2,442,950.1	− 140	0	0	1
	E3030	1,013,616	2,444,769	− 136	0	0	1
	E3033	1,014,891.8	2,447,162.2	− 134	0	0	1
	E3034	1,011,363.2	2,452,718.8	− 150	0	0	1
	E3078	1,012,931.8	2,448,467	− 161	0	0	1
	E3087	1,006,194.1	2,445,682.7	− 160	0	0	1
	E3088	1,009,872.2	2,449,747.5	− 185	0	0	1
	E3091	1,014,489.8	2,449,656.8	− 129	0	0	1
	E3094	1,007,480.1	2,451,506.2	− 152	0	0	1
	E3096	1,010,572.3	2,447,695.7	− 153	0	0	1
	E3099	1,011,863.9	2,442,894.2	− 137	0	0	1
	E3100	1,010,661.2	2,447,676.4	− 153	0	0	1
	E3101	1,009,269.3	2,452,535.8	− 148	0	0	1
	E3300	1,013,394.7	2,449,956.1	− 129	0	0	1
	E3301	1,011,395.5	2,448,938.1	− 172	0	1	1
	E3302	1,009,983.8	2,451,388.6	− 145	0	0	1
	E3304	1,013,385.8	2,446,283	− 131	0	0	1
	E3305	1,011,216.5	2,446,617.3	− 149	0	0	1
	E3306	1,007,340.8	2,446,496.7	− 154	0	0	1
	E3307	1,009,955.2	2,444,680	− 139	0	0	1
	E3308	1,007,578.8	2,448,349.6	− 174	0	1	1
	E3310	1,008,593.7	2,445,272.5	− 147	0	0	1
	E3311	1,009,752.3	2,446,444.8	− 159	0	0	1
	E3312	1,015,300	2,445,164.7	− 128	0	0	1
	E3313	1,008,256.6	2,450,042	− 182	0	1	1
	E3314	1,014,234.2	2,448,519.4	− 147	0	0	1
	E3315	1,009,443.4	2,448,820	− 175	0	1	1
	E3316	1,012,177	2,444,781.8	− 132	0	0	1
	E3317	1,011,370.6	2,450,674.4	− 144	0	1	1

References
Aichholzer C, Duringer P, Orciani S, Genter A. New stratigraphic interpretation of the Soultz-sous-Forêts 30-year-old geothermal wells calibrated on the recent one from Rittershoffen (Upper Rhine Graben, France). Geotherm Energy. 2016;4(1):132.
Aki K. 17. Maximum Likelihood Estimate of b in the Formula logN = a-bM and its Confidence Limits. Bull Earthq Res Inst Univ Tokyo. 1965;43(2):237–9.
Aki K, Richards PG. Quantitative seismology, theory and methods. 1st ed. San Fransisco: W. H. Freeman and Co.; 1980. p. 557.
Azzola J, Valley B, Schmittbuhl J, Genter A. Stress characterization and temporal evolution of borehole failure at the Rittershoffen geothermal project. Solid Earth. 2019;10:1155–80. https://doi.org/10.5194/se-10-1155-2019
Bachmann CE, Wiemer S, Woessner J, Hainzl S. Statistical analysis of the induced Basel 2006 earthquake sequence: introducing a probability-based monitoring approach for enhanced geothermal systems. Geophys J Int. 2011;186(2):793–807.
Baillieux P, Schill E, Edel J-B, Mauri G. Localization of temperature anomalies in the Upper Rhine Graben: insights from geophysics and neotectonic activity. Int Geol Rev. 2013;55(14):1744–62.
Baisch S, Rothert E, Stang H, Vörös R, Koch C, McMahon A. Continued geothermal reservoir stimulation experiments in the cooper basin (Australia). Bull Seismol Soc Am. 2015;105(1):198–209.
Bakun WH, Joyner WB. The ML scale in central California. Bull Seismol Soc Am. 1984;74(5):1827–43.
Baujard C, Genter A, Dalmais E, Maurer V, Hehn R, Rosillette R, Vidal J, Schmittbuhl J. Hydrothermal characterization of wells GRT-1 and GRT-2 in Rittershoffen, France: implications on the understanding of natural flow systems in the rhine graben. Geothermics. 2017;65:255–68.
Baujard C, Genter A, Cuenot N, Mouchot J, Maurer V, Hehn R, Ravier G, Seibel O, Vidal J. Experience from a successful soft stimulation and operational feedback after 2 years of geothermal power and heat production in Rittershoffen and Soultz-sous-Forêts plants (Alsace, France). Reno: Geothermal Resources Council Transactions; 2018. p. 2241–52.
Clinton J, Grigoli F, Diehl T, Kraft T, Scarabello L, Hermann M, Kaestli P, Boese M, Wiemer S. Advanced real-time monitoring for natural and induced seismic sequences. In: Geophyscial Research Abracts, vol. 20, EGU General Assembly; 2018. **(abstract: EGU2018-9480-2)**.
Cornet FH. Comment on 'Large-scale in situ permeability tensor of rocks from induced microseismicity' by S. A. Shapiro, P. Audigane and J.-J. Royer. Geophys J Int. 2000; 140(2): 465–9.
Cornet FH, Bérard T, Bourouis S. How close to failure is a granite rock mass at a 5 km depth? Int J Rock Mech Min Sci Geomech Abstracts. 2007;44(1):47–66.
Cuenot N, Genter A. Microseismic activity induced during recent circulation tests at the Soultz-sous-Forêts EGS power plant. In: World geothermal congress 2015. World Geothermal Congress, Melbourne, Australia. April 20–24. IGA; 2015.
Cuenot N, Dorbath C, Dorbath L. Analysis of the microseismicity induced by fluid injections at the EGS site of Soultz-sous-Forêts (Alsace, France): implications for the characterization of the geothermal reservoir properties. Pure Appl Geophys. 2008;165(5):797–828.
Deichmann N, Giardini D. Earthquakes induced by the stimulation of an enhanced geothermal system below Basel (Switzerland). Seismol Res Lett. 2009;80(5):784–98.
Dezayes C, Genter A, Valley B. Structure of the low permeable naturally fractured geothermal reservoir at Soultz. CR Geosci. 2010;342(7–8):517–30.
Dorbath L, Cuenot N, Genter A, Frogneux M. Seismic response of the fractured and faulted granite of Soultz-sous-Forêts (France) to 5 km deep massive water injections. Geophys J Int. 2009;177(2):653–75.
Duringer P, Aichholzer C, Orciani S, Genter A. The complete lithostratigraphic section of the geothermal wells at Rittershoffen (Upper Rhine Graben, eastern France): a key for future geothermal wells. BSGF Earth Sci Bull; in press.
Edel JB, Maurer V, Dalmais E, Genter A, Richard A, Letourneau O, Hehn R. Structure and nature of the Palaeozoic basement based on magnetic, gravimetric and seismic investigations in the central Upper Rhinegraben. Geotherm Energy. 2018;6(1):747.
El-Isa ZH, Eaton DW. Spatiotemporal variations in the b-value of earthquake magnitude–frequency distributions: classification and causes. Tectonophysics. 2014;615–616:1–11.
Équipe du projet GeORG. Potentiel géologique profond du Fossé rhénan supérieur. Parties 1 à 4; 2013. http://www.geopotenziale.eu. Accessed 5 Apr 2019.
Ester M, Kriegel H-P, Sander J, Xu X. A density-based algorithm for discovering clusters in large spatial databases with noise. In: International conference on knowledge discovery and data mining (AAAI), Portland, OR, USA. August 2–4; 1996.
Evans KF, Zappone A, Kraft T, Deichmann N, Moia F. A survey of the induced seismic responses to fluid injection in geothermal and CO2 reservoirs in Europe. Geothermics. 2012;41:30–54.
Galis M, Ampuero JP, Mai PM, Cappa F. Induced seismicity provides insight into why earthquake ruptures stop. Sci Adv. 2017;3(12):eaap7528.
Ganz B, Schellschmidt R, Schulz R, Sanner B. Geothermal energy use in Germany. In: European geothermal congress 2013. European Geothermal Congress, Pisa, Italy. June 3–7; 2013.
Gaucher E, Maurer V, Wodling H, Grunberg M. Towards a dense passive seismic network over Rittershoffen geothermal field. In: European geothermal workshop 2013b, Strasbourg, France. October 24–25; 2013.

193

Gaucher E, Schoenball M, Heidbach O, Zang A, Fokker PA, van Wees J-D, Kohl T. Induced seismicity in geothermal reservoirs: a review of forecasting approaches. Renew Sustain Energy Rev. 2015;52:1473–90.

Gaucher E, Maurer V, Grunberg M. Temporary passive seismic data acquired at Rittershoffen geothermal field (Alsace, France, 2013–2014). Scientific Technical Report, GIPP Experiment and Data Archive, Potsdam, Germany; 2018.

Genter A, Evans K, Cuenot N, Fritsch D, Sanjuan B. Contribution of the exploration of deep crystalline fractured reservoir of Soultz to the knowledge of enhanced geothermal systems (EGS). Comptes Rendus Geosci. 2010;342(7–8):502–16.

Genter A, Baujard C, Cuenot N, Hehn R, Maurer V, Mouchot J, Seibel O, Vidal J. Exploiting fractured granites for producing heat or electricity—dream or reality? In: 80th EAGE conference and exhibition 2018. 80th EAGE conference and exhibition 2018, Copenhagen, Denmark. 6/11/2018–6/14/2018. EAGE Publications BV Netherlands; 2018.

Gentier S, Hosni A, Dezayes C, Genter A. Modélisation du comportement hydro-thermomécanique des milieux fracturés (module 1), Projet GEFRAC, Open file report No. BRGM/RP-52702-FR; 2004.

Glaas C, Genter A, Girard JF, Patrier P, Vidal J. Correction to: how do the geological and geophysical signatures of permeable fractures in granitic basement evolve after long periods of natural circulation? Insights from the Rittershoffen geothermal wells (France). Geotherm Energy. 2018a;6(1):243.

Glaas C, Genter A, Girard JF, Patrier P, Vidal J. How do the geological and geophysical signatures of permeable fractures in granitic basement evolve after long periods of natural circulation? Insights from the Rittershoffen geothermal wells (France). Geotherm Energy. 2018b;6(1):54.

Grigoli F, Boese M, Scarabello L, Diehl T, Weber B, Wiemer S, Clinton JF. Picking vs Waveform based detection and location methods for induced seismicity monitoring. In: Geophyscial Research Abracts, vol. 19, EGU General Assembly; 2017. **(abstract: EGU2017-10562)**.

Hanka W, Saul J, Weber B, Becker J, Harjadi P, Fauzi, GITEWS Seismology Group. Real-time earthquake monitoring for tsunami warning in the Indian Ocean and beyond. Nat Hazards Earth Syst Sci. 2010;10(12):2611–22. https://doi.org/10.5194/nhess-10-2611-2010

Hehn R, Genter A, Vidal J, Baujard C. Stress field rotation in the EGS well GRT-1 (Rittershoffen, France). In: European geothermal congress, Strasbourg, France. September 19–26; 2016.

Kaiser J. An investigation in the occurence of noises in tensile tests or a study of acoustic phenomena in tensile tests. Ph.D. Thesis. Tech. Hoch. München, Germany; 1950.

Kendall JM, Butcher A, Stork AL, Verdon JP, Luckett R, Baptie BJ. How big is a small earthquake? Challenges in determining microseismic magnitudes. First Break. 2019;37(2):51–6.

Kinnaert X, Gaucher E, Achauer U, Kohl T. Modelling earthquake location errors at a reservoir scale: a case study in the Upper Rhine Graben. Geophys J Int. 2016;206:861–79.

Küperkoch L, Olbert K, Meier T. Long-term monitoring of induced seismicity at the Insheim geothermal site, Germany. Bull Seismol Soc Am. 2018;108(6):3668–83.

Kwiatek G, Bulut F, Bohnhoff M, Dresen G. High-resolution analysis of seismicity induced at Berlín geothermal field, El Salvador. Geothermics. 2014;52:98–111.

Lavrov A. The Kaiser effect in rocks: principles and stress estimation techniques. Int J Rock Mech Min Sci. 2003;40(2):151–71.

Lengliné O, Boubacar M, Schmittbuhl J. Seismicity related to the hydraulic stimulation of GRT1, Rittershoffen, France. Geophys J Int. 2017;208(3):1704–15.

Lomax A. The NonLinLoc home page; 2018. http://alomax.free.fr/nlloc/. Accessed 15 May 2018.

Lomax A, Curtis A. Fast, probabilistic earthquake location in 3D models using oct-tree importance sampling. Geophys Res Abstr 3:955; 2001. http://www.alomax.net/nlloc/octtree. Accessed 15 May 2018.

Lomax A, Virieux J, Volant P, Berge-Thierry C. Probabilistic earthquake location in 3D and layered models. In: Thurber C, Rabinowitz N, editors. Advances in seismic event location, vol. 18., Modern approaches in geophysics-Dordrecht: Springer; 2000. p. 101–34.

Lomax A, Michelini A, Curtis A. Earthquake location, direct, global-search methods. In: Meyers RA, editor. Encyclopedia of complexity and systems science. New York: Springer; 2009. p. 2449–73.

Majer EL, Baria R, Stark M, Oates S, Bommer J, Smith B, Asanuma H. Induced seismicity associated with enhanced geothermal systems. Geothermics. 2007;36(3):185–222.

Maurer V, Cuenot N, Gaucher E, Grunberg M, Vergne J, Wodling H, Lehujeur M, Schmittbuhl J. Seismic monitoring of the Rittershoffen EGS project (Alsace, France). In: World geothermal congress 2015. World geothermal congress, Melbourne, Australia. April 20–24. IGA; 2015.

Maurer V, Perrinel N, Dalmais E, Richard A, Plevy L, Genter A. Towards a 3D velocity model deduced from 2D seismic processing and interpretation of in Northern Alsace (France). In: European geothermal congress 2016, Strasbourg, France. September 19–26; 2016.

McGarr A. Maximum magnitude earthquakes induced by fluid injection. J Geophys Res Solid Earth. 2014;119(2):1008–19.

Megies T, Wassermann J. Microseismicity observed at a non-pressure-stimulated geothermal power plant. Geothermics. 2014;52:36–49.

Meller C, Kohl T. The significance of hydrothermal alteration zones for the mechanical behavior of a geothermal reservoir. Geotherm Energy. 2014;2(1):12.

Nami P, Schellschmidt R, Schindler M, Tischner T. Chemical stimulation operations for reservoir development of the deep crystalline HDR/EGS system at Soultz-sous-Forêts (France). In: 33th workshop on geothermal reservoir engineering. 33th workshop on geothermal reservoir engineering, Stanford, CA, USA. January 28–30; 2008.

Poliannikov OV, Prange M, Malcolm A, Djikpesse H. A unified Bayesian framework for relative microseismic location. Geophys J Int. 2013;194(1):557–71.

Portier S, Vuataz F-D, Nami P, Sanjuan B, Gérard A. Chemical stimulation techniques for geothermal wells: experiments on the three-well EGS system at Soultz-sous-Forêts, France. Geothermics. 2009;38(4):349–59.

Sanjuan B, Millot R, Innocent C, Dezayes C, Scheiber J, Brach M. Major geochemical characteristics of geothermal brines from the Upper Rhine Graben granitic basement with constraints on temperature and circulation. Chem Geol. 2016;428:27–47.

Schindler M, Baumgärtner J, Gandy T, Hauffe P, Hettkamp T, Menzel H, Penzkofer P, Teza D, Tischner T, Wahl G. Successful hydraulic stimulation techniques for electric power production in the Upper Rhine graben, Central Europe, In: World geothermal congress 2010. World geothermal congress, Bali, Indonesia. April 25–29; 2010.

Scholz CH. The frequency-magnitude relation of microfracturing in rock and its relation to earthquakes. Bull Seismol Soc Am. 1968;58(1):399–415.

Schumacher ME. Upper Rhine Graben: role of preexisting structures during rift evolution. Tectonics. 2002;21(1):6.

Shapiro SA, Dinske C, Kummerow J. Probability of a given-magnitude earthquake induced by a fluid injection. Geophys Res Lett. 2007;34(22):L22314.

Snoke AJ. FOCMEC: FOCal MEChanism determinations; 2017. p. 31. http://www.iris.edu/pub/programs/focmec/. Accessed 17 Sept 2018.

Tarantola A, Valette B. Inverse problems = quest for information. J Geophys. 1982;50:159–70.

Vidal J, Genter A, Schmittbuhl J. Pre- and post-stimulation characterization of geothermal well GRT-1, Rittershoffen, France: insights from acoustic image logs of hard fractured rock. Geophys J Int. 2016;206:845–60.

Vidal J, Hehn R, Glaas C, Genter A. How can temperature logs help identify permeable fractures and define a conceptual model of fluid circulation? an example from deep geothermal wells in the upper rhine graben. Geofluids. 2019;2019:1–14.

Waldhauser F, Ellsworth WL. A double-difference earthquake location algorithm: method and application to the Northern Hayward fault, California. Bull Seismol Soc Am. 2000;90(6):1353–68.

Wang HF, Bonner BP, Carlson SR, Kowallis BJ, Heard HC. Thermal stress cracking in granite. J Geophys Res Solid Earth Planets. 1989;94(B2):1745.

Wiemer S, Wyss M. Minimum magnitude of completeness in earthquake catalogs: examples from Alaska, the western United States, and Japan. Bull Seismol Soc Am. 2000;90(4):859–69.

Zang A, Oye V, Jousset P, Deichmann N, Gritto R, McGarr A, Majer E, Bruhn D. Analysis of induced seismicity in geothermal reservoirs—an overview. Geothermics. 2014;52:6–21.

Ziegler PA. European cenozoic rift system. Tectonophysics. 1992;208(1–3):91–111.

Publisher's Note

Appendix B

Accuracy of the PPFN

Table B.1 – Quantification of the results for the application of the PPFN to dataset 2a for the different weighting methods and parameters, $\sigma_f = 5°$.

Method	Center as easting/northing/depth (deviation from true center in m)	Dip/dip direction in ° (deviation from true value in °)		Determined dimension of the planes (m) length/width/height		Mean distance from plane (m)	
Synthetic dataset 2a: σ_d and $\sigma_M(\overline{M}) = 250$ m							
Distance PPFN	0.45/1.45/0.97 (77.24)	47.6/220.0 (2.6/39.9)	51.1/205.0 (6.1/25.0)	740/650/640	640/650/600	116	138
Magnitude PPFN	0.45/1.45/0.98 (68.44)	48.3/225.4 (3.3/45.4)	52.7/217.6 (7.7/37.6)	780/650/670	600/550/600	123	130
Distance and focal mechanism PPFN	0.53/1.36/0.90 (178.03)	44.8/180.4 (0.3/0.4)	45.2/180.6 (0.2/0.6)	1060/950/70	850/900/70	162	176
Magnitude and focal mechanism PPFN	0.54/1.37/0.90 (169.61)	44.7/180.3 (0.3/0.3)	45.6/180.8 (0.6/0.8)	1060/950/70	850/850/40	152	181
Synthetic dataset 2a: σ_d and $\sigma_M(\overline{M}) = 125$ m							
Distance PPFN	0.49/1.43/0.97 (74.78)	48.0/194.3 (3.0/14.3)	47.3/179.0 (2.3/1.0)	600/400/350	530/400/350	54	77
Magnitude PPFN	0.49/1.45/0.98 (54.61)	45.6/184.0 (0.5/4.0)	46.2/177.7 (1.2/2.2)	600/450/390	490/400/350	57	74
Distance and focal mechanism PPFN	0.49/1.42/0.97 (84.84)	44.6/180.9 (0.4/0.9)	44.0/178.8 (1.0/1.2)	710/500/180	570/550/180	69	67
Magnitude and focal mechanism PPFN	0.49/1.44/0.98 (63.38)	44.8/181.0 (0.2/0.9)	44.5/179.6 (0.5/0.5)	710/550/180	650/600/180	78	75
Synthetic dataset 2a: σ_d and $\sigma_M(\overline{M}) = 83$ m							
Distance PPFN	0.49/1.43/0.97 (74.58)	46.8/179.2 (1.8/0.8)	46.1/179.9 (1.1/0.1)	490/250/210	420/300/210	31	45
Magnitude PPFN	0.49/1.43/0.97 (76.59)	46.8/181.5 (1.8/1.5)	45.8/179.8 (0.8/0.2)	530/250/210	420/300/210	49	49
Distance and focal mechanism PPFN	0.49/1.42/0.96 (88.83)	46.1/181.4 (1.1/1.4)	45.3/181.7 (0.3/1.7)	570/350/140	570/400/180	48	56
Magnitude and focal mechanism PPFN	0.49/1.42/0.96 (88.55)	45.7/181.6 (0.7/1.6)	45.4/181.6 (0.4/1.6)	570/350/140	570/450/180	50	61

Table **B.2** – Quantification of the results for the application of the combined magnitude and focal mechanism PPFN to dataset 2a for different values for σ_f and with/without random choice of nodal plane.

Method: Magnitude and focal mechanism PPFN	Center as easting/northing/depth (deviation from true center in m)	Dip/dip direction in ° (deviation from true value in °)		Determined dimension of the planes (m) length/width/height		Mean distance from plane (m)	
Synthetic dataset 2a: $\sigma_M(\overline{M}) = 250$ m and $\sigma_f = 5°$							
Variation of focal mech. on plane by 5°	0.52/1.46/1.00 (44.77)	46.5/180.4 (1.5/0.4)	42.5/180.5 (2.5/0.5)	810/800/40	710/800/210	130	135
Random choice between nodal planes	0.50/1.45/1.00 (46.38)	43.1/180.5 (1.9/0.5)	45.1/181.8 (0.1/1.8)	490/650/70	280/500/40	106	86
Synthetic dataset 2a: $\sigma_M(\overline{M}) = 250$ m and $\sigma_f = 10°$							
Variation of focal mech. on plane by 10°	0.43/1.45/0.99 (82.28)	43.8/179.9 (1.2/0.1)	44.9/182.1 (0.1/2.1)	780/700/250	640/600/140	114	117
Random choice between nodal planes	0.49/1.41/0.94 (102.83)	41.8/186.7 (3.2/6.7)	40.2/185.1 (4.8/5.1)	350/400/180	350/450/250	42	112
Synthetic dataset 2a: $\sigma_M(\overline{M}) = 250$ m and $\sigma_f = 20°$							
Variation of focal mech. on plane by 20°	0.45/1.45/1.01 (70.66)	40.7/186.0 (4.3/6.0)	43.5/177.8 (1.5/2.3)	740/650/420	710/700/460	118	126
Random choice between nodal planes	0.43/1.42/0.98 (112.04)	48.1/193.1 (3.1/13.1)	32.7/177.7 (12.3/2.4)	780/700/530	600/650/490	128	124